Universidade do Minho
Escola de Ciências

Cátia Sofia dos Santos Pereira

Novel insights on the interaction of lactoferrin with proton pumping ATPases towards understanding its antifungal and anticancer activities

maio de 2021

Novel insights on the interaction of lactoferrin with proton pumping ATPases towards understanding its antifungal and anticancer activities

Cátia Sofia dos Santos Pereira

Uminho | 2021

Universidade do Minho
Escola de Ciências

Cátia Sofia dos Santos Pereira

Novel insights on the interaction of lactoferrin with proton pumping ATPases towards understanding its antifungal and anticancer activities

Tese de Doutoramento em Biologia
Especialidade em Biologia Celular e Saúde

Trabalho efetuado sobre a orientação de:
Professora Doutora Manuela Côrte-Real
Professora Doutora Lígia Rodrigues

maio de 2021

DIREITOS DE AUTOR E CONDIÇÕES DE UTILIZAÇÃO DO TRABALHO POR TERCEIROS

ACKNOWLEDGEMENTS

É com muita alegria que inicio esta tese agradecendo às inúmeras pessoas que me acompanharam ao longo desta caminhada e que me deram força e carinho para continuar em frente mesmo nas alturas mais difíceis. A todas elas o meu sincero obrigada!

Em primeiro lugar quero agradecer às duas pessoas sem as quais este trabalho não seria possível, às minhas orientadoras, mentores, conselheiras... Professoras Manuela e Lígia! É impossível descrever num parágrafo o quanto vos estou grata e quão sortuda me sinto pelas nossas vidas se terem cruzado há já 8 anos atrás. Vocês acompanham-me desde os meus primeiros passinhos na Ciência. Obrigada de coração por toda a confiança que sempre depositaram em mim, por toda a aprendizagem que me proporcionaram e por me terem feito crescer enquanto investigadora e pessoa.

Não posso também deixar de agradecer à Susana Chaves e ao professor Hernâni por me terem também acompanhado e apoiado ao longo dos anos e por sempre contribuírem com ideias excelentes para o meu trabalho, obrigada pelo vosso apoio e disponibilidade. Muchas gracias Fernando y Teresa por haberme recebido en Oviedo, lo he pasado genial y espero visitaros pronto en Asturias! Stéphen, Nadine et Muriel, merci beaucoup de m'avoir reçu et pour tout l'apprentissage!

Quero deixar também um enorme agradecimento ao Sérgio e a todo o BioSIM: professor Nuno, Henrique, Juliana, Rita, André, Tatiana, Carla, Carlos, Cristina, Andreia, Pedro e Fábio, muito obrigada por me terem acolhido tão bem, senti-me perfeitamente integrada desde a primeira vez que entrei no BioSIM. Foi uma jornada de enorme aprendizagem e desafios diários que não teria um desfecho tão bom se não fosse pela vossa amizade e paciência inacabável para esclarecer todas as minhas dúvidas. Mesmo quando achava que ia ser impossível realizar uma determinada tarefa vocês estavam sempre lá para não me deixarem desanimar e para me ajudar. Foi espetacular ter aprendido todas estas ferramentas computacionais que me serão certamente muito úteis no futuro.

Agradeço também ao programa doutoral em Microbiologia Aplicada e Ambiental (DP_AEM) na pessoa da professora Margarida Casal e à Fundação para a Ciência e Tecnologia pelo financiamento através da bolsa PD/BD/128032/2016. Fazer parte deste programa doutoral foi uma experiência incrível por todas as aprendizagens e intercâmbio de ideias que nos proporcionou e por me ter levado a conhecer pessoas incríveis, obrigada a todos os meus colegas do DP_AEM, nunca vou esquecer aquele Santo António memorável!

Nenhum trabalho científico é possível sem trabalho de equipa e eu sou uma sortuda por ter os melhores colegas do mundo ao meu lado, todos os dias!! Vocês fazem com que qualquer mau resultado

seja encarado com um sorriso na cara e com que aquelas experiências intermináveis sejam divertidas, foi um enorme prazer trabalhar, cantar, rir, dançar, conversar convosco amigos!! Meus meninos da Micro I: Joana, Fi, António, Vitória, Marta, Leslie, Joana Terra, Flávia, Ritas, João, Anabela e todos os que por lá passaram! Amigos dos labs vizinhos que tantas vezes me ajudaram com material/ideias mas muitas mais vezes com uma palavra amiga ou com aquele abraço, Gusto, minha Cat, Anabela, Joaninha, muito obrigada por estarem lá. A todos os outros amigos do DB que fizerem com que cada ida ao fundo do corredor buscar material se tornasse muito mais animada Maria, Guida, Mário, Clau, Bárbara, pessoal do LBA, LBV, ... é impossível nomear toda a gente, o meu sincero obrigada. Não posso também esquecer as minhas meninas das células, Débora e Diana, que estavam sempre lá quando eu precisava, juntas conseguimos decifrar os mistérios das células mesmo quando parecia que elas tinham vontade própria. Obrigada ao CBMA, ao CEB, ao BIOVAL e a todo o pessoal técnico por me terem acolhido, por toda a disponibilidade e por fazerem com que nada nos faltasse, obrigada em especial à Manela, Sr. Luís, Núria, Lídia, Inês, Diana Vilas Boas, Paula e Nicole.

E porque uma vida sem amigos é uma vida muito triste e porque eles foram os principais responsáveis pela minha sanidade mental ao longo deste percurso, não posso deixar de agradecer aos meus amigos do coração, os que estão sempre lá e nunca me deixam cair e que sabem sempre o que dizer para me fazerem sentir melhor! Às minhas daminhas Mana, Tatxi, Rita, Paty, Duda, Joana; às minhas meninas do "Grupo" Soraia, João, Ângela, Aninha, Laçinho; aos meus malucos do "Gang Machado" Nuno, António, Fi, Tatxi, Jo, TT, Beli, Carlinha, Rita, Taty; e aos meus bailarinos Dani, Barbosa, Durães, Bruna, Sara e Márcia. Obrigada por fazerem parte da minha vida e me fazerem sorrir.

E por fim, mas não menos importante, quero agradecer a toda a minha linda família por fazerem de mim quem sou. Quero que saibam que me sinto uma sortuda por fazer parte desta grande família e que os nossos encontros são dos momentos mais felizes da minha vida e das minhas memórias mais felizes que tenho de criança. A todos os meus tios e primos que sempre acreditaram em mim. Aos meus lindos avós que são os meninos dos meus olhos e a minha inspiração. Ao meu irmão por estar sempre lá mesmo que seja para andarmos à "batatada". Àquele que já era e que durante o doutoramento se tornou oficialmente o homem da minha vida, o meu pilar, o meu porto de abrigo e a fonte da minha alegria: João. É impossível descrever em palavras tudo o que significas para mim e escusado será dizer que sem ti e sem o teu apoio nada disto seria possível. E àqueles que nada do que eu possa escrever fará jus a tudo o que representam para mim: os meus pais. Obrigada por tudo o que sempre fizeram e continuam a fazer por mim, por sempre me apoiarem e por me tornarem uma melhor pessoa a cada dia. A todos vocês eu dedico este trabalho!

STATEMENT OF INTEGRITY

I hereby declare having conducted this academic work with integrity. I confirm that I have not used plagiarism or any form of undue use of information or falsification of results along the process leading to its elaboration.

I further declare that I have fully acknowledged the Code of Ethical Conduct of the University of Minho.

ABSTRACT

NOVEL INSIGHTS ON THE INTERACTION OF LACTOFERRIN WITH PROTON PUMPING ATPASES TOWARDS UNDERSTANDING ITS ANTIFUNGAL AND ANTICANCER ACTIVITIES

Lactoferrin (Lf) is a naturally occurring iron-binding protein and one of the most well-known milk bioactive compounds. In addition to milk, it is also found in different fluids of mammals including several mucosal surfaces. A multitude of biological activities, such as antimicrobial, antiviral, immunomodulatory and anticancer, have been ascribed to this protein, revealing its multifunctional character. Among them, its antifungal and anticancer activities stand out, as toxicity against a wide collection of yeasts and filamentous fungi, and a broad range of cancer types has been demonstrated. However, the molecular mechanisms underlying these activities are still poorly elucidated, which limits Lf applications as an anticancer and antifungal agent. In the present thesis, we sought to improve the current knowledge on the mechanisms through which Lf exerts its cytotoxicity against fungal and cancer cells, aiming to contribute to its rational, targeted and more efficient application. Since previous studies have identified proton pumping ATPases as Lf molecular targets, we focused on exploring the interaction between Lf and these proton pumps, as well as on the consequences of these interactions. A combination of biochemical, genetic and computational approaches was employed to attain the envisioned goals. Our work revealed a novel effect of bovine Lf (bLf) against yeast, that was further validated in cancer cells, through perturbation of ergosterol/cholesterol-rich lipid rafts, membrane microdomains that function as platforms for signalling and protein trafficking. These results reinforced the advantages of using yeast as a simple unicellular eukaryotic complementary model to elucidate the mechanisms underlying the anticancer activity of Lf. These alterations were intimately related with the bLf inhibitory effect towards the proton pump Pma1p in yeast, and V-ATPase in both yeast and cancer cells. Specifically, we found that lipid rafts composition, as well as Pma1p-lipid rafts association are critical for bLf yeast killing activity. Regarding bLf anticancer activity, we showed that bLf-driven lipid rafts disruption is associated with cellular trafficking perturbations, downregulation of components of the PI3K/AKT signalling pathway and inhibition of glycolysis. The computational approach herein developed allowed to predict a mechanism of Lf-induced V-ATPase inhibition, and to identify critical residues for their interaction. Altogether, the work developed in this thesis uncovered novel cellular and molecular events triggered by Lf in the context of its antifungal and anticancer activities that have great potential to pave the way for future Lf-based applications.

Keyworks: cancer, fungi, lactoferrin, Pma1p, V-ATPase

RESUMO

NOVOS CONTRIBUTOS SOBRE A INTERAÇÃO DA LACTOFERRINA COM BOMBAS DE PROTÕES ATPASES PARA A COMPREENSÃO DAS SUAS ATIVIDADES ANTIFÚNGICA E ANTICANCERÍGENA

A lactoferrina (Lf) é uma proteína natural que se liga a ferro e um dos compostos bioativos do leite mais conhecidos. A Lf está também presente em diferentes fluidos de mamíferos incluindo em várias mucosas. Diversas atividades biológicas, como antimicrobiana, antiviral, imuno-moduladora e anticancerígena têm sido atribuídas à Lf, revelando o seu caráter multifuncional. Destas, destacam-se as suas atividades antifúngica e anticancerígena que já foram demonstradas contra várias espécies de leveduras e fungos filamentosos, bem como contra vários tipos de cancro, respetivamente. No entanto, os mecanismos moleculares subjacentes a essas atividades são ainda pouco conhecidos, limitando as aplicações da Lf como agente antifúngico e anticancerígeno. Na presente tese, pretendemos melhorar o conhecimento dos mecanismos pelos quais a Lf exerce citotoxicidade contra fungos e células de cancro, e assim contribuir para sua aplicação mais racional, direcionada e eficiente. Dado que estudos anteriores identificaram as bombas de protões ATPases como alvos moleculares da Lf, focámos o nosso trabalho na interação entre a Lf e estas bombas bem como nas suas consequências. Usámos uma combinação de abordagens bioquímicas, genéticas e computacionais para atingir os objetivos propostos. Os resultados revelaram um novo efeito de Lf bovina (bLf) que consiste na perturbação de microdomínios lipídicos ricos em ergosterol/colesterol, os quais funcionam como plataformas para sinalização e tráfego de proteínas. Estes resultados reforçam o uso da levedura como modelo unicelular eucariota complementar para elucidar os mecanismos subjacentes à atividade anticancerígena da Lf. Essas alterações estão relacionadas com o efeito inibidor da Lf sobre as bombas de protões Pma1p da levedura e V-ATPase da levedura e de células de cancro. Especificamente, descobrimos que a composição dos microdomínios lipídicos, bem como a associação destes com a Pma1p, são críticas para a atividade da bLf contra leveduras. Relativamente à sua atividade anticancerígena, demonstrámos que a perturbação dos microdomínios lipídicos induzida pela bLf está associada a perturbações de tráfego celular, a diminuição da expressão de componentes da via de sinalização PI3K/AKT e a inibição da glicólise. Por fim, a abordagem computacional aqui desenvolvida permitiu prever o mecanismo pelo qual a Lf inibe a V-ATPase e identificar resíduos críticos para esta interação. Resumindo, este trabalho permitiu avançar o conhecimento sobre os eventos celulares e moleculares desencadeados pela Lf no contexto das suas atividades antifúngica e anticancerígena com potencial para abrir caminho para futuras aplicações da Lf.

Palavras-chave: cancro, fungos, lactoferrina, Pma1p, V-ATPase

TABLE OF CONTENTS

OUTPUTS

Peer-reviewed publications

- Cátia Santos-Pereira, Lígia R. Rodrigues, Manuela Côrte-Real (2021) Emerging insights on the role of V-ATPase in human diseases: therapeutic challenges and opportunities. *Medicinal Research Reviews*. doi: 10.1002/ med.21782
- Cátia Santos-Pereira, María T. Andrés, Susana R. Chaves, José F. Fierro, Hernâni Gerós, Stéphen Manon, Lígia R. Rodrigues, Manuela Côrte-Real (2021) Lactoferrin perturbs lipid rafts and requires integrity of Pma1p-lipid rafts association to exert its antifungal activity against *Saccharomyces cerevisiae*. *International Journal of Biological Macromolecules*. 171:343-357. doi:10.1016/j.ijbiomac.2020.12.224
- Cátia Santos-Pereira, Joana P. Guedes, Débora Ferreira, Lígia R. Rodrigues, Manuela Côrte-Real. Lactoferrin disrupts cholesterol-rich lipid rafts of highly metastatic cancer cells inhibiting PI3K/AKT/mTOR pathway and glycolysis. Under review in *Biochemical Pharmacology*
- Cátia Santos-Pereira, Juliana F. Rocha, Henrique S. Fernandes, Lígia R. Rodrigues, Manuela Côrte-Real, Sérgio F. Sousa. The milk-derived lactoferrin inhibits V-ATPase activity by targeting its V1 domain. Under minor revision in the *International Journal of Biological Macromolecules*
- Cátia Santos-Pereira, María T. Andrés, Fernando F. Fierro, Lígia R. Rodrigues, Manuela Côrte-Real. Lactoferrin as a novel proton pump inhibitor. *Manuscript in preparation*

Book chapter

- Jorge Rodrigues*, Cátia Santos-Pereira*, Natasha Fontes, Hernâni Gerós, Manuela Côrte-Real M (2018) Flow Cytometry and Fluorescence Microscopy as Tools for Structural and Functional Analysis of Vacuoles Isolated from Yeast and Plant Cells. In Cláudia Pereira (eds), Plant Vacuolar Trafficking, vol. 1789, chapter 8. ISBN: 978-1-4939-7855-7. doi: 10.1007/978-1-4939-7856-4_8

  *Both authors contributed equally

Oral communications

- Cátia Santos-Pereira, Juliana F. Rocha, Henrique S. Fernandes, Lígia R. Rodrigues, Manuela Côrte-Real, Sérgio F. Sousa (2021) "Deciphering the interaction of lactoferrin with V-ATPase towards a deeper understanding of its mechanisms of action", X Bioinformatics Open Days, Braga, Portugal

- Cátia Santos-Pereira, Joana P. Guedes, Hernâni Gerós, Lígia R. Rodrigues, Manuela Côrte-Real (2019) "Lactoferrin is selectively cytotoxic for highly metastatic cancer cells by inhibiting plasmalemmal V-ATPase", 14th International Conference on Lactoferrin Structure, Function and Applications, Lima, Peru
- Cátia Santos-Pereira, Joana P. Guedes, Susana R. Chaves, Hernâni Gerós, Lígia R. Rodrigues, Manuela Côrte-Real (2018) "How can a milk protein selectively kill cancer cells? Mechanisms underlying lactoferrin-induced apoptosis", 26th Euroconference on Apoptosis: Cell death in disease: from small molecules to translational medicine, Saint Petersburg, Russia
- Cátia Santos-Pereira, Joana P. Guedes, Susana R. Chaves, María T. Andrés, José F. Fierro, Hernâni Gerós, Lígia R. Rodrigues, Manuela Côrte-Real (2018) "Deciphering the mechanisms underlying bovine milk lactoferrin anticancer activity using yeast and cancer cell lines as complementary models", XXI Jornadas de Biologia de Leveduras "Professor van Uden, Braga, Portugal
- Cátia Santos-Pereira, Joana P. Guedes, Marília Gonçalves, Luís Loureiro, Lisandra Castro, Hernâni Gerós, Lígia R. Rodrigues, Manuela Côrte-Real (2018) "How can a milk protein selectively kill cancer cells?", Seminars of the Department of Biology, University of Minho, Braga, Portugal
- Cátia Santos-Pereira, Joana P. Guedes, Susana R. Chaves, Hernâni Gerós, Lígia R. Rodrigues, Manuela Côrte-Real (2017) "Understanding the interplay between the pro-apoptotic protein lactoferrin and biomembranes: from yeast to human cells", 12th International meeting on yeast apoptosis (IMYA), Bari, Italy

Awards

- Best poster presentation award at the symposium "Molecular Microbiology and Microbial Physiology" from MICROBIOTEC 17, held at Porto, Portugal from 7 to 9th December 2017 (Chapter 3)
- Scholarship attributed by the European Cell Death Organization (ECDO) to the 26th Conference of the European Cell Death Organization held at Saint Petersburg, Russia from 10 to 12th October 2018 (Chapter 4)
- Student award of the "14th International Conference on Lactoferrin: Structure, Function and Applications" held at Lima, Peru from 4 to 8th November 2019 (Chapter 4)
- Best poster presentation award at "Encontro de Jovens Investigadores de Biologia Computacional Estrutural" held at Lisboa, Portugal on 20th December 2019 (Chapter 5)

LIST OF ABBREVIATIONS AND ACRONYMS

[ATP]i	**i**ntracellular **ATP** concentration
2-DG	**2-D**eoxy-D-**G**lucose
ABC	**A**TP **B**inding **C**assete
ACMA	9-**A**mino-6-**C**hloro-2-**M**ethoxy**a**cridine
AHA2	*A**rabidopsis thaliana*** **H**1-**A**TPase **2**
AKT	Protein kinase B
AmpB	**Amp**hothericin **B**
ANOVA	**An**alysis **o**f **Va**riance
ATCC	**A**merican **T**ype **C**ulture **C**ollection
ATP	**A**denosine **Tri**phosphate
au	**a**rbitrary **u**nits
BafA1	**Baf**ilomycin **A1**
bLf	**b**ovine **L**acto**f**errin
bs	**b**est **s**olution
BSA	**B**ovine **S**erum **A**lbumin
c.f.u	**c**olony **f**orming **u**nits
C2-cer	**C2-cer**amide
carboxy-DCFDA	5-(and-6)-**carboxy**-2',7'-**D**i**c**hloro**f**luorescein **D**i**a**cetate
CAT	**Cat**alase
CD	**C**luster of **D**ifferentiation
CHL	**Ch**o**l**esterol
CIVS	**C**ylindrical **I**ntra**v**acuolar **S**tructures
CNS	**C**entral **N**ervous **S**ystem
ConcA	**Conc**anamycin **A**
cryo-EM	**Cryo**-**E**lectron **M**icroscopy
cyt	**Cyt**osol
Cα-RMSD	Backbone **R**oot-**M**ean-**S**quare **D**eviation
DAPI	4′,6-**Dia**midino-2-**P**heny**l**indole
DES	**Die**thyl**s**tilbestrol
DFT	**D**ensity **F**unctional **T**heory
DMEM	**D**ulbecco's **M**odified **E**agle's **M**edium
DMSO	**Dim**ethyl **S**ul**f**oxide
DNA	**D**eoxyribo**n**ucleic **A**cid
DOPC	**Dio**leoyl **P**hosphatidyl**c**holine
DPPC	**Dip**almitoyl **P**hosphatidyl**c**holine
DRMs	**D**etergent **R**esistant **M**embrane**s**
DTT	**Dith**io**th**reitol
ECAR	**E**xtra**c**ellular **A**cidification **R**ate
EDTA	**E**thylene**d**iamine **T**etraacetic **Acid**
EFSA	**E**uropean **F**ood **S**afety **A**uthority
EGF	**E**pidermal **G**rowth **F**actor
EGFR	**E**pidermal **G**rowth **F**actor **R**eceptor

EGTA	**E**thylene **G**lycol **T**etraacetic **A**cid
EMT	**E**pithelial-to-**M**esenchymal **T**ransition
ER	**E**ndoplasmic **R**eticulum
ext	**ext**racellular millieu
FBS	**F**etal **B**ovine **S**erum
FC	**F**low **C**ytometry
FCC	**F**raction of **C**ommon **C**ontacts
FITC	**F**luorescein-5-**I**so**th**io**c**yanate
GAGs	**G**lycos**a**mino**g**lycan**s**
GB	**G**eneralized **B**orn
GF	**G**rowth **F**actor
GFP	**G**reen **F**luorescent **P**rotein
GPI	**G**lycosyl**p**hosphatidyl**i**nositol
HADDOCK	**H**igh **A**mbiguity **D**riven protein–protein **Dock**ing
HIF-1	**Hy**poxia-**I**nducible **F**actor **1**
hLf	**h**uman **L**acto**f**errin
HS	**H**addock **S**core
IF	**I**mmuno**f**luorescence
IL-1, -2, -6	**I**nter**l**eukin-**1, 2, -6**
LCPO	**L**inear **C**ombinations of **P**airwise **O**verlaps
Ld	**L**iquid **d**isordered
Lf	**L**acto**f**errin
Lfampin	**L**acto**ferr**a**mpin**
Lfcin	**L**acto**ferri**c**in**
LINCS	**Lin**ear **C**onstraint **S**olver
Lo	**L**iquid **o**rdered
LPS	**L**ipo**p**oly**s**accharide
lys	**lys**osome
MCPB	**M**etal **C**enter **P**arameter **B**uilder
MD	**Mo**lecular **D**ynamics
MM-GBSA	**M**olecular **M**echanics-**G**eneralized **B**orn **S**urface **A**rea
MMP	**M**atrix **M**etallo**p**roteinases
MOPS	3-(N-**M**orph**o**lino)**P**ropane **S**ulfonic Acid
mRNA	**m**ensenger **R**ibo**n**ucleic **A**cid
mTOR	**m**ammalian **T**arget **o**f **R**apamycin
mTORC1/2	**mTOR C**omplex **1/2**
MβCD	**M**ethyl-**β**-c**yclod**extrin
NK	**N**atural **k**iller
ns	**n**ano**s**econds
NSCLC	**N**on-**S**mall **C**ell **L**ung **C**ancer
OD640	**O**ptical **D**ensity at **640** nm
PBS	**P**hosphate **B**uffered **S**aline
PC	**P**rimary **C**ulture
PCR	**P**olymerase **C**hain **Re**action
PDK1	**P**hosphoinositide **D**ependent **K**inase-**1**
PFA	**P**ara**form**a**l**dehyde

Pgk1	**P**hospho**g**lycerate **K**inase 1
pHe	**ext**racellular **pH**
pHi	**i**ntracellular **pH**
pHlys	**lys**osomal **pH**
pHvac	**vac**uolar **pH**
Pi	**i**norganic **P**hosphate
PI3K	**P**hospho**i**nositide **3**-**k**inase
PIP2	**P**hosphatidyl**i**nositol 4,5-Bi**p**hosphate
PIP3	**P**hosphatidyl**i**nositol 3,4,5-Tri**p**hosphate
PM	Plasma Membrane
PMA1	**P**lasma **M**embrane **A**TPase **1**
PMSF	**P**henyl**m**ethyl**s**ulfonyl **F**luoride
POPA	1-**P**almitoyl-2-**O**leoyl **P**hosphatidyl**a**mine
POPE	1-**P**almitoyl-2-**O**leoyl **P**hosphatidyl**e**thanolamine
POPS	1-**P**almitoyl-2-**O**leoyl **P**hosphatidyl**s**erine
PPIs	**P**roton **P**ump **I**nhibitor**s**
rhLf	**r**ecombinant **h**uman **L**acto**f**errin
RMSD	**R**oot-**M**ean-**S**quare **D**eviation
RMSF	**R**oot-**M**ean-**S**quare **F**luctuation
RNA	**R**ibo**n**ucleic **A**cid
ROS	**R**eactive **o**xygen **s**pecies
rRNA	**r**ibosomal **R**ibo**n**ucleic **A**cid
RT	**R**oom **t**emperature
RTK	**R**eceptor **T**irosine **K**inase
SASA	**S**olvent **A**ccessible **S**urface **A**rea
SC Glu	**S**ynthetic **C**omplete **Glu**cose
SDS	**S**odium **D**odecyl **S**ulfate
SEM	**S**tandard **E**rror of the **M**ean
shRNA	**s**hort **h**airpin **R**ibo**n**ucleic **A**cid
siRNA	**s**mall **i**nterfering **R**ibo**n**ucleic **A**cid
SOD	**S**uper**o**xide **D**ismutase
SRB	**S**ulfo**r**hodamine **B**
TBS	**T**ris-**B**uffered **S**aline
TFP	**T**etra**f**luoro**p**henyl
TME	**T**umor **M**icro**e**nvironment
TS	**T**issue **S**ections
V-ATPase	**V**acuolar-**ATPase**
vac	**vacuole**
VDW	**V**an **d**er **W**aals
VEGF	**V**ascular **E**ndothelial **G**rowth **F**actor
VMD	**V**isual **M**olecular **D**ynamics
VVC	**V**ulvo**v**aginal **C**andidiasis
WB	**W**estern **b**lot
YEPD	**Y**east **E**xtract-**P**eptone-**D**extrose
Ψpm	**p**lasma **m**embrane potential

LIST OF FIGURES

LIST OF TABLES

CHAPTER 1

Motivation, aims and thesis outline

1.1 Motivation

"*Basic science ... provides the essential raw material for translation and ... represents humanity's best hope to meet a wide range of public health challenges*" [1]

The search for the mechanisms of action of a given drug or compound is of paramount importance for drug discovery and development. The most intelligent and effective route to approve a drug is to perform mechanistic studies aiming to find how the drug works and what its targets are. This helps driving and focusing clinical trials in patients that are most likely to respond, promotes a more accurate and sharp evaluation of both drug effectiveness and side effects, increasing the chances of drug success/approval and preventing failures in the late stages of clinical trials [2,3]. Hence, the knowledge provided by decoding the drugs mechanisms of action "can save money, time and, most importantly, the lives of patients" [2]. The combination of cell-based assays, which allow the discovery of such mechanisms in a more disease-like context, with biochemical, genetic and computational methods has been regarded as an effective path for finding both the targets and modes of action of drugs [4]. Translational medicine should thus go hand-in-hand with basic science to fuel drug development pipelines with mechanistic insights that will prompt clinically effective outcomes and avoid off-target effects. All in all, successful translational medicine is that aiming to "build a bridge that extends from the laboratory to the clinic to the community" [3].

In the present thesis, the mechanisms underlying the action of a multifunctional milk-derived protein called lactoferrin (Lf) were studied, and several steps of the intricate cascade of molecular events triggered by this protein were unraveled. Lf holds several special features that sustain its well-recognized potential as a therapeutic agent against a wide variety of human diseases, from which cancer and fungal infections were deeply explored in this thesis. First, it is a natural low-cost and non-toxic dietary protein, which shows reduced toxicity, side effects and drug resistance risk when applied in humans. At the same time, its intake exerts several beneficial effects including modulation of the immune system, improvement of the intestinal microbial flora, cancer prevention and treatment, antimicrobial, antioxidant and anti-inflammatory effects [5,6]. Two additional features contribute to the great potential of Lf for various applications: (i) owing to its well-established large-scale manufacturing process, it is widely available and is produced by several companies worldwide [7]; (ii) it has been approved by the European Food Safety Authority (EFSA) as a safe ingredient for various applications, including for medical purposes [8]. As such, nowadays, there are different Lf-containing commercial products such as infant formula, prebiotic foods,

yogurts, pet food and skin and oral care products [9]. As a curiosity, Lf is one of the few proteins with its own dedicated congress, highlighting its importance as a multifunctional macromolecule (last conference: https://www.lactoferrinconference2019.com).

1.2 Aims

Inspired by the promising results documented in *in vitro*, pre-clinical and clinical studies regarding the strong Lf antifungal and anticancer activities [10–14], and by the fact that there's still room for improvement [15], while believing that unveiling the Lf mechanisms of action is the key for its successful application, the main research aims of this thesis were:

- to uncover the molecular mechanisms underlying Lf antifungal activity by exploring its previously reported interaction with the fungal proton pumping ATPase Pma1p, and the close interplay between Pma1p and special membrane niches called ergosterol-rich lipid rafts;

- to elucidate the cascade of molecular events triggered by Lf in cancer cells by studying its inhibitory action towards the proton pump V-ATPase, and the consequences of this interaction in terms of cholesterol-rich lipid rafts, cell signalling, intracellular trafficking and glycolytic metabolism;

- to decipher how Lf interacts with V-ATPase by implementing a computational approach that aims to predict and evaluate the V-ATPase-Lf complexes and identify the key binding residues, to ultimately achieve a better understanding of this interaction in both yeast and cancer cells.

This work presents an interesting set of data that brings novel insights on the mechanisms through which Lf exerts cytotoxicity against fungal and highly metastatic cancer cells, which will certainly pave the way for more rational and targeted studies aiming to potentiate Lf clinical effectiveness against cancer and fungal infections.

1.3 Thesis Outline

The present thesis is organized according to its specific goals as depicted in Figure 1.1.

- In **Chapter 1,** an overview of the motivation, aims and thesis organization is provided.

- **Chapter 2** comprises a general introduction that aims to contextualize the reader in the different topics addressed in this thesis. It starts by exploring the features of Lf with special focus on its multifunctionally and detailing the clinical studies and mechanisms described so far regarding its antifungal and anticancer activities. Afterwards, the importance and characteristics of the proton pumping ATPases Pma1p and V-ATPase in fungal and cancer cells, respectively, is provided. Finally, the interactions of Lf with proton pumping ATPases, as well as their interplay with membrane microdomains called lipid rafts are highlighted.

- **Chapter 3** includes the work performed to unravel the molecular basis of the antifungal activity of Lf. The yeast *Saccharomyces cerevisiae* is used as a model organism, and the effect of Lf on lipid rafts, and on mutant strains lacking lipid rafts associated proteins or enzymes that are involved in the synthesis of lipid rafts major components, is studied. The relevance of the Pma1p localization at the lipid rafts is also addressed. The results described in this chapter identify a novel lipid rafts-disrupting activity of Lf that can be explored as an antifungal strategy alone or in combination with other antifungals.

- In **Chapter 4**, the molecular mechanisms underlying the Lf cytotoxicity against highly metastatic cancer cells derived from different cancer types are elucidated. Specifically, the effect of Lf on cholesterol-rich lipid rafts localization, as well as on intracellular trafficking, cell signalling and metabolism is evaluated and a novel cascade of molecular events unveiled. A Lf bidirectional *modus operandi* is identified that can be explored for the development of tailored Lf-based anticancer therapies.

- **Chapter 5** presents a computational approach designed to decipher how Lf and V-ATPase interact, and to identify the key binding residues for their interaction. A five-stage computational pipeline is developed based on molecular dynamics simulations, protein-protein docking and free binding energy calculations. The more favorable binding poses between both proteins are studied in more detail allowing the proposal of a putative inhibitory mechanism. Moreover, crucial binding residues that can be explored experimentally are identified.

- In **Chapter 6**, the general conclusions of the work performed in the scope of the present thesis, which was conducted to serve the *common good* of contributing to a deeper understanding of

the Lf mechanisms of action, are discussed and integrated. Future directions based on the open questions left by the present work are also presented.

- At the end of the thesis, an **Appendix** is included that contains additional information of the main chapters.

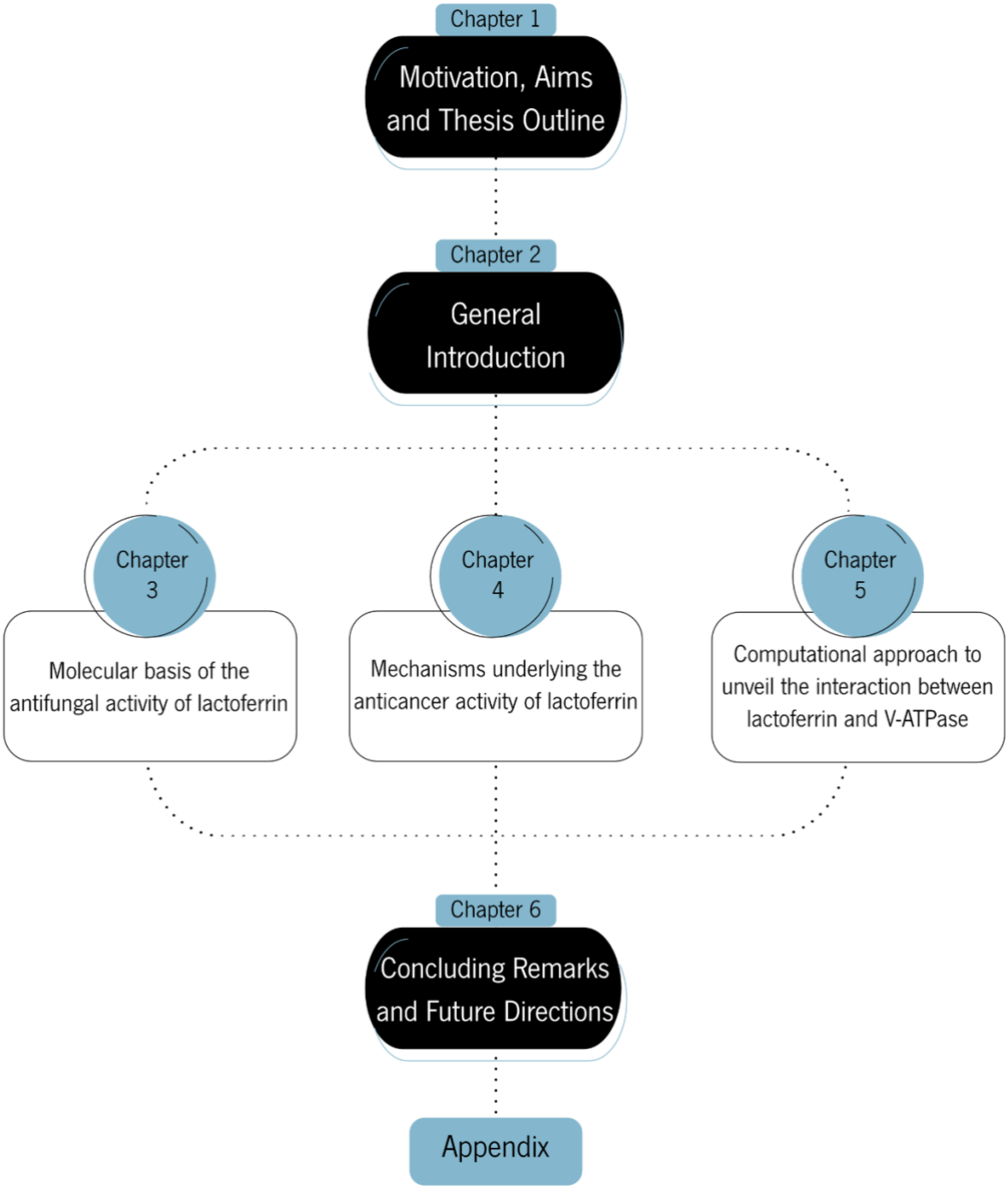

Figure 1.1: Overview of the thesis outline.

References

1. Morrison R. Lost in translation - Basic science in the era of translational research. Infect Immun. 2010;78: 563–566. doi:10.1128/IAI.01318-09
2. Editorial NM. Mechanism matters. Nat Med. 2010;16: 347. doi:10.1038/nm0410-347
3. Schor NF. Why our patients (and we) need basic science research. Neurology. 2013;80: 2070–2075. doi:10.1212/WNL.0b013e318294b48a
4. Schenone M, Dančík V, Wagner BK, Clemons PA. Target identification and mechanism of action in chemical biology and drug discovery. Nat Chem Biol. 2013;9: 232–240. doi:10.1038/nchembio.1199
5. Vega-Bautista A, de la Garza M, Carrero JC, Campos-Rodríguez R, Godínez-Victoria M, Drago-Serrano ME. The impact of lactoferrin on the growth of intestinal inhabitant bacteria. Int J Mol Sci. 2019;20. doi:10.3390/ijms20194707
6. Cutone A, Rosa L, Ianiro G, Lepanto MS, Di Patti MCB, Valenti P, et al. Lactoferrin's anti-cancer properties: Safety, selectivity, and wide range of action. Biomolecules. 2020;10: 1–26. doi:10.3390/biom10030456
7. Tomita M, Wakabayashi H, Shin K, Yamauchi K, Yaeshima T, Iwatsuki K. Twenty-five years of research on bovine lactoferrin applications. Biochimie. 2009;91: 52–7. doi:10.1016/j.biochi.2008.05.021
8. Authority EFS. EFSA Panel on Dietetic Products, Nutrition and Allergies (NDA); Scientific Opinion on bovine lactoferrin. EFSA J. 2012;10.
9. Superti F. Lactoferrin from bovine milk: A protective companion for life. Nutrients. 2020;12: 1–26. doi:10.3390/nu12092562
10. Velliyagounder K, Rozario SD, Fine DH. The effects of human lactoferrin in experimentally induced systemic candidiasis. J Med Microbiol. 2019;68: 1802–1812. doi:10.1099/jmm.0.001098
11. Russo R, Superti F, Karadja E, De Seta F. Randomised clinical trial in women with recurrent vulvovaginal candidiasis: Efficacy of probiotics and lactoferrin as maintenance treatment. Mycoses. 2019;62: 328–335. doi:10.1111/myc.12883
12. Digumarti R, Wang Y, Raman G, Doval DC, Advani SH, Julka PK, et al. A randomized, double-blind, placebo-controlled, phase II study of oral talactoferrin in combination with carboplatin and paclitaxel in previously untreated locally advanced or metastatic non-small cell lung cancer. J Thorac Oncol. 2011;6: 1098–1103. doi:10.1097/JTO.0b013e3182156250
13. Hayes TG, Falchook GS, Varadhachary A. Phase IB trial of oral talactoferrin in the treatment of patients with metastatic solid tumors. Invest New Drugs. 2010;28: 156–162. doi:10.1007/s10637-009-9233-9
14. Kozu T, Iinuma G, Ohashi Y, Saito Y, Akasu T, Saito D, et al. Effect of orally administered bovine lactoferrin on the growth of adenomatous colorectal polyps in a randomized, placebo-controlled clinical trial. Cancer Prev Res. 2009;2: 975–83. doi:10.1158/1940-6207.CAPR-08-0208
15. Ramalingam S, Crawford J, Chang A, Manegold C, Perez-Soler R, Douillard JY, et al. Talactoferrin alfa versus placebo in patients with refractory advanced non-small-cell lung cancer (FORTIS-M trial). Ann Oncol. 2013;24: 2875–2880. doi:10.1093/annonc/mdt371

CHAPTER 2

General Introduction

This chapter comprises parts of the following publications:

Cátia Santos-Pereira, Lígia R. Rodrigues, Manuela Côrte-Real (2021) **Emerging insights on the role of V-ATPase in human diseases: therapeutic challenges and opportunities**. *Medicinal Research Reviews*. doi: 10.1002/ med.21782

Cátia Santos-Pereira, María T. Andrés, Fernando F. Fierro, Lígia R. Rodrigues, Manuela Côrte-Real. **Lactoferrin as a novel proton pump inhibitor.** *Manuscript in preparation*

2.1. Structure and properties of lactoferrin

Lactoferrin (Lf) is an iron-binding glycoprotein of about 80 kDa abundant in milk and colostrum that was first identified in bovine milk in 1939 [1] and was later isolated and purified from both bovine [2] and human milk [3]. Lf is a cell-secreted protein whose synthesis can be constitutive at the mucosal surfaces, hormone-dependent in the case of the genital tract or mammary gland, or even occur at well-defined stages of cell differentiation namely by neutrophils during their differentiation process [4]. It has been identified in several tissues from different mammalian species including humans, cows, goats, buffalos, pigs, camels, horses, fishes and several rodents [5,6], displaying high homology among them. In fact, bovine Lf (bLf) shares 69% sequence similarity with human Lf (hLf) and 64% with murine Lf at the protein level [7], and 77% homology at the mRNA level with hLf [8]. Interestingly, Lfs from different species were demonstrated to have similar activities [9].

Besides milk and colostrum, Lf is also present within the specific granules of neutrophils and in several biological fluids such as saliva, tears, sweat, semen, nasal and bronchial mucosa, airway fluids and in the genital, urinary and gastrointestinal fluids [10]. However, though the concentration is extremely dependent on the lactation stage, milk is by far the most abundant source of Lf [11]. The higher Lf concentrations are found in colostrum being approximately 7 mg/ml for hLf and 1.5 mg/ml for bLf [12]. Interestingly, the Lf concentration in colostrum varies with the region, being higher (around 9 mg/ml) in African women and lower (around 3.5 mg/ml) in Asian women [11].

The amino acid sequence of Lf was disclosed in 1984 and it was found to be a polypeptide of approximately ~690 amino acids (Figure 2.1A) that exhibits a high degree (~60%) of identity with serum transferrin, as well as similar disulphide bonding patterns [13]. Hence, this protein belongs to the transferrin protein family, which is a family of proteins widely present in the physiological fluids exhibiting many functions related with their ability to sequester iron. The features of Lf that mostly distinguish it from the other members of this family are its higher isoelectric point and tighter iron binding [14]. Indeed, Lf is the only transferrin able to bind iron over a wide pH range. Specifically, it was shown that, at pH 10.5, bLf is 100% saturated with iron; at pH 5.0, it retains 50% of iron; and at pH 4.0 and 2.0 it retains 25% and 10% of iron, respectively [15]. In contrast, iron release from transferrin occurs at a pH range from 6.2 to 4.0 [16]. Remarkably, Lf was demonstrated to be more active at acidic pH values [17,18].

It is also noteworthy that the primary structure of Lf shows a number of cysteine residues that allow the formation of disulphide bridges and also reveals several asparagine residues that provide N-glycosylation sites [13]. Importantly, N-glycans and N-glycosylation patterns have been shown to modulate Lf activities and to influence its *in vivo* half-life as recently reviewed by Zlatina *et al.* [19]. For

example, Lf de-N-glycosylation decreases the iron binding capacity of the protein [20] and its inhibitory effect on the adhesion of *Salmonella enterica typhimurium* to human cells [21]. Moreover, hLf, bLf and recombinant hLf (rhLf) produced in transgenic cows showed different amounts and enrichment in different types of N-glycans [22]. Thus, it is suggested that the N-glycosylation status of Lf should be taken into account, particularly for *in vivo* Lf applications [19].

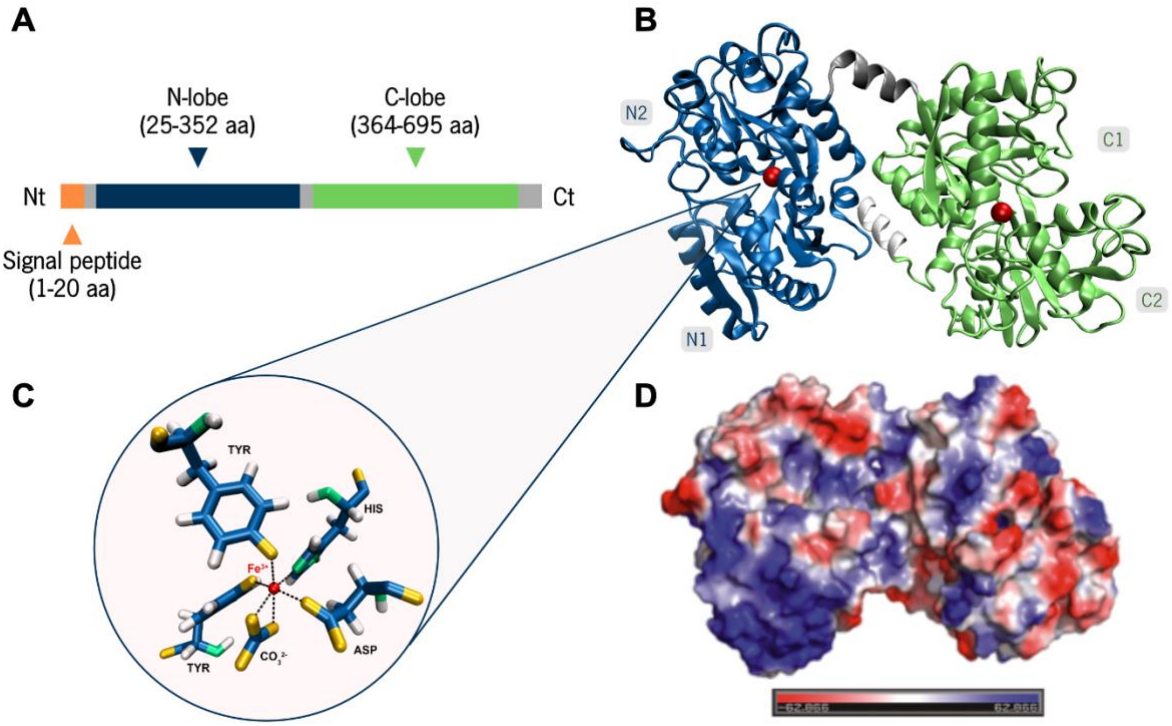

Figure 2.1: Sequence and structure of lactoferrin. (A) Schematic representation of Lf protein sequence. Lf transduction gives rise to a pre-protein of 710 amino acids containing a signal peptide for extracellular secretion, while mature protein has 691 amino acids and contains two domains, N-lobe and C-lobe (adapted from [4]). **(B)** Structure of iron-saturated holo-bLf. The N-lobe is represented in blue and the C-lobe in green. Each lobe is further divided into two domains as depicted (N1, N2, C1 and C2). The loop connecting the two lobes is coloured in grey whereas the C-terminal is in white. The iron ions are represented by two red spheres. **(C)** Iron binding site of Lf. The same organization is found in both lobes and in all Lfs. The image shows the iron binding site of the N-lobe of bLf, where an aspartate, a histidine and two tyrosine residues as well as a bicarbonate anion bind to Fe^{3+}. The latter binds in bidentate mode. The visual representations in B and C were designed using VMD (Visual Molecular Dynamics) [23] with the pdb structure 1BLF published by [24]. **(D)** Distribution of surface charge on bLf. Blue for positive, red for negative and white for neutral charges (adapted from[25]).

The three-dimensional structure of bLf was determined in the 90's [24] but the structure of hLf was already known in the 80's [26]. Lf has a similar bilobal structural organization to the other transferrins, being folded into two lobes, N and C, which represent its N- and C-terminal halves, joined by

a short α-helix. Each lobe is further divided into two domains: N1 and N2 and C1 and C2, respectively. Lf is capable of binding two iron ions together with two CO_3^{2-} and the iron binding sites are located in the clefts between the two domains in each lobe (Figure 2.1B) [27]. The Lf iron coordination sphere is composed by 1 aspartate, 1 histidine and 2 tyrosine residues as well as a bicarbonate anion (Figure 2.1C), which is identical to the transferrin iron-binding site. According to its ability to bind iron, Lf can exist in two forms depending on its metal ion state: free of iron (apo-Lf) or iron-saturated (holo-Lf). Metal binding and release is associated with large-scale conformational changes. In its iron-bound state, the most stable, it adopts a closed structure since the two domains of each lobe fully close over the bound ion. In its metal-free state, Lf adopts an open form in which the two domains of each lobe open [25].

Although Lf primary function is to bind iron, some of its biological activities do not derive from the binding to iron but from its capacity to bind to a vast number of other molecules, microorganisms and mammalian cells. Lf is a basic and highly positively charged protein with an isoelectric point of 9-10. It is widely accepted that its characteristic cationic character (Figure 2.1D), especially a hot spot of positive charge located on the N-lobe (N1), is the main reason why Lf can bind to such a variety of molecules [25]. Accordingly, it was demonstrated that the N-terminal stretch of four consecutive arginine residues (2-5) plays a decisive role in the interaction of hLf with heparin, lipid A, lysozyme and DNA [28]. Lf can also bind to other cations besides iron such as Al^{3+}, Cu^{2+} and Zn^{2+}, as well as to other anions besides CO_3^{2-} like oxalates and carboxylates (reviewed by [29]). Furthermore, Lf can bind to isomeric drugs like ursolic and oleanolic acids [30], lipid A and bacterial lipopolysaccharides [31], virulence factors [32], DNA [33], plant-derived flavonoids [34], cell surface receptors [35] and phenothiazine dyes [36].

It is precisely on the cationic N-terminal region (Figure 2.1D) that two well-known Lf-derived peptides, lactoferricin (Lfcin) and lactoferrampin (Lfampin), are located [37]. Throughout the years, an increasing number of Lf functions have been identified and associated with the generation of bioactive peptides without iron-binding ability derived from the entire protein [38,39]. Interestingly, Lfcin was detected in unfractionated gastric contents recovered from an adult 10 min after bLf ingestion [40], and can also be found at the infection sites due to the action of bacterial or mammalian proteases [41]. In addition, other Lf-derived peptides are being studied regarding different activities, such as Lf (1-11) (comprises the first 11 amino acids of Lf) [37], LFchimera (contains parts of Lfcin and Lfampin) [42], and, very recently, a new C-lobe Lf-derived peptide with marked antifungal activity termed lactofungin was described [43].

2.1.1. Biological activities of lactoferrin

Originally seen as simply an iron-binding protein, with the advances in the Lf research field, scientists quickly realized that Lf is far more than that. Indeed, words like multifunctional, multifaceted, pleiotropic, bioactive, among others are now repeatedly used to describe the Lf protein. Since its discovery, multiple biological activities and functions either at the physiological, cellular and/or molecular levels have been attributed to Lf. Overall, Lf exhibits antimicrobial, anticancer, anti-inflammatory, immunomodulatory, antioxidant, enzymatic and proteolytic activities as recently reviewed by [39,44,45] (Figure 2.2). The main focus of the present thesis is the Lf antifungal and anticancer activities, which will be discussed in more depth in the following sections. However, a brief description of its most important functions will be presented to emphasize the Lf multifunctional character.

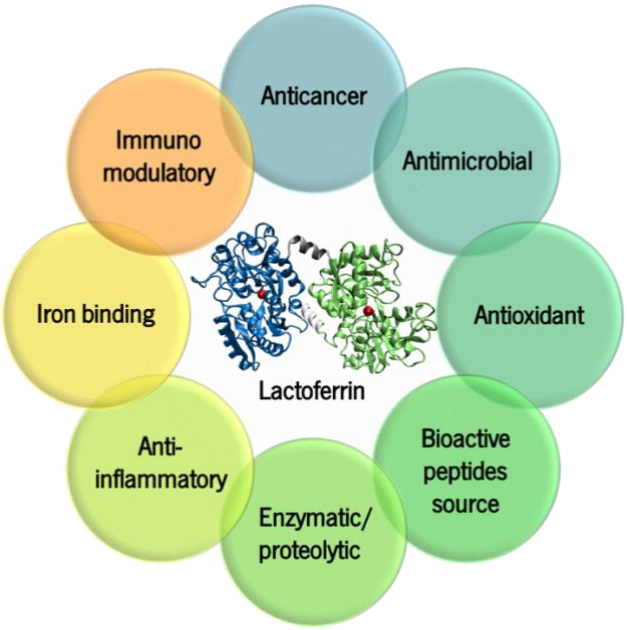

Figure 2.2: Main biological activities attributed to lactoferrin.

The antimicrobial activity is the most widely studied trait of Lf. Initial studies focused on the antibacterial activity of Lf, however, there is currently a great number of reports demonstrating the antifungal, antiviral and antiparasitic activities of Lf and its derived peptides. Indeed, Lf exhibits a strong antimicrobial activity against a broad spectrum of Gram(+) and Gram(-) bacteria, unicellular and filamentous fungi, RNA and DNA viruses, as well as parasites [39,46]. Several studies conducted throughout the years have put forward a considerable number of mechanisms by which Lf can exert its antimicrobial activity, such as competition with siderophores by iron sequestering [47], direct interaction with cell surface [48] or its components like lipopolysaccharide [49], inhibition of the adhesion to host

cells [50], prevention of biofilm formation [51], proteolysis of colonization factors [52], binding to virus particles [53], impairment of viral entry [54], among others.

One of the discoveries that revolutionized the way of looking at Lf was the finding of its presence in the secondary granules of polymorphonuclear neutrophils [55]. Since then, a new field of Lf research arose and the reports on the role of Lf in the immune system increased exponentially. Nowadays, it is well recognized that Lf is a component of the immune system and a first line defense protein that protects against a plethora of microbial infections and prevents systemic inflammation [56]. When released, Lf can modulate the production of cytokines, promote leucocyte recruitment and dendritic cells activation, thus modulating innate and adaptive immune responses and acting as an alarmin [57]. The immunomodulatory activity of Lf is often associated to other biological activities, such as its antiviral effect [58].

Another interesting characteristic of Lf is that it can act as an enzyme. In fact, Lf has proteolytic activity [59], and different subfractions of the protein were shown to have RNase [60,61], DNase, ATPase, phosphatase and amylase activities *in vitro* [62]. Remarkably, the DNase activity was shown to contribute to the anti-biofilm effect of Lf. In fact, Lf inhibited *Streptococcus pneumoniae* biofilm formation and acquisition of antibiotic resistance by degrading the extracellular DNA, which is secreted to the biofilm matrix [51]. Lf can also function as an antioxidant and a reactive oxygen species (ROS) scavenger, protecting DNA from oxidative damage. Specifically, Lf was shown to protect DNA from fragmentation induced by ultraviolet irradiation in the presence of hydrogen peroxide [63]. Furthermore, pretreatment with Lf protected human umbilical vein endothelial cells from hydrogen peroxide-induced oxidative stress *in vitro* [64], and reduced renal oxidative tubular damage in a rat model of ferric nitrilotriacetate-induced renal tubular oxidative injury [65], demonstrating its antioxidant and cytoprotective effects. It can also act as a transcription factor inducing transcriptional activation of genes and regulating gene expression. For instance, in human intestinal cells, hLf was shown to go to the nucleus, where it bound the interleukin 1 (IL-1) promoter, activating its transcription and promoting IL-1 upregulation [66]. On the other hand, a role of Lf in iron transport, absorption and metabolism has been suggested since the beginning of Lf research owing to Lf iron binding ability, however this is not unequivocally proven as discussed by [45]. For instance, Lf was shown to increase hemoglobin in pregnant women suffering from iron deficiency anemia [67], yet in infants fed with Lf-fortified formulas some studies do not report any effect [68] while others do [69]. Thus, additional work is required to unveil the role of Lf in iron homeostasis. Finally, studies have shown that Lf stimulates bone growth by promoting the differentiation of osteoblasts, the cells that produce bone [70], and also promotes fracture healing [71] and wound healing *in vivo* [72].

2.1.1.1 The antifungal activity of lactoferrin

Fungal infections represent a worldwide burden, accounting for millions of cases and showing an increasing trend [73,74]. Although research led to the identification of potent antifungals, systemic infections caused by fungi from *Candida*, *Aspergillus* and *Cryptococcus* species as well as endemic dimorphic fungi are still a major public health concern, especially among more susceptible patients like immunosuppressed individuals [73,75]. Moreover, the number of multidrug resistant fungi has been increasing over the past decades, which is a serious concern in the clinical practice [76]. Hence, the search for new antifungals and innovative antifungal therapies is of utmost importance to counteract these problematics.

Although initial studies were focused on the antibacterial activity of Lf, throughout the years several researchers identified Lf as an effective antifungal agent against different types of fungi. Pioneer studies were mainly dedicated to fungi from the *Candida* genus. Xu *et al.* found that the bLf candidacidal activity was species-dependent being more prominent in *Candida tropicalis* followed by *C. krusei*, *C. albicans* and *C. guilliermondii*, while *C. parapsilosis and C. glabrata* were the most resistant to Lf [77]. These interspecies differences in susceptibility to Lf were actually reported before for two *Candida* species [78]. Later on, Lf was shown to inhibit the growth of the dermatophytic fungi *Trichophyton mentagrophytes* and *T. rubrum*, as well as to diminish the fungal burden in a guinea pig model of dermatophytosis infected with *T. mentagrophytes* on the foot [79]. The Lf antifungal activity was further demonstrated against fungi isolated from plants and soils including *Aspergillus niger*, *Trichoderma viride*, *Sclerotinia sclerotiorum*, *Sclerotium rolfsii*, *Rhizoctonia solani* and *Phoma exigua* [80]. Lf also exhibited a promising antifungal activity against *Botrytis cinerea,* the so-called gray mold that affects many horticultural crops, as it inhibited spore germination and mycelial growth *in vitro* and decreased the disease index without associated phytotoxicity *in vivo* [81]. More recently, a work aiming to evaluate Lf antifungal activity against a wide range of yeasts and molds including clinical, veterinary and environmental isolates concluded that it is toxic against all the tested strains (46 in total) from the genus *Candida*, *Saccharomyces*, *Cryptococcus*, *Meyerozyma*, *Kluyveromyces*, *Pichia* and *Clavispora* [82]. These observations suggest that Lf is a broad-spectrum antifungal agent.

Although the Lf activity against fungi is not yet completely understood, some mechanisms have been proposed. Though initially, its iron-binding ability was pointed as the main player, soon thereafter, increasing evidence reporting the interaction of this protein with the fungal cell surface was documented, and more recently an apoptotic-like cell death process and the interaction with a plasma membrane proton pump were described (Table 2.1, Figure 2.3).

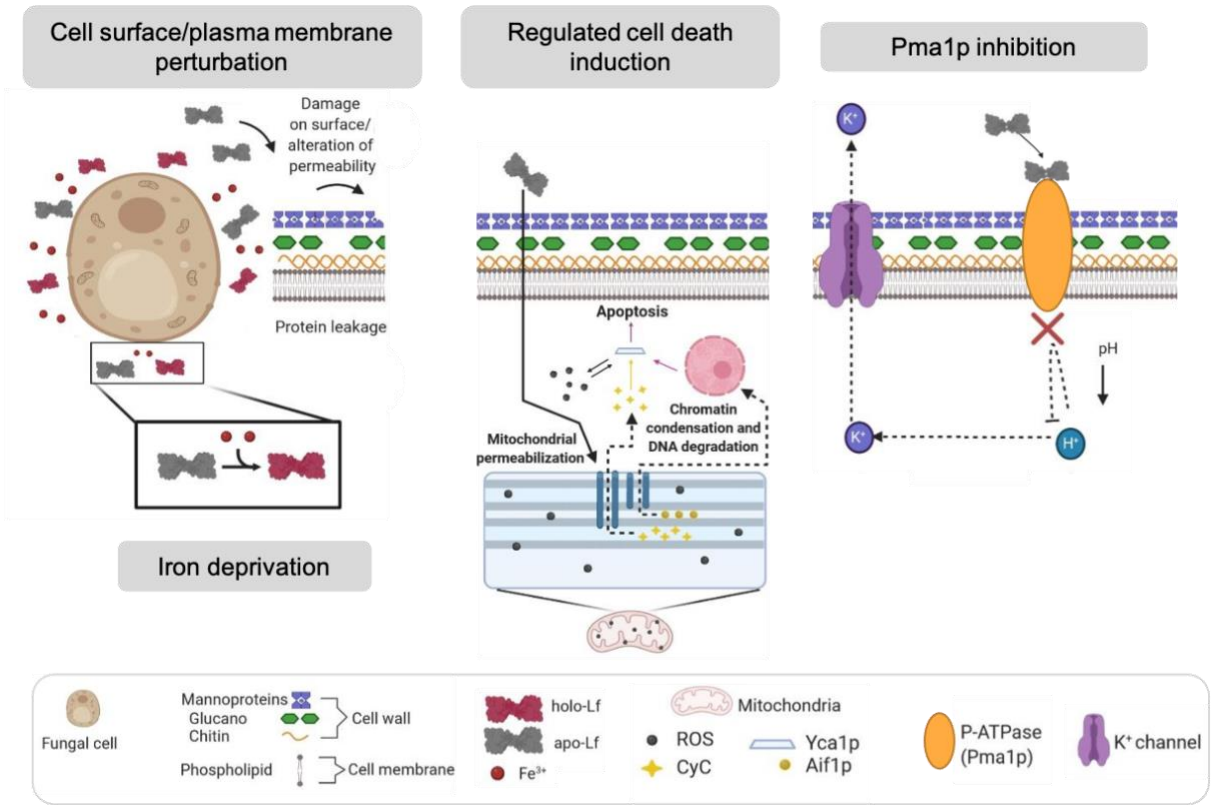

Figure 2.3: Mechanisms underlying the antifungal activity of lactoferrin. Research performed throughout the years allowed the finding of mechanisms by which Lf kills fungal cells. Damage of the cell surface and plasma membrane causing cytosolic leakage; iron chelation; ROS-, mitochondria- and metacaspase-dependent regulated cell death; as well as binding to the proton pumping Pma1p leading to cytosolic acidification and potassium efflux, are the main pathways by which Lf is believed to exert its antifungal activity (adapted from [39]).

The notion that the iron scavenging properties of Lf are critical for its activity against fungi is supported by several studies showing that this activity is impaired by iron supplementation or by using iron-rich Lf forms. In fact, in an early work, Soukka *et al.* reported the antifungal activity of iron-free apo-Lf against *C. albicans* that was not observed for holo-Lf [83]. This actually is well aligned with the results of a very recent study showing that the Lf activity against two species of *Candida* and *Cryptococcus* is dependent on its iron saturation status [82]. The hLf-induced growth inhibition of *Aspergillus fumigatus* conidia was completely hindered by both addition of ferritin (protein-iron complex) or by dialyzing Lf against ferrous ammonium sulfate, which promotes iron loading into Lf [84]. Addition of both iron (III) or iron (II) restored the growth of Lf-treated *Cryptococcus neoformans* and *S. cerevisiae* cells. However, it did not restore the growth of cells treated with a synergistic combination of Lf and amphothericin B (AmpB), thus indicating that Lf is potentiating AmpB cytotoxicity by other mechanisms besides iron sequestering [85]. Taken together, these evidences demonstrate that iron chelation promoted by Lf is critical for its antifungal activity, but it is not the sole determinant.

Table 2.1: Antifungal activity of lactoferrin and its mode of action. PM: plasma membrane, CAT: catalase, SOD: superoxide dismutase, ROS: reactive oxygen species.

Fungi	Lf type and concentration	Observed phenotypes	Mode of action	Reference
C. albicans	Apo-hLf, 25-100 µg/ml	Decreased cell survival by apo-hLf but not holo-hLf	Iron sequestration	[83]
C. albicans, *C. tropicalis*, *C. krusei*, *C. guilliermondii*, *C. parapsilosis*, *C. glabrata*	bLf and hLf, 5-20 µg/ml	Surface blebs, pits and fissures	Cell surface perturbation	[77]
C. albicans	Apo-hLf, 500 µg/ml	Cytosolic acidification, membrane depolarization, reduced potassium but not sodium leakage	Regulated cell death induction	[17]
C. albicans	Apo-hLf, 500 µg/ml	No cytosolic leakage, no PM permeabilization	Regulated cell death induction	[86]
Erysiphe necator	bLf, 20 µg/ml	Collapse of conidia and hyphae	Cell surface/PM perturbation	[87]
A. fumigatus	Apo-hLf, 10-40 µg/ml	Inhibition of conidial growth by apo-hLf but not holo-hLf	Iron sequestration	[84]
C. albicans	rhLf, 500 µg/ml	DNA fragmentation, chromatin condensation, phosphatidylserine exposure, PM integrity, ROS production, mitochondrial membrane potential decrease	Regulated cell death induction	[88]
B. cinerea	bLf, 25-100 µg/ml	Inhibition of spore germination, germ tube elongation and mycelial growth, PM permeabilization, cellular leakage, decreased enzymatic activity of CAT and SOD, decreased *in vivo* disease index	Cell surface/PM perturbation	[81]
P. expansum	Not specified, 500-1000 µg/ml	Inhibition of spore germination and germ tube elongation, PM permeabilization, leakage of proteins and sugars	Cell surface/PM perturbation	[89]
C. neoformans, *S. cerevisiae*	bLf, 16-64 µg/ml	Addition of exogenous iron rescued Lf-induced growth inhibition	Iron sequestration	[85]
S. cerevisiae	hLf, 125-500 µg/ml	Chromatin condensation, PM integrity, caspase activation, ROS production, cytochrome *c* release	Regulated cell death induction	[90]

Table 2.1: Antifungal activity of lactoferrin and its mode of action (cont.). PM: plasma membrane, CAT: catalase, SOD: superoxide dismutase, ROS: reactive oxygen species.

Fungi	Lf type and concentration	Observed phenotypes	Mode of action	Reference
C. albicans	Apo-rhLf, 125-500 μg/ml	Increased intracellular ATP concentration, inhibition of extracellular acidification and PM ATPase activity, binding to Pma1p	Binding to Pma1p	[91]
C. albicans	Apo-rhLf, 500 μg/ml	Intracellular acidification, resistance to Lf-induced cell death by treatment with K^+-channel blockers or by deletion of K^+ channels	Cell death is activated by cytosolic acidification followed by K^+-efflux	[92]
Different species from the genus *Candida*, *Saccharomyces*, *Cryptococcus*, *Meyerozyma*, *Kluyveromyces*, *Pichia* and *Clavispora*	bLf, 8-64 μg/ml	Inhibition of growth by apo- and native-hLf but not holo-hLf	Iron sequestering	[82]

The interaction of Lf with the plasma membrane and fungal surface has been pinpointed by several authors as the main mechanism by which Lf exerts its antifungal activity. Indeed, ultrastructural changes were observed by cryo-scanning electron microscopy (SEM) when different *Candida* species were incubated with Lf including surface blebs, pits and fissures aside from swelling and cell collapse [77]. The toxicity of Lf against *B. cinerea* spores was associated with loss of membrane integrity and cellular leakage of proteins and carbohydrates [81]. A similar scenario was described for *Penicillium expansum*, which causes the blue mold in apples, where Lf treatment reduced plasma membrane integrity of the spores, causing leakage of proteins and sugars [89]; and for *Erysiphe necator*, which produces the grapevine powdery mildew, where conidia and hyphae were significantly damaged and ruptured after 48 h of being sprayed with Lf, as observed by SEM [87]. In these reports, Lf appears to cause damage in fungal cells or spores with necrotic features (i.e. plasma membrane rupture and leakage of cytosolic content), however Fernandes *et al.* found that only a small percentage of *Candida* and *Cryptococcus* cells exhibited significant morphological alterations at the cell surface, suggesting that other mechanisms may underlie the observed Lf toxicity [82]. Accordingly, Viejo-Díaz *et al.* undertook mechanistic studies on *C. albicans* cells treated with hLf where no necrotic features were found. Indeed, no membrane permeabilization and no cytosolic leakage were detected [86]. Instead, hLf induced membrane depolarization, cytosolic acidification, a 19% K^+ leakage and no alterations in the Na^+ intracellular levels. Nonetheless, cell wall-free spheroplasts were more resistant to hLf than intact cells, attesting the importance of the cell surface interactions to hLf candidacidal activity [17].

In this line, an apoptotic cell death process has been observed when *C. albicans* [88] and *S. cerevisiae* [90] cells were incubated with hLf. Apoptosis is a regulated cell death process characterized by the involvement of pro-apoptotic machinery, and by the occurrence of specific morphological alterations including phosphatidylserine exposure, DNA fragmentation, among others [93]. When *C. albicans* cells were incubated with rhLf, several hallmarks characteristic of mammalian apoptosis were identified namely the appearance of DNA strand breaks, chromatin condensation, externalization of phosphatidylserine, maintenance of plasma membrane integrity, ROS accumulation and decrease of mitochondrial membrane potential. Pre-incubation of cells with blockers of K^+ channels impaired rhLf-induced cell death [88], suggesting that the previously observed release of K^+ induced by Lf [17] is mediated by K^+ channels, and is essential for the triggering of cell death by Lf in *C. albicans* [88]. Years later, our group further characterized hLf-induced apoptosis and showed that it is not restricted to *C. albicans* as it also occurs in *S. cerevisiae*. In fact, we showed that the cell death process is dependent on energy and *de novo* protein synthesis and is associated with maintenance of plasma membrane integrity, chromatin condensation and mitochondrial outer membrane permeabilization associated with release of the pro-apoptotic cytochrome *c* to the cytosol. Moreover, a mutant lacking the yeast metacaspase was resistant to hLf, and increased caspase activity was detected indicating that the process is dependent on caspase activation. Furthermore, we found that hLf-induced apoptosis is dependent on mitochondria and mitochondrial energetic metabolism [90]. Combined, these works demonstrate that hLf induces a ROS-, caspase- and mitochondria-dependent apoptotic process in yeast.

The binding and inhibitory interaction of Lf with the plasma membrane proton pump Pma1p [91] and cytosolic acidification [92] have more recently been identified as crucial events for Lf antifungal activity, a subject that is further explored in section 2.3 of this chapter.

In addition to the above-mentioned mechanistic studies, some promising pre-clinical and clinical studies have been published recently that demonstrate the excellent potential of Lf as an antifungal agent. The effect of hLf against invasive candidiasis was evaluated in a mouse model of systemic infection caused by *C. albicans* lacking the endogenous mouse lactoferrin gene (Lft-/- mouse). The protein was effective in promoting the clearance of *C. albicans* in most organs; in decreasing the amount of infection foci; and in downregulating several virulence-associated genes [94]. An interesting work reported a strategy against vulvovaginal candidiasis (VVC) based on the use of a hetelogous *Lactobacillus casei* strain secreting bLf. *L. casei* is considered safe and is widely used in different products for human consumption. Using a VVC mouse model, the authors showed the effectiveness of bLf in preventing the growth and invasion of *C. albicans* and diminishing the infection burden either given prophylactically or as a

therapeutic against VVC [95]. In agreement, a clinical trial in women with recurrent VVC infections using a similar strategy (a lactobacilli mixture in combination with bLf but with an intake of clotrimazole in the beginning of the trial) concluded that the treatment significantly decreased the candidiasis recurrence [96]. Importantly, several works also highlight the significant synergy of Lf with classical antifungals including amphotericin B and fluconazole, which allows decreasing the concentration of antifungal required for cytotoxicity against fungi, and possibly overcoming the putative fungal resistance to the classical therapeutics [82,85,97].

2.1.1.2 The anticancer activity of lactoferrin

Cancer is one of the leading causes of deaths worldwide that accounted for nearly 10 million deaths in 2020. It is a term used to describe a group of diseases characterized by the rapid and uncontrolled growth of abnormal cells, which can then invade and spread to other organs [98]. Cancer development is a complex and multistep process during which cancer cells undergo a series of changes that are known as the hallmarks of cancer. Those include, among others, evasion of cell death and immune response, energy metabolism reprogramming, creation of a distinctive tumor microenvironment and angiogenesis [99].

The anticancer activity of Lf was established in the mid 90's after the findings that the whey fraction of bovine milk [100] and hLf [101] inhibit tumor growth and metastasis in rats and mice, respectively. Since then, a myriad of studies have demonstrated the anticancer effects of Lf in a broad range of cancer types including breast [102], lung [103], leukemia [104], melanoma [105], osteosarcoma, prostate [106], among others. Importantly, this protein has the remarkable advantage of only being cytotoxic to cancer cells, since the non-cancer cell counterparts are resistant to similar concentrations [106–108]. Therefore, it has the desirable features to be successfully applied in cancer therapy. However, although some mechanisms of action have been proposed (Figure 2.4), the molecular basis of its anticancer activity is still not completely elucidated, which reinforces the need for further in-depth mechanistic studies to boost selective and effective Lf clinical application.

One of the mechanisms by which Lf prevents tumor growth is by inhibiting cell proliferation and inducing cell cycle arrest associated with the modulation of cell cycle-related proteins. This arrest has been shown to preferentially occur at the G0/G1 phase of the cell cycle [105,109–113], but G2 [114] and S phase arrests [102] have also been reported. Moreover, different cell cycle regulatory proteins are modulated by Lf, particularly those involved in the G1 phase and the G1 to S phase transition. In fact, Lf was shown to downregulate cyclins D1 and D4 in glioblastoma cell lines [109], D1 in oral squamous cell

carcinoma cells [113] and E in head and neck cancer cell lines [110]. hLf was also demonstrated to maintain the retinoblastoma protein, an inhibitor of cell cycle progression, in its active/hypophosphorylated form [110,111].

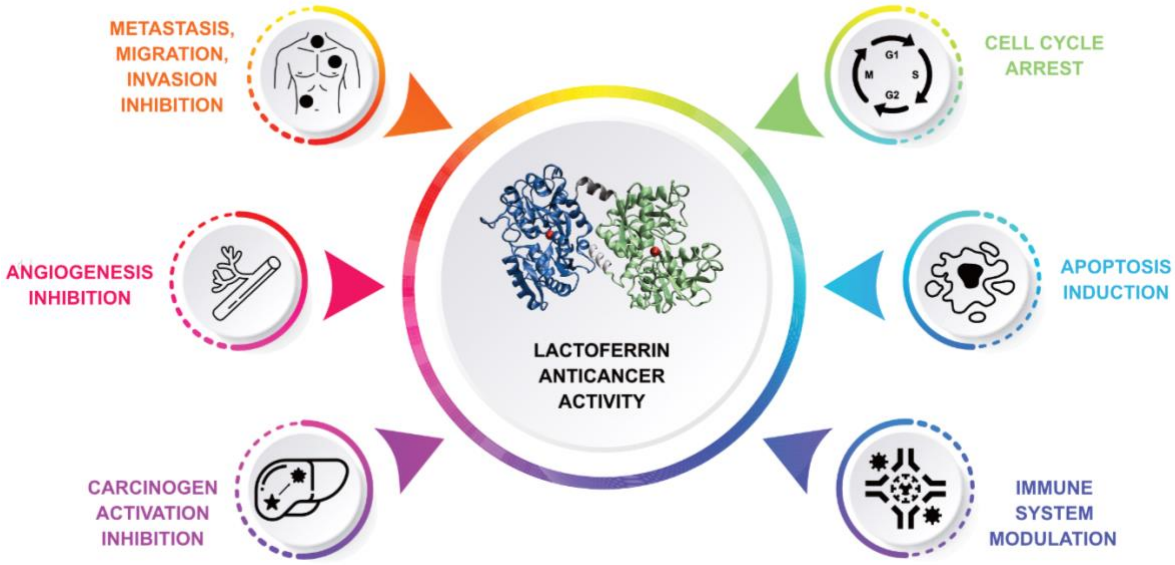

Figure 2.4: Overall perspective of the mechanisms proposed to underly the anticancer activity of lactoferrin. Cell cycle arrest, apoptosis induction, anti-angiogenic activity, anti-metastatic activity and inhibition of both invasion and migration, modulation of the immune system against cancer cells and inhibition of carcinogen activation are the main mechanisms by which Lf exerts its anticancer activity as stated in the main text.

Several data support that the Lf anticancer activity relies on its ability to trigger apoptosis. As aforementioned, apoptosis is a form of regulated cell death through which a cell dies and is packaged into apoptotic bodies that are then removed by neighboring cells and phagocytes, generating minimal inflammation. As cancer cells usually escape apoptosis in order to survive, cancer therapeutic approaches based on apoptosis induction have been explored [115]. Typical apoptotic markers have been observed after exposure of different *in vitro* and *in vivo* cancer models to Lf, including phosphatidylserine exposure to the outer leaflet of the plasma membrane [107,113], caspase activation [113,116], chromatin condensation [102,117,118], and DNA fragmentation [119,120]. Moreover, Lf was found to modulate the levels of key apoptosis-related proteins, whose balance determines cell fate. Particularly, it was found to decrease the levels of the anti-apoptotic protein Bcl-2 [118,121] and to increase the levels of the pro-apoptotic Bax protein [117,119] and Fas receptor [120], favoring cell death. Accordingly, by using an apoptosis protein array, Gibbons *et al.* found that Lf modifies the levels of p53, Bcl-2 family proteins and inhibitors of apoptosis proteins, like survivin, and their inhibitors [108]. A large-scale proteomic analysis

of breast cancer cells treated with Lf revealed that 9% of the upregulated proteins were proteins involved in apoptosis execution [122].

The ability of Lf to hinder cancer cell invasion, migration and metastasis has been demonstrated by numerous researchers in different cancer models [108,123,124]. Indeed, bLf inhibited/decreased lung metastatic colony formation induced by highly metastatic melanoma cells, lymphoma cells [125] and colon carcinoma cells [126,127], in mice. It also inhibited liver metastasis by lymphoma cells [125]. More recently, a molecular explanation for these observations was reported. Lf was shown to revert the epithelial-to-mesenchymal transition (EMT) in oral carcinoma [124] and glioblastoma cells [123]. The EMT is the process through which epithelial cells loose cell-to-cell contacts acquiring the invasive properties of mesenchymal cells. This process contributes to cancer cells detachment and metastatization. During EMT, cells downregulate the adhesion marker E-cadherin and upregulate vimentin, a mesenchymal marker. Lf was shown to inhibit migration/invasion of cancer cells by increasing E-cadherin expression and decreasing vimentin, thus reverting EMT [123,124], and also by inhibiting IL-6/STAT3 axis, which is an essential pathway involved in glioblastoma cell migration [123].

Additionally, Lf was shown to inhibit angiogenesis, the formation of new blood vessels that is vital for tumor growth. In fact, various studies demonstrated that Lf inhibits vascular endothelial growth factor (VEGF)-induced angiogenesis [103,128,129], and the proliferation of endothelial cells *in vitro* [129]. It also downregulates the expression of VEGF both at the mRNA and protein levels [103,130].

An interesting role of Lf in modulating the immune system against the tumor has also been documented. Indeed, Lf was shown to stimulate the production of anticarcinogenic cytokines and increase the levels of immune cells that display marked cytotoxicity against cancer cells [131,132]. For example, in mice bearing U14 cervical tumors, the administration of an adenovirus carrying hLf inhibited tumor growth by upregulating tumor-killing natural killer (NK) cells, increasing the levels of $CD4^+$ (cluster of differentiation 4) and $CD8^+$ T lymphocytes (which act against cancer cells), and augmenting the levels of the cytokines IL-2 and tumor necrosis factor-α (which are associated with NK cells activity) [130]. Moreover, hLf inhibited the release of pro-metastatic cytokines such as IL-8 and IL-6 in an *in vivo* model of head and neck carcinoma [112]. An increase in the levels of NK cells in response to hLf administration was also reported in a clinical trial with lung cancer patients [133]. More recently, bLf inhibitory effects against osteosarcoma were attributed to its role in downregulation various cytokines involved in osteoclast formation, decreasing the number of osteoclasts, which is a desirable feature for an anti-osteosarcoma compound [134].

Moreover, Lf can exert anticancer activity by inhibiting carcinogen activation. This mechanism is especially important in the case of chemically-induced carcinogenesis. This process requires two phases that depend on the enzymes belonging to the liver detoxication metabolism. The first phase encompasses the activity of phase I enzymes that activate carcinogens causing DNA damage in the target organs. This activation can be blocked by phase II enzymes involved in detoxication and excretion of carcinogen-derived products, thus inhibiting the proliferation of pre-malignant cells [135]. bLf was found to inhibit carcinogenesis by either inhibiting phase I enzymes or stimulating the activity of phase II enzymes thus preventing the carcinogenic process. These evidences were achieved in rat and hamster models of chemically-induced carcinogenesis where orally administered bLf significantly inhibited esophagus, bladder, colon, buccal pouch and lung carcinogenesis [135,136].

New insights on the anticancer role of Lf arose when researchers found that the Lf gene expression is negatively associated with cancer progression and metastasis [137,138], and positively associated with patient life expectancy [139]. Indeed, the Lf gene (*LTF*) is downregulated in many types of cancer cells in comparison with their normal counterparts [140], and overexpression of the Lf gene inhibits the proliferation of cancer cells [141]. Thus, Lf has been suggested to act as a tumor suppressor gene [137,141]. Recently, *LTF* deficiency in mice was shown to promote metastatization of melanoma cells to lungs as compared to $LTF^{+/+}$ mice [142].

Some of the research on Lf anticancer activity was already translated to the clinics and several clinical trials have been performed, where encouraging results have been obtained. Kozu *et al.* reported that 1-year daily oral intake of 3 g of bLf is efficient in delaying the growth of colorectal polyps size in participants less than 64 years-old, and bLf intake was suggested as a good adjuvant for colorectal polyp extraction [143]. The combination of rhLf with carboplatin and paclitaxel rendered an overall patient survival improvement in patients with non-small cell lung cancer (NSCLC) [144]. rhLf was further tested in patients with metastatic renal carcinoma and NSCLC who had previously been subjected to conventional chemotherapy, where encouraging anticancer effects were detected [145,146]. The rhLf efficacy against NSCLC was further tested in a phase II and III clinical trials with patients who already had two or more failed chemotherapy regimens. A 65% improvement in overall survival was observed in the phase II trial [147], whereas no improvement was observed in the phase III [148]. Importantly, Lf was well tolerated in all these studies, with no serious side-effects, while signs of immunomodulation were detected. Moreover, when given in combination with chemotherapeutics, bLf was found to minimize the side effects such as anemia and mucositis [149]. It is worth mentioning that almost all of the clinical trials were performed in patients heavily pre-treated and with highly advanced disease, which is probably

the reason for the modest effects of Lf in some trials. Finding the most susceptible cancer types to Lf as well as its targets and mechanisms of action in cancer cells is thus of paramount importance to potentiate the Lf clinical effect. In this line, our group found that bLf targets the plasmalemmal proton pump V-ATPase of highly metastatic cancer cells, and proposed that the presence of this proton pump at the plasma membrane can be used as a biomarker for bLf use as a personalized therapy, a subject that will be addressed in more detail in section 2.3 of this chapter.

2.2. Proton pumping ATPases: master orchestrators of pH control

The intracellular pH regulation is essential for cellular homeostasis in all organisms. Intracellular pH variations dictate the acid-base balance and the protonation state of the acid-base groups, which can have a deep impact on the function of peptides/proteins and, consequently, on most biological reactions [150,151]. Indeed, the protein's structure, function, solubility and interactions, as well as several enzymatic and metabolic processes, and even the cell cycle control are all dependent on specific pH conditions [152,153]. In addition to the cytosolic pH, the function of each organelle has specific pH requirements that must be fulfilled to accomplish the organellar processes. In fact, organelles exhibit pH values that vary up to 3 units from the cytosolic pH [154,155]. One example is the secretory pathway in which the processing and sorting of the cargo is strongly dependent on a progressive acidification along the pathway [156]. Therefore, it is not surprising that the dysregulation of steady-state pH contributes to the pathology of a variety of diseases [157,158].

Proton homeostasis implies that a tight regulation between proton extrusion and import exists in all cells [153]. The mechanisms that regulate the intracellular pH, essential for the functioning of the whole cell and individual organelles, involve a myriad of membrane transporters that have been reviewed several decades ago. These mechanisms include $Na^+(K^+)$-H^+-exchangers, Na^+-HCO_3^- co-transporters, Na^+-K^+ ATPases, Cl-HCO_3^- exchangers, H^+-ATPases, Ca^{2+}-ATPases, vacuolar-ATPases, monocarboxylate-H^+ co-transporters, among many others [152–154,159]. Together, they comprise a set of dynamic and sustained mechanisms that ensure a pH balance within cells by counteracting: the constant tendency of H^+ to move across intracellular compartments according to their concentration gradient; the proton uptake from the extracellular milieu driven by the proton gradient and by the negative potential of the plasma membrane; and the accumulation of H^+ and/or acid equivalents by metabolic pathways [153,154].

Proton-pumping ATPases are a class of these membrane transporters that act as master players in the transport of protons across membranes from Archaea to humans. They are characterized by either using the energy of ATP hydrolysis to actively transport protons, or using the proton gradient to synthesize

ATP, driving a multitude of cellular processes [160]. They belong to the ATPases family, which comprises four broad classes: the F- and A-type ATP synthases, the V-type transporters, the P-type transporters, and the ATP binding cassette (ABC) multidrug efflux pumps [160–162]. The ATP-driven proton pumping is accomplished by distinct mechanisms across the members of this family as discussed below.

Given the great implications of proton pumping ATPases in an almost overwhelming number of vital cellular functions, the term therapeutic/drug target has been ascribed to them by several researchers throughout the years [163–168]. Indeed, the findings in this field have contributed to design novel therapies for diverse diseases such as cancer, fungal infections, and several others [162]. The P-type ATPase Pma1p and V-ATPase, as well as their involvement in fungal infections and cancer, respectively, will be further explored in the context of this work.

2.2.1 Structure and function of the fungal plasma membrane proton pump Pma1p

The earliest work performed by Slayman, Goffeau, Serrano and many others allowed the identification of an enzyme at the yeast plasma membrane, which functioned as an electrogenic proton ATPase that could be activated by glucose, and that was insensitive to oligomycin, in contrast with the mitochondrial F-type ATPase, as recently reviewed by [169]. Nowadays, this proton pump is known as Plasma Membrane ATPase 1 (Pma1) and is encoded by the *PMA1* gene. It is a single-subunit polypeptide of 100 kDa belonging to the P-type ATPases, the same family as the mammalian Na^+/K^+-ATPases and Ca^{2+}-ATPases, sharing several regions of amino acid sequence homology with them. Pma1p has homologues in all fungi and plants, displaying high percentages of sequence similarity among species [170].

Pma1p is the most abundant protein of the yeast plasma membrane and the *PMA1* gene is essential for cell growth [171,172]. Its functioning leads to the extrusion of protons to the extracellular space driven by ATP hydrolysis. Pma1p is considered the major determinant of the plasma membrane potential and cytosolic pH, as well as the main consumer of cellular ATP [172]. The electrochemical gradient created by Pma1p is crucial for a multitude of other of secondary solute transport systems that are responsible for the uptake of various nutrients. Given its pivotal role in overall fungi physiology, it has been implicated in fungal pathogenicity [173]. Indeed, the dimorphic switch of *C. albicans* from yeast to hyphal growth, an important virulence feature, was shown to be accompanied by a tight regulation of Pma1p activity [174].

Although no high-resolution structure of a fungal Pma1p is available, the structure of its plant homolog from *Arabidopsis thaliana*, H1-ATPase 2 (AHA2), has been determined by X-ray crystallography at 3.5 Å resolution [175] and refined afterwards [176]. The refined model is presented in Figure 2.5A. AHA2 is folded into three cytosolic domains: the nucleotide (N) binding domain, the phosphorylation (P) domain, and the actuator (A) domain; as well as ten transmembrane segments where the proton binding site is located. Both N- and C-termini are cytosolic [175]. This structural organization is similar to other previously characterized P-type ATPases [177,178]. Homology models have been created for the *S. cerevisiae* Pma1p incorporating the information of related ATPases, such as from *Neurospora crassa*, which show a similar overall architecture (Figure 2.5B). During the catalytic cycle of the proton ATPase that culminates in proton transport, the enzyme undergoes conformational changes that give rise to two distinct states: E1, in which the enzyme has high affinity for protons; and E2, where it has low affinity. These states arise from the formation and breakdown of an aspartyl-phosphate intermediate that is generated by the autophosphorylation of a conserved aspartate residue (Asp 329 in AHA2) located at the P domain. Throughout this cycle, the interaction of the P domain with the N domain (where ATP binds) and the A domain leads to autophosphorylation and dephosphorylation, respectively. These movements are intimately linked to the transmembrane domains. An autoinhibitory mechanism of Pma1p operated by a regulatory domain at the C-terminal is also believed to regulate Pma1p activity. As a consequence of the following steps: ATP binding, phosphorylation, dephosphorylation, and phosphate release; the protons are transported from one side of the lipid bilayer to the other [179,180].

A close interplay between Pma1p and the vacuolar proton pump V-ATPase, which is the central responsible for fungal vacuolar acidification, exists in fungal cells. This interconnection is crucial for the response to different environmental factors including variations of glucose levels and pH. Both proton pumps depend on ATP and are activated by glucose [172]. The interdependence between both proton pumps was demonstrated in *vma* mutants (yeast mutants lacking single V-ATPase subunits), in which Pma1p was found at intracellular locations, including at the vacuole and its ubiquitination and endocytosis was increased [181]. Moreover, glucose-activated proton extrusion, which is mainly performed by Pma1p, was much lower in *vma* mutants. Thus, the coordinated activity of both proton pumps greatly contributes to pH homeostasis [182].

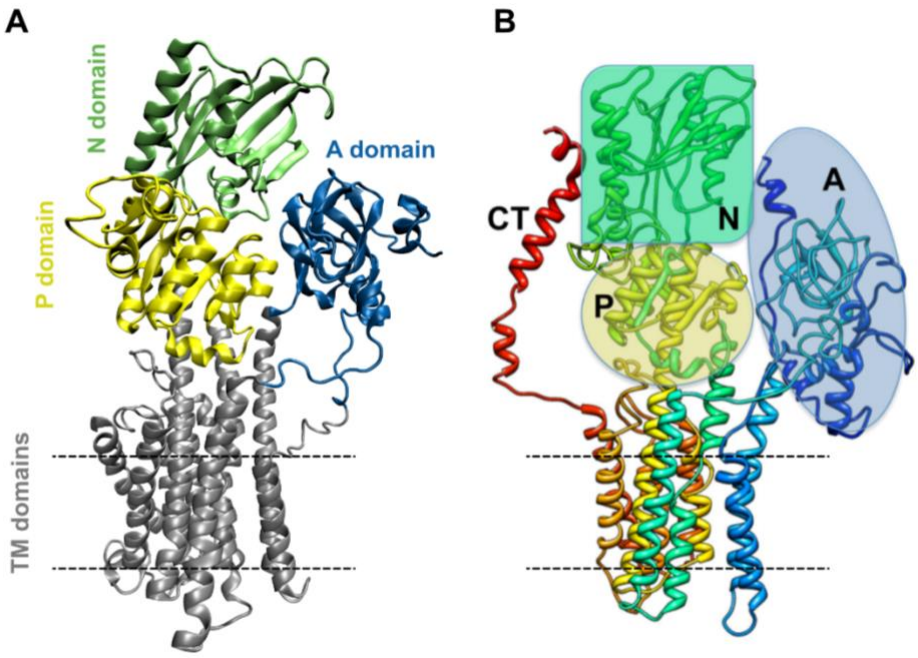

Figure 2.5: Structure of P-type proton pumping ATPases. (A) Refined crystallographic structure of *Arabidopsis thaliana* H1-ATPase 2. Each domain is coloured differently as indicated. The visual representation was designed using VMD with the pdb structure 5KSD published by [176]. **(B)** Model of the structure of *Saccharomyces cerevisiae* Pma1p created based on the *Neurospora crassa* plasma membrane proton ATPase model. The putative positions of the three cytosolic domains (A, N and P) are indicated based on the model depicted in A. The cytosolic C-terminal is also shown (adapted from [172]). The dashed lines indicate the approximate location of the plasma membrane.

2.2.1.1 Pma1 as an antifungal drug target

Given its vital role in fungal physiology, wide distribution among fungi and absence from higher eukaryotes, Pma1p has been explored as a specific target for broad-spectrum antifungal drug development [172,173]. In fact, Pma1p inhibition has been shown to be an effective antifungal therapy generally leading to hydrolytic activity impairment, glucose-activated proton extrusion hindering, intracellular ATP accumulation and intracellular acidification, which culminates in growth inhibition and cell death [91,183].

Several Pma1p inhibitors have been developed throughout the years. The classical Pma1p inhibitor vanadate, which is widely used in biochemical assays using purified cellular fractions, is not an effective antifungal as it cannot penetrate membranes, therefore lacking activity against whole cells [184]. Also, the classical stomach Na^+/K^+-ATPase inhibitor omeprazole showed good Pma1p inhibition and fungicidal effect, however its activity requires activation at low pH [185]. Novel inhibitors have therefore been explored. A compound that has been receiving increasing attention in the last decade is ebselen (2-phenyl-1,2-benzisoselenazol-3(2H)-one), a fungicidal organoselenium compound that was shown to inhibit fungal

growth, induce cell death and target Pma1p as demonstrated by its ability to thwart ATPase activity and ensuing medium acidification [183]. Different works aiming to explore the antifungal potential of ebselen analogs have been published afterwards that reinforce the potent antifungal effect of organoselenium compounds, even against fluconazole-resistant strains, owing to the targeting of Pma1p (demonstrated in whole cells and purified Pma1p fractions) [186,187]. A conjugated styryl ketone called NC1175 was also shown to inhibit glucose-induced extracellular acidification in several *Candida*, *Saccharomyces* and *Aspergillus* species. Pma1p was suggested to be the target of NC1175 since it completely blocked the inhibitory effect of vanadate towards ATP hydrolysis in isolated membrane fractions [188]. Natural compounds have also been explored. Eugenol and thymol, the major phenolic components of clove and thyme essential oils, have shown promising antifungal activity against various *Candida* isolates including azole-resistant isolates. This activity was associated to their inhibitory effects towards Pma1p as suggested by the inhibition of glucose-stimulated proton efflux and intracellular acidification induced by both compounds [189].

Screening of compound libraries is an interesting approach to identify novel Pma1p inhibitors. Kjellerup *et al*. performed a screening with 191 000 compounds aiming to find those that could inhibit ATP hydrolysis. Compounds holding the desired activity at low concentrations were further tested for their effects on membrane potential, intracellular ATP concentration, extracellular acidification and *S. cerevisiae* growth inhibition. A series of compounds containing a pyrido-thieno-pyrimidine group were particularly interesting as they selectively inhibited Pma1p activity as compared to other mammalian P-type ATPases [184]. Another screening tested the effect of crude extracts of 33 plant species on the ATPase activity of plasma membranes isolated from *S. cerevisiae*. After the initial results, high resolution analysis was carried out to identify the active compounds. Chebulagic acid and tellimagrandin II were identified as antifungal agents with Pma1p inhibitory capacity [190]. The search for novel Pma1p inhibitors is thus a promising approach for antifungal therapy.

2.2.2 Structure and functions of V-ATPases

Vacuolar H^+-ATPases (V-ATPases) were first discovered in the vacuoles of yeast [191,192] and plants [193,194] and afterwards identified in a myriad of intracellular organelles including mammalian lysosomes, secretory vesicles, endosomes, Golgi-derived vesicles, among many other subcellular locations [195]. Besides its intracellular membrane distribution, V-ATPases are also present at the plasma membrane of highly metastatic cancer cells [196,197], as well as in a variety of specialized cells [198,199]. Such a cellular localization diversity is consistent with the multiple roles exerted by V-ATPases

including intracellular trafficking, synthesis and processing of biomolecules, uptake of nutrients, urine acidification, maturation of hormones, bone remodeling, sperm maturation, among others, as recently reviewed [195,200,201].

V-ATPases are highly conserved among prokaryotes and eukaryotes and their overall multi-subunit structure is well conserved. The V-ATPase structure will be more thoroughly described here as, in Chapter 5, a computational approach that aims to predict how Lf binds to V-ATPase is explored. It consists of two functional domains, the V_o domain, embedded in the cellular membranes and responsible for the proton translocation; and the V_1 domain, cytosolic and responsible for the ATP hydrolysis (Figure 2.6). These domains comprise different subunits with defined stoichiometry [202]. Curiously, the mature V-ATPase has 30 polypeptides generated from 12-16 gene products, which results in a complex of ca. 1 MDa [203]. The best-known eukaryotic V-ATPase subunit organization is from the budding yeast *Saccharomyces cerevisiae*, for which several cryo-electron microscopy (cryo-EM) or X-ray diffraction structures of the biological assembly of the complex [202,204,205] or of individual subunits [206–208] and domains [209–211] are deposited at the Protein Databank (https://www.rcsb.org). The V_o domain consists of subunits *a*,*d*,*e*, a *c*-ring composed of subunits c_8, *c'*, *c''*, and the recently identified subunit *f* [210], and the assembly factor Voa1p [209,211]. In turn, the V1 domain contains the subunits A_3, B_3, C, D, E_3, F, G_3, H [202]. The stoichiometry is indicated by the numbers in subscript. The three AB subunit pairs form three catalytic sites, the so-called catalytic hexamer A_3B_3, where ATP is hydrolyzed. Subunit *a* from the V_o domain has a dual role, namely its cytosolic N-terminal part is involved in the targeting of V-ATPase to the appropriate cellular location, whereas its membrane C-terminal part forms two half-channels, where protons are translocated. Together with subunits H and C, subunit *a* also connects the two domains. Each of the subunits of the *c*-ring has conserved glutamate residues (c - Glu137, c' - Glu145, c'' - Glu108) that bind and transport protons during ATP hydrolysis [210]. Very recently, Wang *et al.* described for the first time the structure of the human V-ATPase at up to 2.9 Å resolution (Figure 2.6), where they found a crucial role for the assembly subunit ATP6AP1 as a hub for the V_o domain assembly by interacting with various V_o subunits and lipids. Moreover, they pinpointed the role of glycolipids, phospholipids and N-glycans linked to V_o subunits in V-ATPase assembly, localization and protection from hydrolases [212]. Here, we only highlight the roles of the most prominent subunits. For a comprehensive review on V-ATPase subunits' functions please refer to [205] and [210]. A fascinating feature of V-ATPase is the existence of cell/tissue-specific isoforms of some subunits that determine its subcellular localization, and whose mutations originate different human diseases. Indeed, mammals have different isoforms of subunits V_o*a*, V_o*d*, V_1B, V_1C, V_1E and V_1G, besides the ubiquitous ones [195,213].

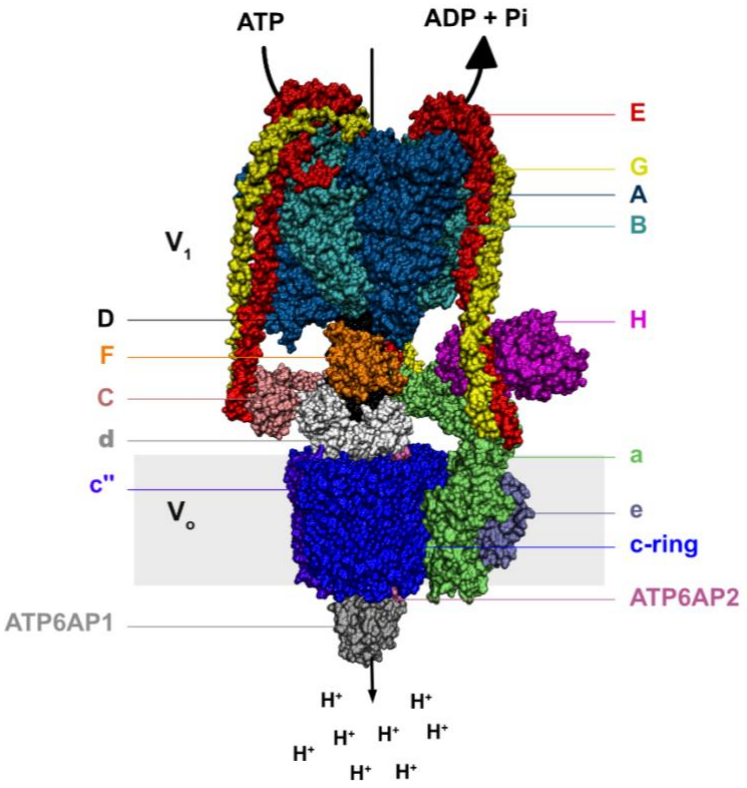

Figure 2.6: Structure of the human V-ATPase. The V_1 and V_o domains, responsible for ATP hydrolysis and proton transport, respectively, are indicated. The different subunits are coloured differently. The visual representation was designed using VMD with the pdb structure 6WM2 published by [212].

V-ATPases operate by a rotary mechanism and are considered nanoscale rotary motors [203]. Three distinct rotational states have been observed in the cryo-EM V-ATPase structures, where conformational changes occur in the majority of the subunits during the transition from one state to another [202,204,205,212]. Indeed, in functional terms, V-ATPases are divided in a central rotor and a peripheral stator complex. ATP hydrolysis is coupled to proton translocation through the rotation of the central rotor, while the stator complex stabilizes the motor by preventing the entire complex from turning with the rotor. This complex structural organization allows V-ATPases to efficiently transport protons across membranes creating an electrochemical potential that drives a series of secondary active transport systems [205].

2.2.2.1 V-ATPases as attractive targets for cancer therapy

V-ATPases are emerging as potential drug targets in cancer therapy since a growing number of evidence shows a link between V-ATPases dysregulation and cancer survival and, metastasis. Indeed, the overexpression and altered subcellular localization of V-ATPase in cancer cells, in comparison with their

non-cancer counterparts, as well as the role of different V-ATPase isoforms and mutations in cancer have been reported by several researchers [163]. Overall, the most important roles of V-ATPase in tumors are related to invasiveness, angiogenesis, proliferation, tumorigenesis and drug resistance [214,215].

With the exception of some specialized cells, V-ATPases are generally localized at the membranes of intracellular organelles, ensuring their acidification [200]. However, our group and others, using different methodological tools, demonstrated that V-ATPase is at the plasma membrane of highly metastatic cancer cells derived from different types of cancer (Table 2.2), but not in lowly metastatic or non-tumorigenic cells [107,196,216]. Moreover, highly metastatic cancer cells were shown to preferentially use plasmalemmal V-ATPase to maintain their intra- and extracellular pH balance, while lowly metastatic cancer cells resort to Na^+/H^+ exchangers or HCO_3^- - based H^+-transporters [196,217]. The V_o*a4* isoform was shown to be responsible for the targeting of V-ATPase to the plasma membrane in MDA-MB-231 highly metastatic breast cancer cells as its silencing by siRNA decreases the V-ATPase plasma membrane staining [197]. The V_o*a3* isoform also seems to play a role in the plasmalemmal targeting of V-ATPase given that its overexpression in a non-invasive immortalized breast cell line significantly increased the localization of V-ATPase at the plasma membrane [218]. The link between the presence of V-ATPase at the plasma membrane and enhanced invasive and metastatic capacities of cancer cells is well documented [197,218,219]. Indeed, several studies demonstrated that the *in vitro* invasion capacity of highly, but not lowly, metastatic cancer cells is dramatically impaired by V-ATPase inhibition [196,218]. The targeting of V-ATPase to the cell surface has been proposed to both contribute to the alkalization of the tumor cell cytoplasm and to the acidification of the extracellular tumor microenvironment (TME) [197,218]. By maintaining an aberrant acidic pH at the TME, V-ATPase contributes to the activation, secretion, and cellular distribution of many proteases involved in the digestion of the extracellular matrix, including matrix metalloproteinases (MMP), thus promoting local invasion and metastasis [220].

Besides its plasmalemmal localization, V-ATPase is also overexpressed in different types of cancer cells [218,226,230–232]. Indeed, we showed that V-ATPase is overexpressed in highly metastatic cancer cells derived from osteosarcoma, breast and prostate cancer, which is associated with higher extracellular acidification rate and more acidic lysosomes [106,107]. On the other hand, numerous works focusing on specific V-ATPase isoforms reported they are overexpressed in cancer cells with high invasive capacity, as compared to non-cancer cells or lowly invasive cancer cells (Figure 2.7). Looking at the overall picture, the overexpression of V_o*a2-4*, V_o*c* and V_1C1 subunits are those that gather a greater piece of evidence in breast and ovarian; musculoskeletal and prostate; and head and neck cancer, respectively. Very recently,

an interesting work reported the expression of all V-ATPase subunit isoforms in esophageal squamous cell carcinoma, followed by a comparative analysis with other types of cancer. This study revealed the peculiar presence of V-ATPases harbouring distinct subunit isoform combinations, specific of different cancer types (V-ATPase molecular signatures). The knowledge of these combinations is particularly relevant as their can either function as cancer biomarkers or be used as basis for drug development [233]. Indeed, ablation of specific subunits diminishes the invasive capacity of cells [216,231,234].

Table 2.2: Evidence and methodological tools used to detect the presence of V-ATPase at the plasma membrane of highly metastatic/invasive cancer cells as compared, in some studies, to lowly metastatic/less invasive cancer cells and/or non-cancer cells. Unless otherwise indicated, commercially available cell lines are depicted. IF: immunofluorescence, WB: western blot, FC: flow cytometry, PC: primary culture, TS: tissue sections.

Cancer type	Technique	Highly metastatic cancer cells	Lowly metastatic cancer cells	Non-cancer cells	References
Breast	IF	Hs 578T	T-47D	MCF-10-2A	[107]
	IF, WB	MDA-MB-231	MCF-7		[196,197]
	IF	MCF10CA1a		MCF10a	[218]
	IF	MCF10CA1a, MB231, SUM149		MCF10a	[219,221]
	IF	SKBR3		MCF10a	[222]
Musculoskeletal	IF	MG-63, RD, SW1353			[223]
	IF	SK-N-MC, A-673, SK-ES-1, RD-ES			[224]
Pancreatic	IF	Panc-1	BXPC3		[216]
Prostate	WB	C4-2B	LNCaP		[225]
Liver	IF, WB	Hepatocellular carcinoma cells (PC)		Normal hepatocytes (PC)	[226]
Lung	IF	Non-small cell lung cancer cells (PC)			[214]
Ovarian	FC, IF	TOV-112D, A2780, SKOV-3		Normal ovarian (TS)	[227]
Esophageal	IF	Esophageal squamous cancer cells (TS)			[215]
Melanoma	WB	WM115, SK-Mel-28, WM239A, WM164	SBCl2, WM793		[228]
	IF	B16-F10	B16		[229]

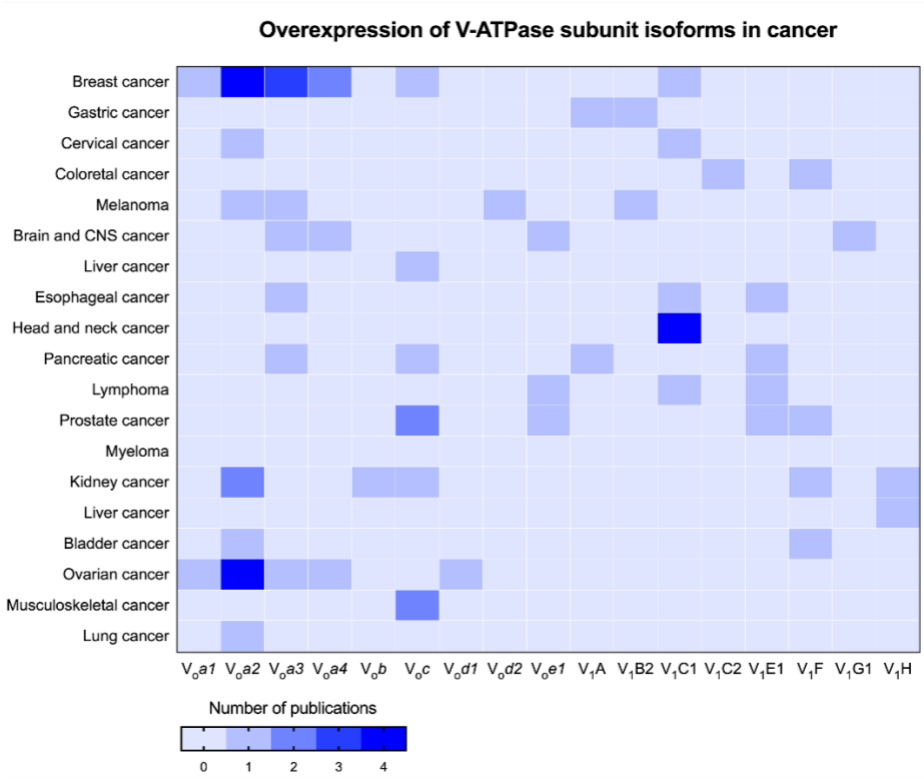

Figure 2.7: Evidence supporting the overexpression of V-ATPase subunit isoforms at mRNA and/or protein levels in different types of cancer, as compared to their lowly invasive and/or non-cancer counterparts. The blue scale colour map represents the number of publications where a specific isoform overexpression was reported. This heatmap was built based on the following publications: [197,216,218,221,223,226,227,229–253]. CNS: central nervous system.

Since V-ATPases are housekeeping ubiquitously expressed proton pumps, their inhibition in terms of clinical prospects faces serious barriers. Selectivity should be the leading concept in the development of therapeutic V-ATPase inhibitors, because off-target V-ATPase inhibition is detrimental for the organism [220,254]. There are different families of V-ATPase inhibitors [220,255] but, despite all the efforts by the scientific community, these inhibitors have not reached human clinical trials so far, and therefore their clinical use is very limited owing to their high *in vivo* toxicity [220,254]. Hence, rational strategies based on the targeting of specific subunit isoforms/interactions signatures, and of V-ATPases localized in specific environments known to be associated with disease, have been exploited [256,257].

V-ATPase inhibition has been regarded as a very promising strategy in the fight against cancer as several *in vitro* and *in vivo* studies show its effectiveness in preventing cancer cell survival, invasiveness and metastasis (Table A1, Appendix). Indeed, old and more recent V-ATPase inhibitors are effective against different types of cancer models, generally leading to imbalanced pH regulation [106,258–260], decreased expression of metalloproteinases [258,259] and inhibition of both migration and invasion [258,260–263] (Figure 2.8).

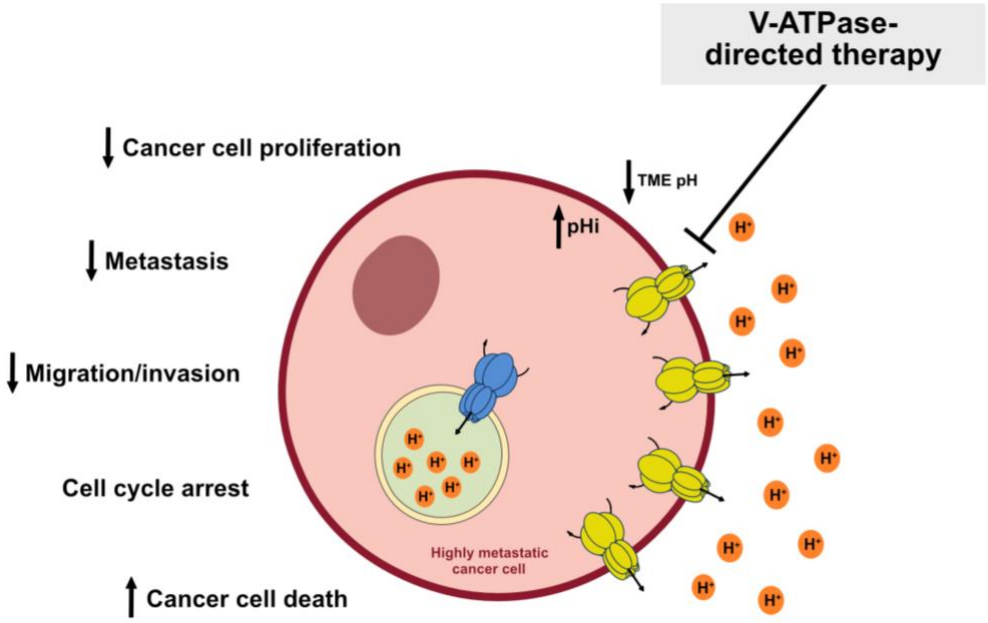

Figure 2.8: Effects of V-ATPase inhibition in highly metastatic cancer cells. The inhibition of V-ATPases at the plasma membrane of highly metastatic cancer cells, which display V$_o$*a3*/*a4* subunit isoforms, is a promising therapeutic strategy for cancer, as it will hinder intracellular alkalinization and acidification of tumor microenvironment (TME). The consequences of V-ATPase inhibition described on the left are based in several *in vitro* and *in vivo* studies described throughout the text either as an outcome of exposure to V-ATPase inhibitors or deletion of V-ATPase subunit genes.

Table A1 (Appendix) describes the advances of the last few years regarding V-ATPase inhibition-based approaches towards anticancer therapy. Recently, non-classical natural compounds, such as the plant-derived myrtenal [261] and cleistanthin A or its derivatives [258,262], lactoferrin [106,107], the natural cyclodepsipeptide verucopeptin [264] and vitamin D [265] have been tested showing good anticancer activity. Also, the proton pump inhibitors (PPIs), originally developed to inhibit the stomach Na^+/K^+-ATPase, were found to inhibit V-ATPase and explored for anticancer therapy [266,267]. Some of the V-ATPase inhibitors depicted in Table A1 (Appendix) display good selectivity towards cancer cells [268,269], while the classical V-ATPase inhibitors like bafilomycin A1 (BafA1) and concanamycin A (ConcA) would require targeted delivery and maintenance at the tumor site to be considered therapeutic agents [220]. The rational discovery of V-ATPase inhibitors using virtual screening has also been explored and a new bisbenzimidazole analog with marked cytotoxicity against breast and ovarian cancer cell lines was identified. This is a very promising approach for drug discovery against a specific enzyme/protein, which explores databases containing millions of molecules [270]. Similar approaches aiming to find inhibitors that target specific subunit isoform combinations may also be a very favorable strategy.

2.3. Novel interactions of lactoferrin with proton pumping ATPases

The search for the mechanisms underlying Lf antimicrobial and anticancer activities led to the identification, in the last years, of novel interactions between Lf and different proton pumping ATPases in bacteria, yeast and cancer cells (Figure 2.9). These interactions constitute the launchpad of all the work developed throughout the present thesis. Indeed, taking them as a starting point, we performed a series of experimental approaches to characterize the molecular basis of the antifungal and anticancer activities of Lf in-depth, with the aim of potentiating its application as both an antifungal and an anticancer compound.

One of the studies on the interaction of Lf with proton pumping ATPases was performed by our group. We identified plasmalemmal V-ATPase as a bLf molecular target. Indeed, we found that bLf is selectively cytotoxic to highly metastatic breast cancer cells displaying V-ATPase at the plasma membrane. Lowly metastatic breast cancer cells and non-tumorigenic cells, which exhibited only intracellular V-ATPase, were resistant to bLf. This selectivity was also associated with increased V-ATPase activity. Besides inducing apoptosis in the highly metastatic cancer cells, bLf inhibited the basal extracellular acidification rate, which in these cells is mainly dependent on V-ATPase, and promoted intracellular acidification, consistent with the inhibition this proton pump activity. Accordingly, bLf inhibited V-ATPase proton pumping and hydrolytic activities in lysosomes isolated from rat liver and microsomes isolated from cancer cells [107]. A few years later, this selectivity was further demonstrated against highly metastatic cancer cells derived from other cancer types that also displayed V-ATPase at the plasma membrane, namely prostate cancer and osteosarcoma. In this work, the bLf cytotoxicity was associated with the overexpression of V-ATPase and a direct or indirect inhibitory effect of bLf towards the lysosomal V-ATPase was also reported. Indeed, bLf treatment led to lysosomal alkalinization likely due to V-ATPase inhibition [106].

Despite yeast cells do not display plasmalemmal V-ATPase, they exhibit Pma1p which, though structurally different, is functionally similar to V-ATPase. Indeed, Andrés *et al*. identified Pma1p as a target of hLf in *C. albicans*. In fact, hLf treatment led to the intracellular accumulation of ATP, inhibition of glucose-induced extracellular acidification and impairment of ATP hydrolysis in isolated plasma membrane fractions. As all these phenotypes were consistent with Pma1p inhibition, the authors next showed the direct binding of hLf to Pma1p by far-western blot [91]. More recently, the same research group demonstrated that the cytosolic acidification caused by the binding of hLf to Pma1p is the first transduction signal that triggers the subsequent cascade of events. Downstream events include perturbation of both plasma and mitochondrial membrane potential, as well as K^+ cytosolic efflux that

culminates in regulated cell death through apoptosis [92]. Also, in the fungus *Penicillium expansum*, an interaction between Lf and P-ATPases was previously suggested, though not demonstrated [271].

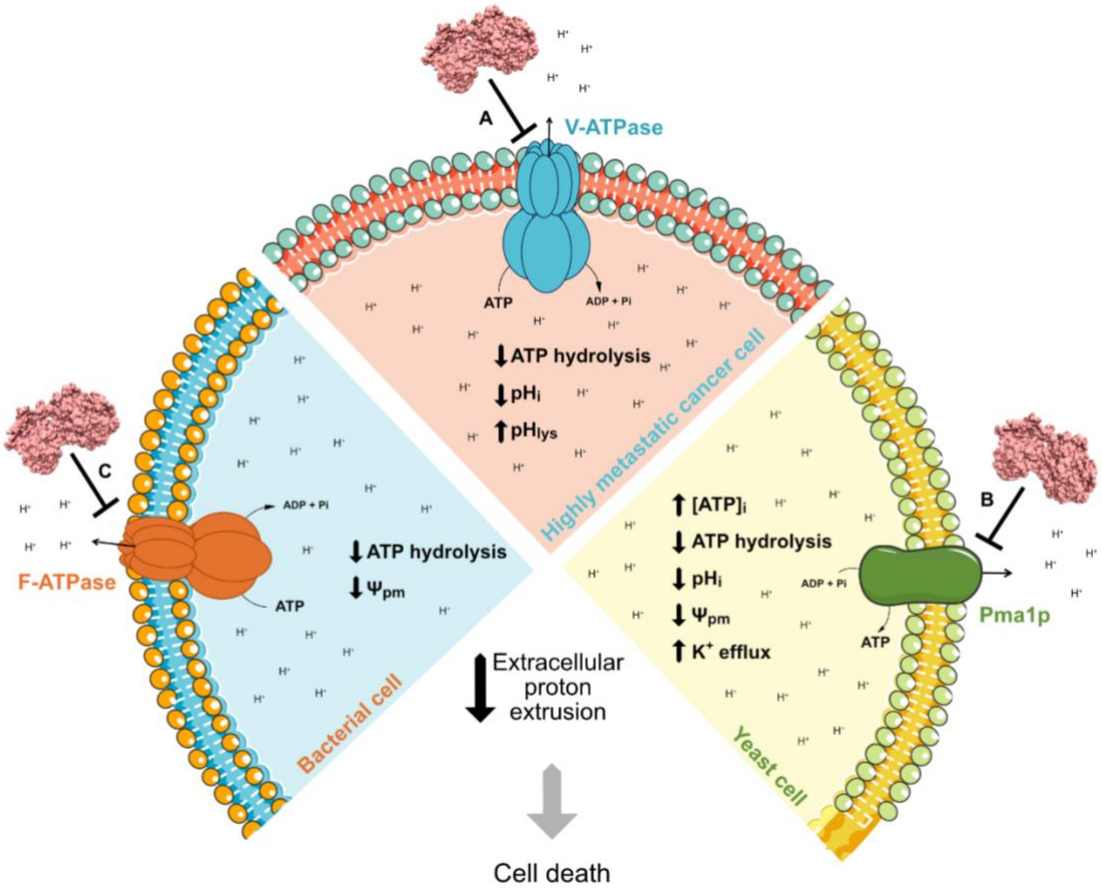

Figure 2.9: Overview of the interaction of lactoferrin with plasmalemmal proton pumping ATPases. Lf inhibits the activity of **(A)** V-ATPase in highly metastatic cancer cells, **(B)** Pma1p in *Candida albicans*, and **(C)** F-ATPase in *Lactococcus lactis*. These inhibitory interactions induce cellular dysfunctions including those depicted for each cell type. In all cellular models an inhibition of the extracellular acidification rate is observed, and all these changes ultimately lead to cell death. pHi, intracellular pH; pHlys, lysosomal pH; [ATP]i, intracellular ATP concentration; Ψpm, plasma membrane potential.

rhLf was also reported to inhibit the activity of the bacterial F-type H^+-ATPase of *Lactococcus lactis* [18]. F-ATPases are proton-pumping ATP synthases that can either synthetize ATP using the transmembrane proton motive force generated in cells under respiratory conditions, through the process known as oxidative phosphorylation, or hydrolyze ATP to generate the proton motive force and extrude protons in fermentative conditions [272]. Incubation of glucose-fermenting *L. lactis* with rhLf resulted in loss of cell viability associated with loss of plasma membrane potential while preserving plasma membrane integrity. Using inverted membrane vesicles isolated from *L. lactis*, Andrés *et al.* demonstrated that rhLf inhibits the ATP-dependent proton translocation induced by F-ATPase. The ATP hydrolysis was

also impaired, as evaluated in *L. lactis* purified membrane fractions. These inhibitory effects are suggested to induce intracellular H^+ accumulation and loss of pH regulation, which ultimately results in cell death [18].

Altogether, these studies reinforce proton pumping ATPases as targets of Lf in different cell models and physiological scenarios. Although the consequences of the interplay between Lf and these proton pumps have been studied, how this correlates with other phenotypes associated with Lf antifungal and anticancer activities, and how the membrane niches that house these proton pumps are affected is still largely unknown and will be studied in the present thesis. Since yeast, as highly metastatic cancer cells, display the Lf molecular target at the plasma membrane, it can be used as a simpler model to mimic these cells and the anticancer effect of Lf.

2.4. Sterol- and sphingolipid-rich lipid rafts of cellular membranes

The classical vision of the cell membranes as homogeneous and fluid mosaics proposed by Singer and Nicolson [273] has evolved to a novel concept that implies lateral heterogeneity and order. Originally proposed by Simons and Ikonen in 1997, the lipid rafts theory hypothesized that close interactions between specific lipid species, mainly sphingolipids and cholesterol, prompt the formation of packed and ordered membrane domains that recruit certain lipids and proteins and are involved in membrane trafficking and cell signalling [274]. The lipid rafts hypothesis was based on two main evidences: the fact that detergent-resistant membranes (DRMs), which are enriched in cholesterol and sphingolipids, can be obtained by fractionation of cells/tissues with non-ionic detergents at cold temperatures [275]; and the observation that artificial model membranes composed of different lipids can form liquid ordered (Lo) and liquid disordered (Ld) phases, which have distinct packing, rigidity and permeability. The Lo phase is rich in saturated lipid species and cholesterol [276,277]. Since then, the field underwent a boom, with the number of publications increasing exponentially (Figure 2.10A), along with the controversy on their existence and biological importance. Indeed, since lipid rafts are extremely small and highly dynamic, their direct observation has been a great challenge that remains until now. This together with the lack of definition in structural, biophysical and biochemistry terms, has promoted a long-standing debate among the scientific community [278].

In order to clarify the definition of these membrane domains, a meeting that brought together a broad group of scientists in the field was held in 2006, where the following definition was put forward: “Membrane rafts are small (10–200 nm), heterogeneous, highly dynamic, sterol- and sphingolipid-enriched domains that compartmentalize cellular processes. Small rafts can sometimes be stabilized to

form larger platforms through protein-protein and protein-lipid interactions" [279]. Although the nature of lipid rafts is still a matter of debate, the advent of cutting-edge biochemical and biophysical techniques, their association with a variety of cellular functions [280], as well as the proposed presence of analogous raft-like domains in bacteria [281] and intracellular organelles like vacuoles [282] and mitochondria [283], support their existence and biological relevance [278,280].

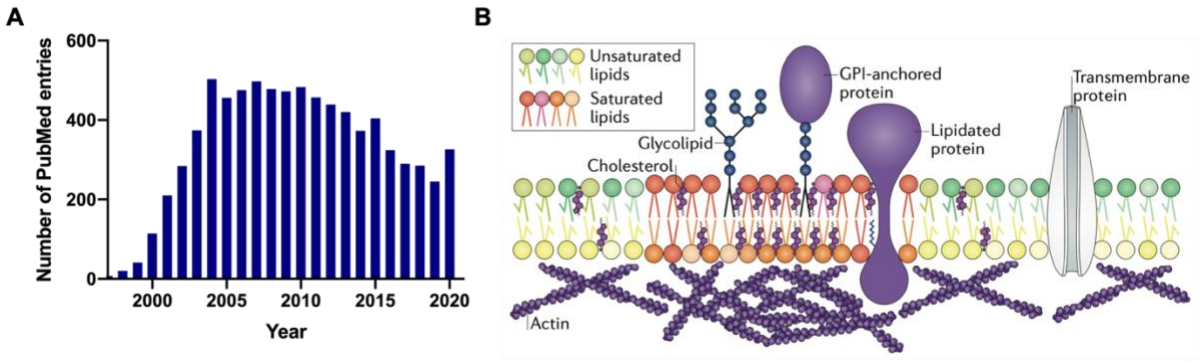

Figure 2.10: Research on lipid rafts and their composition. (A) Number of publications in PubMed by year using the search term "lipid rafts" (from 1997 to 2020). The number of papers increased exponentially since the publication of the lipid rafts hypothesis in 1997, reaching a maximum of 503 papers in 2003. Since then, an average of 401 papers/year was published. **(B)** Proposed composition and organization of lipid rafts. These membrane domains are rich in saturated lipids, sphingolipids, sterols and lipidated proteins. Interaction with actin is also suggested to contribute to lipid rafts maintenance and remodeling (adapted from [280]).

Currently, there is a consensus that lipid rafts are membrane domains with distinct physical properties than their surrounding environment including lower fluidity and higher lipid packing and order, which promote lateral heterogeneity. In mammalian cells, they are formed by the preferential association of sterols and glycosylated/saturated lipids with certain proteins, being enriched in sphingolipids, cholesterol, saturated phospholipids, glycolipids, lipidated proteins and glycosylphosphatidylinositol (GPI)-anchored proteins (Figure 2.10B) [280]. They are present in both outer and inner leaflets of the plasma membrane [284]. Lipid rafts have been implied in a plethora of biological functions such as cellular signalling, protein trafficking and host pathogen interactions; and their association with disorders like cancer and cardiovascular diseases has been reported [280]. In this thesis, the relevance of lipid rafts to the physiology of fungal and cancer cells, as well as their interplay with the proton pumps Pma1p and V-ATPase will be explored.

2.4.1 Yeast lipid rafts and Pma1p

Yeast lipid rafts are much less studied than their mammalian counterparts, although some specific features and biological functions have been reported. In *S. cerevisiae*, lipid rafts are composed of ergosterol and complex sphingolipids [285]. Ergosterol is the main sterol from yeast and has been shown to be better at forming ordered and packed lipid domains in model membranes than cholesterol [286]. While in mammalian cells, lipid rafts formation occurs in the Golgi apparatus [287], in yeast it takes place in the endoplasmic reticulum [288]. Lipid rafts have been identified in different yeast species including budding [288] and fission yeasts [289], and the contribution of their polarization for hyphal growth in *C. albicans* has been addressed [290]. While lipid rafts are distributed throughout the plasma membrane in the budding yeasts, in the fission yeasts they preferentially localize to the regions of polarized growth [289]. Lipid rafts were found at actively growing sites, at the hyphae tips and at the septation sites of the pathogenic yeast *C. albicans* [290]. Besides being involved in fungal pathogenicity, yeast lipid rafts have been implicated in different vital cellular functions including protein and nutrient transport, membrane trafficking, intracellular pH regulation, mating, virulence and cytoskeleton organization. On these grounds, proteins involved in ion homeostasis, nutrient transport, stress response, mating and cytoskeleton regulation have been identified in lipid rafts. Some of these proteins have been found in non-overlapping raft domains, suggesting the existence of different raft-like subcellular compartments in yeast [291–294]. Recently, special focus has been given to the yeast vacuolar lipid rafts and their role in global vacuolar function [295].

By DRMs isolation, Pma1p was found to localize at the plasma membrane lipid rafts [288,296], and is nowadays recognized as a typical lipid rafts marker in yeast [291]. DRMs localization of Pma1p was abolished in mutant strains unable to synthetize ergosterol or sphingolipids [288] and lipid rafts disruption resulted in vacuolar instead of plasma membrane localization of the proton pump, which highlights the critical role of lipid rafts in the surface delivery of Pma1p [296]. Actually, Pma1p was shown to associate with sphingolipids at the endoplasmic reticulum (ER), and then the Pma1p-sphingolipid complex is sorted to the plasma membrane. Sphingolipids perturbation specifically by alteration of the fatty acid chain length impaired lipid rafts localization of Pma1p [297,298]. Sphingolipids were further demonstrated to be required for Pma1p ER oligomerization, plasma membrane delivery and stability [299,300]. Moreover, Pma1p association with lipid rafts is thought to contribute to its stability at the plasma membrane [301]. Interestingly, Pma1p displacement from lipid rafts triggered by the anticancer lysophospholipid edelfosine was shown to induce yeast cell death [302]. The interplay between Pma1p

and lipid rafts will be further discussed in Chapter 3, aiming a better understanding of the Lf antifungal activity.

2.4.2 Lipid rafts in cancer cells and their interplay with V-ATPase

Several evidences have pinpointed an important role of lipid rafts in cancer and cancer-associated signalling. Remarkably, higher levels of lipid rafts have been detected in cancer cells as compared to their non-cancer counterparts. Li *et al.* showed that human prostate and breast cancer cell lines exhibit a stronger staining of cholesterol and glycosphingolipid GM1 (a lipid rafts marker) than the non-tumorigenic cells [303]. Also in melanoma, cancer cells were found to have 1.5 to 2-fold higher cholesterol and liquid-ordered membrane phases than non-cancer cells [304]. In this line, cancer cells were shown to be more sensitive to cell death induced by lipid rafts-disrupting compounds than normal cells [303].

These high lipid rafts levels in cancer cells are tought to be closely associated with oncogenic signalling, and the anticancer effects of lipid raft-disrupting agents is often associated to the inhibition of tumor-promoting signalling pathways [303,305]. Indeed, it has been demonstrated that the spacial compartmentalization of the components of signalling pathways improves the efficiency of the signal transduction [306]. In agreement, lipid rafts are known to house important signalling molecules involved in the major cell survival pathway, the PI3K (phosphoinositide 3-kinase)/AKT (protein kinase B) pathway, which is frequently constitutively activated in cancer [305]. The raft localization of these proteins is suggested to facilitate AKT recruitment and activation [284], and perturbation of this raft localization inhibits the pathway [306]. Lipid rafts have also been implicated in epidermal growth factor receptor (EGFR) signalling in cancer cells. Lipidomic analysis of glioblastoma cells expressing a constitutively active EGFR, which is often associated with glioblastoma onset, revealed that activated EGFR promoted membrane lipid remodelling by increasing the levels of saturated phosphatidylcholine species, which in turn enhanced membrane order. These phenotypes are associated with augmented EGFR signalling, driven by its association with the lipid rafts, and tumor growth [307]. Furthermore, EGFR lipid rafts localization in breast cancer cells has been associated with resistance of these cells to tyrosine kinase inhibitors. Cholesterol depletion with lovastatin sensitized cells to these inhibitors, attesting to the synergy of agents targeting lipid rafts and anticancer drugs [308].

Besides signalling, lipid rafts have also been implicated in invasion and metastasis (as reviewed by [309]), based on the following observations: molecules involved in cell adhesion and spread have been found at lipid rafts; association of specific proteins in the lipid rafts was shown to promote migration [310]; and lipid rafts disruption was shown to hinder of lamellipodia formation, surface protusions crucial

for tumor cell locomotion and migration [311]. Given all these evidences, lipid rafts have been proposed as therapeutic targets, and compounds that perturb lipid rafts as promissing anticancer agents [309,312,313].

An interesting interplay between V-ATPase and lipid rafts has been reported in cancer cells. Indeed, V-ATPase has been found at the lipid rafts of different types of cancer cells including cells derived from melanoma [228], leukemia [314] and cervical cancer [315]. In melanoma cells, V-ATPase presence at DRMs was found to be directly associated with the degree of malignancy as lipid rafts V-ATPase localization was prominent in highly metastatic cancer cells in comparison with lowly metastatic melanoma cells [228]. Different reports also support the existence of an interdependence between V-ATPase and lipid rafts, since V-ATPase activity seems to be crucial for lipid rafts assembly, and, in turn, lipid rafts are essencial for proper V-ATPase activity. Indeed, V-ATPase inhibition was found to impair lipid rafts clustering [316], and to alter the composition of cholesteryl-ester species as well as membrane fluidity and polarity of liver cancer cells [263]. In turn, lipid rafts perturbation was shown to hinder V-ATPase activity in different cell models [317–319], and changes in lipid composition alter the reversible disassembly mechanism of V-ATPase [317]. This close interplay between V-ATPase and lipid rafts will be will be further detailed in Chapter 4, in the context of Lf anticancer activity.

2.5. Assembling all pieces together to uncover lactoferrin mechanisms of action

Given the interplay between Lf and proton pumping ATPases, and considering the relevance of lipid rafts for Pma1p and V-ATPase functioning and regulation, in the present thesis we aimed to study the putative axis between Lf, proton pumping ATPases and lipid rafts, in order to decipher the mechanisms underlying Lf antifungal and anticancer activities. A computational approach to predict how Lf interacts with V-ATPase is also presented.

References

1. Soerensen M, Soerensen SPL. The proteins in whey. C R Trav Lab Carlsb. 1939;23: 55–99.
2. Groves ML. The isolation of a red protein from milk. J Am Chem Soc. 1960;82: 3345– 3350.
3. Johansson B. Isolation of an iron-containing red protein from human milk. Acta Chem Scand. 1960;14: 510–512.
4. Mayeur S, Spahis S, Pouliot Y, Levy E. Lactoferrin, a pleiotropic protein in health and disease. Antioxid Redox Signal. 2016;24: 813–836. doi:10.1089/ars.2015.6458
5. González-Chávez SA, Arévalo-Gallegos S, Rascón-Cruz Q. Lactoferrin: structure, function and applications. Int J Antimicrob Agents. 2009;33. doi:10.1016/j.ijantimicag.2008.07.020
6. Redwan EM, Uversky VN, El-Fakharany EM, Al-Mehdar H. Potential lactoferrin activity against pathogenic viruses. Comptes Rendus - Biol. 2014;337: 581–595. doi:10.1016/j.crvi.2014.08.003
7. Pierce A, Colavizza D, Benaissa M, Maes P, Tartar A, Montreuil J, et al. Molecular cloning and sequence analysis of bovine lactotransferrin. Eur J Biochem. 1991;196: 177–84. doi:10.1111/j.1432-1033.1991.tb15801.x
8. Liao YL, Jiang RL, Lonnerdal B. Biochemical and molecular impacts of lactoferrin on small intestinal growth and development during early life. Biochem Cell Biol Biol Cell. 2012;90: 476–484. doi:10.1139/o11-075
9. El-Fakharany EM, Sánchez L, Al-Mehdar H, Redwan EM. Effectiveness of human, camel, bovine and sheep lactoferrin on the hepatitis C virus cellular infectivity: comparison study. Virol J. 2013;10: 199. doi:10.1186/1743-422X-10-199
10. Hao L, Shan Q, Wei J, Ma F, Sun P. Lactoferrin: major physiological functions and applications. Curr Protein Pept Sci. 2019;20: 139–144. doi:10.2174/1389203719666180514150921
11. Rai D, Adelman AS, Zhuang W, Rai GP, Boettcher J, Lönnerdal B. Longitudinal changes in lactoferrin concentrations in human milk: a global systematic review. Crit Rev Food Sci Nutr. 2014;54: 1539–1547. doi:10.1080/10408398.2011.642422
12. Rodrigues L, Teixeira J, Schmitt F, Paulsson M, Månsson HL. Lactoferrin and cancer disease prevention. Crit Rev Food Sci Nutr. 2009;49: 203–217. doi:10.1080/10408390701856157
13. Metz-Boutigue M-H, Jollès J, Mazurier J, Schoentgen F, Legrand D, Spik G, et al. Human lactotransferrin: amino acid sequence and structural comparisons with other transferrins. Eur J Biochem. 1984;145: 659–676. doi:10.1111/j.1432-1033.1984.tb08607.x
14. Lambert LA, Perri H, Halbrooks PJ, Mason AB. Evolution of the transferrin family: Conservation of residues associated with iron and anion binding. Comp Biochem Physiol - Part B. 2005;142: 129–141. doi:10.1016/j.cbpb.2005.07.007
15. Rastogi N, Singh A, Singh PK, Tyagi TK, Pandey S, Shin K, et al. Structure of iron saturated C-lobe of bovine lactoferrin at pH 6.8 indicates a weakening of iron coordination. Proteins Struct Funct Bioinforma. 2016;84: 591–599. doi:10.1002/prot.25004
16. Day CL, Stowell KM, Baker EN, Tweedie JW. Studies of the N-terminal half of human lactoferrin produced from the cloned cDNA demonstrate that interlobe interactions modulate iron release. J Biol Chem. 1992;267: 13857–13862.

17. Viejo-díaz M, Andrés MT, Fierro JF. Modulation of *in vitro* fungicidal activity of human lactoferrin against *Candida albicans* by extracellular cation concentration and target cell metabolic activity. Antimicrob Agents Chemother. 2004;48: 1242–1248. doi:10.1128/AAC.48.4.1242

18. Andrés MT, Fierro JF. Antimicrobial mechanism of action of transferrins: Selective inhibition of H+-ATPase. Antimicrob Agents Chemother. 2010;54: 4335–4342. doi:10.1128/AAC.01620-09

19. Zlatina K, Galuska SP. The N-glycans of lactoferrin: more than just a sweet decoration . Biochem Cell Biol. 2020;doi:10.1139/bcb-2020-0106

20. Li Z, Furmanski P. Role of sialic acid residues in iron binding by human Lactoferrin - α. Chinese J Cancer Res. 1995;7: 79–85. doi:10.1007/BF03014401

21. Barboza M, Pinzon J, Wickramasinghe S, Froehlich JW, Moeller I, Smilowitz JT, et al. Glycosylation of human milk lactoferrin exhibits dynamic changes during early lactation enhancing its role in pathogenic bacteria-host interactions. Mol Cell Proteomics. 2012;11: 1–10. doi:10.1074/mcp.M111.015248

22. Le Parc A, Karav S, Rouquié C, Maga EA, Bunyatratchata A, Barile D. Characterization of recombinant human lactoferrin N-glycans expressed in the milk of transgenic cows. PLoS One. 2017;12: 1–15. doi:10.1371/journal.pone.0171477

23. Humphrey W, Dalke A, Schulten K. VMD: Visual Molecular Dynamics. J Molec Graph. 1996;14: 33–38. doi:10.1016/0263-7855(96)00018-5

24. Moore S, Anderson BF, Groom CR, Haridas M, Baker EN. Three-dimensional structure of diferric bovine lactoferrin at 2.8 Å resolution. J Mol Biol. 1997;274: 222–236. doi:10.1006/jmbi.1997.1386

25. Baker HM, Baker EN. A structural perspective on lactoferrin function. Biochem Cell Biol. 2012;90: 320–328.

26. Anderson BF, Baker HM, Dodson EJ, Norris GE, Rumball S V, Waters JM, et al. Structure of human lactoferrin at 3.2-Å resolution. Proc Natl Acad Sci U S A. 1987;84: 1769–1773. doi:10.1073/pnas.84.7.1769

27. Baker HM, Baker EN. Lactoferrin and Iron: Structural and dynamic aspects of binding and release. BioMetals. 2004;17: 209–216. doi:10.1023/B:BIOM.0000027694.40260.70

28. van Berkel PH, Geerts ME, van Veen HA, Mericskay M, de Boer HA, Nuijens JH. N-terminal stretch Arg2, Arg3, Arg4 and Arg5 of human lactoferrin is essential for binding to heparin, bacterial lipopolysaccharide, human lysozyme and DNA. Biochem J. 1997;328: 145–151. doi:10.1042/bj3280145

29. Adlerova L, Bartoskova A, Faldyna M. Lactoferrin: A review. Vet Med (Praha). 2008;53: 457–468. doi: 0.17221/1978-VETMED

30. Guo M, Lu X, Wang Y, Brodelius PE. Comparison of the interaction between lactoferrin and isomeric drugs. Spectrochim Acta - Part A Mol Biomol Spectrosc. 2016;173: 593–607. doi:10.1016/j.saa.2016.10.029

31. Brandenburg K, Jürgens G, Müller M, Fukuoka S, Koch MHJ. Biophysical characterization of lipopolysaccharide and lipid A inactivation by lactoferrin. Biol Chem. 2001;382: 1215–1225. doi:10.1515/BC.2001.152

32. Rivera FP, Medina AM, Bezada S, Valencia R, Bernal M, Meza R, et al. Bovine lactoferrin decreases cholera-toxin-induced intestinal fluid accumulation in mice by ganglioside interaction. PLoS One.

2013;8: 1–8. doi:10.1371/journal.pone.0059253

33. Bennett R, Davis J. Lactoferrin interacts with deoxyribonucleic acid: a preferential reactivity with double-stranded DNA and dissociation of DNA-anti-DNA complexes. J Lab Clin Med. 1982;99: 27–38.

34. Huang J, Liu Z, Ma Q, He Z, Niu Z, Zhang M, et al. Studies on the interaction between three small flavonoid molecules and bovine lactoferrin. Biomed Res Int. 2018;2018. doi:10.1155/2018/7523165

35. Zheng Y, Zhang W, Ye Q, Zhou Y, Xiong W, He W, et al. Inhibition of epstein-barr virus infection by lactoferrin. J Innate Immun. 2012;4: 387–398. doi:10.1159/000336178

36. Coelho YL, de Paula HMC, Agudelo AJP, de Castro ASB, Hudson EA, Pires ACS, et al. Lactoferrin-phenothiazine dye interactions: Thermodynamic and kinetic approach. Int J Biol Macromol. 2019;136: 559–569. doi:10.1016/j.ijbiomac.2019.06.097

37. Bruni N, Capucchio MT, Biasibetti E, Pessione E, Cirrincione S, Giraudo L, et al. Antimicrobial activity of lactoferrin-related peptides and applications in human and veterinary medicine. Molecules. 2016;21. doi:10.3390/molecules21060752

38. Giansanti F, Panella G, Leboffe L, Antonini G. Lactoferrin from milk: Nutraceutical and pharmacological properties. Pharmaceuticals. 2016;9: 1–15. doi:10.3390/ph9040061

39. Zarzosa-Moreno D, Avalos-Gómez C, Ramírez-Texcalco L, Torres-López E, Ramírez-Mondragón R, Hernández-Ramírez J, et al. Lactoferrin and its derived peptides : an alternative for combating virulence mechanisms developed by pathogens. Molecules. 2020;25: 5763. doi:10.3390/molecules25245763

40. Kuwata H, Yip TT, Tomita M, Hutchens TW. Direct evidence of the generation in human stomach of an antimicrobial peptide domain (lactoferricin) from ingested lactoferrin. Biochim Biophys Acta - Protein Struct Mol Enzymol. 1998;1429: 129–141. doi:10.1016/S0167-4838(98)00224-6

41. Britigan BE, Hayek MB, Doebbeling BN, Fick RB. Transferrin and lactoferrin undergo proteolytic cleavage in the *Pseudomonas aeruginosa*-infected lungs of patients with cystic fibrosis. Infect Immun. 1993;61: 5049–55. doi: 10.1128/IAI.61.12.5049-5055.1993

42. Sijbrandij T, Ligtenberg AJ, Nazmi K, Veerman ECI, Bolscher JGM, Bikker FJ. Effects of lactoferrin derived peptides on simulants of biological warfare agents. World J Microbiol Biotechnol. 2017;33: 1–9. doi:10.1007/s11274-016-2171-8

43. Fernandes KE, Payne RJ, Carter DA. Lactoferrin-derived peptide lactofungin is potently synergistic with amphotericin B. Antimicrob Agents Chemother. 2020;64. doi:10.1128/AAC.00842-20

44. Cutone A, Rosa L, Ianiro G, Lepanto MS, Di Patti MCB, Valenti P, et al. Lactoferrin's anti-cancer properties: Safety, selectivity, and wide range of action. Biomolecules. 2020;10: 1–26. doi:10.3390/biom10030456

45. Wang B, Timilsena YP, Blanch E, Adhikari B. Lactoferrin: Structure, function, denaturation and digestion. Crit Rev Food Sci Nutr. 2019;59: 580–596. doi:10.1080/10408398.2017.1381583

46. Moreno-Expósito L, Illescas-Montes R, Melguizo-Rodríguez L, Ruiz C, Ramos-Torrecillas J, de Luna-Bertos E. Multifunctional capacity and therapeutic potential of lactoferrin. Life Sci. 2018;195: 61–64. doi:10.1016/j.lfs.2018.01.002

47. Byrd TF, Horwitz MA. Lactoferrin inhibits or promotes *Legionella pneumophila* intracellular multiplication in nonactivated and interferon gamma-activated human monocytes depending upon

its degree of iron saturation. J Clin Invest. 1991;88: 1103–1112. doi: 10.1172/JCI115409.

48. Avalos-Gómez C, Reyes-López M, Ramírez-Rico G, Díaz-Aparicio E, Zenteno E, González-Ruiz C, et al. Effect of apo-lactoferrin on leukotoxin and outer membrane vesicles of *Mannheimia haemolytica* A2. Vet Res. 2020;51: 1–13. doi:10.1186/s13567-020-00759-z

49. Drago-Serrano ME, De La Garza-Amaya M, Luna JS, Campos-Rodríguez R. Lactoferrin-lipopolysaccharide (LPS) binding as key to antibacterial and antiendotoxic effects. Int Immunopharmacol. 2012;12: 1–9. doi:10.1016/j.intimp.2011.11.002

50. Diarra MS, Petitclerc D, Deschênes É, Lessard N, Grondin G, Talbot BG, et al. Lactoferrin against *Staphylococcus aureus* mastitis: Lactoferrin alone or in combination with penicillin G on bovine polymorphonuclear function and mammary epithelial cells colonisation by *Staphylococcus aureus*. Vet Immunol Immunopathol. 2003;95: 33–42. doi:10.1016/S0165-2427(03)00098-9

51. Angulo-Zamudio UA, Vidal JE, Nazmi K, Bolscher JGM, Leon-Sicairos C, Antezana BS, et al. Lactoferrin disaggregates pneumococcal biofilms and inhibits acquisition of resistance through its DNase activity. Front Microbiol. 2019;10. doi:10.3389/fmicb.2019.02386

52. Qiu J, Hendrixson DR, Baker EN, Murphy TF, St Geme JW, Plaut AG. Human milk lactoferrin inactivates two putative colonization factors expressed by *Haemophilus influenzae*. Proc Natl Acad Sci U S A. 1998;95: 12641–6. doi:10.1073/pnas.95.21.12641

53. Pietrantoni A, Di Biase AM, Tinari A, Marchetti M, Valenti P, Seganti L, et al. Bovine lactoferrin inhibits adenovirus infection by interacting with viral structural polypeptides. Antimicrob Agents Chemother. 2003;47: 2688–2691. doi:10.1128/AAC.47.8.2688–2691.2003

54. Liao Y, El-Fakkarany E, Lönnerdal B, Redwan EM. Inhibitory effects of native and recombinant full-length camel lactoferrin and its N and C lobes on hepatitis C virus infection of Huh7.5 cells. J Med Microbiol. 2012;61: 375–383. doi:10.1099/jmm.0.033894-0

55. Masson PL, Heremans JF, Schonne E. Lactoferrin, an iron-binding protein in neutrophilic leukocytes. J Exp Med. 1969;130: 643–58. doi:10.1084/jem.130.3.643

56. Legrand D. Overview of lactoferrin as a natural immune modulator. J Pediatr. 2016;173: S10–S15. doi:10.1016/j.jpeds.2016.02.071

57. de la Rosa G, De Y, Tewary P, Varadhachary A, Oppenheim J. Lactoferrin acts as an alarmin to promote the recruitment and activation of antigen-presenting cells and antigen-specific immune responses. J Immunol. 2008;180: 6868–6876. doi:10.1038/jid.2014.371

58. Ishikawa H, Awano N, Fukui T, Sasaki H, Kyuwa S. The protective effects of lactoferrin against murine norovirus infection through inhibition of both viral attachment and replication. Biochem Biophys Res Commun. 2013;434: 791–796. doi:10.1016/j.bbrc.2013.04.013

59. Hendrixson DR, Qiu J, Shewry SC, Fink DL, Petty S, Baker EN, et al. Human milk lactoferrin is a serine protease that cleaves *Haemophilus* surface proteins at arginine-rich sites. Mol Microbiol. 2003;47: 607–617. doi:10.1046/j.1365-2958.2003.03327.x

60. Furmanski BYP, Li Z, Fortuna MB, CV S, MR D. Multiple molecular forms of human lactoferrin. Identification of a class of lactoferrins that possess ribonuclease activity and lack iron-binding capacity. J Exp Med. 1989;170: 415–29.

61. Sharada Devi A, Das MR, Pandit MW. Lactoferrin contains structural motifs of ribonuclease. Biochim Biophys Acta (BBA)/Protein Struct Mol. 1994;1205: 275–281. doi:10.1016/0167-4838(94)90245-3

62. Kanyshkova TG, Babina SE, Semenov D V., Isaeva N, Vlassov A V., Neustroev KN, et al. Multiple enzymic activities of human milk lactoferrin. Eur J Biochem. 2003;270: 3353–3361. doi:10.1046/j.1432-1033.2003.03715.x

63. Ogasawara Y, Imase M, Oda H, Wakabayashi H, Ishii K. Lactoferrin directly scavenges hydroxyl radicals and undergoes oxidative self-degradation: A possible role in protection against oxidative DNA damage. Int J Mol Sci. 2014;15: 1003–1013. doi:10.3390/ijms15011003

64. Safaeian L, Javanmard S, Mollanoori Y, Dana N. Cytoprotective and antioxidant effects of human lactoferrin against H_2O_2-induced oxidative stress in human umbilical vein endothelial cells. Adv Biomed Res. 2015;4: 188. doi:10.4103/2277-9175.164010

65. Okazaki Y, Kono I, Kuriki T, Funahashi S, Fushimi S, Iqbal M, et al. Bovine lactoferrin ameliorates ferric nitrilotriacetate-induced renal oxidative damage in rats. J Clin Biochem Nutr. 2012;51: 84–90. doi:10.3164/jcbn.11-100

66. Jiang R, Lönnerdal B. Bovine lactoferrin is a transcription factor stimulating IL-1 beta gene expression in the small intestine. Nutrition. 2015;29. doi:10.1096/fasebj.29.1_supplement.582.1

67. Rezk M, Dawood R, Abo-Elnasr M, Al Halaby A, Marawan H. Lactoferrin versus ferrous sulphate for the treatment of iron deficiency anemia during pregnancy: A randomized clinical trial. J Matern Neonatal Med. 2016;29: 1387–1390. doi:10.3109/14767058.2015.1049149

68. Hernell O, Lönnerdal B. Iron status of infants fed low-iron formula: No effect of added bovine lactoferrin or nucleotides. Am J Clin Nutr. 2002;76: 858–864. doi:10.1093/ajcn/76.4.858

69. Ke C, Lan Z, Hua L, Ying Z, Humina X, Jia S, et al. Iron metabolism in infants: Influence of bovine lactoferrin from iron-fortified formula. Nutrition. 2015;31: 304–309. doi:10.1016/j.nut.2014.07.006

70. Li Q, Zhao J, Hu W, Wang J, Yu T, Dai Y, et al. Effects of recombinant human lactoferrin on osteoblast growth and bone status in piglets. Anim Biotechnol. 2018;29: 90–99. doi:10.1080/10495398.2017.1313269

71. Li W, Hu J, Ji P, Zhu S, Zhu Y. Oral administration of bovine lactoferrin accelerates the healing of fracture in ovariectomized rats. J Bone Miner Metab. 2020;38: 648–657. doi:10.1007/s00774-020-01105-1

72. Engelmayer J, Blezinger P, Varadhachary A. Talactoferrin stimulates wound healing with modulation of inflammation. J Surg Res. 2008;149: 278–286. doi:10.1016/j.jss.2007.12.754

73. Papon N, Bougnoux ME, d'Enfert C. Tracing the Origin of Invasive Fungal Infections. Trends Microbiol. 2020;28: 240–242. doi:10.1016/j.tim.2020.01.007

74. Lockhart SR, Guarner J. Emerging and reemerging fungal infections. Semin Diagn Pathol. 2019;36: 177–181. doi:10.1053/j.semdp.2019.04.010

75. Bongomin F, Gago S, Oladele RO, Denning DW. Global and multi-national prevalence of fungal diseases - estimate precision. J Fungi. 2017;3. doi:10.3390/jof3040057

76. Hokken MWJ, Zwaan BJ, Melchers WJG, Verweij PE. Facilitators of adaptation and antifungal resistance mechanisms in clinically relevant fungi. Fungal Genet Biol. 2019;132: 103254. doi:10.1016/j.fgb.2019.103254

77. Xu YY, Samaranayake YH, Samaranayake LP, Nikawa H. *In vitro* susceptibility of *Candida* species to lactoferrin. Med Mycol. 1999;37: 35–41. doi:10.1046/j.1365-280X.1999.00198.x

78. Samaranayake YH, Samaranayake LP, Wu PC, So M. The antifungal effect of lactoferrin and lysozyme on *Candida krusei* and *Candida albicans*. Apmis. 1997;105: 875–883. doi:10.1111/j.1699-0463.1997.tb05097.x

79. Wakabayashi H, Uchida K, Yamauchi K, Teraguchi S, Hayasawa H, Yamaguchi H. Lactoferrin given in food facilitates dermatophytosis cure in guinea pig models. J Antimicrob Chemother. 2000;46: 595–601. doi:10.1093/jac/46.4.595

80. Lahoz E, Pisacane A, Iannaccone M, Palumbo D, Capparelli R. Fungistatic activity of iron-free bovin lactoferrin against several fungal plant pathogens and antagonists. Nat Prod Res. 2008;22: 955–961. doi:10.1080/14786410701650253

81. Wang J, Xia XM, Wang HY, Li PP, Wang KY. Inhibitory effect of lactoferrin against gray mould on tomato plants caused by *Botrytis cinerea* and possible mechanisms of action. Int J Food Microbiol. 2013;161: 151–157. doi:10.1016/j.ijfoodmicro.2012.11.025

82. Fernandes KE, Weeks K, Carter DA. Lactoferrin is broadly active against yeasts and highly synergistic with amphotericin B. Antimicrob Agents Chemother. 2020;64: 1–22. doi:10.1128/AAC.02284-19

83. Soukka T, Tenovuo J, Lenander-Lumikari M. Fungicidal effect of human lactoferrin against Candida albicans. FEMS Microbiol Lett. 1992;90: 223–228. doi:10.1016/0378-1097(92)90650-D

84. Zarember KA, Sugui JA, Chang YC, Kwon-Chung KJ, Gallin JI. Human polymorphonuclear leukocytes inhibit *Aspergillus fumigatus* conidial growth by lactoferrin-mediated iron depletion . J Immunol. 2007;178: 6367–6373. doi:10.4049/jimmunol.178.10.6367

85. Lai YW, Campbell LT, Wilkins MR, Pang CNI, Chen S, Carter DA. Synergy and antagonism between iron chelators and antifungal drugs in *Cryptococcus*. Int J Antimicrob Agents. 2016;48: 388–394. doi:10.1016/j.ijantimicag.2016.06.012

86. Viejo-Díaz M, Andrés MT, Fierro JF. Effects of human lactoferrin on the cytoplasmic membrane of *Candida albicans* cells related with its candidacidal activity. FEMS Immunol Med Microbiol. 2004;42: 181–185. doi:10.1016/j.femsim.2004.04.005

87. Crisp P, Wicks TJ, Troup G, Scott ES. Mode of action of milk and whey in the control of grapevine powdery mildew. Australas Plant Pathol. 2006;35: 487–493. doi:10.1071/AP06052

88. Andrés MT, Viejo-Díaz M, Fierro JF. Human lactoferrin induces apoptosis-like cell death in *Candida albicans*: critical role of K+-channel-mediated K+ efflux. Antimicrob Agents Chemother. 2008;52: 4081–8. doi:10.1128/AAC.01597-07

89. Wang J, Shi X, Wang H, Xia X, Wang K. Effects of esterified lactoferrin and lactoferrin on control of postharvest blue mold of apple fruit and their possible mechanisms of action. J Agric Food Chem. 2012;60: 6432–6438.

90. Acosta-Zaldívar M, Andrés MT, Rego A, Pereira CS, Fierro JF, Côrte-Real M. Human lactoferrin triggers a mitochondrial- and caspase-dependent regulated cell death in *Saccharomyces cerevisiae*. Apoptosis. 2016;21: 163–173. doi:10.1007/s10495-015-1199-9

91. Andrés MT, Acosta-Zaldívar M, Fierro JF. Antifungal mechanism of action of lactoferrin: Identification of H+-ATPase (P3A-type) as a new apoptotic-cell membrane receptor. Antimicrob Agents Chemother. 2016;60: 4206–4216. doi:10.1128/AAC.03130-15

92. Andrés MT, Acosta-Zaldívar M, González-Seisdedos J, Fierro JF. Cytosolic acidification is the first transduction signal of lactoferrin-induced regulated cell death pathway. Int J Mol Sci. 2019;20:

5838. doi:10.3390/ijms20235838

93. Carmona-Gutierrez D, Bauer MA, Zimmermann A, Aguilera A, Austriaco N, Ayscough K, et al. Guidelines and recommendations on yeast cell death nomenclature. Microb Cell. 2018;5: 4–31. doi:10.15698/mic2018.01.607

94. Velliyagounder K, Rozario SD, Fine DH. The effects of human lactoferrin in experimentally induced systemic candidiasis. J Med Microbiol. 2019;68: 1802–1812. doi:10.1099/jmm.0.001098

95. Liao H, Liu S, Wang H, Su H, Liu Z. Enhanced antifungal activity of bovine lactoferrin-producing probiotic *Lactobacillus casei* in the murine model of vulvovaginal candidiasis. BMC Microbiol. 2019;19: 1–13. doi:10.1186/s12866-018-1370-x

96. Russo R, Superti F, Karadja E, De Seta F. Randomised clinical trial in women with Recurrent Vulvovaginal Candidiasis: Efficacy of probiotics and lactoferrin as maintenance treatment. Mycoses. 2019;62: 328–335. doi:10.1111/myc.12883

97. Kuipers ME, De Vries HG, Eikelboom MC, Meijer DKF, Swart PJ. Synergistic fungistatic effects of lactoferrin in combination with antifungal drugs against clinical *Candida* isolates. Antimicrob Agents Chemother. 1999;43: 2635–2641. doi:10.1128/aac.43.11.2635

98. WHO - Cancer. 2021. Retrieved from: https://www.who.int/news-room/fact-sheets/detail/cancer (visited at 20th April 2021)

99. Hanahan D, Weinberg RA. Hallmarks of cancer: The next generation. Cell. 2011;144: 646–674. doi:10.1016/j.cell.2011.02.013

100. McIntosh GH, Regester GO, Royle PJ, Smithers GW. Biochemical and molecular roles of nutrients dairy proteins protect against dimethylhydrazine-induced intestinal cancers in rats. J Nutr. 1995; 809–816.

101. Bezault JA, Bhimani R, Wiprovnick J, Furmanski P. Human lactoferrin inhibits growth of solid tumors and development of experimental metastases in mice. Cancer Res. 1994;54: 2310–2312.

102. Iglesias-Figueroa BF, Siqueiros-Cendón TS, Gutierrez DA, Aguilera RJ, Espinoza-Sánchez EA, Arévalo-Gallegos S, et al. Recombinant human lactoferrin induces apoptosis, disruption of F-actin structure and cell cycle arrest with selective cytotoxicity on human triple negative breast cancer cells. Apoptosis. 2019;24: 562–567. doi:10.1007/s10495-019-01539-7

103. Tung Y-T, Chen H-L, Yen C-C, Lee P-Y, Tsai H-C, Lin M-F, et al. Bovine lactoferrin inhibits lung cancer growth through suppression of both inflammation and expression of vascular endothelial growth factor. J Dairy Sci. 2013;96: 2095–106. doi:10.3168/jds.2012-6153

104. Nakamura-Bencomo S, Gutierrez DA, Robles-Escajeda E, Iglesias-Figueroa B, Siqueiros-Cendón TS, Espinoza-Sánchez EA, et al. Recombinant human lactoferrin carrying humanized glycosylation exhibits antileukemia selective cytotoxicity, microfilament disruption, cell cycle arrest, and apoptosis activities. Invest New Drugs. 2020. doi:10.1007/s10637-020-01020-2

105. Roseanu A, Florian PE, Moisei M, Sima LE, Evans RW, Trif M. Liposomalization of lactoferrin enhanced its anti-tumoral effects on melanoma cells. BioMetals. 2010;23: 485–492. doi:10.1007/s10534-010-9312-6

106. Guedes J, Pereira C, Rodrigues L, Côrte-real M. Bovine milk lactoferrin selectively kills highly metastatic prostate cancer PC-3 and osteosarcoma MG-63 cells in vitro. Front Oncol. 2018;8: 1–12. doi:10.3389/fonc.2018.00200

107. Pereira CS, Guedes JP, Gonçalves M, Loureiro L, Castro L, Gerós H, et al. Lactoferrin selectively

triggers apoptosis in highly metastatic breast cancer cells through inhibition of plasmalemmal V-H+-ATPase. Oncotarget. 2016;7: 62144–62158. doi:10.18632/oncotarget.11394

108. Gibbons JA, Kanwar JR, Kanwar RK. Iron-free and iron-saturated bovine lactoferrin inhibit survivin expression and differentially modulate apoptosis in breast cancer. BMC Cancer. 2015;15: 425. doi:10.1186/s12885-015-1441-4

109. Arcella A, Oliva MA, Staffieri S, Aalberti S, Grillea G, Madonna M, et al. *In vitro* and *in vivo* effect of human lactoferrin on glioblastoma growth. J Neurosurg. 2015;123: 1026–35. doi:10.3171/2014.12.JNS14512

110. Xiao Y, Monitto CL, Minhas KM, Sidransky D. Lactoferrin down-regulates G1 cyclin-dependent kinases during growth arrest of head and neck cancer cells. Clin Cancer Res. 2004;10: 8683–8686.

111. Damiens E, El Yazidi I, Mazurier J, Duthille I, Spik G, Boilly-Marer Y. Lactoferrin inhibits G1 cyclin-dependent kinases during growth arrest of human breast carcinoma cells. J Cell Biochem. 1999;74: 486–498. doi:10.1002/(SICI)1097-4644(19990901)74:3<486::AID-JCB16>3.0.CO;2-6

112. Wolf JS, Li G, Varadhachary A, Petrak K, Schneyer M, Li D, et al. Oral lactoferrin results in T cell-dependent tumor inhibition of head and neck squamous cell carcinoma *in vivo*. Clin Cancer Res. 2007;13: 1601–1610. doi:10.1158/1078-0432.CCR-06-2008

113. Chea C, Miyauchi M, Inubushi T, Ayuningtyas NF, Subarnbhesaj A, Nguyen PT, et al. Molecular mechanism of inhibitory effects of bovine lactoferrin on the growth of oral squamous cell carcinoma. PLoS One. 2018;13: 1–19. doi:10.1371/journal.pone.0191683

114. Zhang Y, Nicolau A, Lima CF, Rodrigues LR. Bovine lactoferrin induces cell cycle arrest and inhibits mTOR signaling in breast cancer cells. Nutr Cancer. 2014;66: 1371–85. doi:10.1080/01635581.2014.956260

115. Pfeffer CM, Singh ATK. Apoptosis: A target for anticancer therapy. Int J Mol Sci. 2018;19. doi:10.3390/ijms19020448

116. Duarte DC, Nicolau A, Teixeira JA, Rodrigues LR. The effect of bovine milk lactoferrin on human breast cancer cell lines. J Dairy Sci. 2011;94: 66–76. doi:10.3168/jds.2010-3629

117. Wang J, Li Q, Ou Y, Li K, Han Z, Wang P, et al. Recombination adenovirus-mediated human lactoferrin cDNA inhibits the growth of human MCF-7 breast cancer cells. J Pharm Pharmacol. 2012;64: 457–63. doi:10.1111/j.2042-7158.2011.01410.x

118. Zhang Y, Lima CF, Rodrigues LR. *In vitro* evaluation of bovine lactoferrin potential as an anticancer agent. Int Dairy J. 2015;40: 6–15. doi:10.1016/j.idairyj.2014.08.016

119. Wang J, Li Q, Ou Y, Han Z, Li K, Wang P, et al. Inhibition of tumor growth by recombinant adenovirus containing human lactoferrin through inducing tumor cell apoptosis in mice bearing EMT6 breast cancer. Arch Pharm Res. 2011;34: 987–995. doi:10.1007/s12272-011-0616-z

120. Fujita KI, Matsuda E, Sekine K, Iigo M, Tsuda H. Lactoferrin enhances Fas expression and apoptosis in the colon mucosa of azoxymethane-treated rats. Carcinogenesis. 2004;25: 1961–1966. doi:10.1093/carcin/bgh205

121. Xu XX, Jiang HR, Li HB, Zhang TN, Zhou Q, Liu N. Apoptosis of stomach cancer cell SGC-7901 and regulation of Akt signaling way induced by bovine lactoferrin. J Dairy Sci. 2010;93: 2344–2350. doi:10.3168/jds.2009-2926

122. Hoedt E, Chaoui K, Huvent I, Mariller C, Monsarrat B, Burlet-Schiltz O, et al. SILAC-based proteomic profiling of the human MDA-MB-231 metastatic breast cancer cell line in response to the two antitumoral lactoferrin isoforms: The secreted lactoferrin and the intracellular delta-lactoferrin. PLoS One. 2014;9. doi:10.1371/journal.pone.0104563

123. Cutone A, Colella B, Pagliaro A, Rosa L, Lepanto MS, Bonaccorsi di Patti MC, et al. Native and iron-saturated bovine lactoferrin differently hinder migration in a model of human glioblastoma by reverting epithelial-to-mesenchymal transition-like process and inhibiting interleukin-6/STAT3 axis. Cell Signal. 2020;65: 109461. doi:10.1016/j.cellsig.2019.109461

124. Chea C, Miyauchi M, Inubushi T, Okamoto K, Haing S, Nguyen PT, et al. Bovine lactoferrin reverses programming of epithelial-to-mesenchymal transition to mesenchymal-to-epithelial transition in oral squamous cell carcinoma. Biochem Biophys Res Commun. 2018;507: 142–147. doi:10.1016/j.bbrc.2018.10.193

125. Yoo Y, Watanabe S, Watanabe R, Hata K, Shimazaki K, Azuma I. Bovine lactoferrin and lactoferricin, a peptide derived from bovine lactoferrin, inhibit tumor metastasis in mice. Jpn J Cancer Res. 1997;88: 184–90. doi:10.1111/j.1349-7006.1997.tb00364.x

126. Iigo M, Kuhara T, Ushida Y, Sekine K, Moore MA. Inhibitory effects of bovine lactoferrin on colon carcinoma 26 lung metastasis in mice. Clin Exp Metastasis. 1999;17: 35–40. doi: 10.1023/a:1026452110786

127. Tsuda H, Sekine K, Takasuka N, Toriyama-Baba H, Iigo M. Prevention of colon carcinogenesis and carcinoma metastasis by orally administered bovine lactoferrin in animals. Biofactors. 2000;12: 83–88. doi: 10.1002/biof.5520120113

128. Norrby K, Mattsby-Baltzer I, Innocenti M, Tuneberg S. Orally administered bovine lactoferrin systemically inhibits $VEGF_{165}$-mediated angiogenesis in the rat. Int J Cancer. 2001;91: 236–240. oi: 10.1002/1097-0215(200002)9999:9999<::aid-ijc1024>3.3.co;2-k

129. Shimamura M, Yamamoto Y, Ashino H, Oikawa T, Hazato T, Tsuda H, et al. Bovine lactoferrin inhibits tumor-induced angiogenesis. Int J Cancer. 2004;111: 111–116. doi:10.1002/ijc.20187

130. Shi H, Li W. Inhibitory effects of human lactoferrin on U14 cervical carcinoma through upregulation of the immune response. Oncol Lett. 2014;7: 820–826. doi:10.3892/ol.2013.1776

131. Wang WP, Iigo M, Sato J, Sekine K, Adachi I, Tsuda H. Activation of intestinal mucosal immunity in tumor-bearing mice by lactoferrin. Jpn J Cancer Res. 2000;91: 1022–1027. doi:10.1111/j.1349-7006.2000.tb00880.x

132. Zhang Y, Lima CF, Rodrigues LR. Anticancer effects of lactoferrin: Underlying mechanisms and future trends in cancer therapy. Nutr Rev. 2014;72: 763–773. doi:10.1111/nure.12155

133. Madan R, Tsang K, Bilusic M, Vergati M, Poole D, Jochems C, et al. Effect of talactoferrin alfa on the immune system in adults with non-small cell lung cancer. Oncologist. 2013;18: 821–822. doi:10.1634/theoncologist.12-1-1

134. Chea C, Haing S, Miyauchi M, Shrestha M, Imanaka H, Takata T. Molecular mechanisms underlying the inhibitory effects of bovine lactoferrin on osteosarcoma. Biochem Biophys Res Commun. 2019;508: 946–952. doi:10.1016/j.bbrc.2018.11.204

135. Tsuda H, Sekine K, Fujita K, Iigo M, Ligo M. Cancer prevention by bovine lactoferrin and underlying mechanisms - a review of experimental and clinical studies. Biochem Cell Biol. 2002;80: 131–6. doi:10.1139/o01-239

136. Chandra Mohan KVP, Devaraj H, Prathiba D, Hara Y, Nagini S. Antiproliferative and apoptosis inducing effect of lactoferrin and black tea polyphenol combination on hamster buccal pouch carcinogenesis. Biochim Biophys Acta - Gen Subj. 2006;1760: 1536–1544. doi:10.1016/j.bbagen.2006.06.009

137. Deng M, Zhang W, Tang H, Ye Q, Liao Q, Zhou Y, et al. Lactotransferrin acts as a tumor suppressor in nasopharyngeal carcinoma by repressing AKT through multiple mechanisms. Oncogene. 2013;32: 4273–4283. doi:10.1038/onc.2012.434

138. Shaheduzzaman S, Vishwanath A, Furusato B, Cullen J, Chen Y, Bañez L, et al. Silencing of lactotransferrin expression by methylation in prostate cancer progression. Cancer Biol Ther. 2007;6: 1088–95.

139. Naleskina LA, Lukianova NY, Sobchenko SO, Storchai DM, Chekhun VF. Lactoferrin expression in breast cancer in relation to biologic properties of tumors and clinical features of disease. Exp Oncol. 2016;38: 181–186.

140. Hoedt E, Hardivillé S, Mariller C, Elass E, Perraudin JP, Pierce A. Discrimination and evaluation of lactoferrin and delta-lactoferrin gene expression levels in cancer cells and under inflammatory stimuli using TaqMan real-time PCR. BioMetals. 2010;23: 441–452. doi:10.1007/s10534-010-9305-5

141. Zhou Y, Zeng Z, Zhang W, Xiong W, Wu M, Tan Y, et al. Lactotransferrin: a candidate tumor suppressor-Deficient expression in human nasopharyngeal carcinoma and inhibition of NPC cell proliferation by modulating the mitogen-activated protein kinase pathway. Int J Cancer. 2008;123: 2065–72. doi:10.1002/ijc.23727

142. Wei L, Zhang X, Wang J, Ye Q, Zheng X, Peng Q, et al. Lactoferrin deficiency induces a pro-metastatic tumor microenvironment through recruiting myeloid-derived suppressor cells in mice. Oncogene. 2020;39: 122–135. doi:10.1038/s41388-019-0970-8

143. Kozu T, Iinuma G, Ohashi Y, Saito Y, Akasu T, Saito D, et al. Effect of orally administered bovine lactoferrin on the growth of adenomatous colorectal polyps in a randomized, placebo-controlled clinical trial. Cancer Prev Res. 2009;2: 975–83. doi:10.1158/1940-6207.CAPR-08-0208

144. Digumarti R, Wang Y, Raman G, Doval DC, Advani SH, Julka PK, et al. A randomized, double-blind, placebo-controlled, phase II study of oral talactoferrin in combination with carboplatin and paclitaxel in previously untreated locally advanced or metastatic non-small cell lung cancer. J Thorac Oncol. 2011;6: 1098–1103. doi:10.1097/JTO.0b013e3182156250

145. Jonasch E, Stadler WM, Bukowski RM, Hayes TG, Varadhachary A, Malik R, et al. Phase 2 trial of talactoferrin in previously treated patients with metastatic renal cell carcinoma. Cancer. 2008;113: 72–77. doi:10.1002/cncr.23519

146. Hayes TG, Falchook GS, Varadhachary A. Phase IB trial of oral talactoferrin in the treatment of patients with metastatic solid tumors. Invest New Drugs. 2010;28: 156–162. doi:10.1007/s10637-009-9233-9

147. Parikh PM, Vaid A, Advani SH, Digumarti R, Madhavan J, Nag S, et al. Randomized, double-blind, placebo-controlled phase II study of single-agent oral talactoferrin in patients with locally advanced or metastatic non-small-cell lung cancer that progressed after chemotherapy. J Clin Oncol. 2011;29: 4129–4136. doi:10.1200/jco.2010.34.4127

148. Ramalingam S, Crawford J, Chang A, Manegold C, Perez-Soler R, Douillard JY, et al. Talactoferrin alfa versus placebo in patients with refractory advanced non-small-cell lung cancer (FORTIS-M

trial). Ann Oncol. 2013;24: 2875–2880. doi:10.1093/annonc/mdt371

149. Moastafa TM, El-Sissy AE-DE, El-Saeed GK, Koura MSE-D. Study on the therapeutic benefit on lactoferrin in patients with colorectal cancer receiving chemotherapy. Int Sch Res Not. 2015;2015: 1–3. doi:10.1155/2015/424603

150. Boron WF. Regulation of intracellular pH. Am J Physiol - Adv Physiol Educ. 2004;28: 160–179. doi:10.1152/advan.00045.2004

151. Bouret Y, Argentina M, Counillon L. Capturing intracellular pH dynamics by coupling its molecular mechanisms within a fully tractable mathematical model. PLoS One. 2014;9: e85449. doi:10.1371/journal.pone.0085449

152. Madshus IH. Regulation of intracellular pH in eukaryotic cells. Biochem J. 1988;250: 1–8. doi:10.1042/bj2500001

153. Casey JR, Grinstein S, Orlowski J. Sensors and regulators of intracellular pH. Nat Rev Mol Cell Biol. 2010;11: 50–61. doi:10.1038/nrm2820

154. Goss G, Grinstein S. Mechanisms of intracellular pH regulation. Princ Med Biol. 1996;4: 221–241. doi:10.1016/S1569-2582(96)80094-8

155. Paroutis P, Touret N, Grinstein S. The pH of the secretory pathway: Measurement, determinants, and regulation. Physiology. 2004;19: 207–215. doi:10.1152/physiol.00005.2004

156. Pittman JK. Multiple transport pathways for mediating intracellular pH homeostasis: The contribution of H+/ion exchangers. Front Plant Sci. 2012;3: 1–8. doi:10.3389/fpls.2012.00011

157. Harguindey S, Stanciu D, Devesa J, Alfarouk K, Cardone RA, Polo Orozco JD, et al. Cellular acidification as a new approach to cancer treatment and to the understanding and therapeutics of neurodegenerative diseases. Semin Cancer Biol. 2017;43: 157–179. doi:10.1016/j.semcancer.2017.02.003

158. Weisz OA. Organelle acidification and disease. Traffic. 2003;4: 57–64. doi:10.1034/j.1600-0854.2003.40201.x

159. Kurkdjian A, Guern J. Intracellular pH: Measurement and Importance in Cell Activity. Annu Rev Plant Physiol Plant Mol Biol. 1989;40: 271–303. doi:10.1146/annurev.pp.40.060189.001415

160. Anandakrishnan R, Zuckerman DM. Biophysical comparison of ATP-driven proton pumping mechanisms suggests a kinetic advantage for the rotary process depending on coupling ratio. PLoS One. 2017;12: 1–14. doi:10.1371/journal.pone.0173500

161. Pedersen PL, Carafoli E. Ion motive ATPases. I. Ubiquity, properties, and significance to cell function. Trends Biochem Sci. 1987;12: 146–150. doi:10.1016/0968-0004(87)90071-5

162. Pedersen PL. Transport ATPases into the year 2008: A brief overview related to types, structures, functions and roles in health and disease. J Bioenerg Biomembr. 2007;39: 349–355. doi:10.1007/s10863-007-9123-9

163. Whitton B, Okamoto H, Packham G, Crabb SJ. Vacuolar ATPase as a potential therapeutic target and mediator of treatment resistance in cancer. Cancer Med. 2018;7: 3800–3811. doi:10.1002/cam4.1594

164. Perlin DS, Seto-Young D, Monk BC. The plasma membrane H+-ATPase of fungi. A candidate drug target? Ann N Y Acad Sci. 1997;834: 609–617. doi:10.1111/j.1749-6632.1997.tb52330.x

165. Turner H. Spiroindolone NITD609 is a novel antimalarial drug that targets the P-type ATPase

PfATP4. Futur Med Chem. 2016;8: 221–238. doi:10.4155/fmc.15.177

166. Lu P, Lill H, Bald D. ATP synthase in mycobacteria: Special features and implications for a function as drug target. Biochim Biophys Acta - Bioenerg. 2014;1837: 1208–1218. doi:10.1016/j.bbabio.2014.01.022

167. Ahmad Z, Okafor F, Azim S, F. Laughlin T. ATP synthase: a molecular therapeutic drug target for antimicrobial and antitumor peptides. Curr Med Chem. 2013;20: 1956–1973. doi:10.2174/0929867311320150003

168. Chène P. ATPases as drug targets: learning from their structure. Nat Rev Drug Discov. 2002;1: 665–673. doi:10.1038/nrd894

169. Palmgren M, Morsomme P. The plasma membrane H + -ATPase, a simple polypeptide with a long history. Yeast. 2019;36: 201–210. doi:10.1002/yea.3365

170. Wach A, Schlesser A, Goffeau A. An alignment of 17 deduced protein sequences from plant, fungi, and ciliate H+-ATPase genes. J Bioenerg Biomembr. 1992;24: 309–317. doi:10.1007/BF00768851

171. Serrano R, Kielland-Brandt MC, Fink GR. Yeast plasma membrane ATPase is essential for growth and has homology with (Na+ + K+), K+- and Ca2+-ATPases. Nature. 1986;319: 689–693. doi:10.1038/319689a0

172. Kane P. Proton Transport and pH Control in Fungi. Adv Exp Med Biol. 2016;892: 33–68. doi:10.1007/978-3-319-25304-6

173. Manzoor N. Plasma membrane ATPase: potential target for antifungal drug therapy. In: Chakraborti S, Dhalla N (eds). Regulation of Ca^{2+}-ATPases,V-ATPases and F-ATPases. Advances in biochemistry in health and disease. vol. 14, Springer, Cham.; 2016. pp 519–530. doi:10.1007/978-3-319-24780-9

174. Kaur S, Mishra P. Dimorphism-associated changes in plasma membrane H+-ATPase activity of *Candida albicans*. Arch Microbiol. 1991;156: 412–415. doi:10.1007/BF00248719

175. Pedersen BP, Buch-Pedersen MJ, Preben Morth J, Palmgren MG, Nissen P. Crystal structure of the plasma membrane proton pump. Nature. 2007;450: 1111–1114. doi:10.1038/nature06417

176. Focht D, Croll TI, Pedersen BP, Nissen P. Improved model of proton pump crystal structure obtained by interactive molecular dynamics flexible fitting expands the mechanistic model for proton translocation in P-type ATPases. Front Physiol. 2017;8. doi:10.3389/fphys.2017.00202

177. Toyoshima C, Nakasako M, Nomura H, Ogawa H. Structure determination of the calcium pump of sarcoplasmic reticulum. Tanpakushitsu Kakusan Koso. 2001;46: 1374–1380.

178. Morth JP, Pedersen BP, Toustrup-Jensen MS, Sørensen TLM, Petersen J, Andersen JP, et al. Crystal structure of the sodium-potassium pump. Nature. 2007;450: 1043–1049. doi:10.1038/nature06419

179. Yatime L, Buch-Pedersen MJ, Musgaard M, Morth JP, Winther AML, Pedersen BP, et al. P-type ATPases as drug targets: Tools for medicine and science. Biochim Biophys Acta - Bioenerg. 2009;1787: 207–220. doi:10.1016/j.bbabio.2008.12.019

180. Morth JP, Pedersen BP, Buch-Pedersen MJ, Andersen JP, Vilsen B, Palmgren MG, et al. A structural overview of the plasma membrane Na+,K+-ATPase and H+-ATPase ion pumps. Nat Rev Mol Cell Biol. 2011;12: 60–70. doi:10.1038/nrm3031

181. Smardon AM, Kane PM. Loss of vacuolar H+-ATPase activity in organelles signals ubiquitination and endocytosis of the yeast plasma membrane proton pump Pma1p. J Biol Chem. 2014;289: 32316–32326. doi:10.1074/jbc.M114.574442

182. Martínez-Muñoz GA, Kane P. Vacuolar and plasma membrane proton pumps collaborate to achieve cytosolic pH homeostasis in yeast. J Biol Chem. 2008;283: 20309–20319. doi:10.1074/jbc.M710470200

183. Chan G, Hardej D, Santoro M, Lau-Cam C, Billack B. Evaluation of the antimicrobial activity of ebselen: Role of the yeast plasma membrane H+-ATPase. J Biochem Mol Toxicol. 2007;21: 252–264. doi:10.1002/jbt.20189

184. Kjellerup L, Gordon S, Cohrt K, Brown W, Fuglsang A, Winther A-M. Identification of antifungal H+-ATPase inhibitors with effect on plasma membrane potential. Antimicrob Agents Chemother. 2017;61: e00032-17. doi:10.1128/AAC.00032-17

185. Monk BC, Mason AB, Abramochkin G, Haber JE, Seto-Young D, Perlin DS. The yeast plasma membrane proton pumping ATPase is a viable antifungal target. I. Effects of the cysteine-modifying reagent omeprazole. BBA - Biomembr. 1995;1239: 81–90. doi:10.1016/0005-2736(95)00133-N

186. Billack B, Pietka-Ottlik M, Santoro M, Nicholson S, Młochowski J, Lau-Cam C. Evaluation of the antifungal and plasma membrane H+-ATPase inhibitory action of ebselen and two ebselen analogs in *S. cerevisiae* cultures. J Enzyme Inhib Med Chem. 2010;25: 312–317. doi:10.3109/14756360903179419

187. Orie NN, Warren AR, Basaric J, Lau-Cam C, Piętka-Ottlik M, Młochowski J, et al. *In vitro* assessment of the growth and plasma membrane H+-ATPase inhibitory activity of ebselen and structurally related selenium- and sulfur-containing compounds in *Candida albicans*. J Biochem Mol Toxicol. 2017;31: 8–11. doi:10.1002/jbt.21892

188. Manavathu EK, Dimmock JR, Vashishtha SC, Chandrasekar PH. Proton-pumping-ATPase-targeted antifungal activity of a novel conjugated styryl ketone. Antimicrob Agents Chemother. 1999;43: 2950–2959. doi:10.1128/aac.43.12.2950

189. Ahmad A, Khan A, Yousuf S, Khan LA, Manzoor N. Proton translocating ATPase mediated fungicidal activity of eugenol and thymol. Fitoterapia. 2010;81: 1157–1162. doi:10.1016/j.fitote.2010.07.020

190. Kongstad KT, Wubshet SG, Johannesen A, Kjellerup L, Winther AL, Katharina A, et al. High-resolution screening combined with HPLC-HRMS-SPE-NMR for identification of fungal plasma membrane H+-ATPase inhibitors from plants. J Agric Food Chem. 2014;62: 5595–5602. doi:10.1021/jf501605z

191. Bowman EJ, Bowman JB. Identification and properties of an ATPase in vacuolar membranes of *Neurospora crassa*. J Bacteriol. 1982;151: 1326–1337. doi:10.1128/jb.151.3.1326-1337.1982

192. Kakinuma Y, Ohsumi Y, Anraku Y. Properties of H+-translocating adenosine triphosphatase in vacuolar membranes of *Saccharomyces cerevisae*. J Biol Chem. 1981;256: 10859–10863.

193. Hager A, Frenzel R, Laible D. ATP-dependent proton transport into vesicles of microsomal membranes of Zea mays coleoptiles. Z Naturforsch C Biosci. 1980;35: 783–793. doi:10.1515/znc-1980-9-1021

194. Churchill KA, Sze H. Anion-Sensitive, H+-Pumping ATPase in Membrane Vesicles from Oat Roots. Plant Physiol. 1983;71: 610–617.

195. Futai BM, Sun-Wada G, Wada Y, Matsumoto N, Nakanish-Matsui M. Vacuolar-type ATPase: A proton pump to lysosomal trafficking. Jpn Acad Ser B Phys Biol Sci. 2019;95: 261–277.

196. Sennoune SR, Bakunts K, Martínez GM, Chua-Tuan JL, Kebir Y, Attaya MN, et al. Vacuolar H+-ATPase in human breast cancer cells with distinct metastatic potential: distribution and functional activity. Am J Physiol Cell Physiol. 2004;286: C1443–C1452. doi:10.1152/ajpcell.00407.2003

197. Hinton A, Sennoune SR, Bond S, Fang M, Reuveni M, Sahagian GG, et al. Function of a subunit isoforms of the V-ATPase in pH homeostasis and *in vitro* invasion of MDA-MB231 human breast cancer cells. J Biol Chem. 2009;284: 16400–16408. doi:10.1074/jbc.M901201200

198. Toyomura T, Murata Y, Yamamoto A, Oka T, Sun-Wada GH, Wada Y, et al. From lysosomes to the plasma membrane. Localization of vacuolar type H+-ATPase with the a3 isoform during osteoclast differentiation. J Biol Chem. 2003;278: 22023–22030. doi:10.1074/jbc.M302436200

199. Hermo L, Adamali HI, Andonian S. Immunolocalization of CA II and H+ V-ATPase in epithelial cells of the mouse and rat epididymis. J Androl. 2000;21: 376–391. doi:10.1002/j.1939-4640.2000.tb03392.x

200. Pamarthy S, Kulshrestha A, Katara GK, Beaman KD. The curious case of vacuolar ATPase: Regulation of signaling pathways. Mol Cancer. 2018;17: 1–9. doi:10.1186/s12943-018-0811-3

201. Vasanthakumar T, Rubinstein JL. Structure and roles of V-type ATPases. Trends Biochem Sci. 2020;45: 295–307. doi:10.1016/j.tibs.2019.12.007

202. Vasanthakumar T, Bueler SA, Wu D, Beilsten-Edmands V, Robinson C V., Rubinstein JL. Structural comparison of the vacuolar and Golgi V-ATPases from *Saccharomyces cerevisiae*. Proc Natl Acad Sci U S A. 2019;116: 7272–7277. doi:10.1073/pnas.1814818116

203. Harrison MA, Muench SP. The vacuolar ATPase – A nano-scale motor that drives cell biology. Subcell Biochem. 2018;87: 409–459. doi:10.1007/978-981-10-7757-9_14

204. Zhao J, Beyrakhova K, Liu Y, Alvarez CP, Bueler SA, Xu L, et al. Molecular basis for the binding and modulation of V-ATPase by a bacterial effector protein. PLoS Pathog. 2017;13: 1–21. doi:10.1371/journal.ppat.1006394

205. Zhao J, Benlekbir S, Rubinstein JL. Electron cryomicroscopy observation of rotational states in a eukaryotic V-ATPase. Nature. 2015;521: 241–245. doi:10.1038/nature14365

206. Basak S, Lim J, Manimekalai MSS, Balakrishna AM, Grüber G. Crystal and NMR structures give insights into the role and dynamics of Subunit F of the eukaryotic V-ATPase from *Saccharomyces cerevisiae*. J Biol Chem. 2013;288: 11930–11939. doi:10.1074/jbc.M113.461533

207. Balakrishna AM, Basak S, Manimekalai MSS, Grüber G. Crystal structure of subunits D and F in complex gives insight into energy transmission of the eukaryotic V-ATPase from *Saccharomyces cerevisiae*. J Biol Chem. 2015;290: 3183–3196. doi:10.1074/jbc.M114.622688

208. Drory O, Frolow F, Nelson N. Crystal structure of yeast V-ATPase subunit C reveals its stator function. EMBO Rep. 2004;5: 1148–1152. doi:10.1038/sj.embor.7400294

209. Roh SH, Stam NJ, Hryc CF, Couoh-Cardel S, Pintilie G, Chiu W, et al. The 3.5-Å CryoEM Structure of Nanodisc-Reconstituted Yeast Vacuolar ATPase V_o Proton Channel. Mol Cell. 2018;69: 993–1004. doi:10.1016/j.molcel.2018.02.006

210. Mazhab-Jafari MT, Rohou A, Schmidt C, Bueler SA, Benlekbir S, Robinson C V., et al. Atomic model for the membrane-embedded V_o motor of a eukaryotic V-ATPase. Nature. 2016;539: 118–122. doi:10.1038/nature19828

211. Roh SH, Shekhar M, Pintilie G, Chipot C, Wilkens S, Singharoy A, et al. Cryo-EM and MD infer water-mediated proton transport and autoinhibition mechanisms of V_o complex. Sci Adv. 2020;6: 1–10. doi:10.1126/sciadv.abb9605

212. Wang L, Wu D, Robinson C V., Wu H, Fu T-M. Structures of a complete human V-ATPase reveal mechanisms of its assembly.Mol Cell. 2020;80: 501-511.e3. doi:10.1016/j.molcel.2020.09.029

213. Toei M, Saum R, Forgac M. Regulation and isoform function of the V-ATPases. Biochemistry. 2010;49: 4715–4723. doi:10.1021/bi100397s

214. Lu Q, Lu S, Huang L, Wang T, Wan Y, Zhou CX, et al. The expression of V-ATPase is associated with drug resistance and pathology of non-small-cell lung cancer. Diagn Pathol. 2013;8: 1–7. doi:10.1186/1746-1596-8-145

215. Huang L, Lu Q, Han Y, Li Z, Zhang Z, Li X. ABCG2/V-ATPase was associated with the drug resistance and tumor metastasis of esophageal squamous cancer cells. Diagn Pathol. 2012;7: 1–7. doi:10.1186/1746-1596-7-180

216. Chung C, Mader CC, Schmitz J, Atladottir J, Fitchev P, Cornwell M, et al. The vacuolar-ATPase (V-ATPase) modulates matrix metalloproteinase (MMP) isoforms in human pancreatic cancer. Lab Invest. 2011;91: 732–743. doi:10.1038/nmeth.3252.Orchestrating

217. Salyer SA, Olberding JR, Distler AA, Lederer ED, Clark BJ, Delamere NA, et al. Vacuolar ATPase driven potassium transport in highly metastatic breast cancer cells. BBA - Mol Basis Dis. 2013;1832: 1734–1743. doi:10.1016/j.bbadis.2013.04.023

218. Capecci J, Forgac M. The function of vacuolar ATPase (V-ATPase) a subunit isoforms in invasiveness of MCF10a and MCF10CA1a human breast cancer cells. J Biol Chem. 2013;288: 32731–32741. doi:10.1074/jbc.M113.503771

219. Cotter K, Capecci J, Sennoune S, Huss M, Maier M, Martinez-Zaguilan R, et al. Activity of plasma membrane V-ATPases is critical for the invasion of MDA-MB231 breast cancer cells. J Biol Chem. 2015;290: 3680–3692. doi:10.1074/jbc.M114.611210

220. Pérez-Sayáns M, Somoza-Martín JM, Barros-Angueira F, Rey JMG, García-García A. V-ATPase inhibitors and implication in cancer treatment. Cancer Treat Rev. 2009;35: 707–13. doi:10.1016/j.ctrv.2009.08.003

221. Cotter K, Liberman R, Sun-Wada GH, Wada Y, Sgroi D, Naber S, et al. The a3 isoform of subunit a of the vacuolar ATPase localizes to the plasma membrane of invasive breast tumor cells and is overexpressed in human breast cancer. Oncotarget. 2016;7: 46142–46157. doi:10.18632/oncotarget.10063

222. Wiedmann RM, von Schwarzenberg K, Palamidessi A, Schreiner L, Kubisch R, Liebl J, et al. The V-ATPase-inhibitor archazolid abrogates tumor metastasis via inhibition of endocytic activation of the Rho-GTPase Rac1. Cancer Res. 2012;72: 5976–87. doi:10.1158/0008-5472.CAN-12-1772

223. Perut F, Avnet S, Fotia C, Baglìo SR, Salerno M, Hosogi S, et al. V-ATPase as an effective therapeutic target for sarcomas. Exp Cell Res. 2014;320: 21–32. doi:10.1016/j.yexcr.2013.10.011

224. Avnet S, Di Pompo G, Lemma S, Salerno M, Perut F, Bonuccelli G, et al. V-ATPase is a candidate therapeutic target for Ewing sarcoma. Biochim Biophys Acta - Mol Basis Dis. 2013;1832: 1105–1116. doi:10.1016/j.bbadis.2013.04.003

225. Michel V, Licon-Munoz Y, Trujillo K, Bisoffi M, Parra KJ. Inhibitors of vacuolar ATPase proton

pumps inhibit human prostate cancer cell invasion and prostate-specific antigen expression and secretion. Int J Cancer. 2012;132: E1-10. doi:10.1002/ijc.27811

226. Xu J, Xie R, Liu X, Wen G, Jin H, Yu Z, et al. Expression and functional role of vacuolar H+-ATPase in human hepatocellular carcinoma. Carcinogenesis. 2012;33: 2432–2440. doi:10.1093/carcin/bgs277

227. Kulshrestha A, Katara GK, Ibrahim S, Pamarthy S, Jaiswal MK, Sachs AG, et al. Vacuolar ATPase "a2" isoform exhibits distinct cell surface accumulation and modulates matrix metalloproteinase activity in ovarian cancer. Oncotarget. 2015;6: 3797–3810. doi:10.18632/oncotarget.2902

228. Baruthio F, Quadroni M, Rüegg C, Mariotti A. Proteomic analysis of membrane rafts of melanoma cells identifies protein patterns characteristic of the tumor progression stage. Proteomics. 2008;8: 4733–47. doi:10.1002/pmic.200800169

229. Nishisho T, Hata K, Nakanishi M, Morita Y, Sun-Wada G-H, Wada Y, et al. The a3 isoform vacuolar type H^+-ATPase promotes distant metastasis in the mouse B16 melanoma cells. Mol cancer Res. 2011;9: 845–855. doi:10.1158/1541-7786.MCR-10-0449

230. Flinck M, Hagelund S, Gorbatenko A, Severin M, Pedraz-Cuesta E, Novak I, et al. The Vacuolar H+ ATPase α3 Subunit Negatively Regulates Migration and Invasion of Human Pancreatic Ductal Adenocarcinoma Cells. Cells. 2020;9: 1–22. doi:10.3390/cells9020465

231. Liu P, Chen H, Han L, Zou X, Shen W. Expression and role of V1A subunit of V-ATPases in gastric cancer cells. Int J Clin Oncol. 2015;20: 725–735. doi:10.1007/s10147-015-0782-y

232. García-García A, Pérez-Sayáns Garca M, Rodríguez MJ, Antuínez-Loípez J, Barros-Angueira F, Somoza-Martín M, et al. Immunohistochemical localization of C1 subunit of V-ATPase (ATPase C1) in oral squamous cell cancer and normal oral mucosa. Biotech Histochem. 2012;87: 133–139. doi:10.3109/10520295.2011.574647

233. Couto-Vieira J, Nicolau-Neto P, Costa EP, Figueira FF, Simão T de A, Okorokova-Façanha AL, et al. Multi-cancer V-ATPase molecular signatures: A distinctive balance of subunit C isoforms in esophageal carcinoma. EBioMedicine. 2020;51: 102581. doi:10.1016/j.ebiom.2019.11.042

234. di Cristofori A, Ferrero S, Bertolini I, Gaudioso G, Russo MV, Berno V, et al. The vacuolar H+ ATPase is a novel therapeutic target for glioblastoma. Oncotarget. 2015;6: 17514–17531. doi:10.18632/oncotarget.4239

235. Ohta T, Numata M, Yagishita H, Futagami F, Tsukioka Y, Kitagawa H, et al. Expression of 16 kDa proteolipid of vacuolar-type H+-ATPase in human pancreatic cancer. Br J Cancer. 1996;73: 1511–1517. doi:10.1038/bjc.1996.285

236. Otero-Rey EM, Somoza-Martín M, Barros-Angueira F, García-García A. Intracellular pH regulation in oral squamous cell carcinoma is mediated by increased V-ATPase activity via over-expression of the ATP6V1C1 gene. Oral Oncol. 2008;44: 193–199. doi:10.1016/j.oraloncology.2007.02.011

237. Pérez-Sayáns M, Reboiras-López MD, Somoza-Martín JM, Barros-Angueira F, Diz PG, Rey JMG, et al. Measurement of ATP6V1C1 expression in brush cytology samples as a diagnostic and prognostic marker in oral squamous cell carcinoma. Cancer Biol Ther. 2010;9: 1057–1064. doi:10.4161/cbt.9.12.11880

238. Gleize V, Boisselier B, Marie Y, Poëa-Guyon S, Sanson M, Morel N. The renal v-ATPase a4 subunit is expressed in specific subtypes of human gliomas. Glia. 2012;60: 1004–1012. doi:10.1002/glia.22332

239. Son SW, Kim SH, Moon EY, Kim DH, Pyo S, Um SH. Prognostic significance and function of the vacuolar H+-ATPase subunit V1E1 in esophageal squamous cell carcinoma. Oncotarget. 2016;7: 49334–49348. doi:10.18632/oncotarget.10340

240. Song T, Jeon HK, Hong JE, Choi JJ, Kim TJ, Choi CH, et al. Proton pump inhibition enhances the cytotoxicity of paclitaxel in cervical cancer. Cancer Res Treat. 2017;49: 595–606. doi:10.4143/crt.2016.034

241. Katara GK, Kulshrestha A, Mao L, Wang X, Sahoo M, Ibrahim S, et al. Mammary epithelium-specific inactivation of V-ATPase reduces stiffness of extracellular matrix and enhances metastasis of breast cancer. Mol Oncol. 2018;12: 208–223. doi:10.1002/1878-0261.12159

242. McGuire CM, Collins MP, Sun-Wada G, Wada Y, Forgac M. Isoform-specific gene disruptions reveal a role for the V-ATPase subunit a4 isoform in the invasiveness of 4T1-12B breast cancer cells. J Biol Chem. 2019;294: 11248–11258. doi:10.1074/jbc.RA119.007713

243. Ibrahim SA, Kulshrestha A, Katara GK, Riehl V, Sahoo M, Beaman KD. Cancer-associated V-ATPase induces delayed apoptosis of protumorigenic neutrophils. Mol Oncol. 2020;14: 590–610. doi:10.1002/1878-0261.12630

244. Ibrahim SA, Katara GK, Kulshrestha A, Jaiswal MK, Amin MA, Beaman KD. Breast cancer associated a2 isoform vacuolar ATPase immunomodulates neutrophils: Potential role in tumor progression. Oncotarget. 2015;6: 33033–33045. doi:10.18632/oncotarget.5439

245. Pamarthy S, Jaiswal MK, Kulshreshtha A, Katara GK, Gilman-Sachs A, Beaman KD. The Vacuolar ATPase a2-subunit regulates Notch signaling in triple-negative breast cancer cells. Oncotarget. 2015;6: 34206–34220. doi:10.18632/oncotarget.5275

246. Katara GK, Jaiswal MK, Kulshrestha A, Kolli B, Gilman-Sachs A, Beaman KD. Tumor-associated vacuolar ATPase subunit promotes tumorigenic characteristics in macrophages. Oncogene. 2014;33: 5649–5654. doi:10.1038/onc.2013.532

247. Zou P, Yang Y, Xu X, Liu B, Mei F, You J, et al. Silencing of vacuolar ATPase c subunit ATP6V0C inhibits invasion of prostate cancer cells. Oncol Rep. 2017;39: 298-306. doi: 10.3892/or.2017.6092

248. Nardi F, Fitchev P, Brooks KM, Franco OE, Cheng K, Hayward SW, et al. Lipid droplet velocity is a microenvironmental sensor of aggressive tumors regulated by V-ATPase and PEDF. Lab Investig. 2019;99: 1822–1834. doi:10.1038/s41374-019-0296-8

249. Kulshrestha A, Katara GK, Ibrahim SA, Riehl V, Sahoo M, Dolan J, et al. Targeting V-ATPase isoform restores cisplatin activity in resistant ovarian cancer: inhibition of autophagy, endosome function, and ERK/MEK pathway. J Oncol. 2019;2019: 2343876. doi:10.1155/2019/2343876

250. Kulshrestha A, Katara GK, Ibrahim SA, Riehl VE, Schneiderman S, Bilal M, et al. *In vivo* anti-V-ATPase antibody treatment delays ovarian tumor growth by increasing antitumor immune responses. Mol Oncol. 2020;14: 2436–2454. doi:10.1002/1878-0261.12782

251. Kulshrestha A, Katara GK, Ginter J, Pamarthy S, Ibrahim SA, Jaiswal MK, et al. Selective inhibition of tumor cell associated Vacuolar-ATPase “a2” isoform overcomes cisplatin resistance in ovarian cancer cells. Mol Oncol. 2016;10: 789–805. doi:10.1016/j.molonc.2016.01.003

252. He J, Shi XY, Li ZM, Pan XH, Li ZL, Chen Y, et al. Proton pump inhibitors can reverse the YAP mediated paclitaxel resistance in epithelial ovarian cancer. BMC Mol Cell Biol. 2019;20: 1–14. doi:10.1186/s12860-019-0227-y

253. Yang J, Guo F, Yuan L, Lv G, Gong J, Chen J. Elevated expression of the V-ATPase D2 subunit triggers increased energy metabolite levels in KrasG12D-driven cancer cells. J Cell Biochem. 2019;120: 11690–11701. doi:10.1002/jcb.28448

254. Kinashi H, Someno K, Sakaguchi K. Isolation and characterization of concanamycins A, B and C. J Antibiot (Tokyo). 1984;37: 1333–1343. doi:10.7164/antibiotics.37.1333

255. Hernandez A, Serrano-Bueno G, R. Perez-Castineira J, Serrano A. Intracellular proton pumps as targets in chemotherapy: V-ATPases and cancer. Curr Pharm Des. 2012;18: 1383–1394. doi:10.2174/138161212799504821

256. Kane PM. Targeting reversible disassembly as a mechanism of controlling V-ATPase activity. Curr Protein Pept Sci. 2012;13: 117–123. doi:10.2174/138920312800493142

257. Holliday LS. Vacuolar H+-ATPases (V-ATPases) as therapeutic targets: a brief review and recent developments. Biotarget. 2017;1: 18–18. doi:10.21037/biotarget.2017.12.01

258. Pan S, Cai H, Gu L, Cao S. Cleistanthin A inhibits the invasion and metastasis of human melanoma cells by inhibiting the expression of matrix metallopeptidase-2 and-9. Oncol Lett. 2017;14: 6217–6223. doi:10.3892/ol.2017.6917

259. Zou P, Yang Y, Xu X, Liu B, Mei F, You J, et al. Silencing of vacuolar ATPase c subunit ATP6V0C inhibits the invasion of prostate cancer cells through a LASS2/TMSG1-independent manner. Oncol Rep. 2018;39: 298–306. doi:10.3892/or.2017.6092

260. Costa GA, de Souza SB, da Silva Teixeira LR, Okorokov LA, Arnholdt ACV, Okorokova-Façanha AL, et al. Tumor cell cholesterol depletion and V-ATPase inhibition as an inhibitory mechanism to prevent cell migration and invasiveness in melanoma. Biochim Biophys Acta - Gen Subj. 2018;1862: 684–691. doi:10.1016/j.bbagen.2017.12.006

261. Martins BX, Arruda RF, Costa GA, Jerdy H, de Souza SB, Santos JM, et al. Myrtenal-induced V-ATPase inhibition - A toxicity mechanism behind tumor cell death and suppressed migration and invasion in melanoma. Biochim Biophys Acta - Gen Subj. 2019;1863: 1–12. doi:10.1016/j.bbagen.2018.09.006

262. Liu S, Wang L, Ding W, Wang D, Wang X, Luo Q, et al. Cleistanthin A inhibits the invasion of MDA-MB-231 human breast cancer cells: involvement of the β-catenin pathway. Pharmacol Reports. 2020;72: 188–198. doi:10.1007/s43440-019-00012-1

263. Bartel K, Winzi M, Ulrich M, Koeberle A, Menche D, Werz O, et al. V-ATPase inhibition increases cancer cell stiffness and blocks membrane related Ras signaling - A new option for HCC therapy. Oncotarget. 2017;8: 9476–9487. doi:10.18632/oncotarget.14339

264. Wang Y, Zhang L, Wei Y, Huang W, Li L, Wu A an, et al. Pharmacological targeting of vacuolar H+-ATPase via subunit V_1G combats multidrug-resistant cancer. Cell Chem Biol. 2020;27: 1359–1370. doi:10.1016/j.chembiol.2020.06.011

265. Santos JM, Hussain F. VD3 mitigates breast cancer aggressiveness by targeting V-H+-ATPase. J Nutr Biochem. 2019;70: 185–193. doi:10.1016/j.jnutbio.2019.05.005

266. Lu ZN, Shi ZY, Dang YF, Cheng YN, Guan YH, Hao ZJ, et al. Pantoprazole pretreatment elevates sensitivity to vincristine in drug-resistant oral epidermoid carcinoma *in vitro* and *in vivo*. Biomed Pharmacother. 2019;120: 109478. doi:10.1016/j.biopha.2019.109478

267. Ihraiz WG, Ahram M, Bardaweel SK. Proton pump inhibitors enhance chemosensitivity, promote apoptosis, and suppress migration of breast cancer cells. Acta Pharm. 2020;70: 179–190.

doi:10.2478/acph-2020-0020

268. Bartel K, Müller R, Von Schwarzenberg K. Differential regulation of AMP-activated protein kinase in healthy and cancer cells explains why V-ATPase inhibition selectively kills cancer cells. J Biol Chem. 2019;294: 17239–17248. doi:10.1074/jbc.RA119.010243

269. Lu Y, Zhang R, Liu S, Zhao Y, Gao J, Zhu L. ZT-25, a new vacuolar H+-ATPase inhibitor, induces apoptosis and protective autophagy through ROS generation in HepG2 cells. Eur J Pharmacol. 2016;771: 130–138. doi:10.1016/j.ejphar.2015.12.026

270. Patil R, Kulshrestha A, Tikoo A, Fleetwood S, Katara G, Kolli B, et al. Identification of novel bisbenzimidazole derivatives as anticancer vacuolar (H+)-ATPase inhibitors. Molecules. 2017;22: 1–14. doi:10.3390/molecules22091559

271. Wang J, Shi XG, Wang HY, Xia XM, Wang KY. Effects of esterified lactoferrin and lactoferrin on control of postharvest blue mold of apple fruit and their possible mechanisms of action. J Agric Food Chem. 2012;60: 6432–6438. doi:10.1021/jf300483v

272. Cotter PD, Hill C. Surviving the acid test: responses of Gram-positive bacteria to low pH. Microbiol Mol Biol Rev. 2003;67: 429–453. doi:10.1128/mmbr.67.3.429-453.2003

273. Singer S., Nicolson GL. The fluid mosaic model of the structure of cell membranes. Science. 1972;175: 720–731. doi:10.1126/science.175.4023.720

274. Simons K, Ikonen E. Functional rafts in cell membranes. Nature. 1997;387: 569–572. doi: 10.1038/42408

275. Hanada K, Nishijima M, Akamatsu Y, Pagano RE. Both sphingolipids and cholesterol participate in the detergent insolubility of alkaline phosphatase, a glycosylphosphatidylinositol-anchored protein, in mammalian membranes. J Biol Chem. 1995;270: 6254–6260. doi:10.1074/jbc.270.11.6254

276. Veatch SL, Keller SL. Separation of liquid phases in giant vesicles of ternary mixtures of phospholipids and cholesterol. Biophys J. 2003;85: 3074–3083. doi:10.1016/S0006-3495(03)74726-2

277. Hjort Ipsen J, Karlström G, Mourtisen OG, Wennerström H, Zuckermann MJ. Phase equilibria in the phosphatidylcholine-cholesterol system. BBA - Biomembr. 1987;905: 162–172. doi:10.1016/0005-2736(87)90020-4

278. Levental I, Levental KR, Heberle FA. Lipid rafts: controversies resolved, mysteries remain. Trends Cell Biol. 2020;30: 341–353. doi:10.1016/j.tcb.2020.01.009

279. Pike LJ. Rafts defined: A report on the Keystone symposium on lipid rafts and cell function. J Lipid Res. 2006;47: 1597–1598. doi:10.1194/jlr.E600002-JLR200

280. Sezgin E, Levental I, Mayor S, Eggeling C. The mystery of membrane organization: Composition, regulation and roles of lipid rafts. Nat Rev Mol Cell Biol. 2017;18: 361–374. doi:10.1038/nrm.2017.16

281. Huang Z, London E. Cholesterol lipids and cholesterol-containing lipid rafts in bacteria. Chem Phys Lipids. 2016;199: 11–16. doi:10.1016/j.chemphyslip.2016.03.002

282. Toulmay A, Prinz WA. Direct imaging reveals stable, micrometer-scale lipid domains that segregate proteins in live cells. J Cell Biol. 2013;202: 35–44. doi:10.1083/jcb.201301039

283. Poston C, Duong E, Cao Y, Bazemore-Walker C. Proteomic analysis of lipid raft-enriched

membranes isolated from internal organelles. Biochem Biophys Res Commun. 2011;415: 355–360. doi:10.1016/j.bbrc.2011.10.072.Proteomic

284. Lasserre R, Guo XJ, Conchonaud F, Hamon Y, Hawchar O, Bernard AM, et al. Raft nanodomains contribute to Akt/PKB plasma membrane recruitment and activation. Nat Chem Biol. 2008;4: 538–547. doi:10.1038/nchembio.103

285. Klose C, Ejsing CS, García-Sáez AJ, Kaiser HJ, Sampaio JL, Surma MA, et al. Yeast lipids can phase-separate into micrometer-scale membrane domains. J Biol Chem. 2010;285: 30224–30232. doi:10.1074/jbc.M110.123554

286. Xu X, Bittman R, Duportail G, Heissler D, Vilcheze C, London E. Effect of the structure of natural sterols and sphingolipids on the formation of ordered sphingolipid/sterol domains (rafts). Comparison of cholesterol to plant, fungal, and disease-associated sterols and comparison of sphingomyelin, cerebrosides, and cer. J Biol Chem. 2001;276: 33540–33546. doi:10.1074/jbc.M104776200

287. Short B. Lipid rafts inflate at the trans-Golgi. J Cell Biol. 2009;185: 567. doi:10.1083/jcb.1854if

288. Bagnat M, Keränen S, Shevchenko A, Shevchenko A, Simons K. Lipid rafts function in biosynthetic delivery of proteins to the cell surface in yeast. Proc Natl Acad Sci U S A. 2000;97: 3254–3259. doi:10.1073/pnas.97.7.3254

289. Wachtler V, Rajagopalan S, Balasubramanian MK. Sterol-rich plasma membrane domains in the fission yeast *Schizosaccharomyces pombe*. J Cell Sci. 2003;116: 867–874. doi:10.1242/jcs.00299

290. Martin SW, Konopka JB. Lipid raft polarization contributes to hyphal growth in *Candida albicans*. Eukaryot Cell. 2004;3: 675–684. doi:10.1128/EC.3.3.675-684.2004

291. Mollinedo F. Lipid raft involvement in yeast cell growth and death. Front Oncol. 2012;2: 1–15. doi:10.3389/fonc.2012.00140

292. Malínská K, Malínsky J, Opekarová M, Tanner W. Visualization of protein compartmentation within the plasma membrane of living yeast cells. Mol Biol Cell. 2003;14: 4427–4436. doi:10.1091/mbc.e03-04-0221

293. Ziółkowska NE, Christiano R, Walther TC. Organized living: Formation mechanisms and functions of plasma membrane domains in yeast. Trends Cell Biol. 2012;22: 151–158. doi:10.1016/j.tcb.2011.12.002

294. Rella A, Farnoud A, Del Poeta M. Plasma membrane lipids and their role in fungal virulence. Prog Lipid Res. 2016;61: 63–72. doi:10.1016/j.plipres.2015.11.003

295. Hurst LR, Fratti RA. Lipid rafts, sphingolipids, and ergosterol in yeast vacuole fusion and maturation. Front Cell Dev Biol. 2020;8: 1–7. doi:10.3389/fcell.2020.00539

296. Bagnat M, Chang A, Simons K. Plasma membrane proton ATPase Pma1p requires raft association for surface delivery in yeast. Mol Biol Cell. 2001;12: 4129–4138. doi:10.1091/mbc.12.12.4129

297. Gaigg B, Timischl B, Corbino L, Schneiter R. Synthesis of sphingolipids with very long chain fatty acids but not ergosterol is required for routing of newly synthesized plasma membrane ATPase to the cell surface of yeast. J Biol Chem. 2005;280: 22515–22522. doi:10.1074/jbc.M413472200

298. Toulmay A, Schneiter R. Lipid-dependent surface transport of the proton pumping ATPase: A model to study plasma membrane biogenesis in yeast. Biochimie. 2007;89: 249–254. doi:10.1016/j.biochi.2006.07.020

299. Wang Q, Chang A. Sphingoid base synthesis is required for oligomerization and cell surface stability of the yeast plasma membrane ATPase, Pma1. Proc Natl Acad Sci U S A. 2002;99: 12853–12858. doi:10.1073/pnas.202115499

300. Lee MCS, Hamamoto S, Schekman R. Ceramide biosynthesis is required for the formation of the oligomeric H+-ATPase Pma1p in the yeast endoplasmic reticulum. J Biol Chem. 2002;277: 22395–22401. doi:10.1074/jbc.M200450200

301. Gong X, Chang A. A mutant plasma membrane ATPase, Pma1-10, is defective in stability at the yeast cell surface. Proc Natl Acad Sci. 2001;98: 9104–9109. doi:10.1073/pnas.161282998

302. Zaremberg V, Gajate C, Cacharro LM, Mollinedo F, McMaster CR. Cytotoxicity of an anti-cancer lysophospholipid through selective modification of lipid raft composition. J Biol Chem. 2005;280: 38047–38058. doi:10.1074/jbc.M502849200

303. Li YC, Park MJ, Ye SK, Kim CW, Kim YN. Elevated levels of cholesterol-rich lipid rafts in cancer cells are correlated with apoptosis sensitivity induced by cholesterol-depleting agents. Am J Pathol. 2006;168: 1107–1118. doi:10.2353/ajpath.2006.050959

304. Levin-Gromiko U, Koshelev V, Kushnir P, Fedida-Metula S, Voronov E, Fishman D. Amplified lipid rafts of malignant cells constitute a target for inhibition of aberrantly active NFAT and melanoma tumor growth by the aminobisphosphonate zoledronic acid. Carcinogenesis. 2014;35: 2555–2566. doi:10.1093/carcin/bgu178

305. Reis-Sobreiro M, Roue G, Moros A, Gajate C, De La Iglesia-Vicente J, Colomer D, et al. Lipid raft-mediated Akt signaling as a therapeutic target in mantle cell lymphoma. Blood Cancer J. 2013;3. doi:10.1038/bcj.2013.15

306. Gao X, Lowry PR, Zhou X, Depry C, Wei Z, Wong GW, et al. PI3K/Akt signaling requires spatial compartmentalization in plasma membrane microdomains. Proc Natl Acad Sci U S A. 2011;108: 14509–14514. doi:10.1073/pnas.1019386108

307. Bi J, Ichu TA, Zanca C, Yang H, Zhang W, Gu Y, et al. Oncogene amplification in growth factor signaling pathways renders cancers dependent on membrane lipid remodeling. Cell Metab. 2019;30: 525-538.e8. doi:10.1016/j.cmet.2019.06.014

308. Irwin M, Mueller K, Bohin N, Ge Y, Boerner J. Lipid raft localization of EGFR alters the response of cancer cells to the EGFR tyrosine kinase inhibitor gefitinib. J Cell Physiol. 2011;226: 2316–2328. doi:10.1002/jcp.22570

309. Hryniewicz-Jankowska A, Augoff K, Biernatowska A, Podkalicka J, Sikorski AF. Membrane rafts as a novel target in cancer therapy. Biochim Biophys Acta - Rev Cancer. 2014;1845: 155–165. doi:10.1016/j.bbcan.2014.01.006

310. Grolez GP, Gordiendko D V., Clarisse M, Hammadi M, Desruelles E, Fromont G, et al. TRPM8-androgen receptor association within lipid rafts promotes prostate cancer cell migration. Cell Death Dis. 2019;10. doi:10.1038/s41419-019-1891-8

311. Bi J, Wang R, Zeng X. Lipid rafts regulate the lamellipodia formation of melanoma A375 cells via actin cytoskeleton-mediated recruitment of β1 and β3 integrin. Oncol Lett. 2018;16: 6540–6546. doi:10.3892/ol.2018.9466

312. Badana AK, Chintala M, Gavara MM, Naik S, Kumari S, Kappala VR, et al. Lipid rafts disruption induces apoptosis by attenuating expression of LRP6 and survivin in triple negative breast cancer. Biomed Pharmacother. 2018;97: 359–368. doi:10.1016/j.biopha.2017.10.045

313. Gupta VK, Sharma NS, Kesh K, Dauer P, Nomura A, Giri B, et al. Metastasis and chemoresistance in CD133 expressing pancreatic cancer cells are dependent on their lipid raft integrity. Cancer Lett. 2018;439: 101–112. doi:10.1016/j.canlet.2018.09.028

314. von Haller PD, Donohoe S, Goodlett DR, Aebersold R, Watts JD. Mass spectrometric characterization of proteins extracted from Jurkat T cell detergent-resistant membrane domains. Proteomics. 2001;1: 1010–1021. doi:10.1002/1615-9861(200108)1:8<1010::aid-prot1010>3.0.co;2-l

315. Foster LJ, De Hoog CL, Mann M. Unbiased quantitative proteomics of lipid rafts reveals high specificity for signaling factors. Proc Natl Acad Sci U S A. 2003;100: 5813–5818. doi:10.1073/pnas.0631608100

316. Xu M, Xia M, Li XX, Han WQ, Boini KM, Zhang F, et al. Requirement of translocated lysosomal V1 H +-ATPase for activation of membrane acid sphingomyelinase and raft clustering in coronary endothelial cells. Mol Biol Cell. 2012;23: 1546–1557. doi:10.1091/mbc.E11-09-0821

317. Lafourcade C, Sobo K, Kieffer-Jaquinod S, Garin J, van der Goot FG. Regulation of the V-ATPase along the endocytic pathway occurs through reversible subunit association and membrane localization. PLoS One. 2008;3. doi:10.1371/journal.pone.0002758

318. Yoshinaka K, Kumanogoh H, Nakamura S, Maekawa S. Identification of V-ATPase as a major component in the raft fraction prepared from the synaptic plasma membrane and the synaptic vesicle of rat brain. Neurosci Lett. 2004;363: 168–172. doi:10.1016/j.neulet.2004.04.002

319. Ryu J, Kim H, Chang EJ, Kim HJ, Lee Y, Kim HH. Proteomic analysis of osteoclast lipid rafts: The role of the integrity of lipid rafts on V-ATPase activity in osteoclasts. J Bone Miner Metab. 2010;28: 410–417. doi:10.1007/s00774-009-0150-y

CHAPTER 3

Molecular basis of the antifungal activity of lactoferrin

This chapter is adapted from the following publication:

Cátia Santos-Pereira, María T. Andrés, Susana R. Chaves, José F. Fierro, Hernâni Gerós, Stéphen Manon, Lígia R. Rodrigues, Manuela Côrte-Real (2021) **Lactoferrin perturbs lipid rafts and requires integrity of Pma1p-lipid rafts association to exert its antifungal activity against *Saccharomyces cerevisiae*.** *International Journal of Biological Macromolecules*. 171:343-357. doi:10.1016/j.ijbiomac.2020.12.224

This chapter comprises parts of the following publication:

Jorge Rodrigues*, Cátia Santos-Pereira*, Natasha Fontes, Hernâni Gerós, Manuela Côrte-Real M (2018) **Flow Cytometry and Fluorescence Microscopy as Tools for Structural and Functional Analysis of Vacuoles Isolated from Yeast and Plant Cells.** In Cláudia Pereira (Eds), Plant Vacuolar Trafficking, vol. 1789, chapter 8. ISBN: 978-1-4939-7855-7. doi: 10.1007/978-1-4939-7856-4_8

*Both authors contributed equally

3.1 Background

The yeast Pma1p is localized at microdomains of the plasma membrane called lipid rafts [1,2], and different reports support the importance of these membrane niches for Pma1p activity. Indeed, lipid raft association is crucial for proper surface targeting and stability of Pma1p at the plasma membrane [3], and disruption of lipid rafts leads to mistargeting of Pma1p to the vacuole [4]. Sphingolipids, which are critical and abundant in lipid rafts, are also required for Pma1p oligomerization at the ER, its targeting to the plasma membrane, and for its stability at the cell surface [5,6] (see Chapter 2.4.1 for detailed information). Moreover, lipid rafts affect the mechanical properties of the plasma membrane and are involved in fungal pathogenicity and biofilm formation [7]. The combination of antifungal peptides targeting lipid rafts with conventional antifungal drugs has been suggested as a powerful antifungal strategy [8].

Given the interplay and interdependence between Pma1p and lipid rafts, and because Lf binds and inhibits this proton pump, in the present chapter we aimed to uncover the role of lipid rafts in Lf-induced cell death, and to explore the Lf-Pma1p-lipid rafts axis. As human and bovine Lfs share a high degree of sequence identity (69%) [9], a similar structure [10] and function/activity against fungi [11], we used bovine Lf (bLf) in the present work. The effect of lipid raft composition on bLf cytotoxicity was studied using yeast mutant strains lacking lipid raft-associated proteins or enzymes that are involved in the synthesis of ergosterol and sphingolipids, the major components of DRMs. Rvs161p (encoded by *RVS161/END6*) is a protein localized at lipid rafts [12]. The *ERG6* gene encodes the sterol C-24 methyltransferase that catalyses one of the final steps of the ergosterol biosynthesis by converting zymosterol to fecosterol (Figure 3.1A). Therefore, *erg6*Δ mutants accumulate mainly zymosterol and cholesta-5,7,24-trienol instead of ergosterol [13]. The other two genes under study are involved in sphingolipid metabolism (Figure 3.1B). *LAC1* encodes a component of ceramide synthase, which is involved in *de novo* synthesis of ceramide by N-acylation of sphingoid bases. The *ISC1* gene encodes the mitochondrial inositol phosphosphingolipid phospholipase C that is involved in the synthesis of ceramide by hydrolysis of complex sphingolipids (Figure 3.1B) [14].

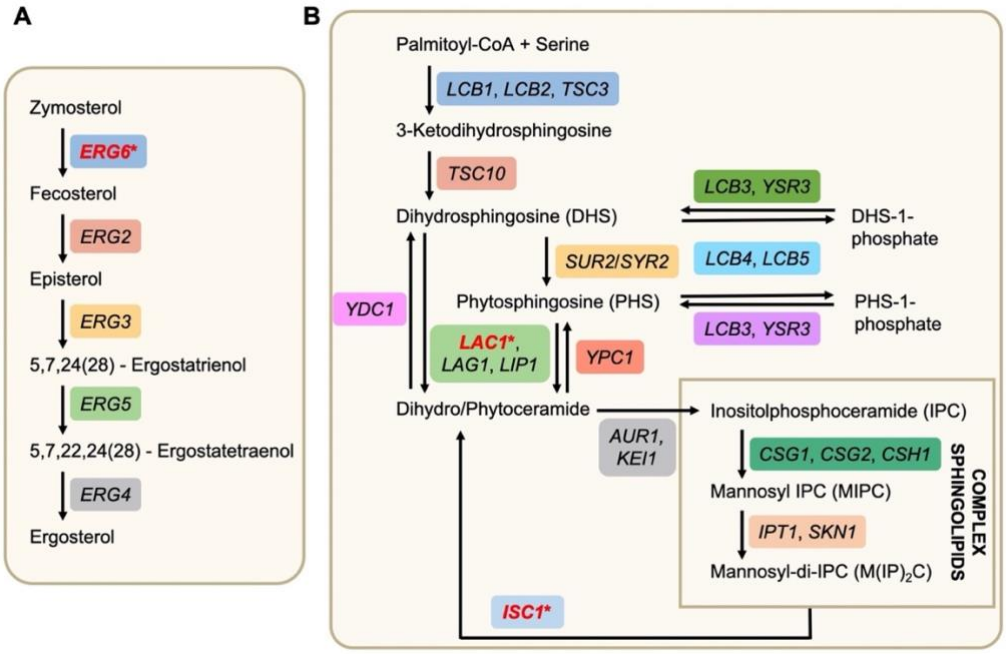

Figure 3.1: Ergosterol (A) and sphingolipids (B) biosynthetic pathways in *Saccharomyces cerevisiae*. For ergosterol, only the last steps of the biosynthetic pathway are represented. The genes that were deleted to construct the mutant strains used in this work are marked in red with an asterisk (*).

3.2 Materials and Methods

3.2.1 Strains and plasmids

All *S. cerevisiae* strains and plasmids used in this study are listed in Table 3.1. BY4741 and L3852 were used as wild type strains. BY4741, *erg6*Δ, *rvs161*Δ, *lac1*Δ, *isc1*Δ and *ast1*Δ strains were transformed with pRS316 Pma1-GFP using the LiAc/SS Carrier DNA/PEG method [15]. The *ast1*Δ strain was transformed with the high copy pAC49 AST1 plasmid using the same method. The XGY32 strain harbours the *pma1-10* mutations, produced by pop-in/pop-out gene replacement of the *PMA1* gene [3].

3.2.2. Growth conditions

All strains were grown in YEPD (yeast extract-peptone-dextrose) medium [1% (w/v) yeast extract, 2% (w/v) peptone, 2% (w/v) glucose], with the exception of the strains expressing plasmids that were grown in Synthetic Complete Glucose medium [SC Glu pH 5.5; 2% (w/v) glucose; 0.67% (w/v) yeast nitrogen base without amino acids and ammonium sulphate; 0.5% (w/v) ammonium sulphate; 0.1% (w/v) potassium phosphate, 0.2% (w/v) drop-out mixture lacking histidine, leucine, tryptophan and uracil; 0.01% (w/v) histidine, 0.02% (w/v) leucine and 0.01% (w/v) tryptophan. The yeast strains were grown at 30 °C

(and/or at 37 °C in the case of L3852 and XGY32 strains) in an orbital shaker at 200 rpm, with a ratio of flask volume/medium of 5:1 until exponential phase (OD640 0.6 - 0.8).

Table 3.1: List of *S. cerevisiae* strains and plasmids used in this chapter.

Strain	Genotype	Reference/ Source
BY4741	MATa his3Δ1 leu2Δ0 met15Δ0 ura3Δ0	Euroscarf
*erg6*Δ	MATa his3Δ1 leu2Δ0 met15Δ0 ura3Δ0 *erg6*Δ::KanMX4	Euroscarf
*rvs161*Δ	MATa his3Δ1 leu2Δ0 met15Δ0 ura3Δ0 *rvs161*Δ::KanMX4	Euroscarf
*lac1*Δ	MATa his3Δ1 leu2Δ0 met15Δ0 ura3Δ0 *lac1*Δ::KanMX4	Euroscarf
*isc1*Δ	MATa his3Δ1 leu2Δ0 met15Δ0 ura3Δ0 *isc1*Δ::KanMX4	Euroscarf
*ast1*Δ	MATa his3Δ1 leu2Δ0 met15Δ0 ura3Δ0 *ast1*Δ::KanMX4	Euroscarf
BY4741 *PMA1*-GFP	BY4741 harbouring pRS316 *PMA1*-GFP	This study
*erg6*Δ *PMA1*-GFP	*erg6*Δ harbouring pRS316 *PMA1*-GFP	This study
*rvs161*Δ *PMA1*-GFP	*rvs161*Δ harbouring pRS316 *PMA1*-GFP	This study
*lac1*Δ *PMA1*-GFP	*lac1*Δ harbouring pRS316 *PMA1*-GFP	This study
*isc1*Δ *PMA1*-GFP	*isc1*Δ harbouring pRS316 *PMA1*-GFP	This study
*ast1*Δ *PMA1*-GFP	*ast1*Δ harbouring pRS316 *PMA1*-GFP	This study
*ast1*Δ *AST1*	*ast1*Δ harbouring pAC49-*AST1*	This study
L3852	MATa his3Δ200 lys2Δ201 leu2-3,112 ura3-52 ade2	[34]
XGY32	MATα his3Δ200 lys2Δ201 leu2-3,112 ura3-52 ade2 *pma1-10*	[3]
Plasmid	**Description**	**Reference**
pRS316 Pma1-GFP	URA3, *PMA1* gene fused with the yeast *GFP3* gene	[12]
pAC49-*AST1*	*AST1* URA3 2μ	[34]

3.2.3 Lactoferrin treatment and cell survival assays

After reaching the exponential phase, yeast cells were harvested, resuspended in 10 mM Tris-HCl buffer pH 7.4 [16] and incubated with 0-1500 μg/ml bLf and/or with 20 μM C2-ceramide (N-Acetyl-D-sphingosine, Sigma-Aldrich) or its solvent (absolute ethanol) for 90 min under the same aforementioned growth conditions. Lower incubation times were employed in the experiments with isolated plasma membranes (15 min) and vacuoles (right before ATP addition), as well as with the fluorescence-labelled bLf (bLf-FITC) (75 min). bLf was obtained from DMV (Veghel, The Netherlands). The protein is ca. 80% pure, with 3.5% moisture, and 21% iron-saturated, according to the manufacturer. bLf was dissolved in sterile distilled water (dH_2O) to obtain the different concentrations used throughout this work.

Cell survival was evaluated by counting of colony forming units (c.f.u.). Briefly, four serial dilutions of the cultures were performed, and the 10^{-4} dilution was plated onto YEPD containing 2% (w/v) agar and incubated for 48 h at 30 °C. The percentage of cell survival was calculated from the number of c.f.u. of each condition in relation to time zero and the control without any treatment.

3.2.4 Filipin staining, Pma1-GFP localization and fluorescence microscopy

For visualization of sterol-rich lipid rafts, yeast cells were stained with filipin (Filipin III from *Streptomyces filipinensis*, Sigma-Aldrich), a naturally fluorescent antibiotic widely used to visualize sterols [17]. After treatment with or without bLf, cells were collected at an OD640 of 0.5 and concentrated 20× in sterile water. Immediately before visualization under the fluorescence microscope, cells were incubated for 1 min in the dark with 0.1 mg/ml filipin from a stock solution of 5 mg/ml (w/v) in methanol [18]. Cells were then mounted on slides with the anti-fading agent Vectashield (Vector Laboratories) to overcome the instability of this dye, and then visualized in an epifluorescence microscope. As a positive control of lipid rafts disruption, cells were treated for 30 min at 30 °C in an orbital shaker at 200 rpm with 5 mg/ml methyl-β-cyclodextrin (MβCD) in 10 mM Tris-HCl buffer pH 7.4. For determination of Pma1p localization, Pma1-GFP expressing cells without any treatment were grown until early-exponential phase, collected by centrifugation at 3,000 ×*g* for 3 min, and resuspended in sterile water at an OD640 of 10. Samples were observed under the fluorescence microscope immediately. The percentage of cells with altered Pma1p localization was calculated by counting the number of cells with normal and altered Pma1p localization in each observed field. More than 800 cells were counted.

The images were obtained with a fluorescence microscope (Leica DM 5000B, Leica Microsystems) with appropriate filter settings using a 100× oil-immersion objective with a Leica DCF350FX digital camera, and processed with LAS Leica Microsystems software.

3.2.5 Lactoferrin-FITC labelling

For labelling of bLf with fluorescein-5-isothiocyanate (FITC), 50 µg/ml of FITC (Sigma-Aldrich) were added to a solution of 121 mg/ml of bLf in 1 M sodium bicarbonate buffer, pH 9, and incubated for 2 h in the dark with agitation. Afterwards, the unbound FITC was removed by several spin-separation cycles at 6,000 ×*g* for 5 min using Amicon Ultra-0.5, Ultracel-30 Membrane (30 kDa cutoff), and finally buffer exchange to water was performed using the same approach. A control with only FITC was performed and added to cells. No fluorescence was detected using the same settings as those for bLf-FITC.

3.2.6 Assessment of metabolic activity by FUN-1 staining

Metabolic activity of yeast cells was evaluated by Fun-1 [(2-chloro-4-(2,3-dihydro-3-methyl-(benzo-1,3-thiazol-2-yl)-methylidene)-1-phenylquinolinium Iodide), Molecular Probes] staining. Fun-1 is a membrane-permeant dye that is transported to the vacuole and compacted into cylindrical intravacuolar structures (CIVS) only in metabolically active yeast cells [19]. After 90 min incubation in the absence or presence of 425 µg/ml bLf, 1 mL of cells at an OD640 of 0.1 were harvested, resuspended in phosphate buffered saline (PBS) 1× (PBS 10×; 137 mM NaCl, 2.7 mM KCl, 10 mM Na_2HPO_4, 1.8 mM KH_2PO_4, pH 7) and stained with 4 µM FUN-1 for 30 min at 30 °C in the dark. Wild type cells boiled for 5 min were used as a positive control for absence of metabolic activity. Stained cell suspensions were then analysed in an epifluorescence microscope and in a flow cytometer. Flow cytometry data are presented as the mean FL4 fluorescence intensity in relation to the autofluorescence of each sample and untreated cells of each strain.

3.2.7 Analysis of glucose-dependent extracellular acidification

Extracellular acidification rate was estimated as previously described [20]. Briefly, after growth and treatment without or with 0-1500 µg/ml bLf or 100 µM diethylstilbestrol (DES) as reported for cell survival assays, cells were washed once with 50 mM KCl and then resuspended and concentrated (10^7 cells/ml) in 1 ml of 50 mM KCl and subjected to pH measurements. DES was used as a positive control for Pma1p inhibition [20]. After pH stabilization, 2.5 mM glucose was added and acidification was measured using a pH meter every minute for 12 min, with constant stirring. A sample was taken from each condition to estimate the dry weight after incubation at 80 °C for two days. Data is presented as ΔpH/min/mg dry weight.

3.2.8 Plasma membrane isolation

Plasma membranes were obtained as described previously [20], with some modifications. Briefly, 4 L of yeast culture were grown in YEPD medium until late-log phase. Cells were then harvested, washed twice with distilled sterile water and resuspended in homogenization buffer [2 mM EDTA, 2% (w/v) glucose, 1 mM phenylmethylsulfonyl fluoride (PMSF), 0.2 ng/ml DNase, 50 mM Tris pH 7.4]. Whole cells were then disrupted by three passages at 19,500 lb/in^2 in a French pressure cell (SLM Aminco, Silver Spring, MD). The resulting suspension was centrifuged at 3,000 ×*g* for 10 min, at 4 °C, to remove cell debris and unbroken cells, and the supernatant was centrifuged twice at 14,000 ×*g* for 30 min, at 4 °C.

Afterwards, the homogenate was centrifuged at 100,000 ×*g* for 1 h 30 min, at 4 °C, and the pellet containing the cell membranes was resuspended in ice-cold resuspension buffer [0.5 mM EDTA, 20% (v/v) glycerol, 0.1 mM PMSF, 10 mM Tris, pH7.4]. Protein concentration was estimated by Bradford assay [21] before storage of samples at -80 °C.

3.2.9 Measurement of ATP hydrolysis

ATP hydrolysis assay was performed using the PiColorLock™ Gold Phosphate Detection kit (obtained from Innova Biosciences, Ltd. Cambridge, UK), which allows the quantification of the inorganic phosphate (Pi) concentration, according to the manufacturer's instructions. For all experiments, a calibration curve with a standard range of Pi concentrations was performed. Measurements were performed in isolated plasma membranes at a concentration of 12.5 µg/ml in assay medium containing 0.2 mM ATP. To avoid interference of the activity of vacuolar and mitochondrial ATPases and acid phosphatases, membranes were pre-incubated for 15 min at 30 °C with 50 mM KNO_3, 0.2 mM ammonium molybdate and 5 mM sodium azide [22], respectively. Afterwards, membrane extracts were incubated with 100 µg/ml bLf or 100 µM diethylstilbestrol (DES) for 15 min at 30 °C. Pi concentration was calculated by spectrophotometry at 620 nm. Data are presented as percentage in relation to the untreated control of each strain (considered as 100%).

3.2.10 Evaluation of intracellular ATP concentration

Intracellular ATP concentration was quantified using the BacTiter-Glo™ Microbial Cell Viability kit as recommended. For all experiments, a calibration curve with standard ATP concentrations (10-1000 nM) was performed. Cells were grown as described for cell survival assays and treated in the absence or presence of 250 and 425 µg/ml bLf, and 100 µM DES for 90 min at 30 °C, with 200 rpm agitation. 50 µl of each condition were transferred to a 96-well opaque plate, mixed with an equal volume of BacTiter-Glo reagent, and incubated for 15 min in the dark. The emitted luminescence was read in a Varioskan flash multimode reader (Thermo Scientific). The reagent uses a thermostable luciferase that produces a luminescence signal proportional to the ATP concentration. Data is shown in arbitrary units as fold change expressed in relation to the untreated control of each strain (considered as 1).

3.2.11 Protein extraction and western blot

For preparation of whole cell extracts, 1 mL OD640 of 1 of exponentially growing cells was harvested by centrifugation at 5,000 ×*g* for 3 min and washed once with dH_2O. Cells were then

resuspended in 500 µl water containing 50 µl lysis buffer (3.5% β-mercaptoethanol in 2 M NaOH) and incubated for 15 min on ice. Next, 50 µl of 50% trichloroacetic acid were added and incubated for additional 15 min to precipitate the proteins. The extracts were centrifuged at 10,000 ×*g* for 10 min, at 4 °C, washed with acetone and centrifuged again. Finally, protein extracts were resuspended in Laemmli buffer (2% β-mercaptoethanol, 20% glycerol, 0.02% bromophenol blue, 0.1 M Tris, pH 8.8). Samples were heated at 95 °C and used immediately for western blot or stored at -20 °C.

For detection of Pma1p expression levels, 50 µg of protein extracts were separated by 10% sodium dodecyl sulfate-polyacrylamide gel electrophoresis for 1 h. Proteins were then transferred onto nitrocellulose membranes, and membranes were blocked in 5% non-fat milk in PBS-Tween 0.1% solution (1× PBST) with agitation at RT for 1 h to avoid non-specific interactions. Membranes were then cut into strips and incubated overnight at 4 °C with the primary antibodies mouse monoclonal anti-yeast phosphoglycerate kinase (Pgk1p) (1:5000, Molecular Probes), mouse monoclonal anti-Pma1p (1:1000, 40B7, Invitrogen), and goat polyclonal anti-bLf (1:1000, Abcam). Pgk1p was used as the loading control. Subsequently, membranes were incubated with the secondary antibody Peroxidase-AffiniPure goat anti-mouse IgG or donkey anti-goat IgG (Jackson ImmunoResearch) (1:5000). Chemiluminescence detection was performed using the ECL detection system (Millipore-Merck) in a ChemiDoc XRS system (Bio-Rad).

3.2.12 Isolation of intact yeast vacuoles

Vacuole isolation was performed as previously described [23,24]. After grown until an OD640 of 0.7, 1 L of *S. cerevisiae* BY4741 cell culture was collected, washed twice with ice-cold distilled water, resuspended in washing buffer [5% glucose, 10 mM MES (morpholineethanesulfonic acid)-Tris, pH 6.5] and incubated in a shaker at 30 °C for 30 min. Afterwards, cells were incubated with digestion buffer [1.35 M sorbitol, 10 mM citric acid, 30 mM Na_2HPO_4, 1 mM EGTA (ethylene glycol-bis(β-aminoethyl ether)-N,N,N′,N′-tetraacetic acid), 30 mM DTT (dithiothreitol), pH 7.5] for 15 min at room temperature. Spheroplasts were generated by subsequent incubation with 2 mg/mL of zymolyase in digestion buffer without DTT, and cell wall digestion was monitored in a phase contrast microscope. When digestion was completed, spheroplasts were pelleted by centrifugation at 2,750 ×*g* for 5 min and washed with digestion buffer without DTT. They were then resuspended in 12% (w/v) Ficoll and homogenized in a Potter-Elvehjem to disrupt the cell membrane. To isolate vacuoles by Ficoll gradient centrifugation, the resulting homogenate was centrifuged at 2,750 ×*g* for 3 min and the supernatant was recovered. The gradient was prepared by carefully adding 8% (w/v) Ficoll on the top of the supernatant. Ultracentrifugation was performed at 80,000 ×*g* for 30 min in a SW 28 Ti swinging-bucket rotor. The white fraction on top of the

gradient containing highly purified vacuoles was collected and used in the spectrofluorometric studies. Protein concentration was determined by the Lowry method [25], using BSA (5 μg/μL - 25 μg/μL) to build a standard curve.

3.2.13 Measurement of V-ATPase activity by spectrofluorimetry

The pH-sensitive probe ACMA (9-amino-6-chloro-2-methoxyacridine) was used to determine the proton-pumping activity of V-ATPase in the isolated vacuoles using a Perkin-Elmer LS-5B spectrofluorimeter as previously reported [23,24,26]. 20 μg of isolated vacuoles were added to a buffer containing 1 mM MOPS [3-(N-morpholino)propane sulfonic acid]-Tris pH 7.2, 2 μM ACMA, 1 mM $MgCl_2$ and 100 mM KCl. The excitation/emission wavelengths were set to 415 nm and 485 nm, respectively. Four or 80 μg/ml bLf were added to the assay medium to study their inhibitory effects. After addition of bLf, the reaction was started with 0.1-0.5 mM ATP and the initial rates of fluorescence quenching were regarded as a measure of the initial rates of V-ATPase proton pumping activity [Δ%F min^{-1} 20 μg^{-1} protein]. The results were analysed using the GraphPad Prism Software and the proton pumping kinetics best fitting to the experimental initial acidification curves was determined.

3.2.14 Analysis of vacuolar pH variations using the carboxy-DCFDA probe

Vacuolar pH alterations were detected by both fluorescence microscopy and flow cytometry using the 5-(and-6)-carboxy-2',7'-dichlorofluorescein diacetate (carboxy-DCFDA) probe. Untreated or bLf-treated cells were harvested by centrifugation (1 mL OD640 0.1), washed once with sterile water and resuspended in CF buffer [50 mM glycine, 10 mM NaCl, 5 mM KCl, 1 mM $MgCl_2$, 40 mM Tris, 100 mM MES, pH 4.5 supplemented with 2% glucose] [27]. The cell suspension was then incubated with 1.6 μM carboxy-DCFDA for 20 min at 30 °C with 200 rpm orbital agitation. Afterwards, cells were washed once with CF buffer without glucose, and finally resuspended in the same buffer for further analysis in the flow cytometer or fluorescence microscope. Flow cytometry data are presented as the mean FL1 fluorescence intensity in relation to the autofluorescence of each sample and untreated cells of each strain.

3.2.15 Immunoprecipitation

For immunoprecipitation, 10 ml of yeast culture at an OD640 of 1 were collected and resuspended in a buffer containing 2 mM EGTA, 10 mM Tris/Maleate, pH 6.8, and a cocktail of protease inhibitors (Complete, Roche). Mechanic lysis was then performed using glass beads and a fast prep equipment,

and supernatant was collected and centrifuged at 800 ×*g* for 10 min. 1 mg from the supernatant were solubilized in 1× IP50 buffer (Sigma-Aldrich) for 40 min at 4 °C and incubated overnight with 1 µg of anti-Pma1 (40B7, Invitrogen) or anti-bLf (ab112968, Abcam) antibodies. Protein G-sepharose beads (Sigma-Aldrich) were then added and incubated for additional 4 h. Beads were washed 4 times with 1× IP50 buffer and two times with 0.1× IP50 buffer, and incubated with 25 µL of Laemmli buffer 1×, before SDS-PAGE and Western-blotting.

3.2.16 Flow cytometry

Flow cytometry analysis was performed with an Epics® XLTM (Beckman Coulter) flow cytometer equipped with an argon-ion laser emitting a 488 nm beam at 15 mW. Green fluorescence (carboxy-DCFDA) was collected through a 488 nm blocking filter, a 550 nm long-pass dichroic and a 525 nm band-pass filter. Red fluorescence (FUN-1) was collected through a 560 nm short-pass dichroic, a 640 nm long-pass, and another 670 nm long-pass filter. For each sample, 30,000 events were evaluated. Data were analysed using the FlowJo software.

3.2.17 Statistical analysis

Data are expressed as the mean and standard deviation values of at least three independent experiments. Statistical analyses were carried out using the GraphPad Prism software, one-way or two-way ANOVA and the Tukey post-test. P-values lower than 0.05 were considered to represent a significant difference.

3.3 Results

3.3.1 bLf induces intracellular accumulation of ergosterol perturbing sterol-rich lipid rafts in yeast cells

To ascertain whether sterol-rich lipid rafts play a role in bLf-induced cytotoxicity in yeast, their cellular distribution was assessed. Since sterols are major lipid rafts components, cellular ergosterol localization was monitored using filipin staining after a 90 min exposure to 250-500 µg/ml of bLf, which induces loss of cell viability of 70% - 98%, respectively (Figure 3.2A).

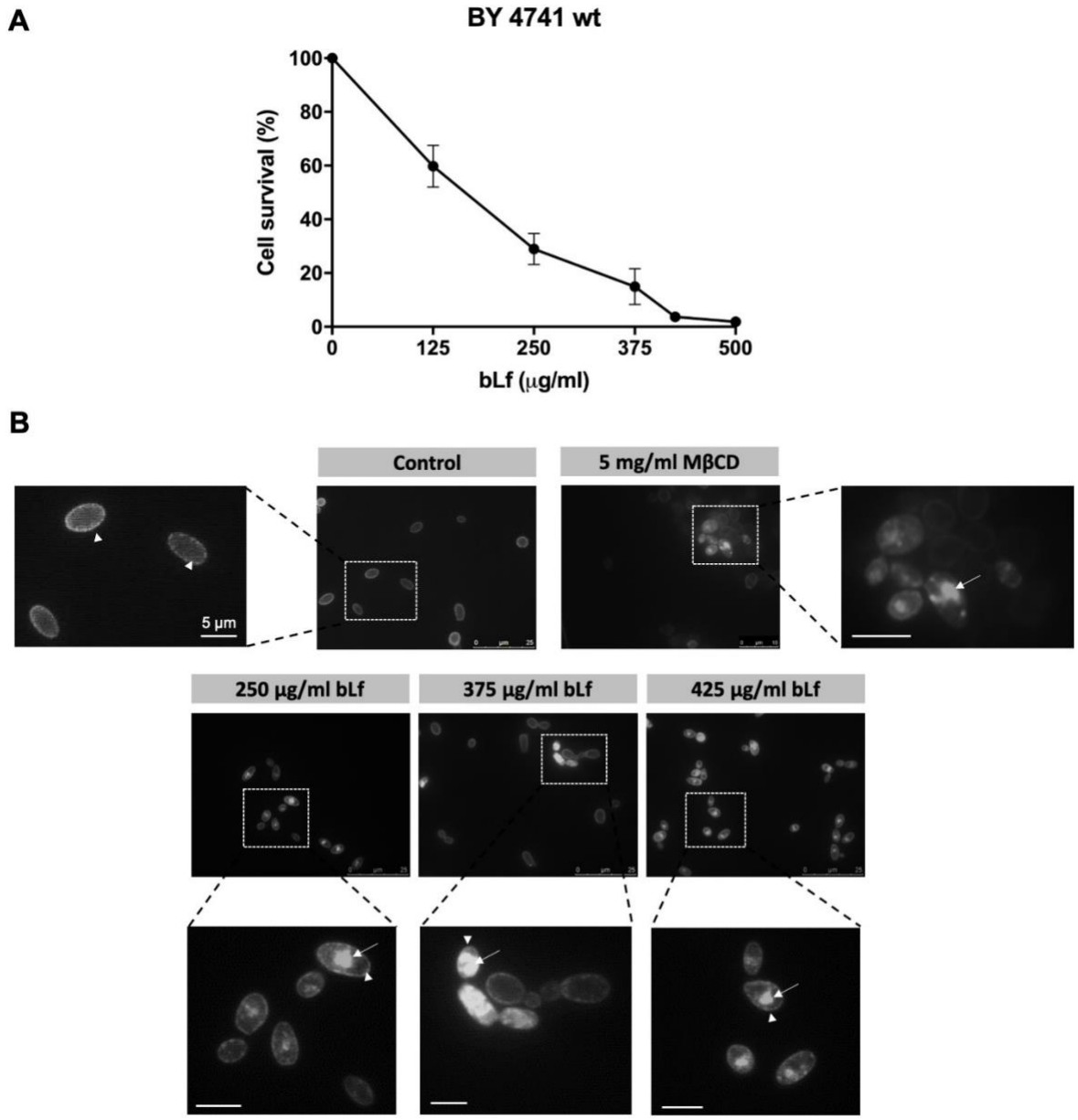

Figure 3.2: Effect of bLf on the localization of sterol-rich lipid rafts in *S. cerevisiae* BY4741 cells. Cells were incubated in the absence or presence of increasing concentrations of bLf (125-500 µg/ml) for 90 min at 30˚C in Tris-HCl 10 mM, pH 7.4. **(A)** Cell survival was assessed by counting colony forming units. **(B)** For lipid rafts visualization, cells were stained in the dark with 0.1 mg/ml filipin immediately before visualization under the microscope. As a positive control of lipid rafts disruption, cells were treated with 5 mg/ml methyl-β-cyclodextrin (MβCD) for 30 min. Representative fluorescence microscopy images of each condition are shown. Arrows: intracellular filipin staining. Head arrows: plasma membrane filipin staining. Bar: 5 µm.

As shown in Figure 3.2B, the characteristic punctuated pattern of the lipid rafts at the plasma membrane (head arrows) is observed in control cells, while intracellular spots of filipin staining (arrows) are visible in bLf-treated cells. Cell treatment with methyl-β-cyclodextrin (MβCD), a sterol chelator known to disrupt lipid rafts by depleting ergosterol from membranes [28], induced an intracellular filipin-staining

pattern similar to that of bLf, confirming that bLf perturbs the normal sterol-rich lipid rafts distribution pattern by causing intracellular accumulation of ergosterol.

3.3.2 Yeast mutants lacking lipid rafts-associated proteins or enzymes involved in the synthesis of the lipid rafts major components are more resistant to bLf-induced cytotoxicity

We next assessed the impact of perturbing lipid rafts composition using yeast mutants lacking proteins that are either present at lipid rafts or are involved in pathways that lead to the synthesis of their major lipid components, ergosterol and sphingolipids, namely *rvs161*Δ, *erg6*Δ, *lac1*Δ and *isc1*Δ mutants (see Introduction section). Results showed that absence of these proteins greatly increases the resistance to bLf-induced cytotoxicity in comparison with the wild type strain (Figure 3.3A). Remarkably, even at 500 μg/ml bLf, which is highly toxic for the wild type strain (only about 2% cell survival), the mutants affected in sphingolipid metabolism exhibit about 23% of cell survival.

Our data further indicates that the metabolic activity of the wild type strain is affected by the bLf treatment using FUN-1 staining (Figure 3.3B, C). FUN-1 is a membrane-permeant dye that is first detected as diffuse green fluorescence in the cytosol before its accumulation in the vacuole of metabolically active yeast cells forming red cylindrical intravacuolar structures (CIVS), as observed in Figure 3.3B (red spots) [29]. The treatment of yeast cells with bLf produced a diffuse bright red fluorescence, suggesting that the cells became metabolically inactive (Figure 3.3B) as they were not able to process the dye at the vacuole, much like heat-killed cells [19,30]. Accordingly, flow cytometry analysis of wild type cells stained with FUN-1 showed that the red mean fluorescence intensity increased 2-fold from control to bLf-treated cells, while no differences in fluorescence intensity were observed in the mutant strains (Figure 3.3C), in agreement with their higher resistance to bLf.

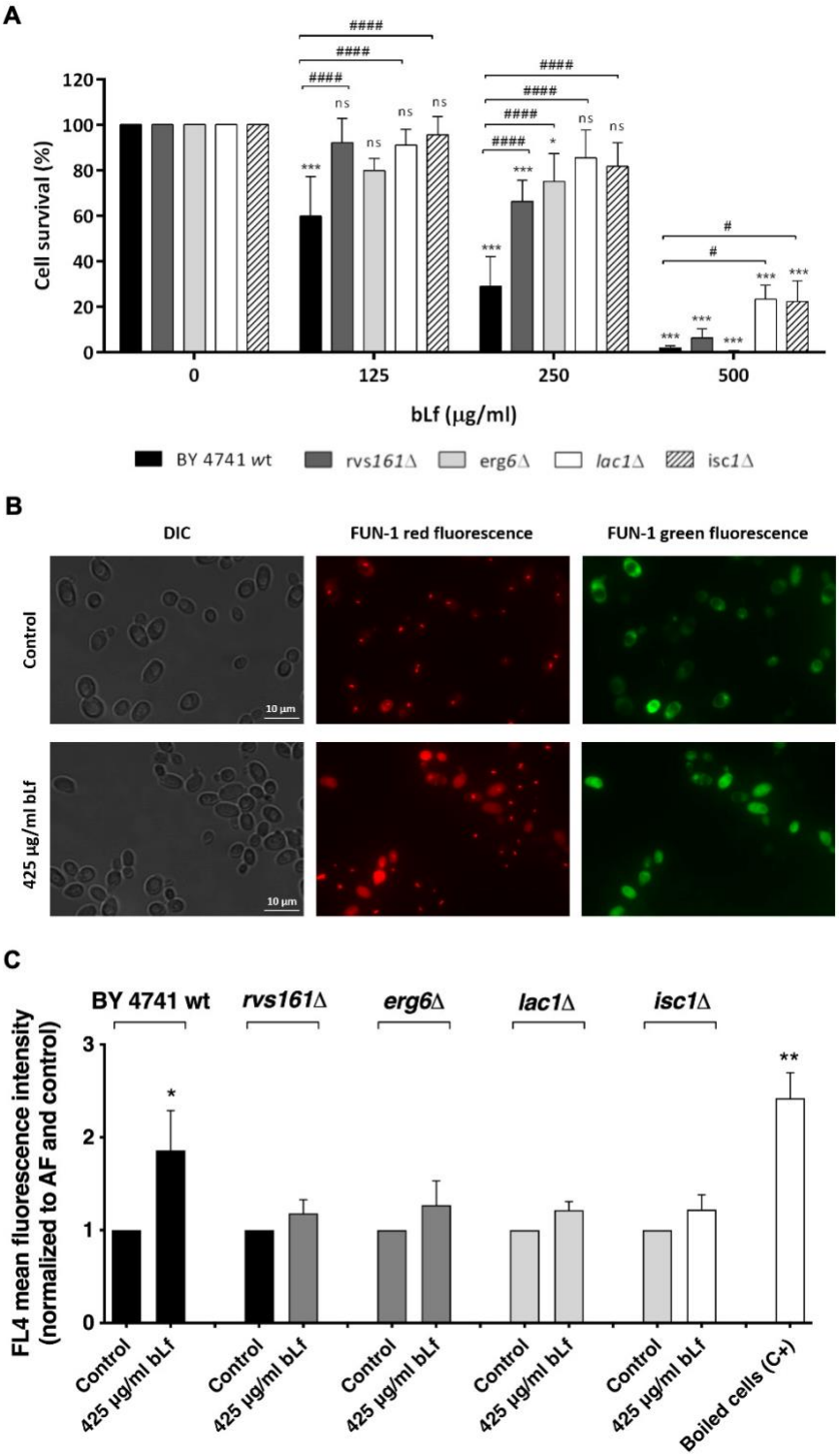

Figure 3.3: Effect of bLf on cell survival and metabolic activity of wild type and *rvs161*Δ, *erg6*Δ, *lac1*Δ and *isc1*Δ mutant strains. (A) Cell survival assays of *S. cerevisiae* wild type BY4741 and indicated mutant strains 90 min after incubation with 0-500 µg/ml bLf in 10 mM Tris-HCl, pH 7.4, at 30˚C, evaluated by colony forming unit counting. Values are mean ± standard deviation normalized to time zero of incubation and considering the control without bLf as 100% cell survival. **(B)** Fluorescence microscopy images showing FUN-1 staining of BY4741 wild type cells non-treated (control) or treated with 425 µg/ml bLf. **(C)** Flow cytometry analysis of FUN-1 staining of the same yeast strains treated as in A without or with 425 µg/ml bLf. 5 min-

boiled cells were used as a control of dead cells (C+). Values represent mean ± standard deviation of red (FL4) fluorescence intensity normalized to autofluorescence of each sample and control of each strain. ns, non-significant; *, **, *** P<0.05, 0.01, 0.001, respectively, in comparison with the control of each strain; #, #### P<0.05, 0.0001, respectively, in comparison with the wild type strain.

3.3.3 bLf does not alter localization of sterol-rich lipid rafts in *rvs161*Δ, *erg6*Δ, *lac1*Δ and *isc1*Δ mutants

As the cytotoxicity of bLf in the wild type strain was associated with intracellular accumulation of ergosterol and perturbation of sterol-rich lipid rafts, the mutants under study were stained with filipin in the presence and absence of bLf. Results showed that bLf only affected ergosterol distribution in the wild type strain, showing no effect on the mutants, which is in agreement with their higher survival rate upon treatment with bLf (Figure 3.4A, B).

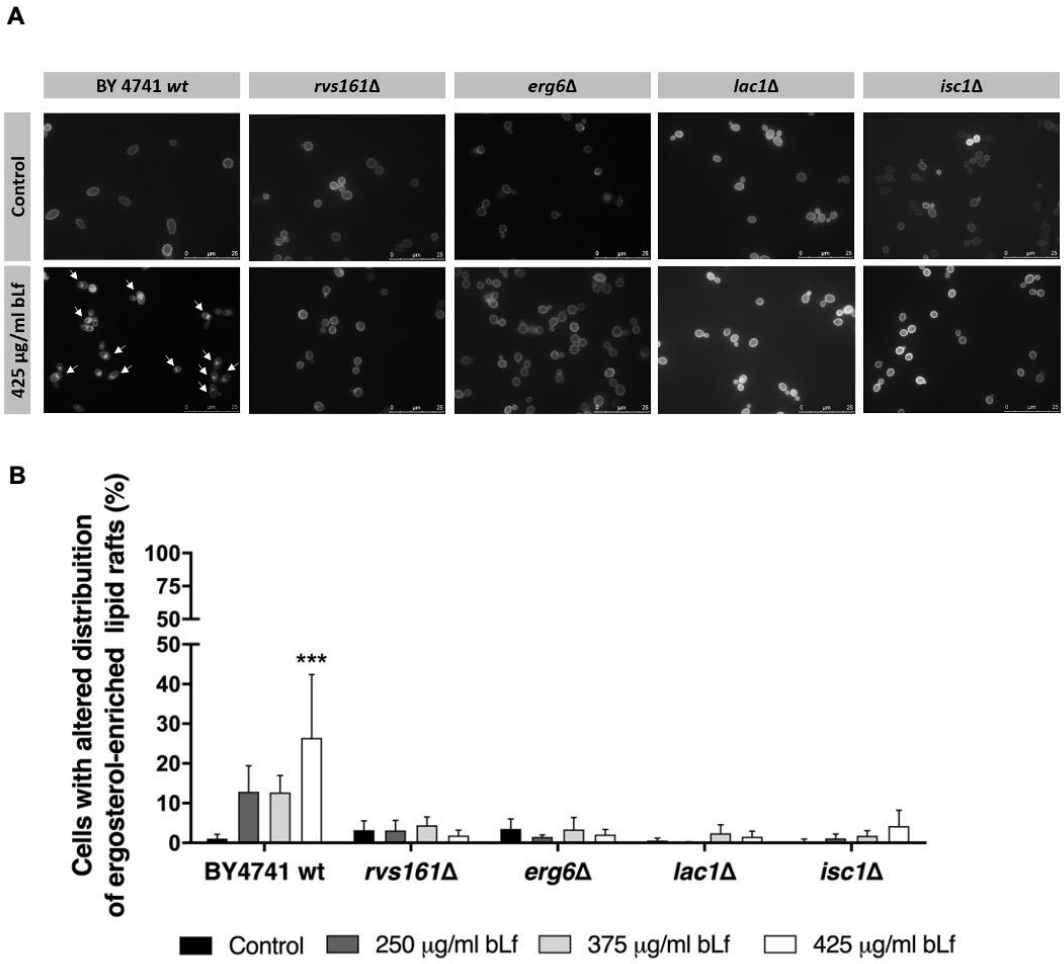

Figure 3.4: Effect of bLf on the localization of sterol-rich lipid rafts of wild type and *rvs161*Δ, *erg6*Δ, *lac1*Δ and *isc1*Δ mutant strains. Cells were incubated in the absence or presence of increasing concentrations of bLf (250-425 µg/ml) for 90 min at 30˚C in Tris-HCl 10 mM, pH 7.4 buffer. **(A)** For lipid rafts visualization, cells were stained in the dark with 0.1 mg/ml filipin

immediately before visualization under the microscope. Representative fluorescence microscopy images of each condition are shown. Although *erg6*Δ cells do not synthetize ergosterol, they are still labelled with filipin as previously reported [31], because it also binds sterol intermediates. **(B)** Quantification of the percentage of cells with altered lipid rafts distribution. At least 300 cells per condition of three independent experiments were counted. *** P<0.001 in comparison with the control of each strain.

3.3.4 Inhibition of Pma1p proton pumping and hydrolytic activities by bLf is prevented in *rvs161*Δ, *erg6*Δ, *lac1*Δ and *isc1*Δ mutants

We next sought to test the hypothesis that the higher resistance of the mutants is due to the lack of sensitivity of their Pma1p to bLf inhibition. As shown in Figure 3.5A, the Pma1p proton pumping activity of wild type cells was inhibited by bLf in a time- and concentration-dependent manner, much like previously observed in the pathogenic yeast *C. albicans* [20]. Diethylstilbestrol (DES) was used as a positive control of Pma1p inhibition [20].

When wild type cells were incubated with fluorescein-5-isothiocyanate (FITC)-labelled bLf, a punctuated pattern was observed at the plasma membrane (Figure 3.5B), suggesting that bLf binds to Pma1p, as further confirmed by immunoprecipitation (Figure 3.5F). Contrarily to the result obtained in the wild type cells, bLf failed to inhibit Pma1p proton pumping activity of the mutant strains *rvs161*Δ, *erg6*Δ, *lac1*Δ and *isc1*Δ, as indicated by the unperturbed extracellular acidification rates (Figure 3.5C). Accordingly, when the hydrolytic activity of Pma1p was measured, the inhibitory effect of bLf over Pi release was much less pronounced in plasma membrane fractions isolated from the mutant strains than from wild type cells (Figure 3.5D). In agreement, incubation of intact cells with bLf led to an increase in intracellular accumulation of ATP in the wild type strain but not in the mutant strains (Figure 3.5E). Immunoprecipitation experiments revealed that, although Pma1p activity is not affected by bLf in the mutant strains, bLf is still able to bind the proton pump (Figure 3.5F, G).

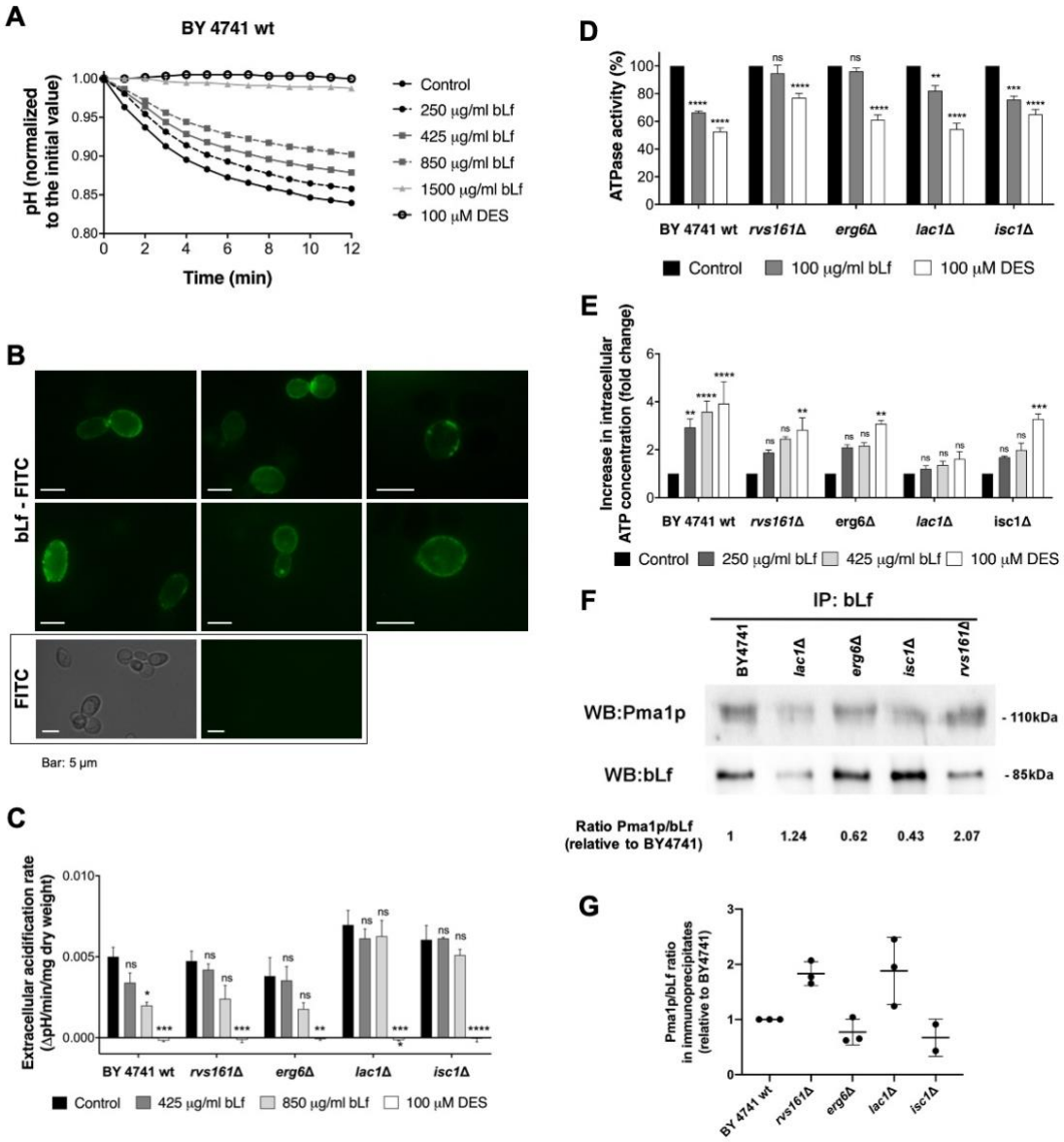

Figure 3.5: Effect of bLf on Pma1p activity of wild type and *rvs161*Δ, *erg6*Δ, *lac1*Δ and *isc1*Δ mutant strains. (A) Pma1p proton pumping activity was assessed by measuring glucose-induced external pH variation with a pH electrode. BY4741 wild type cells were incubated for 90 min in 10 mM Tris-HCl, pH 7.4 with 0-1500 µg/ml bLf or 100 µM DES. After pH stabilization, 2.5 mM glucose was added to induce proton extrusion by Pma1p and pH values were monitored up to 12 min. Data are pH values normalized to the value at timepoint zero min. **(B)** Localization of bLf-FITC (fluorescein-5-isothiocyanate) (500 µg/ml) in the wild type cells 75 min after incubation in the same conditions as in A. A control with only FITC was performed under the same conditions to ensure a specific labelling. Bar: 5 µm. **(C)** Same as in A but with wild type and indicated mutant strains treated with 0, 425 or 850 µg/ml bLf or 100 µM DES. Values are expressed as the pH variation per min per mg of dry weight of four independent experiments. **(D)** ATPase activity of isolated plasma membranes of the indicated strains expressed as percentage in comparison with the control of each strain of three independent experiments. Membranes were treated for 15 min in the absence or in the presence of 100 µg/ml bLf or 100 µM DES in 10 mM Tris-HCl, pH 7.4 buffer supplemented with 0.2 mM $(NH_4)_2MoO_4$, 5 mM NaN_3, and 50 mM KNO_3 to inhibit acid phosphatase, mitochondrial and vacuolar ATPases, respectively. **(E)** Measurement of intracellular ATP levels of cells incubated for 90 min with 0, 250 or 425 µg/ml bLf or 100

μM DES. Values represent the increase in ATP level expressed in fold change in comparison with the control of each strain of three independent experiments. ns, non-significant; *, **, ***, ****, P<0.05, 0.01, 0.001, 0.0001, respectively, in comparison with the control of each strain. **(F)** Representative western blot of the immunoprecipitation between bLf and Pma1p in bLf-treated wild type and mutant strains. **(G)** Quantification of Pma1p/bLf ratio in relation to the wild type strain in the immunoprecipitates of three independent experiments. Values represent the mean of three independent experiments normalized to the wild type strain.

To determine whether these phenotypes could be related to intrinsic differences in Pma1p activity/localization in the mutant strains under study, all strains were transformed with a pRS316 Pma1p-GFP plasmid and stained with filipin to visualize lipid rafts. Fluorescence microscopy showed that Pma1p-GFP co-localizes at the plasma membrane with lipid rafts in all strains (Figure 3.6A). Additionally, immunodetection of Pma1p by western blot demonstrated that the expression levels of this proton pump are similar in all strains (Figure 3.6B, C). Moreover, Pma1p activity of the mutant strains, expressed by the extracellular acidification rate, is similar to the wild type thus demonstrating that Pma1p is functional (Figure 3.6D).

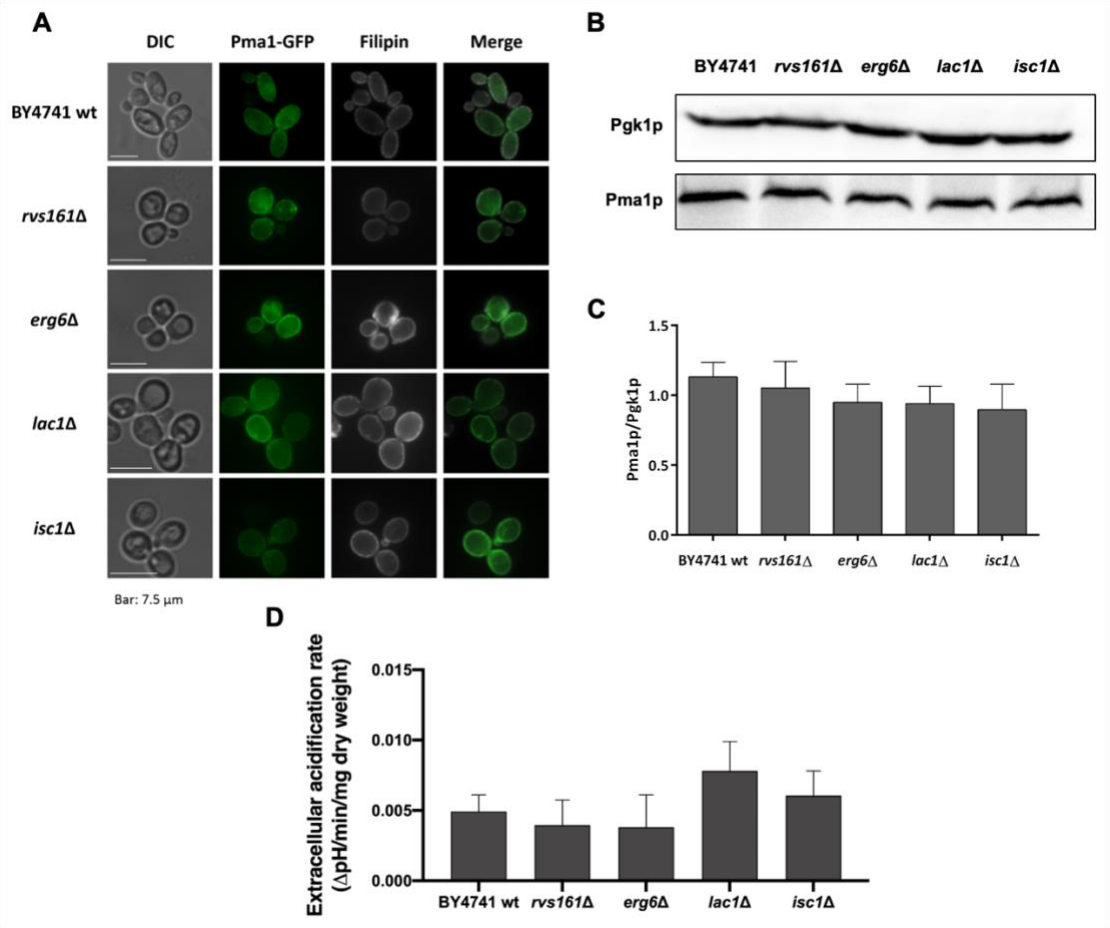

Figure 3.6: Pma1p localization, expression levels and proton pumping activity of wild type and *rvs161*Δ, *erg6*Δ, *lac1*Δ and *isc1*Δ mutant strains. (A) Cells transformed with pRS316 Pma1-GFP plasmid were stained with 0.1 mg/ml filipin and visualized

under a fluorescence microscope with green (Pma1-GFP) and blue (filipin) channels. DIC images are also shown and images are representative of each condition. Bar: 7.5 μm. **(B)** Representative western blot image of endogenous Pma1p expression levels in each strain. Pgk1p was used as loading control. **(C)** Quantification of Pma1p expression levels normalized to Pgk1p levels. Values represent the mean of three independent experiments. **(D)** Pma1p proton pumping activity was assessed by measuring glucose-induced external pH variation using a pH electrode. After pH stabilization, 2.5 mM glucose was added to induce proton extrusion by Pma1p and pH values were monitored up to 12 min. Values are expressed as the mean pH variation per min per mg of dry weight of four independent experiments.

3.3.5 bLf-induced vacuolar pH perturbations are prevented in *rvs161Δ*, *erg6Δ*, *lac1Δ* and *isc1Δ* mutants

Given that bLf inhibits Pma1p activity, likely perturbing the intracellular pH homeostasis, we sought to test its effect on the vacuolar pH. The pH-sensitive probe 5-(and-6)-carboxy-2,7-dichlorofluorescein diacetate (carboxy-DCFDA) is cleaved by intracellular esterases, and the unsterified pH-sensitive form (CDCF) accumulates in the yeast vacuole exhibiting higher fluorescence at higher pH values [27,32]. Results showed that when wild type yeast cells were labelled with this pH-sensitive probe, a higher fluorescence signal was observed in bLf-treated than in untreated cells by both fluorescence microscopy (Figure 3.7A, white arrows) and flow cytometry (Figure 3.7B). On contrary, bLf did not induce vacuolar alkalinisation in the mutant cells (Figure 3.7B). Following our previous reports showing that bLf targets and inhibits V-ATPase activity in cancer cells [26,33], the present results suggest that V-ATPase can be inhibited by bLf in wild type yeast cells but not in mutant cells. Accordingly, results depicted in Figure 3.7C showed for the first time that bLf inhibits the yeast V-ATPase proton pumping activity in a concentration-dependent manner in purified vacuolar fractions isolated from the wild type strain.

3.3.6 Disruption of Pma1p-lipid rafts association induced by Pma1p point mutations or *AST1* deletion renders yeast cells resistant to bLf

To get further insights on the role of Pma1p localization at the lipid rafts for bLf-induced cytotoxicity, we next explored the effect of bLf on a strain harbouring Pma1p point mutations that alter its localization and association with lipid rafts. Pma1-10 (XGY32 strain) harbours the A165G and V197I mutations, both at the first cytoplasmic loop between transmembrane segments 2 and 3 of Pma1p. In this mutant strain, at the restrictive temperature of 37 °C, newly synthesized Pma1-10 fails to associate with the plasma membrane lipid rafts (Triton-insoluble fraction) and is delivered to the vacuole for degradation [3]. Results from cell survival assays showed that cells expressing Pma1-10 are more resistant to 75 μg/ml bLf at

both 30 °C and 37 °C than the L3852 wild type strain, but the difference is more evident at 37 °C (Figure 3.8A). In this experiment, a lower bLf concentration was used because the wild type strain is more sensitive to bLf than the BY4741 strain.

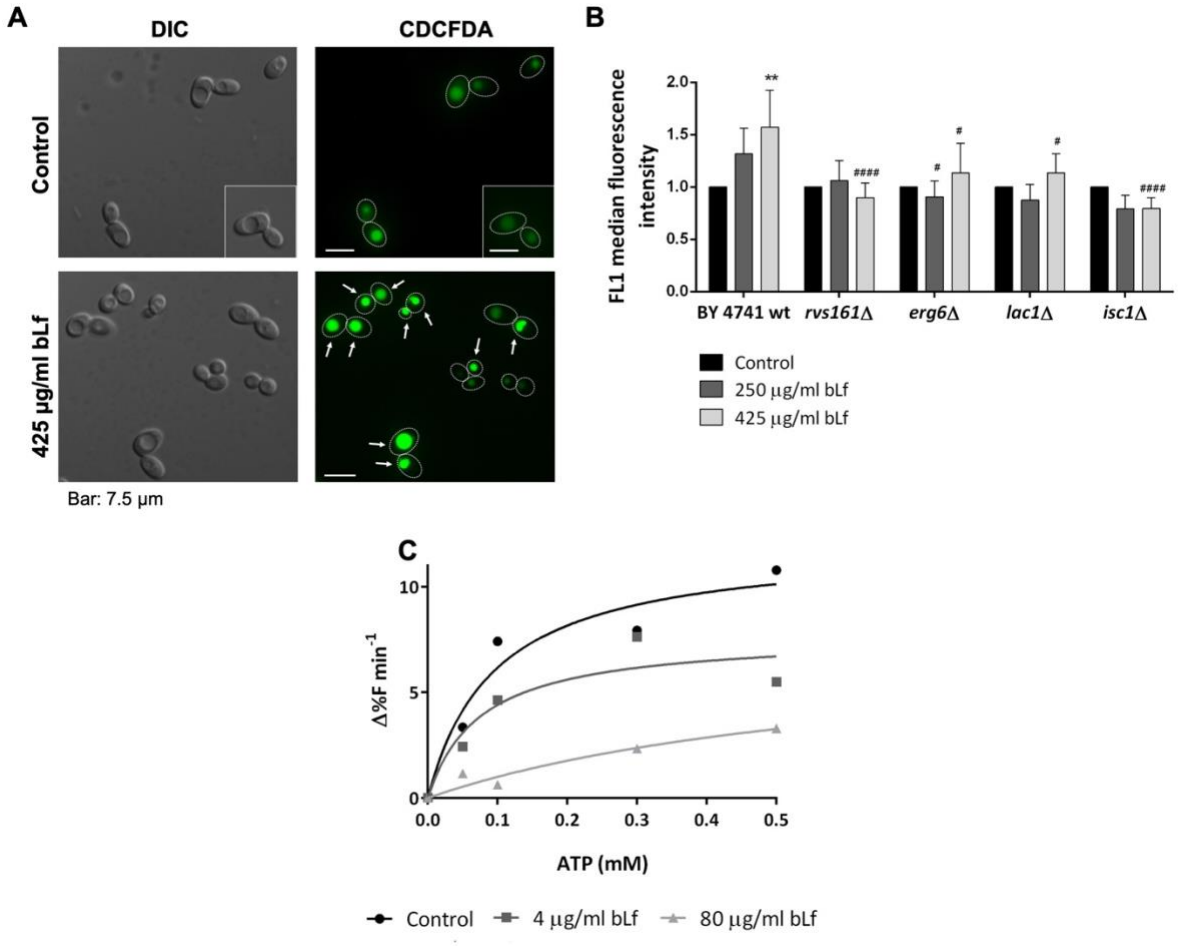

Figure 3.7: Effect of bLf on V-ATPase and vacuolar pH. (A) Representative fluorescence microscopy images of BY4741 wild type cells incubated in the absence (control) or presence of 425 µg/ml bLf for 90 min at 30˚C in Tris-HCl 10 mM, pH 7.4 and then stained with carboxy-DCFDA. White arrows indicate cells with increased vacuolar fluorescence. Bar: 7.5 µm. **(B)** Quantification of the green median fluorescence intensity of BY4741 wild type and *rvs161*Δ, *erg6*Δ, *lac1*Δ and *isc1*Δ mutant strains treated in the same conditions without and with 250 or 425 µg/ml bLf. Values are median of three independent experiments normalized to T0 and control of each strain. ** P<0.01 in comparison with the control of each strain; #, #### P<0.05; 0.0001, respectively, in comparison with the same condition in the wild type strain. **(C)** Kinetics of ATP-dependent V-ATPase proton pumping activity of vacuoles isolated from the wild type BY 4741 strain before (control) and after addition of 4 and 80 µg/ml bLf. The continuous lines are derived by fitting the data points to a Michäelis–Menten kinetics. Vacuolar suspensions were previously stained with the pH-sensitive probe ACMA and analysed by spectrofluorimetry after addition of increasing concentrations of ATP.

Ast1p is a Pma1p-binding protein known to be involved in the delivery of Pma1p to the cell surface and in its association with lipid rafts. When multicopy *AST1* is expressed in mutated Pma1p cells, Pma1p is rerouted to the cell surface and associates with lipid rafts [4,34]. Results showed that deletion of the *AST1* gene renders cells more resistant to bLf, suggesting that its function in promoting the association of Pma1p with lipid rafts is critical for bLf cytotoxicity (Figure 3.8B). Accordingly, when multicopy *AST1* is expressed in this background, cells become sensitive to bLf again, thus demonstrating that the resistance is indeed related with *AST1* deletion, and not with other possible pleiotropic effects (Figure 3.8B). When Pma1p-GFP was expressed in *ast1*Δ cells, about 30% of the cells exhibited bright intracellular spots of Pma1p-GFP (Figure 3.8C, D), indicating an abnormal Pma1p localization in this strain. In agreement with the previous results, absence of Ast1p causes an abnormal intracellular localization of both sterol-rich lipid rafts and Pma1p-GFP (Figure 3.8E), which is consistent with the role of Ast1p in Pma1p-lipid rafts association.

3.4 Discussion

It has been reported that the milk-derived protein Lf displays antifungal activity against different yeast species [35], including *C. albicans* [36] and *S. cerevisiae* [16], as well as against different fungi isolated from plants and soils, including *Aspergillus niger* and *Rhizoctonia solani* [37]. Given its potential to become a wide-spectrum antifungal, herein we sought to deepen our understanding of the mechanisms underlying Lf cytotoxic activity using *S. cerevisiae* as a model. As previously shown in *C. albicans* [20,38], we found that bLf binds to Pma1p and inhibits its proton pumping and hydrolytic activities associated with an increase in intracellular ATP levels. Because lipid rafts are important for cell surface sorting, stability and oligomerization of Pma1p [4], we investigated the effect of bLf in these sterol- and sphingolipid-rich membrane microdomains. Our data revealed a novel mode of action of bLf against yeast by inducing intracellular accumulation of ergosterol and perturbing sterol-rich lipid rafts. This mechanism of action is shared with edelfosine, a compound that, like lactoferrin, exhibits anticancer activity [26,33,39] and a marked activity against yeast [16,39]. Indeed, it was found that edelfosine displaces sterols from the plasma membrane and induces loss of Pma1p from lipid rafts [39]. However, the bLf effect on lipid rafts differs from MβCD, which is known to disrupt lipid rafts by depleting ergosterol from the plasma membrane [28]. Actually, while both compounds led to intracellular accumulation of ergosterol, in contrast to MβCD, bLf-treated cells still preserved ergosterol staining at the plasma membrane, as visualized by the intracellular and plasma membrane filipin staining. This suggests that

bLf impairs the sorting of newly synthetized ergosterol to the lipid rafts of the cell surface, rather than sequestering it from the plasma membrane.

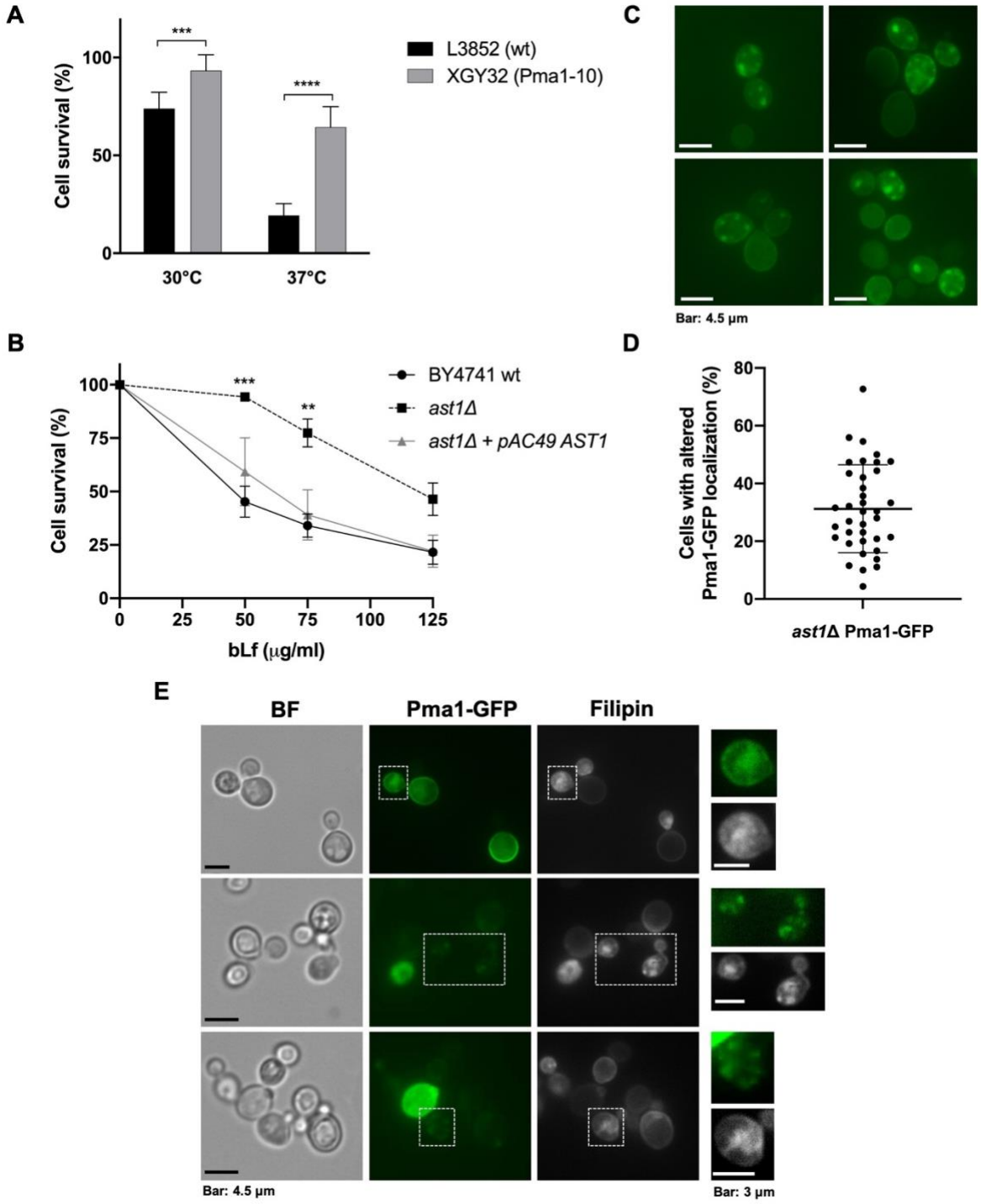

Figure 3.8: Effect of bLf on cell survival of strains with defective association of Pma1p with lipid rafts or lacking Ast1p. (A) L3852 wild type and Pma1-10 (XGY32) expressing cells were cultivated at 30 °C until OD640 0.7 and then transferred to 37 °C in the absence or presence of 75 µg/ml bLf in 10 mM Tris HCl, pH 7.4, for 90 min. Control cells were kept at 30 °C. Values are percentage of cell survival assuming the control without bLf as 100% cell survival. **(B)** BY4741 wild type, *ast1*Δ and

*ast1*Δ+pAC49 AST1 strains were treated with 50 to 125 µg/ml bLf in 10 mM Tris HCl buffer pH 7.4 for 90 min at 30 °C. Values are percentages normalized to the control without bLf of each strain (considered as 100% cell survival). **, *** P<0.01, 0.001, respectively, in comparison with the wild type strain in the same condition. **(C)** *ast1*Δ cells expressing pRS316 Pma1p-GFP were grown until exponential phase and observed under the fluorescence microscope for observation of Pma1p localization. **(D)** Percentage of *ast1*Δ cells with altered Pma1p localization. The individual percentual values of each observed field as well as the mean and standard deviation are presented. More than 800 cells were counted. **(E)** *ast1*Δ cells expressing pRS316 Pma1-GFP were grown in the same conditions as in C and D. For lipid rafts visualization, cells were stained in the dark with 0.1 mg/ml filipin immediately before visualization under the microscope. Right images are the zoom in with higher exposure of the indicated sections of the whole images. Bars: 4.5 µm or 3 µm, as indicated in the figure.

In order to gain insights on the importance of lipid rafts integrity for bLf antifungal activity, a comprehensive characterization of the phenotype of mutant strains lacking the lipid rafts-associated proteins Rvs161p, Erg6p, Lac1p or Isc1p was performed. Ergosterol plays crucial roles in bulk membrane functions and in lipid rafts formation as it is essential for membrane fluidity/rigidity, permeability and for protein sorting along the secretory pathway [40,41]. In *erg6*Δ mutants, the accumulated ergosterol precursors do not allow a tight packing of the lipid bilayer, specifically the lipid acyl chains, and are suggested to create voids in the plasma membrane [40]. Accumulation of ergosterol intermediates can also alter lipid rafts structures, promote missorting of different plasma membrane proteins [42] and modify membrane permeability and fluidity [43]. Sphingolipids are a multifunctional class of lipids critical for lipid rafts formation and for many other functions, including the transport of glycosylphosphatidylinositol (GPI)-anchored proteins out of the endoplasmic reticulum, protein sorting and signalling [44]. In yeast, ceramides can be produced either *de novo* through Lag1p/Lac1p/Lip1p, or from complex sphingolipids hydrolysis through Isc1p [14]. *LAC1* and *LAG1* are highly homologous and have a similar function; along with a small accessory subunit Lip1p, Lac1p and Lag1p are demonstrated constituents of the ceramide synthase complex [45]. Deletion of both genes influences the levels of ceramides and long chain bases [45,46]. Yeast cells lacking Lac1p show an abnormal low amount of GPI-anchored proteins and impaired capacity to link the ceramide moiety into GPI anchors, which are very important for the association of different proteins to lipid rafts [46,47]. In turn, *isc1*Δ cells contain higher amount of complex sphingolipids [48], decreased levels of mitochondrial ceramide and mitochondrial function defects [49]. Another mutant studied herein lacks the Rvs161 protein, a lipid rafts component involved in cytoskeleton organization, cell polarity, endocytosis and in vesicle trafficking [12,50]. Its association with the lipid rafts is thought to be mediated by a putative raft-bound protein, as it has no GPI signal anchor or transmembrane domain [12]. We found that cells lacking Rvs161p, Lac1p, Isc1p and Erg6p are more resistant to bLf-induced cell death than the wild type strain, and exhibited a

lower inhibition of the extracellular acidification rate and Pma1p hydrolytic activity, as well as no enhancement of the intracellular ATP level. Moreover, while 500 µg/ml bLf induced a drastic loss of cell viability in the *erg6*Δ and *rvs161*Δ mutants similarly to the wild type, their metabolic activity was not affected in contrast to the wild type. Indeed, these two mutant strains, and *isc1*Δ and *lac1*Δ were still able to process the FUN-1 dye and form CIVS when incubated with 425 µg/ml bLf, which results in a similar percentage of cell viability as 500 µg/ml bLf in the wild type (Figure 3.2A). These results suggest that normal levels of ergosterol, sphingolipids and lipid rafts-associated proteins determine the bLf killing activity against yeast but not its effect on metabolic activity. However, since c.f.u. counting and FUN-1 staining are evaluated in a different temporal scale (48 h vs 30 min after bLf treatment), we cannot discard that metabolic activity is also affected in the mutants.

We hypothesized that changes in Pma1p localization, expression and activity in the mutant strains could explain the reduced cytotoxic effects of bLf in those strains. However, this hypothesis was discarded as Pma1p localization and levels of expression and activity of the mutants were identical to those of the wild type strain. The results regarding the *erg6*Δ mutant are in agreement with previous works showing that Pma1p localization at the plasma membrane was intact in different *erg* mutants [51,52], and that the extracellular medium acidification kinetics in the *erg24*Δ mutant was identical to the wild type strain [53]. Moreover, it was shown that deletion of *ISC1* in *Cryptococcus neoformans* did not affect the synthesis and transport of Pma1p [54], which is in agreement with our data. Unexpectedly, the lack of inhibition of Pma1p activity by bLf was not associated with lack of Pma1p-bLf binding since this was not abrogated in the mutant strains. In addition, bLf was unable to perturb the sterol-rich lipid rafts distribution in the mutant strains, indicating that this bLf-induced alteration is also dependent on the normal composition of lipid rafts. Altogether this suggests that the perturbation of lipid rafts is intimately related with Pma1p inhibition, and both effects seem to depend on each other.

Evidence supporting the hypothesis that bLf requires the integrity of Pma1p-lipid rafts association to inhibit Pma1p and induce yeast cell death was provided by the experiments with the strain harbouring Pma1p point mutations and with the *ast1*Δ strain. The Pma1-10 mutation renders a defective association of newly synthetized Pma1p with the lipid rafts at 37°C [3], temperature at which the strain became much more resistant to bLf than the wild type strain. Curiously, at the permissive temperature, where Pma1-10 is associated with the lipid rafts, the resistance of the mutant cells to bLf was already slightly higher than the wild type cells. In addition, deletion of the *AST1* gene, which encodes a protein involved in Pma1p association with the lipid rafts [4], rendered yeast cells resistant to bLf, and its overexpression in the deletion background restored sensitivity to bLf. The Pma1p and lipid rafts distribution are affected

in the *ast1*Δ strain, further supporting that the alteration of the Pma1p-lipid rafts association underlies the bLf-resistance phenotype of this strain.

Besides being involved in the association of Pma1p with lipid rafts, Ast1p was also demonstrated to induce Pma1p oligomerization, which is an early event during the surface delivery of Pma1p [4]. Pma1p forms large oligomeric complexes of about 1 MDa [5] and this process seems to be affected by alterations in sphingolipids synthesis. Indeed, deletion of *ISC1* in *C. neoformans* perturbed Pma1p oligomerization, which was restored after supplementation with phytoceramide [54]. Depletion of sphingolipids either by using the *lcb1-100* strain, which is unable to synthetize sphingolipids, or myriocin, an inhibitor of serine palmitoyltransferase activity, inhibits the oligomerization of newly synthetized Pma1p. Addition of the ceramide precursor phytosphingosine restored Pma1p oligomerization, reinforcing the importance of sphingolipid levels for Pma1p oligomerization [5]. Accordingly, the requirement of sphingolipids for Pma1p oligomerization at the ER, plasma membrane targeting, stability and acquisition of detergent resistance of Pma1p has been reported by different authors [6,51]. In agreement with these data, herein we found that exogenous addition of C2-ceramide reduces the *lac1*Δ mutant strain survival to bLf, likely by counteracting defects in Pma1p oligomerization as a result of sphingolipids composition reestablishment (Figure A1, Appendix). Hence, the most likely explanation for the resistance phenotypes of the mutants is that alterations in the lipidic content of cells, namely unbalanced ceramide/complex sphingolipids ratio, accumulation of ergosterol precursors, or the abnormal production of GPI anchors modifies the composition of plasma membrane lipid rafts, affecting Pma1p conformation and oligomerization, and consequently its inhibition by bLf. Accordingly, it has been suggested that perturbation of the lipid rafts functional organization creates a different biophysical environment that may change the conformation of raft-localized proteins, including Pma1p [55].

Another novelty of the present study regards the inhibition of V-ATPase by bLf. The observed inhibition of this proton pump in purified vacuoles from the wild type strain correlated well with the observed increase of the vacuolar pH in whole cells in response to bLf. As for the strains with altered lipid rafts composition, the vacuolar pH was not affected most likely due to the inability of bLf to inhibit Pma1p and cause intracellular acidification. Nonetheless, a possible alteration of the vacuolar membrane lipid composition may also account for the apparent incapacity of bLf to inhibit V-ATPase in these strains. These results are in accordance with our previous data showing that bLf increases the lysosomal pH of highly metastatic cancer cells [33] and inhibits the activity of the V-ATPase that is targeted to the plasma membrane of highly metastatic cancer cells, as well as the activity V-ATPase in purified rat liver lysosomes [26].

3.5 Conclusion

The results gathered in this study demonstrate that the mode of action underlying bLf antifungal activity lies on the perturbation of lipid rafts organization and inhibition of Pma1p activity, and likely of V-ATPase activity, as suggested by our data with whole cells and isolated vacuoles (Figure 3.9). Moreover, the composition of the plasma membrane lipid rafts, Pma1p oligomerization status, as well as the integrity of Ast1p-mediated lipid rafts-Pma1p association seems to be crucial for the interaction of bLf with Pma1p, and for its killing activity against *S. cerevisiae*. We propose that this novel bLf lipid rafts disrupting activity may be explored towards antifungal therapy alone or in combination with classical antifungals.

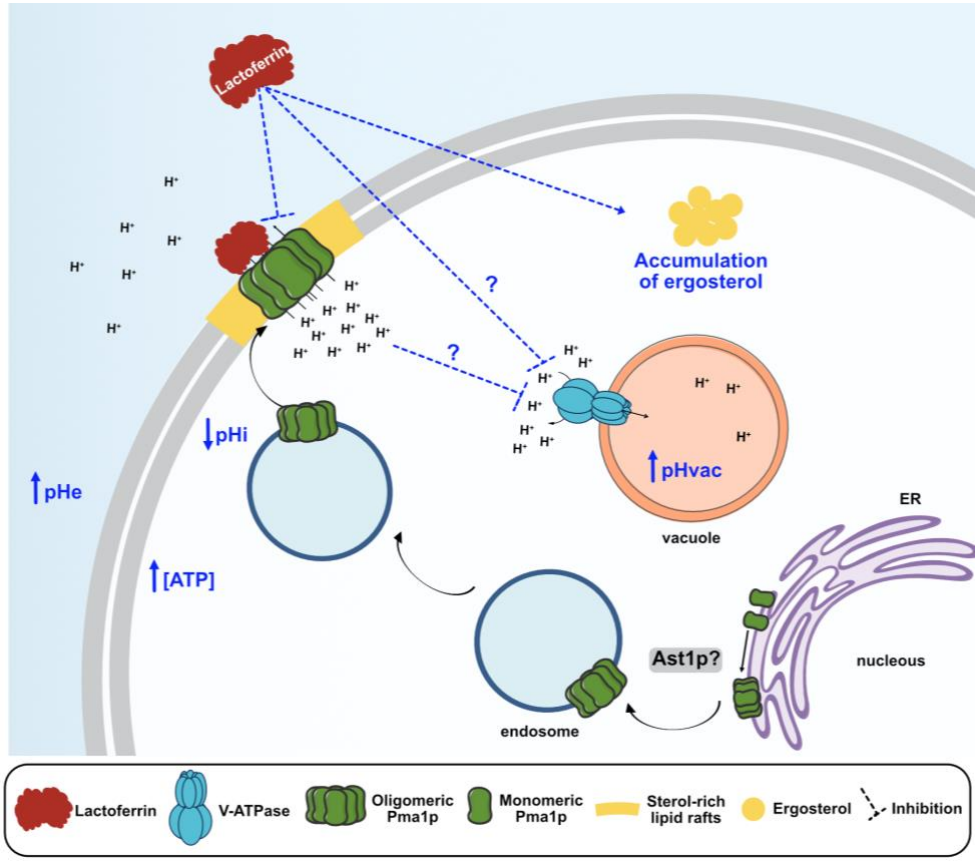

Figure 3.9: Working model of the mode of action underlying bovine lactoferrin antifungal activity. Exposure of yeast cells to bLf leads to inhibition of Pma1p, associated with an inhibition of the extracellular acidification rate and consequent enhancement of intracellular proton accumulation and ATP concentration. In addition, bLf may directly inhibit V-ATPase as observed with purified vacuoles or indirectly through intracellular acidification [56], leading to vacuolar alkalinization. Moreover, bLf binds to Pma1p and induces intracellular accumulation of ergosterol disrupting sterol-rich lipid rafts. Oligomerization of Pma1p is suggested to occur at the ER [57] and the involvement of Ast1p in the process seems to be an early event during plasma membrane delivery [4]. This evidence, together with our data, led to the hypothesis that Pma1p oligomerization is important for bLf-mediated Pma1p inhibition. pHe, extracellular pH; pHi, intracellular pH; pHvac, vacuolar pH; ER, endoplasmic reticulum.

References

1. Bagnat M, Keränen S, Shevchenko A, Shevchenko A, Simons K. Lipid rafts function in biosynthetic delivery of proteins to the cell surface in yeast. Proc Natl Acad Sci U S A. 2000;97: 3254–3259. doi:10.1073/pnas.97.7.3254
2. Mollinedo F. Lipid raft involvement in yeast cell growth and death. Front Oncol. 2012;2: 1–15. doi:10.3389/fonc.2012.00140
3. Gong X, Chang A. A mutant plasma membrane ATPase, Pma1-10, is defective in stability at the yeast cell surface. Proc Natl Acad Sci. 2001;98: 9104–9109. doi:10.1073/pnas.161282998
4. Bagnat M, Chang A, Simons K. Plasma membrane proton ATPase Pma1p requires raft association for surface delivery in yeast. Mol Biol Cell. 2001;12: 4129–4138. doi:10.1091/mbc.12.12.4129
5. Lee MCS, Hamamoto S, Schekman R. Ceramide biosynthesis is required for the formation of the oligomeric H+-ATPase Pma1p in the yeast endoplasmic reticulum. J Biol Chem. 2002;277: 22395–22401. doi:10.1074/jbc.M200450200
6. Wang Q, Chang A. Sphingoid base synthesis is required for oligomerization and cell surface stability of the yeast plasma membrane ATPase, Pma1. Proc Natl Acad Sci U S A. 2002;99: 12853–12858. doi:10.1073/pnas.202115499
7. Kodedová M, Valachovič M, Csáky Z, Sychrová H. Variations in yeast plasma-membrane lipid composition affect killing activity of three families of insect antifungal peptides. Cell Microbiol. 2019;21. doi:10.1111/cmi.13093
8. Rautenbach M, Troskie AM, Vosloo JA. Antifungal peptides: To be or not to be membrane active. Biochimie. 2016;130: 132–145. doi:10.1016/j.biochi.2016.05.013
9. Pierce A, Colavizza D, Benaissa M, Maes P, Tartar A, Montreuil J, et al. Molecular cloning and sequence analysis of bovine lactotransferrin. Eur J Biochem. 1991;196: 177–84. doi:10.1111/j.1432-1033.1991.tb15801.x
10. Steijns JM, van Hooijdonk ACM. Occurrence, structure, biochemical properties and technological characteristics of lactoferrin. Br J Nutr. 2000;84: 11–17. doi:10.1017/s0007114500002191
11. Kuipers ME, De Vries HG, Eikelboom MC, Meijer DKF, Swart PJ. Synergistic fungistatic effects of lactoferrin in combination with antifungal drugs against clinical *Candida* isolates. Antimicrob Agents Chemother. 1999;43: 2635–2641. doi:10.1128/aac.43.11.2635
12. Balguerie A, Bagnat M, Bonneu M, Aigle M, Breton AM. Rvs161p and sphingolipids are required for actin repolarization following salt stress. Eukaryot Cell. 2002;1: 1021–1031. doi:10.1128/EC.1.6.1021-1031.2002
13. Munn AL, Heese-Peck A, Stevenson BJ, Pichler H, Riezman H. Specific sterols required for the internalization step of endocytosis in yeast. Mol Biol Cell. 1999;10: 3943–3957. doi:10.1091/mbc.10.11.3943
14. Cowart L, Obeid LM. Yeast sphingolipids: recent developments in understanding biosynthesis,. Biochim Biophys Acta. 2007;1771: 233–245. doi:10.1016/j.dcn.2011.01.002.The
15. Gietz RD, Woods RA. Yeast Transformation by the LiAc/SS Carrier DNA/PEG Method. Methods in Molecular Biology - Yeast Protocols: Second Edition. 2006. pp 107–120. doi: 10.1385/1-59259-958-3:107

16. Acosta-Zaldívar M, Andrés MT, Rego A, Pereira CS, Fierro JF, Côrte-Real M. Human lactoferrin triggers a mitochondrial- and caspase-dependent regulated cell death in Saccharomyces cerevisiae. Apoptosis. 2016;21: 163–173. doi:10.1007/s10495-015-1199-9

17. Maxfield FR, Wüstner D. Analysis of cholesterol trafficking with fluorescent probes. Methods Cell Biol. 2012;108: 367–393. doi:10.1016/B978-0-12-386487-1.00017-1

18. Pacheco A, Azevedo F, Rego A, Santos J, Chaves SR, Côrte-Real M, et al. C2-phytoceramide perturbs lipid rafts and cell integrity in *Saccharomyces cerevisiae* in a sterol-dependent manner. PLoS One. 2013;8: 1–12. doi:10.1371/journal.pone.0074240

19. Millard P, Roth B, Thi H-G, Yue S, Haugland R. Development of the FUN-1 family of fluorescent probes for vacuole labeling and viability testing of yeasts. Appl Environ Microbiol. 1997;63: 2897–2905.

20. Andrés MT, Acosta-Zaldívar M, Fierro JF. Antifungal mechanism of action of lactoferrin: Identification of H+-ATPase (P3A-type) as a new apoptotic-cell membrane receptor. Antimicrob Agents Chemother. 2016;60: 4206–4216. doi:10.1128/AAC.03130-15

21. Bradford MM. A rapid and sensitive method for the quantitation of microgram quantities of protein utilizing the principle of protein-dye binding. Anal Biochem. 1976;72: 248–254.

22. Monk BC, Kurtz MB, Marrinan JA, Perlin DS. Cloning and characterization of the plasma membrane H+-ATPase from Candida albicans. J Bacteriol. 1991;173: 6826–6836. doi:10.1128/jb.173.21.6826-6836.1991

23. Rodrigues JMP, Pereira CS, Fontes N, Gerós H, Côrte-Real M. Flow Cytometry and Fluorescence Microscopy as Tools from Yeast and Plant Cells. Plant Vacuolar Traffick Methods Protoc. 2018;1789: 101–115. doi: 10.1007/978-1-4939-7856-4_8

24. Rodrigues J, Silva RD, Noronha H, Pedras A, Gerós H, Côrte-Real M. Flow cytometry as a novel tool for structural and functional characterization of isolated yeast vacuoles. Microbiology. 2013;159: 848–56. doi:10.1099/mic.0.062570-0

25. Lowry OH, Rosebrough NJ, Farr L, Randall RJ. Protein measurement with the folin phenol reagent. J Biol Chem. 1951;193.

26. Pereira CS, Guedes JP, Gonçalves M, Loureiro L, Castro L, Gerós H, et al. Lactoferrin selectively triggers apoptosis in highly metastatic breast cancer cells through inhibition of plasmalemmal V-H+-ATPase. Oncotarget. 2016;7: 62144–62158. doi:10.18632/oncotarget.11394

27. Teixeira MC, Raposo LR, Mira NP, Lourenço AB, Sá-Correia I. Genome-wide identification of *Saccharomyces cerevisiae* genes required for maximal tolerance to ethanol. Appl Environ Microbiol. 2009;75: 5761–5772. doi:10.1128/AEM.00845-09

28. Siafakas AR, Wright LC, Sorrell TC, Djordjevic JT. Lipid rafts in *Cryptococcus neoformans* concentrate the virulence determinants phospholipase B1 and Cu/Zn superoxide dismutase. Eukaryot Cell. 2006;5: 488–498. doi:10.1128/EC.5.3.488-498.2006

29. Eggleston MD, Marshall PA. *Saccharomyces cerevisiae* samples stained with FUN-1 dye can be stored at -20°C for later observation. J Microsc. 2007;225: 100–103. doi:10.1111/j.1365-2818.2007.01720.x

30. Prudêncio C, Sansonetty F, Côrte-Real M. Flow cytometric assessment of cell structural and functional changes induced by acetic acid in the yeasts *Zygosaccharomyces bailii* and *Saccharomyces cerevisiae*. Cytometry. 1998;31: 307–313. doi:10.1002/(SICI)1097-

0320(19980401)31:4<307::AID-CYTO11>3.0.CO;2-U

31. Grossmann G, Malinsky J, Stahlschmidt W, Loibl M, Weig-Meckl I, Frommer WB, et al. Plasma membrane microdomains regulate turnover of transport proteins in yeast. J Cell Biol. 2008;183: 1075–1088. doi:10.1083/jcb.200806035

32. Roberts C, Raymond C, Yamashiro C, Stevens TH. Methods for studying the yeast vacuole. Methods Enzymol. 1991;194: 644–661.

33. Guedes J, Pereira C, Rodrigues L, Côrte-real M. Bovine milk lactoferrin selectively kills highly metastatic prostate cancer PC-3 and osteosarcoma MG-63 cells *in vitro*. Front Oncol. 2018;8: 1–12. doi:10.3389/fonc.2018.00200

34. Chang A, Fink GR. Targeting of the yeast plasma membrane [H+]ATPase: A novel gene AST1 prevents mislocalization of mutant ATPase to the vacuole. J Cell Biol. 1995;128: 39–49. doi:10.1083/jcb.128.1.39

35. Fernandes KE, Weeks K, Carter DA. Lactoferrin is broadly active against yeasts and highly synergistic with amphotericin B. Antimicrob Agents Chemother. 2020;64: 1–22. doi:10.1128/AAC.02284-19

36. Andrés MT, Viejo-Díaz M, Fierro JF. Human lactoferrin induces apoptosis-like cell death in *Candida albicans*: critical role of K+-channel-mediated K+ efflux. Antimicrob Agents Chemother. 2008;52: 4081–8. doi:10.1128/AAC.01597-07

37. Lahoz E, Pisacane A, Iannaccone M, Palumbo D, Capparelli R. Fungistatic activity of iron-free bovin lactoferrin against several fungal plant pathogens and antagonists. Nat Prod Res. 2008;22: 955–961. doi:10.1080/14786410701650253

38. Andrés MT, Acosta-Zaldívar M, González-Seisdedos J, Fierro JF. Cytosolic acidification is the first transduction signal of lactoferrin-induced regulated cell death pathway. Int J Mol Sci. 2019;20: 5838. doi:10.3390/ijms20235838

39. Zaremberg V, Gajate C, Cacharro LM, Mollinedo F, McMaster CR. Cytotoxicity of an anti-cancer lysophospholipid through selective modification of lipid raft composition. J Biol Chem. 2005;280: 38047–38058. doi:10.1074/jbc.M502849200

40. Abe F, Hiraki T. Mechanistic role of ergosterol in membrane rigidity and cycloheximide resistance in *Saccharomyces cerevisiae*. Biochim Biophys Acta - Biomembr. 2009;1788: 743–752. doi:10.1016/j.bbamem.2008.12.002

41. Umebayashi K, Nakano A. Ergosterol is required for targeting of tryptophan permease to the yeast plasma membrane. J Cell Biol. 2003;161: 1117–1131. doi:10.1083/jcb.200303088

42. Daicho K, Makino N, Hiraki T, Ueno M, Uritani M, Abe F, et al. Sorting defects of the tryptophan permease Tat2 in an erg2 yeast mutant. FEMS Microbiol Lett. 2009;298: 218–227. doi:10.1111/j.1574-6968.2009.01722.x

43. Gaber RF, Copple DM, Kennedy BK, Vidal M, Bard M. The yeast gene *ERG6* is required for normal membrane function but is not essential for biosynthesis of the cell-cycle-sparking sterol. Mol Cell Biol. 1989;9: 3447–3456. doi:10.1128/MCB.9.8.3447

44. Martinez-Montanes F, Lone MA, Hsu FF, Schneiter R. Accumulation of long-chain bases in yeast promotes their conversion to a long-chain base vinyl ether. J Lipid Res. 2016;57: 2040–2050. doi:10.1080/00140139108967302

45. Schorling S, Vallée B, Barz WP, Riezman H, Oesterhelt D. Lag1p and Lac1p are essential for the

acyl-CoA–dependent ceramide synthase reaction in *Saccharomyces cerevisae*. Mol Biol Cell. 2001;12: 3417–3427. doi:10.1091/mbc.12.11.3417

46. Guillas I, Kirchman PA, Chuard R, Pfefferli M, Jiang JC, Jazwinski SM, et al. C26-CoA-dependent ceramide synthesis of *Saccharomyces cerevisiae* is operated by Lag1p and Lac1p. EMBO J. 2001;20: 2655–2665. doi:10.1093/emboj/20.11.2655

47. Kinoshita T, Fujita M. Biosynthesis of GPI-anchored proteins: special emphasis on GPI lipid remodeling. J Lipid Res. 2016;57: 6–24. doi:10.1194/jlr.R063313

48. Sawai H, Okamoto Y, Luberto C, Mao C, Bielawska A, Domae N, et al. Identification of *ISC1* (YER019w) as inositol phosphosphingolipid phospholipase C in *Saccharomyces cerevisiae*. J Biol Chem. 2000;275: 39793–39798. doi:10.1074/jbc.M007721200

49. Kitagaki H, Cowart LA, Matmati N, Vaena de Avalos S, Novgorodov SA, Zeidan YH, et al. Isc1 regulates sphingolipid metabolism in yeast mitochondria. Biochim Biophys Acta - Biomembr. 2007;1768: 2849–2861. doi:10.1016/j.bbamem.2007.07.019

50. Breton AM, Schaeffer J, Aigle M. The yeast Rvs161 and Rvs167 proteins are involved in secretory vesicles targeting the plasma membrane and in cell integrity. Yeast. 2001;18: 1053–1068. doi:10.1002/yea.755

51. Gaigg B, Timischl B, Corbino L, Schneiter R. Synthesis of sphingolipids with very long chain fatty acids but not ergosterol is required for routing of newly synthesized plasma membrane ATPase to the cell surface of yeast. J Biol Chem. 2005;280: 22515–22522. doi:10.1074/jbc.M413472200

52. Estrada AF, Muruganandam G, Prescianotto-Baschong C, Spang A. The ArfGAP2/3 Glo3 and ergosterol collaborate in transport of a subset of cargoes. Biol Open. 2015;4: 792–802. doi:10.1242/bio.011528

53. Zhang YQ, Gamarra S, Garcia-Effron G, Park S, Perlin DS, Rao R. Requirement for ergosterol in V-ATPase function underlies antifungal activity of azole drugs. PLoS Pathog. 2010;6: e1000939. doi:10.1371/journal.ppat.1000939

54. Farnoud AM, Mor V, Singh A, Del Poeta M. Inositol phosphosphingolipid phospholipase C1 regulates plasma membrane ATPase (Pma1) stability in *Cryptococcus neoformans*. FEBS Lett. 2014;588: 3932–8. doi:10.1016/j.febslet.2014.09.005

55. Pan J, Hu C, Yu JH. Lipid biosynthesis as an antifungal target. J Fungi. 2018;4: 1–13. doi:10.3390/jof4020050

56. Dechant R, Binda M, Lee SS, Pelet S, Winderickx J, Peter M. Cytosolic pH is a second messenger for glucose and regulates the PKA pathway through V-ATPase. EMBO J. 2010;29: 2515–2526. doi:10.1038/emboj.2010.138

57. Toulmay A, Schneiter R. Lipid-dependent surface transport of the proton pumping ATPase: A model to study plasma membrane biogenesis in yeast. Biochimie. 2007;89: 249–254. doi:10.1016/j.biochi.2006.07.020

CHAPTER 4

Molecular mechanisms underlying the anticancer activity of lactoferrin

This chapter is adapted from the following publication:

Cátia Santos-Pereira, Joana P. Guedes, Débora Ferreira, Lígia R. Rodrigues, Manuela Côrte-Real. **Lactoferrin disrupts cholesterol-rich lipid rafts of highly metastatic cancer cells inhibiting PI3K/AKT/mTOR pathway and glycolysis**. Under review in *Biochemical Pharmacology*

4.1 Background

The proton pump V-ATPase, a Lf target that is overexpressed and present at the plasma membrane of cancer cells with high metastatic potential, was shown to localize at the lipid rafts [1]. In line with the important roles of V-ATPase in cancer and tumor microenvironment [2], as well as with the close interdependence between this proton pump and lipid rafts (see Chapter 2.4.2 for detailed information), growing evidence suggests V-ATPase and lipid rafts as therapeutic targets [3]. Therefore, agents targeting these structures are considered promising therapeutic compounds against different types of cancer [4,5].

Our work on *Saccharomyces cerevisiae* presented in Chapter 3 demonstrated that the integrity of ergosterol-rich lipid rafts composition and of their association with the proton pump Pma1p are critical for the bLf fungicidal activity [6]. Given the well-established interplay between V-ATPase and lipid rafts, and also based on the fact that bLf inhibits this proton pump, we hypothesized that lipid rafts may be an important piece in the puzzling mechanisms underlying bLf selective anticancer activity against highly metastatic cancer cells. To test this hypothesis, in this chapter we used highly metastatic cancer cell lines derived from breast cancer (MDA-MB-231 and Hs 578T), prostate cancer (PC-3) and osteosarcoma (MG-63) that were previously demonstrated to exhibit V-ATPase at the plasma membrane [7–10] and to be sensitive to bLf [7,11]. The non-tumorigenic cell lines MCF-10-2A and BJ-5ta, and the lowly metastatic breast cancer cell line T-47D, which are resistant to bLf, were used as controls. MCF-10-2A and T-47D exhibit only intracellular V-ATPase [7,11].

4.2 Materials and Methods

4.2.1 Lactoferrin and reagents

Bovine lactoferrin was acquired from DMV (Veghel, The Netherlands). The protein is approximately 80% pure, with 3.5% moisture, and 21% iron-saturated, according to the manufacture. A stock solution of 3 mM was prepared in phosphate buffered saline (PBS 10×; 1.37 M NaCl, 2.7 mM KCl, 10 mM Na_2HPO_4, 1.8 mM KH_2PO_4, pH 7.4) and sterilized by filtration prior to addition to cell lines.

Concanamycin A (ConcA), paraformaldehyde (PFA), filipin, oligomycin A, 2-deoxy-D-glucose (2-DG), methyl-β-cyclodextrin (MβCD) and the β-actin antibody were obtained from Sigma-Aldrich. Alexa fluor 488-Phalloidin and Alexa Fluor 488 tetrafluorophenyl (TFP) ester were acquired from Molecular Probes. The CellTracker CM-DiI Dye (1,1'-Dioctadecyl-3,3,3',3'-Tetramethylindocarbocyanine Perchlorate) and Lipofetamine 2000 were purchased from Invitrogen. The Vectashield mounting medium was obtained

from Vector Laboratories. DAPI (4′,6-Diamidino-2-Phenylindole, dihydrochloride, 40043) was purchased from Biotium. The V-ATPase *c* subunit antibody (AB5469) was acquired from Merck.

4.2.2 Cell lines and culture conditions

The cancer cell lines MDA-MB-231 (ATCC HTB-26), Hs 578T (ATCC HTB-126), T-47D (ATCC HTB-113), PC-3 (ATCC CRL-1435) and MG-63 (ATCC CLR-1427) were grown in Dulbecco's modified Eagle's medium (DMEM, Biochrom) supplemented with 10% (v/v) fetal bovine serum (FBS, Biochrom) and 1% (v/v) zell shield (Minerva Biolabs). The non-tumorigenic cell line MCF-10-2A (ATCC CRL-10781) was grown in DMEM-F12 medium supplemented with 5% (v/v) horse serum (Biochrom), 1% (v/v) zell shield, 20 ng/ml epidermal growth factor (EGF, Sigma Aldrich), 100 ng/ml cholera toxin (Sigma Aldrich), 0.01 mg/ml insulin (Sigma-Aldrich) and 500 ng/ml hydrocortisone (Sigma-Aldrich). The human fibroblast cell line BJ-5ta (ATCC CRL-4001) was grown in a 4:1 mixture of DMEM and Medium 199 (Biochrom) supplemented with 0.01 mg/ml hygromycin B (Sigma-Aldrich) and 10% (v/v) FBS. All cell lines were acquired from ATCC, were recently verified for their authenticity and were cultured at 37 °C in a humidified atmosphere with 5% CO_2. For all experiments, cells were seeded in 6-well plates at a concentration of 1.5×10^5 cells/ml for MDA-MB-231, PC-3 and T-47D cell lines; 2×10^5 cells/ml for MCF-10-2A and BJ-5ta cell lines; and 1×10^5 cells/ml for Hs 578T and MG-63 cell lines. For ECAR experiments, cells were seeded in XF 24-well plates at a final concentration of 1×10^4 cells/well. All the compounds used in this study were added to the wells only when cells reached at least 70% confluence.

4.2.3 Transfection with the mCherry-D4H cholesterol biosensor

Hs 578T, MDA-MB-231, PC-3, MG-63 and MCF-10-2A cells were transiently transfected with the pGEX-6P1 plasmid containing the mCherry-D4H probe (a kind gift from Dr. Greg Fairn) [12] using Lipofetamine 2000 reagent according to manufacturer's instructions. Briefly, after cell seeding for 24 h, cells were washed with PBS 1× and incubated with Opti-MEM (reduced serum medium, Gibco) for 1 h. Prior to combining the reagents and incubating for 20 min to allow complexes' formation, 2.5 μg plasmid DNA (per well) and lipofetamine 2000 were diluted in Opti-MEM. The lipofetamine-DNA complexes were then added drop by drop to the plates and after 4 h of incubation at 37 °C, 50% FBS in Opti-MEM was added to the wells. After 24 h of incubation, cells were either fixed for immunofluorescence experiments or treated with bLf for timelapse assays.

4.2.4 Immunofluorescence and confocal microscopy

For immunofluorescence experiments, cells were grown in 6-well plates containing glass coverslips. After mCHerry-D4H transfection for 24 h, cells were fixed with 4% PFA for 40 min and then rinsed with PBS 1×, incubated with ammonium chloride 50 mM for 10 min, rinsed again and permeabilized with PBS-SDS 0.1% for 10 min. Afterwards, cells were blocked in PBS-BSA 3% for 20 min and washed again with PBS 1×. Cells were next incubated overnight at 4°C in a humidified chamber with the primary antibody against *c* subunit of V-ATPase (AB5469, Merck) in PBS-BSA 0.1%. Subsequently, cells were washed with PBS-BSA 0.1% and then labelled with the secondary antibody anti-rabbit Alexa Fluor 488 for 1 h in the dark. Cells were then rinsed and coverslips were mounted upside down in Vectashield mounting medium (Vector Laboratories). Images were acquired in a sequential mode by Confocal Scanning Laser Microscope OLYMPUS BX61/FLUOVIEW1000, using a 60× objective and the specific filter settings for Alexa fluor 488 (488 BA 505-540) and mCherry (559 BA 575-675). In order to attest the specific staining of V-ATPase *c* subunit, a negative control corresponding to cells labelled only with the secondary antibody Alexa fluor 488 was performed (Figure A2, Appendix). Fluorescence intensity profiles of red and green fluorescence were calculated using Image J Fiji "line profile analysis" tool across the highlighted membrane regions.

4.2.5 Filipin staining and fluorescence microscopy

For lipid rafts visualization cells were labelled with Filipin III from *Streptomyces filipinensis* (Sigma-Aldrich). Briefly, cells were seeded in 6-well plates containing glass coverslips and allowed to attach for 24 h. Next, cells were incubated with or without 175 μM bLf or 10 nM ConcA up to 48 h, or 0.5 mM MβCD for 2 h followed by 46 h incubation in fresh medium. After a given timepoint, cells were fixed with 4% PFA for 40 min, rinsed with PBS 1× and incubated with 1.5 mg/ml glycine in PBS 1× for 15 min at room temperature. Cells were then stained with 0.01 mg/mL filipin dissolved in PBS 1× supplemented with 0.5% bovine serum albumin (BSA) for 2 h at room temperature in the dark. Finally, cells were washed with PBS 1× and the coverslips were mounted with the anti-fading mounting medium (Vector Laboratories) to overcome the instability of the dye. Samples were visualized in a fluorescence microscope (Leica DM 5000B, Leica Microsystems) with a Leica DCF350FX digital camera using the specific filter settings for this dye and a 60× objective.

4.2.6 Uptake of Alexa Fluor 488-labelled bLf

bLf was labelled with Alexa Fluor 488 TFP ester, which stains the protein amines, following the manufacturer's instructions. Per well of 6-well plates, 18 mg of bLf dissolved in 1 ml of 0.1 M sodium bicarbonate buffer pH 9 were incubated with 1 mg/ml of the dye with agitation for 1 h in the dark at room temperature. The labelled protein was separated from the free dye by performing several washes with PBS 1× by centrifugation at 4,000 ×*g* for 5 min using Amicon Ultra 0.5 ml 30K filters (Merck). A control with only Alexa Fluor 488 TFP ester (without bLf) was performed and added to the cells to ensure that the signal observed under the fluorescence microscope was specific to bLf (Figure A3, Appendix). Alexa Fluor 488-labelled bLf (final concentration of 175 μM) was then added to the cells grown over coverslips and incubated up to 24 h. After a given timepoint, cells were washed with PBS 1× and the coverslips were mounted in Vectashield mounting medium containing 4′,6-diamidino-2-phenylindole (DAPI) to label nucleus (Vector Laboratories). Samples were observed in the Leica DM 5000B fluorescence microscope (Leica Microsystems) using the specific filter settings for Alexa fluor 488 and a 60× objective.

4.2.7 Exosomes production, labelling and uptake

Exosomes were purified by differential centrifugation processes, as previously described [13]. Briefly, the FBS-free media from BJ-5ta cells, cultured as monolayers for 48 h, was collected and subsequently subjected to sequential centrifugation steps: 800 ×*g* for 5 min and 2,000 ×*g* for 10 min. The supernatant was then filtered using 0.2 μm filters and pelleted at 100,000 ×*g* 4 °C for 3 h using a Beckman Optima XL-90 ultracentrifuge. The resulting pellet was then resuspended in PBS 1×. Isolated exosome suspensions were analyzed using the NanoSight NS500 instrument (NanoSight Ltd). All the settings were optimized and kept constant between samples. For exosomes labelling, 1 μL of 1 mM DMSO stock solution of DiI dye (C7001, Invitrogen) was added to 200 μL of the exosome samples. The mixture was incubated at 37 °C for 1 h. The excess unincorporated dye from the labeled exosomes was removed using Amicon Ultra Centrifugal Filters (10 kDa, Merck) following the manufacturer's protocol. In the end, BJ-5ta exosomes were resuspended in 20 μL of PBS 1× and analyzed for total protein content using the Micro BCA Protein Assay Reagent Kit (Thermo Scientific), following the manufacturer's instructions. To ensure the quality of the purified exosomes, typical exosome markers were analyzed by western blot as described below. For exosome uptake experiments, MDA-MB-231 cells (grown in coverslips) were incubated with 175 μM bLf for 24 h, or 1 mM MβCD for 24 h. Afterwards, cells were

washed and incubated with FBS-free medium containing about 4 μg of DiI-labelled exosomes purified from Bj-5ta cells for up to 24 h. Time-lapse microscopy details are explained bellow. For the fluorescence microscopy, cells were washed after incubation with exosomes for 6 or 24 h, mounted upside down in a microscope slide and observed in a fluorescence microscope (Leica DM 5000B, Leica Microsystems) with a 60× objective.

4.2.8 Time-lapse microscopy

After treatment with 175 μM bLf or transfection with the D4H-mCherry probe for 24 h, cells were incubated with DiI-labelled exosomes or 175 μM bLf, respectively, immediately prior to visualization under the fluorescence microscope. Time course of exosome uptake or D4H-mCherry labelling, respectively, was followed using a fluorescence inverted microscope with incubation (5% CO_2, 37 °C) equipped with shutter to avoid phototoxicity and automatic stage (Axio Observer, Zeiss Microscopy), 40× objective. Data were analysed using the ZEN 3.2 software (blue edition) from Zeiss Microscopy. The percentage of cells that taken up exosomes was estimated by considering the cells with internalized exosomes in relation to the total amount of cells per field.

4.2.9 RNA isolation and real-time PCR analysis

For the analysis of the mRNA levels of the proteins involved in PI3K/AKT/mTOR signalling pathway, cells were treated in the presence or absence of 175 μM bLf for 48 h, after which their RNA was extracted using the Trizol reagent (Invitrogen) following the manufacturer's protocol. Succinctly, cells were lysed by incubating 5 min with the Trizol reagent. Lysates were then harvested to a tube and chloroform was added to separate the phase containing RNA. After centrifugation at 12,000 ×*g*, the supernatant was collected, the RNA was precipitated adding isopropanol and washed with ethanol 75%. After air drying, the RNA was resuspended in RNase-free water (Millipore), quantified and analyzed by gel electrophoresis for quality assessment. Possible contamination with genomic DNA was avoided by treating RNA with DNase I (Grisp), according to the manufacturer' recommendations. Afterwards, 1 μg of total RNA from each condition was used for reverse transcription using the iScript cDNA synthesis kit (Bio-Rad) as recommended. Real-time PCR was performed in a CFX 96 Real-Time PCR System (Bio-Rad) using 96-well plates and the KAPA SYBR FAST for Light Cycler 488 mix (Kapa Biosystems) with the following optimized reaction conditions: 95 °C for 3 min, followed by 39 cycles at 95 °C for 15 s, 60 °C for 20 s, and 72 °C for 15 s. The primers used are depicted in Table 4.1. All primers were designed using Primer 3 browser [14] and cross-checked by Blast sequence analysis using Primer Blast, NCBI [15]. A negative

control without template and melt curve analysis were employed to assess the overall specificity of the reactions and of the PCR product. Each measurement was performed in duplicate and at least three independent experiments were performed for each analysis. Relative gene expression was determined by the $2^{-\Delta\Delta Ct}$ method [16], normalized to the 18S rRNA reference gene and expressed as fold change setting the untreated control at a value of 1.0.

Table 4.1: List of primers used in real-time PCR experiments.

Target gene	Primer Forward	Primer Reverse
PI3K	5'-TAGGCAAGTCGAGGCAATG-3'	5'-AAAGCCCTGTAGAGCATCCA-3'
AKT	5'-AGCCTGGGTCAAAGAAGTCA-3'	5'-GCCAACCCTCCTTCACAATA-3'
mTOR	5'-GAAGGTGGAGGTGTTTGAGC-3	5'-ACCCAACCATTGACATGACC-3'
18S rRNA	5'-AAACGGCTACCACATCCAAG-3'	5'-CCTCCAATGGATCCTCGTTA-3'

4.2.10 Total protein extraction and western blotting

Cells were incubated for 48 h with or without 175 μM bLf and then washed twice with ice-cold PBS 1× and lysed with ice-cold RIPA buffer [150 mM NaCl, 2 mM EDTA, NP-40 1% (v/v), 50 mM Tris HCl, pH 7.4] supplemented with a proteinase inhibitor cocktail [20 mM sodium fluoride, 20 mM sodium orthovanadate, 1 mM phenylmethylsulfonyl fluoride and 4 % (v/v) Complete Protease Inhibitor Cocktail (Sigma-Aldrich)]. After 20 min incubation on ice, protein extracts were collected by centrifugation at 12,000 ×*g* for 10 min at 4 °C. The supernatants were stored at -80 °C. Protein concentration was determined by the Bradford method [17] using BSA solutions of known concentration to build a standard curve. For western blot, 30 μg of total protein for each experimental condition or 20 μg of purified exosomes were mixed with 1× sample buffer [2.5% (v/v) sodium dodecyl sulfate (SDS), 10% (v/v) glycerol, 4% β-mercaptoethanol, 0.02% (v/v) bromophenol blue, 62.5 mM Tris-HCl, pH 6.8], boiled for 5 min, and separated using 8% or 15% SDS-polyacrylamide gel electrophoresis and transferred onto nitrocellulose membranes (Protan Amersham, GE Healthcare). Membranes were then blocked in 3% BSA in Tris-buffered saline (TBS 1×; 150 mM NaCl, 50 mM Tris-HCl, pH 7.5) containing 1% Tween 20 (TBST) for 2 h with agitation at room temperature. Subsequently, membranes were incubated overnight at 4 °C with the primary antibodies against β-actin (1:40000 dilution, A3854, Sigma), PI3K (1:1000 dilution, #4249, p110α, Cell Signaling Technology), mTOR (1:500 dilution, sc-293089, Santa Cruz Biotechnology), phospho-mTOR (1:500 dilution, sc-293133, Ser 2448, Santa Cruz Biotechnology), Akt (1:1000 dilution,

#9272S, Cell Signaling Technology), CD63 (1:1000 dilution, ab134045, Abcam), CD9 (1:1000 dilution, ab92726, Abcam) or CD81 (1:200 dilution, sc-166029, Santa Cruz Biotechnology). The membranes were then washed twice with TBST and incubated with secondary antibodies Peroxidase-AffiniPure goat anti-rabbit IgG or goat anti-mouse IgG (1:2000 dilution, Jackson ImmunoResearch) for 1 h at room temperature. After washing 4 times for 15 min with TBST, immunoreactive bands were detected by chemiluminescence using a chemiluminescent substrate (ECL detection system, Merck) and a ChemiDoc XRS system (Bio-Rad). Band intensity was quantified by ImageJ software.

4.2.11 Seahorse metabolic profile analysis

Cells were seeded in XF24 cell culture microplates and incubated overnight at 37 °C with 5% CO_2 to promote cellular adhesion. The extracellular acidification rates (ECAR) of cells incubated for 24 h with 175 μM bLf or 10 nM ConcA were determined using the Seahorse Extracellular Flux (XF24) Analyzer (Seahorse Bioscience). Prior to ECAR measurements, cells were incubated for 1 h at 37 °C (without CO_2) in unbuffered, serum-free DMEM media (DMEM 5030, Sigma-Aldrich) supplemented with 4 mM glutamine and adjusted to pH 7.4 ± 0.1. The glycolytic profiling was performed by monitoring the basal ECAR for 30 min followed by subsequent injections of glucose (10 mM), oligomycin (1 μM), and 2-deoxy-D-glucose (2-DG; 10 mM). The amount of protein present in each well was estimated using the sulforhodamine B (SRB) assay, as previously described [7]. Measurements were normalized to the SRB absorbance of each well using the Wave 2.2.0 software and expressed as mpH per min per SRB absorbance at 540 nm. Glycolytic function parameters were calculated by the mean of the three timepoints after injection of the compounds.

4.2.12 Statistical analysis

Data represent at least three independently conducted experiments. Statistical analysis was performed using two-way ANOVA followed by Tukey post-test using GraphPad Prism, version 6.0. Differences with p-value bellow 0.05 were considered statistically significant.

4.3 Results

4.3.1 V-ATPase co-localizes with cholesterol-rich lipid rafts in highly metastatic cancer cells

To uncover the possible role of lipid rafts in bLf anticancer activity, we initially determined if V-ATPase localizes at these membrane niches in the highly metastatic breast, prostate and osteosarcoma cancer cell lines under study, as previously reported for other cell lines [1,18,19]. To this end, since cholesterol is a major component of lipid rafts, immunofluorescence was performed with a V-ATPase antibody and these structures stained with a cholesterol biosensor termed D4H-mCherry [12]. Figure 4.1 shows a clear co-localization of V-ATPase and cholesterol-rich lipid rafts at the plasma membrane in all cancer cells (Figure 4.1A), as confirmed by the good match of the intensity profiles of both green and red fluorescence (Figure 4.1B). In fact, the D4H-mCherry pattern at the plasma membrane clearly shows regions with higher cholesterol content, which also correspond to higher V-ATPase staining intensity (Figure 4.1A, arrows). In turn, the non-cancer breast cell line MCF-10-2A does not display V-ATPase at the plasma membrane, as expected, and therefore the two fluorescence signals are completely apart in the fluorescence intensity profile (Figure 4.1B). For all cell lines, it is also possible to observe intracellular cholesterol staining.

4.3.2 bLf induces intracellular accumulation of cholesterol in highly metastatic cancer cells

To ascertain the putative effect of bLf on lipid rafts, their localization along 48 h exposure to bLf was assessed by staining cholesterol with filipin. Filipin is a natural antibiotic that binds to cholesterol [20] that renders a cleaner staining of cholesterol-rich lipid rafts at the plasma membrane (Figure 4.2A, head arrows) than D4H-mCherry. The bLf concentration chosen for these assays causes about 50% cell death in highly metastatic cancer cells after 48 h, as defined in our previous studies [7,11]. As observed in Figure 4.2A, bLf induces intracellular accumulation of cholesterol in the highly metastatic breast cancer cell line Hs 578T after 12 h of incubation, perturbing lipid rafts. Indeed, while in the first 6 h filipin staining is only observed at the plasma membrane (Figure 4.2A, head arrows), after 12 h bright intracellular spots of cholesterol are observed inside the cells (Figure 4.2A, arrows). We next evaluated the effect of bLf on the other cell lines under study after 48 h of incubation (Figure 4.2B). Interestingly, bLf induced an identical intracellular filipin staining pattern in the other highly metastatic cancer cells (Figure 4.2B,

arrows). In contrast, no effect was observed in the lowly metastatic T-47D cells and in the non-tumorigenic MCF-10-2A cells, where a clear staining at the plasma membrane remained as in the non-treatment conditions (Figure 4.2B, head arrows). Remarkably, bLf induces a very similar staining pattern as the V-ATPase inhibitor concanamycin A (ConcA) and methyl-β-cyclodextrin (MβCD), a lipid rafts-disrupting compound that depletes cholesterol from the membranes (Figure 4.2B) [21]. However, unlike these compounds, which affect all cell lines, bLf was found to specifically perturb the lipid rafts of highly metastatic cancer cells. Altogether, these data suggest that the perturbation of lipid rafts by bLf depends on the presence of V-ATPase at the plasma membrane lipid rafts.

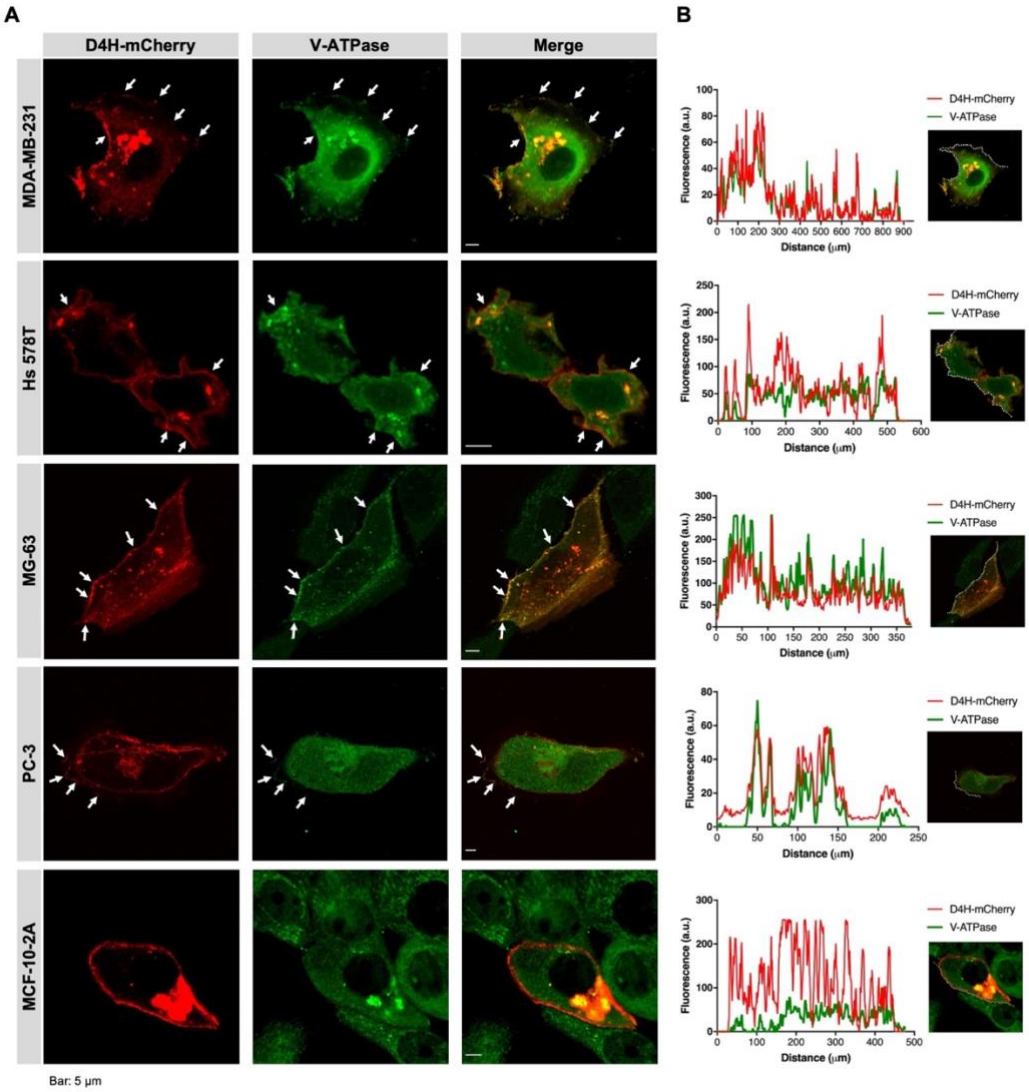

Figure 4.1: Immunofluorescence analysis of the localization of V-ATPase and cholesterol in MDA-MB-231, Hs 578T, PC-3, MG-63 and MCF-10-2A cell lines by confocal microscopy. (A) V-ATPase (green) was stained with a primary antibody against *c* subunit and Alexa-fluor 488 secondary antibody, while cholesterol staining (red) was achieved by transfecting cells with the D4H-mCherry biosensor. Arrows indicate spots of colocalization of red and green fluorescence at the plasma membrane. A representative z plane is shown for each cell line. Bar: 5 μm. **(B)** Fluorescence intensity profiles of red and green fluorescence across the highlighted selection.

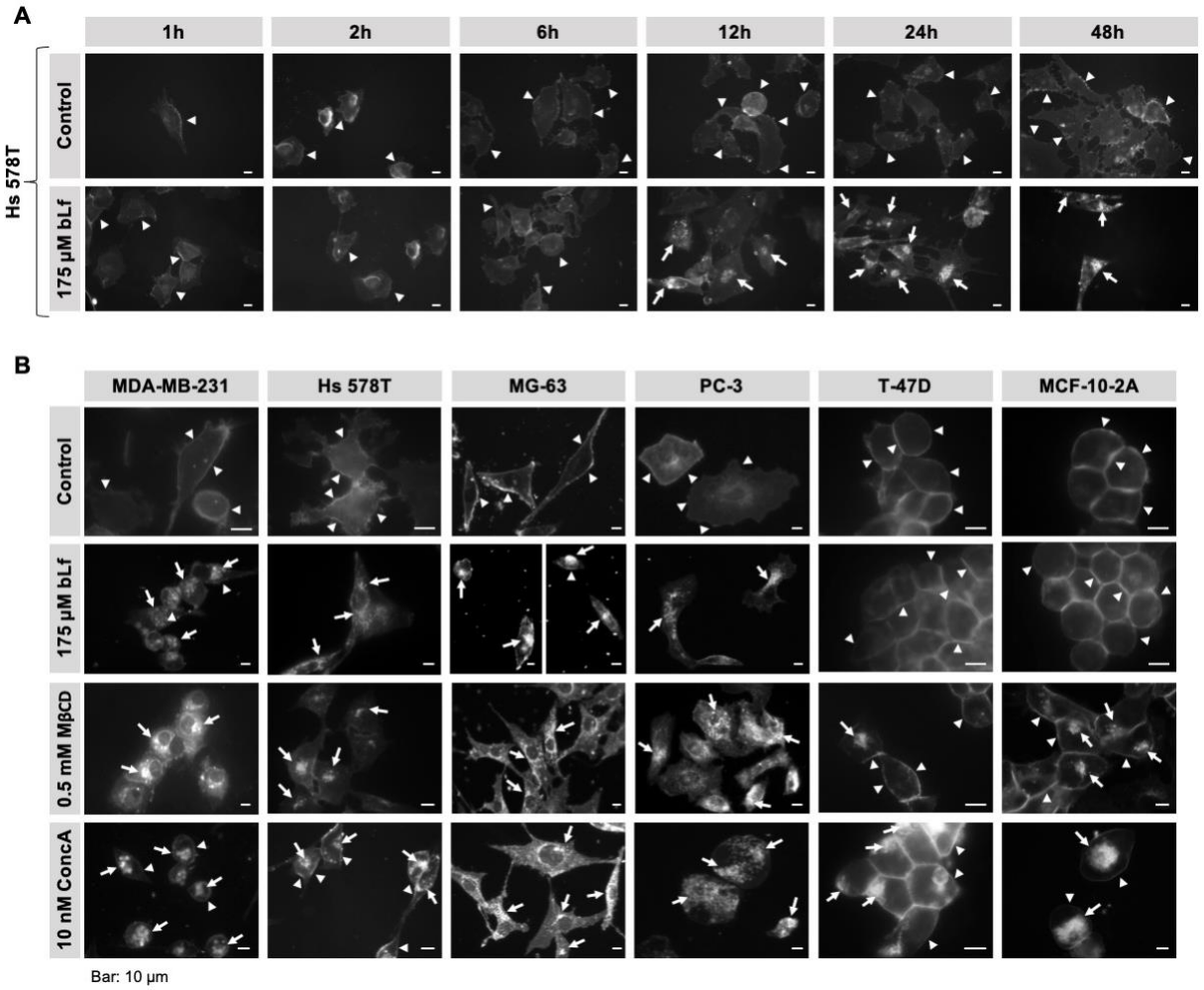

Figure 4.2: Effect of bLf, MβCD and ConcA on the localization of cholesterol in the cell lines under study. Cholesterol-rich lipid rafts were visualized by staining cells with filipin (0.01 mg/ml). **(A)** Fluorescence microscopy analysis of the time-course of Hs 578T cells incubated up to 48 h without (control) or with 175 µM bLf. **(B)** Representative fluorescence microscopy images of MDA-MB-231, Hs 578T, MG-63, PC-3, T-47D and MCF-10-2A cells incubated or not (control) with 175 µM bLf for 48 h, 10 nM ConcA for 48 h or 0.5 mM MβCD for 2 h followed by incubation in fresh culture medium for 46 h. Arrows point to spots of intracellular cholesterol staining while head arrows indicate membrane cholesterol staining. Bar: 10 µm.

4.3.3 The intracellular accumulation of cholesterol induced by bLf occurs before plasma membrane depletion

To study the kinetics of the intracellular accumulation of cholesterol and ensuing lipid rafts disruption triggered by bLf, time-lapse fluorescence microscopy of Hs 578T and PC-3 cells expressing the D4H-mCherry probe was carried out. Cells were observed over 48 h after bLf addition, and the results of the first 9 h are depicted in Figure 4.3. As mentioned above, D4H-mCherry staining does not render a specific labelling of the cholesterol-rich lipid rafts at the plasma membrane as intracellular spots are already observed in the beginning of the experiment for both bLf-treated and untreated cells (Figure 4.3A,

B - 0.5 h). Nevertheless, while in the bLf-treated cells a progressive higher intracellular accumulation is observed over time (Figure 4.3A, B -175 μM bLf), no further accumulation occurs in the non-treated cells as the levels of intracellular staining remain constant throughout the time course (Figure 4.3A, B - Control). Moreover, while plasma membrane staining (Figure 4.3 - arrows) in untreated cells can be detected in the course of time for all images, in bLf-treated cells the membrane labelling disappears after 7 h for Hs 578T cells and 4.5 h for PC-3 cells. Given that a higher intracellular accumulation of cholesterol induced by bLf occurs after 3.5 h and 2.5 h of treatment for Hs 578T and PC-3 cells, respectively (head arrows), while membrane labelling is maintained, we can conclude that intracellular accumulation of cholesterol precedes its plasma membrane depletion.

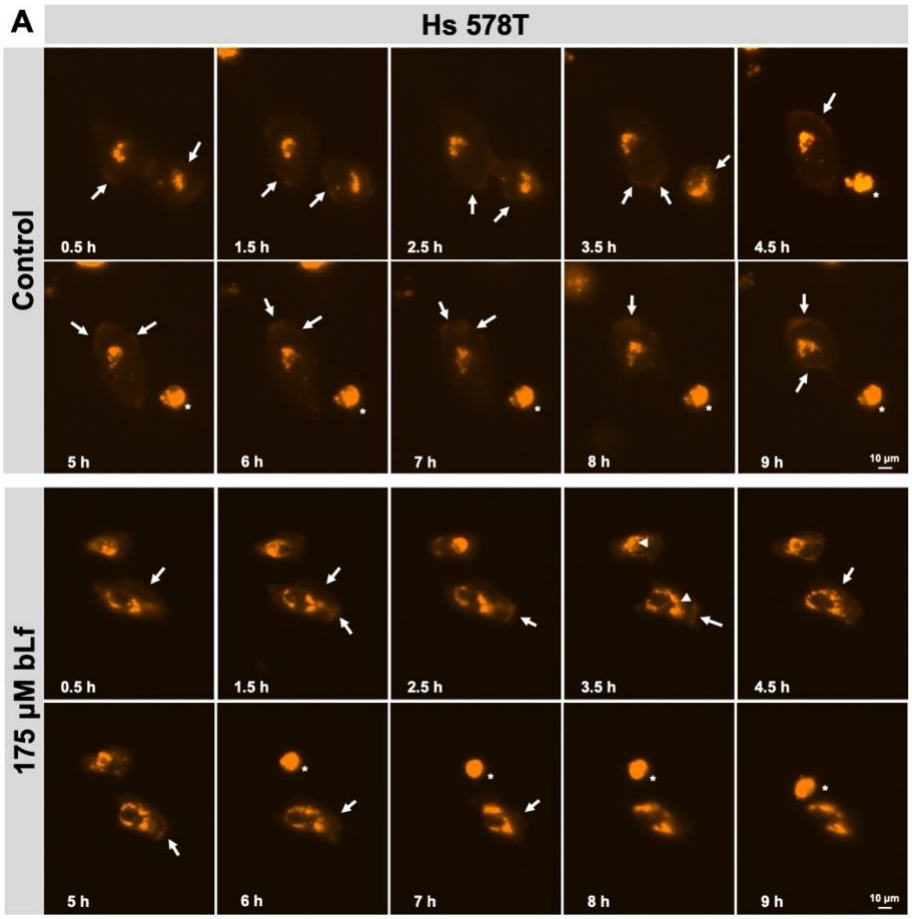

Figure 4.3: Time-lapse microscopy analysis of cholesterol localization in Hs 578T (A) and PC-3 (B) cell lines. Cells were transfected with the D4H-mCherry probe that binds cholesterol and then treated or not (control) with 175 μM bLf. Time-lapse microscopy experiments started right after bLf addition and up to 48 h. The first 9 h are shown (30 min interval for the first 5 h and 1 h interval up to 9 h). Bar: 10 or 100 μm, as indicated. The asterisk (*) indicates dead cells; arrows point to membrane staining and head arrows to the start of higher intracellular cholesterol accumulation induced by bLf.

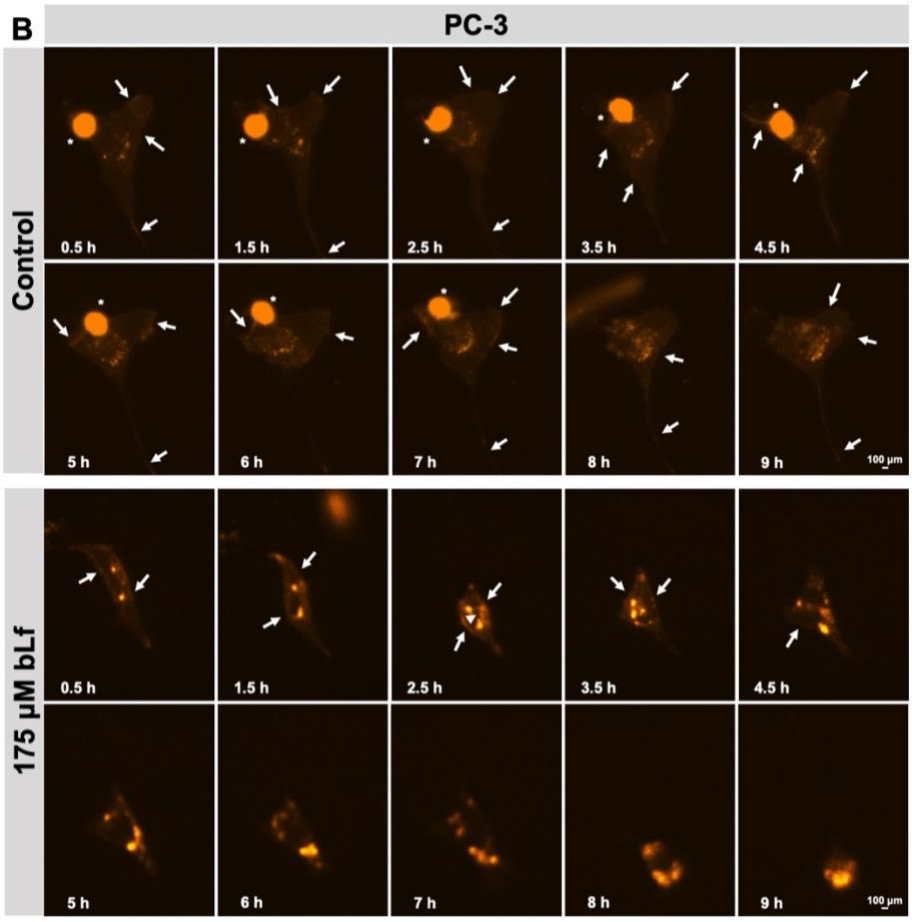

Figure 4.3: Time-lapse microscopy analysis of cholesterol localization in Hs 578T (A) and PC-3 (B) cell lines (cont). Cells were transfected with the D4H-mCherry probe that binds cholesterol and then treated or not (control) with 175 µM bLf. Time-lapse microscopy experiments started right after bLf addition and up to 48 h. The first 9 h are shown (30 min interval for the first 5 h and 1 h interval up to 9 h). Bar: 10 or 100 µm, as indicated. The asterisk (*) indicates dead cells; arrows point to membrane staining and head arrows to the start of higher intracellular cholesterol accumulation induced by bLf.

4.3.4 Cholesterol-rich lipid rafts disruption occurs after bLf uptake

To obtain information regarding bLf uptake in the cell lines under study and on the temporal relation between cholesterol-rich lipid rafts disruption and bLf internalization, cells were incubated with Alexa fluor 488-labelled bLf and followed during 48 h. Time-course of Hs 578T cells demonstrates that bLf first binds to the plasma membrane and only then is internalized (Figure 4.4A). Indeed, after 30 min and 1 h, the bLf staining is predominantly at the plasma membrane (head arrows); after 2 h both plasma membrane and intracellular staining (arrows) are visualized; and from 6 h onwards bLf staining mainly appears as bright green spots in the cytoplasm (Figure 4.4A, arrows). Since bLf-triggered intracellular accumulation of cholesterol was observed after 4.5 h in this cell line (Figure 4.3A), bLf internalization seems to precede lipid rafts disruption. bLf uptake was further studied after 24 h in the other cell lines. A similar bLf staining

pattern at the cytoplasm was observed in all cells including the non-tumorigenic cell lines MCF-10-2A and Bj-5ta (Figure 4.4B). Remarkably, no bLf was found in the nucleus, as no co-localization between bLf and DAPI was identified (Figure 4.4B). Interestingly, even after 24 h, plasma membrane staining of bLf was notorious in the highly metastatic cancer cell lines MG-63 (Figure 4.4C) and MDA-MB-231 (Figure 4.4D). Given that bLf plasma membrane staining has a punctuated pattern, we stained lipid rafts of MDA-MB-231 cells with filipin and observed a co-localization, suggesting that bLf localizes at the plasma membrane lipid rafts of these cells, which also house V-ATPase (Figure 4.4D).

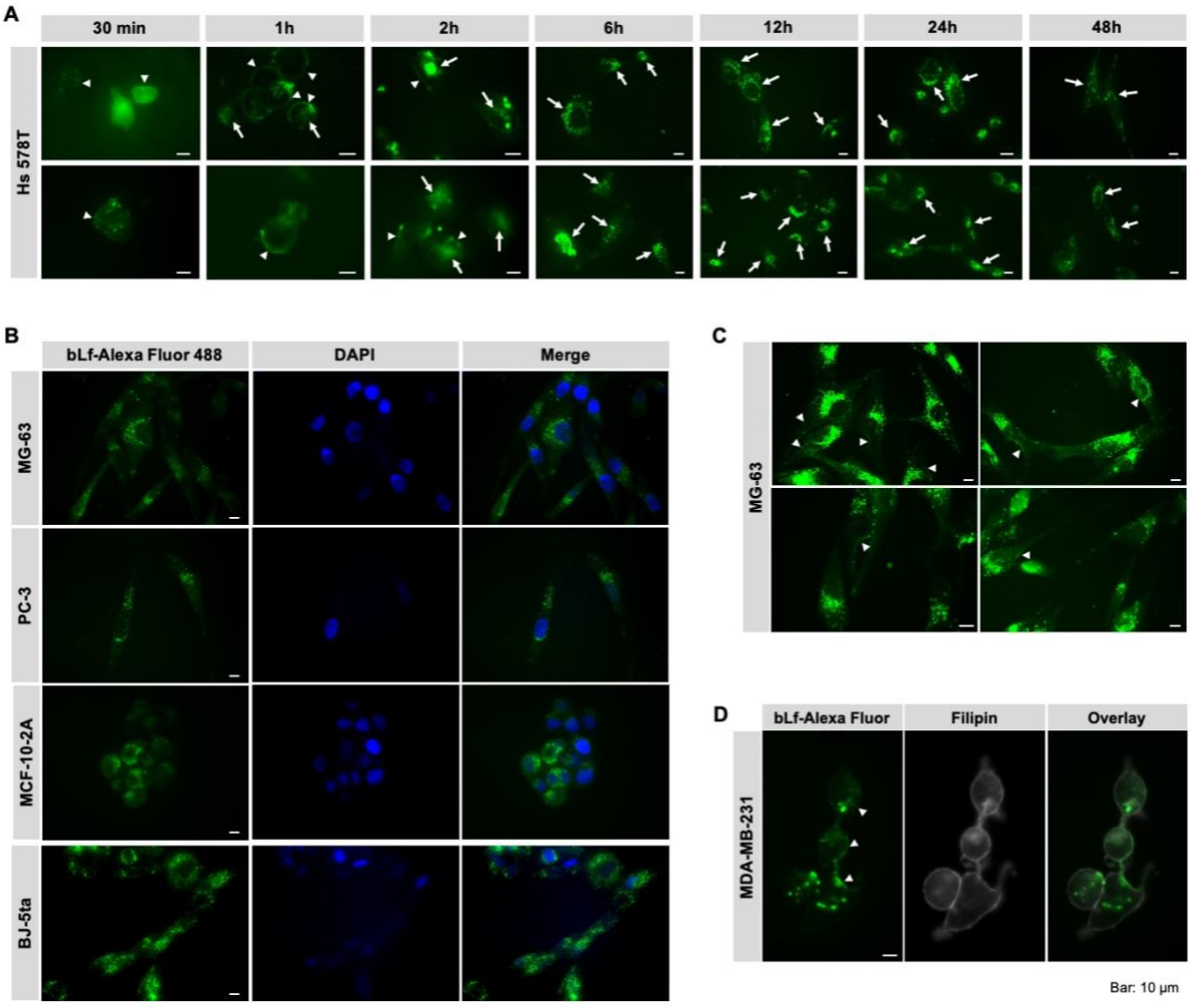

Figure 4.4: Internalization of bLf-Alexa Fluor 488 in the cell lines under study. (A) Time-course of fluorescence microscopy analysis of Hs 578T cells incubated up to 48 h with or without (control) 175 µM Alexa Fluor 488-labelled bLf. Arrows indicate intracellular staining while head arrows point to membrane staining. **(B)** Representative fluorescence microscopy images of MG-63, PC-3, Bj-5ta and MCF-10-2A cells incubated with 175 µM Alexa Fluor 488-labelled bLf for 24 h. Nuclei are labelled with DAPI. **(C)** Highlight of the membrane staining of bLf-Alexa Fluor 488 (head arrows) on MG-63 cells after 24 h of incubation. **(D)** Double staining of bLf-Alexa Fluor 488 (after 24 h of incubation) and filipin (0.1 mg/ml added right before visualization for labelling of the plasma membrane only) on MDA-MB-231 cells. Head arrows indicate membrane staining. Bar: 10 µm.

4.3.5 bLf delays uptake of exosomes and perturbs their intracellular trafficking

Both V-ATPase inhibition and lipid rafts disruption have been implicated in trafficking defects including endocytosis inhibition [22–24]. As bLf induces both effects, we studied if it impacts the uptake of exosomes derived from the Bj-5ta cell line, labelled with 1,1'-Dioctadecyl-3,3,3',3'-Tetramethylindocarbocyanine Perchlorate (DiI), by the MDA-MB-231 cell line. The exosomes have a mean and mode size of 109.4±8.0 and 166.1±6.5 nm, respectively (Figure A4 A, Appendix). Bj-5ta fibroblasts produced high levels of exosomes that were positive for the putative exosome markers CD63, CD9 and CD81 (Figure A4 B, Appendix). Time-lapse microscopy showed that uptake of exosomes by MDA-MB-231 cells is delayed when cells are pre-treated with bLf. Indeed, in the first 12 h, the exosome uptake in bLf-treated cells is about half of that of untreated cells, while after 24 h the percentage is identical (Figure 4.5A). The uptake of exosomes was further analyzed by fluorescence microscopy. Curiously, bLf seems to affect their intracellular trafficking as less exosomes are visible per cell and they aggregate in bright spots with an irregular cellular distribution (Figure 4.5B, arrows). In contrast, untreated cells show higher number of non-aggregated exosomes with a uniform pattern throughout the cell cytoplasm (Figure 4.5B). A similar intracellular aggregation pattern was observed in MβCD-treated cells (Figure A5, Appendix). Altogether, these data indicate that bLf delays the uptake of exosomes and alters their intracellular processing.

4.3.6 bLf downregulates PI3K and AKT expression in highly metastatic cancer cells

The PI3K/AKT/mTOR pathway is crucial for cell survival and proliferation (Figure 4.6A). Its activation has been reported to depend on lipid rafts, since the main signalling molecules of the pathway have been identified in these membrane domains, and lipid rafts disruption impairs the pathway [25–27]. As Lf was previously found to decrease AKT (protein kinase B) [28–30] and mTOR (mammalian target of rapamycin) phosphorylation [28] in cancer cell types other than breast and prostate, we next studied whether Lf affects this pathway in the highly metastatic cancer cells derived from breast (Hs 578T and MDA-MB-231) and from prostate cancer (PC-3), in comparison with the non-cancer Bj-5ta cells.

Real-time PCR showed a clear reduction of the mRNA levels of PI3K (phosphatidylinositol 3-kinase) and AKT in the two highly metastatic breast cancer cells (Hs 578T and MDA-MB-231), whereas no effect was observed in the non-cancer Bj-5ta cells (Figure 4.6B).

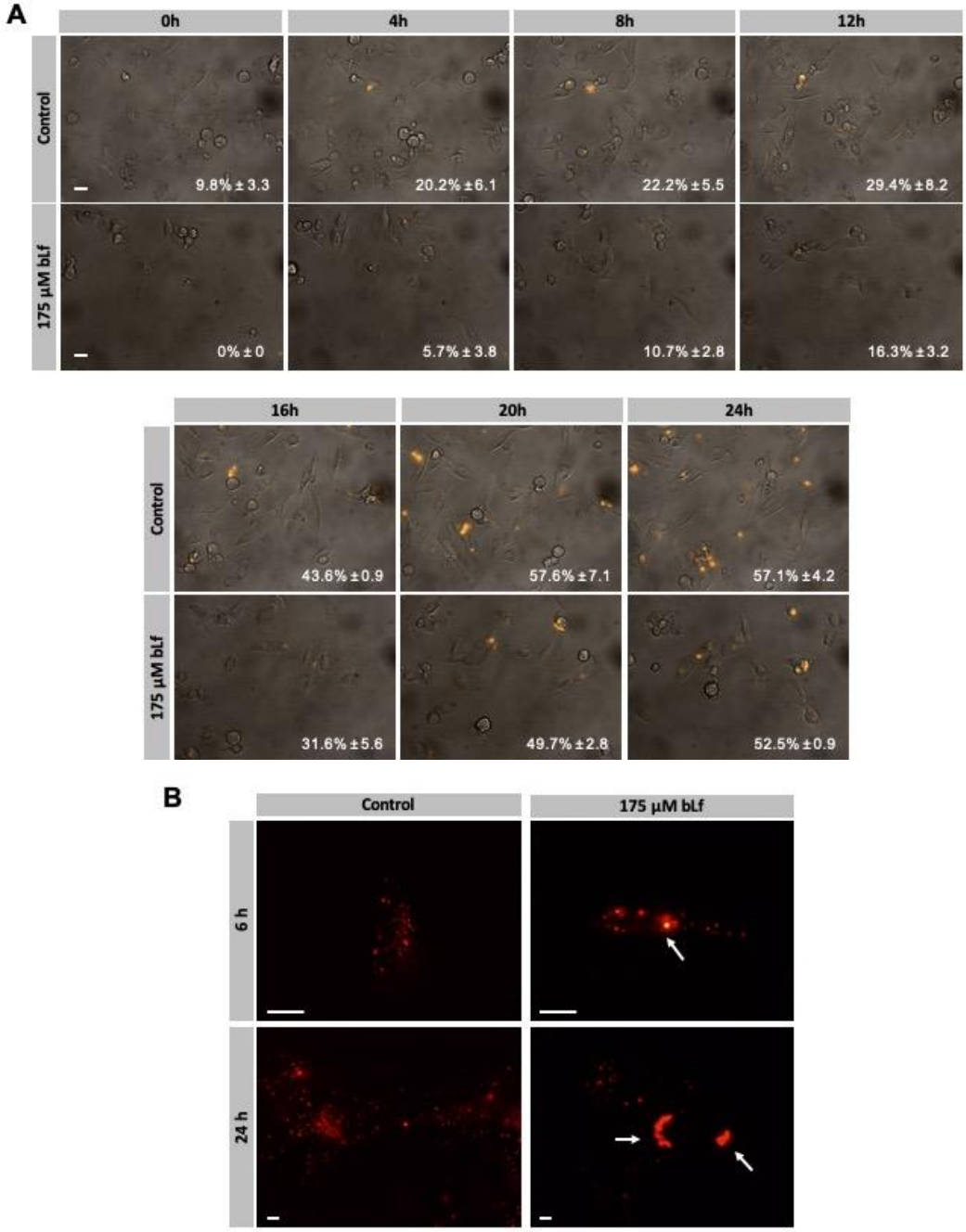

Figure 4.5: Effect of bLf on uptake of DiI-labelled exosomes by MDA-MB-231 cell line. (A) Time-course of DiI-labelled exosomes uptake up to 24 h of incubation by MDA-MB-231 cells pre-treated or not (control) for 24 h with 175 µM bLf. Overlay images of bright field and red fluorescence channel (DiI) are shown. Values are the percentage ± standard deviation of cells that taken up exosomes of three individual fields. Bar: 20 µm. **(B)** Representative fluorescence microscopy images of MDA-MDA-231 cells incubated with or without (control) bLf and exosomes as described in A. Arrows point to aggregated exosomes. Bar: 20 µm.

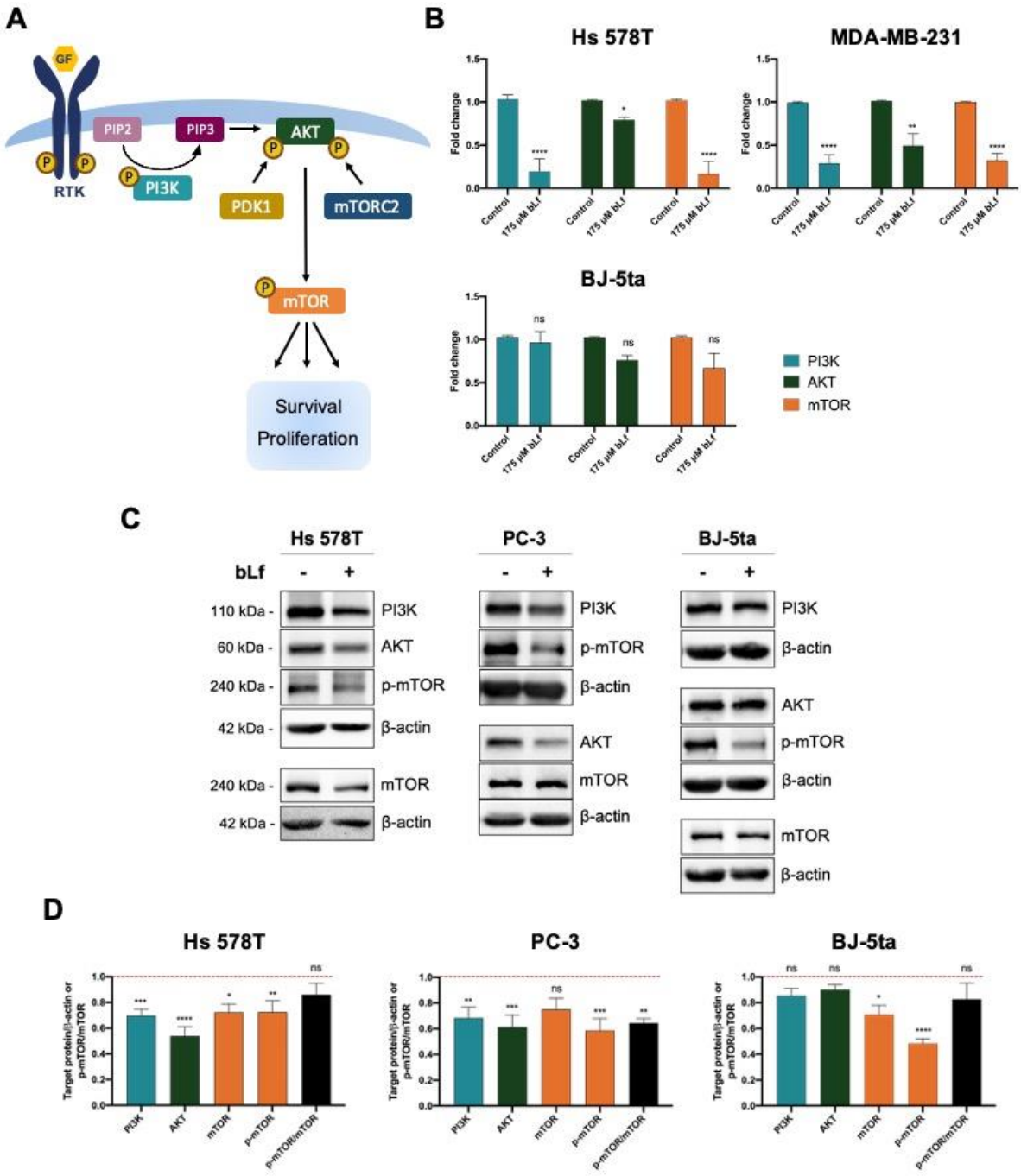

Figure 4.6: Effect of bLf on the PI3K/AKT/mTOR pathway by real-time PCR (B) and western blot (C) analysis. (A) Simplified representation of the PI3K/AKT/mTOR pathway. Binding of growth factors (GF) to receptors tyrosine kinase (RTK) activates PI3K, which catalyzes phosphorylation of phosphatidylinositol 4,5-biphosphate (PIP2) into phosphatidylinositol 3,4,5-triphosphate (PIP3). PIP3 formation prompts AKT phosphorylation at Thr308 by the phosphoinositide dependent kinase-1 (PDK1) and at Ser473 by mTOR complex 2 (mTORC2). Activated AKT regulates a plethora signalling molecules being mTOR one of them. mTOR promotes cell survival and proliferation [31,32]. **(B)** Relative quantification by real-time PCR of PI3K, AKT and mTOR mRNA levels in MDA-MB-231, Hs 578T and Bj-5ta cells as indicated. Cells were incubated in the absence (control) or presence of 175 µM bLf for 48 h. Values are fold change ± SEM to control after normalizing to the reference gene (18S rRNA) of two replicates of three independent experiments. *,**,**** P value < 0.05, 0.01, 0.0001, respectively. **(C)** Representative images of western blotting analysis of the protein expression level of PI3K, AKT, mTOR, and phospho-mTOR in

Hs 578T, PC-3 and Bj-5ta cells treated or not (control) with 175 μM bLf for 48 h. **(D)** Relative densitometric analysis of the expression of the indicated proteins normalized to β-actin levels (loading control) and to the untreated cells (set as expression equal to 1 and represented by the red line). p-mTOR/mTOR ratio normalized to the untreated control is also depicted. Values are the mean ± SEM of at least three independent experiments. ns: non-significant, *,**,***,**** P value < 0.05, 0.01, 0.001, 0.0001, respectively.

As for the protein levels, assessed by western blot, we found that bLf downregulates PI3K and AKT in the highly metastatic Hs 578T and PC-3 cancer cells but not in the non-cancer cells Bj-5ta (Figure 4.6C, D). This suggests that reduction of these two proteins is associated with bLf-mediated lipid raft's disruption. In turn, bLf significantly decreased the mRNA levels of mTOR in the two highly metastatic breast cancer cells, whereas no effect was observed in the non-cancer Bj-5ta cells (Figure 4.6B). However, bLf caused a reduction of mTOR protein levels in Hs 578T, PC-3 and Bj-5ta cell lines, though only statistically significant in Hs 578T and Bj-5ta cells, associated with a significant decrease of phospho-mTOR levels in the three cell lines. As for the ratio between phospho-mTOR and mTOR, it decreased in the same three cell lines, though the difference was statistically significant only in bLf-treated PC-3 cells (Figure 4.6C, D).

4.3.7 bLf inhibits glycolysis of highly metastatic cancer cells

Given that glycolysis is one the main regulators of V-ATPase activity, assembly and distribution [33], and that PI3K/AKT/mTOR pathway has been implicated in glycolysis regulation [34], the ability of bLf to alter the glycolytic function of cells was studied. The glycolytic parameters were evaluated by assessing the extracellular acidification rate (ECAR) after subsequent injections of glucose, oligomycin and 2-deoxy-D-glucoe (2-DG) using a Seahorse extracellular flux analyzer (Figure 4.7A). A very strong inhibition of the glycolytic parameters glycolysis and glycolytic capacity was observed when Hs 578T cells were treated with bLf for 24 h, while no effect was detected in the lowly metastatic T-47D and non-tumorigenic Bj-5ta cells. Though not statistically significant, a decrease of the glycolytic reserve of Hs 578T cells was also observed. ConcA, in turn, affected indistinctly lowly and highly metastatic cancer cells as it inhibited the glycolytic function of both cancer cell lines (Figure 4.7A, B). These data suggest that bLf selective cytotoxicity towards highly metastatic cancer cells is associated with glycolysis inhibition.

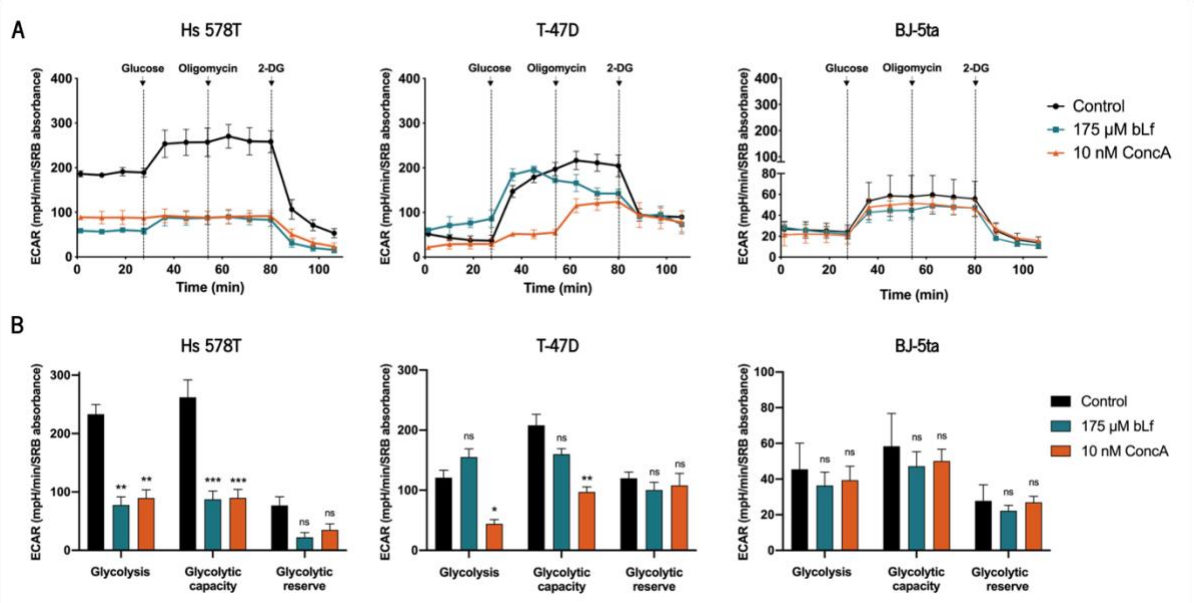

Figure 4.7: Effect of bLf on the glycolytic function of Hs 578T, T-47D and BJ-5ta cell lines. The glycolytic function parameters were calculated by measuring the extracellular acidification rate (ECAR) before and after subsequent injections of glucose, oligomycin and 2-deoxy-D-glucose (2-DG). **(A)** ECAR measured as mpH per min per Sulforhodamine B (SRB) absorbance at 540 nm of indicated cells pre-treated for 24 h without (control) or with 175 µM bLf or 10 nM ConcA along 110 min. **(B)** Plots of the glycolytic function parameters calculated as the mean of the three timepoints after addition of glucose (glycolysis), oligomycin (glycolytic capacity) and 2-DG (glycolytic reserve). Results are expressed in mpH per min per SRB absorbance at 540 nm. Values represent the mean ± SEM of three replicates of three independent experiments. ns: non-significant, *,**,*** *P* value < 0.05, 0.01, 0.001, respectively.

4.4 Discussion

The Lf anticancer activity has been known for more than 25 years [35] and its dedicated studies advanced from basic research to clinical trials, in which encouraging results have been achieved [36,37]. Yet, the clinical efficacy is not always as desired [38]. Studies aiming to dissect the Lf mechanisms of action are therefore crucial to achieve a better efficacy and to prompt its use in clinical practice. Here, we sought to throughly characterize, at the molecular level, the mechanisms underlying the cytotoxicity and selectivity of bLf towards highly metastatic cancer cells demonstrated in our previous works [7,11]. The molecular basis for Lf selectivity for these type of cells relies on the targeting of the proton pump V-ATPase which is differentially located at the plasma membrane of these cells [7].

As previously mentioned, several authors described a close interplay between V-ATPase and cholesterol- and sphingolipid-rich lipid rafts [1,39–41], which led us to hypothesize that lipid rafts may be a hidden player in Lf anticancer activity. To test this assumption, we selected a panel of highly metastatic cancer cell lines that were previously demonstrated to display V-ATPase at the plasma membrane [7–10]

and to be sensitive to bLf [7,11]. Herein, we further demonstrated that these cell lines are a suitable model to test our hypothesis, since we found that V-ATPase specifically localizes at the cholesterol-rich lipid rafts of these highly metastatic cancer cells, much like it was demonstrated for melanoma [1], leukemia [18] and cervical cancer cells [19].

Our data revealed a novel effect of bLf that lies on the intracellular accumulation of cholesterol and its depletion from the plasma membrane, which leads to disruption of cholesterol-rich lipid rafts. The presence of V-ATPase at the plasma membrane lipid rafts seems to be critical for this cellular alteration, since bLf is unable to perturb the lipid rafts of lowly metastatic cancer or non-cancer cells, which do not exhibit plasmalemmal V-ATPase. A similar effect, though not selective for highly metastatic cancer cells as it occurs in all cell lines, is observed in ConcA- and MβCD-treated cells. In aggrement with our results, inhibition of V-ATPase with bafilomycin A1 (BafA1) or knockdown of its subunits induced a very similar perturbation of lipid rafts as assessed by filipin staining yielding an intracellular fluorescence pattern like that produced by bLf treatment [24]. Similarly, V-ATPase inhibition by Archazolid A also led to plasmalemmal cholesterol depletion and intracellular accumulation [42].

There are several pathways for intracellular cholesterol trafficking that include its delivery into late endosomes and lysosomes, where it is hydrolyzed to free cholesterol and then transported to the plasma membrane [43]. Authors have shown that V-ATPase activity impairment results in cholesterol trapping inside the lysosomes caused by endolysosomal pH perturbations, decreased levels of free cholesterol and consequent depletion from the plasma membrane, lipid rafts disruption and alterations of the biophysical properties of the plasma membrane [24,42]. Based on the identical filipin staining pattern induced by bLf, BafA1 and Archazolid A [24,29], we hypothesize that the intracellular cholesterol accumulation observed in bLf-treated cells is a consequence of its trapping inside the less acidic lysosomes/endosomes.

Our time-course experiments are in agreement with this hypothesis as they provide evidence that the bLf-promoted depletion of cholesterol from the plasma membrane occurs after it starts to accumulate inside the cells, suggesting that it is the intracellular accumulation of cholesterol that results in its depletion from the plasma membrane. Moreover, it is noteworthy that perturbation of lipid rafts occurs after bLf uptake, which goes in line with the assumption that bLf-induced intracellular pH alterations, both at cytosolic [7] and lysosomal [11] levels, are the main factors responsible for the subsequent cascade of events that disrupts lipid rafts. Why no disruption of lipid rafts is observed in lowly metastatic or non-cancer cells is likely due to activation of V-ATPase-independent pH control mechanisms, which enable them to maintain lysosomal and cytosolic pH after bLf internalization [7,11] and counteract its cytotoxic

effect. Interestingly, during the time-course of bLf-induced cytotoxicity in highly metastatic cancer cells, bLf is observed at both the plasma membrane and as cytosolic vesicle-like structures, which are precisely the locations where V-ATPase is found suggesting a putative binding of the protein to the proton pump. It is also worth mentioning that bLf was not found at the plasma membrane of non-cancer cells nor at the nucleous in any of the cell lines under study, though it preserved the cytosolic vesicle-like staining. Previous studies have also addressed Lf uptake in different types of cells including colon [44] and breast cancer cells [45] and macrophages [46]. Accumulation at vesicle-like cytosolic structures and no nuclear staining was evident in breast cancer cells [45] and localization at the endosomes was shown in macrophages [46]. Hence, the vesicle-like structures that we and others observe are likely to be endosomes/lysosomes.

Our results additionally show that bLf perturbs the uptake of exosomes, which are generally internalized by endocytosis [23,47], and alters their intracellular distribution/processing. In this line, Kozik *et al.* reported that V-ATPase inhibition blocks clathrin-mediated endocytosis, which is due to aberrant endo/lysosomal acidification and impairment of cholesterol recycling [24]. Accordingly, perturbation of both V-ATPase (by BafA1) or lipid rafts (by MβCD) was shown to decrease the uptake of exosomes in prostate [48], ovarian [23] and breast cancer cells [49], supporting that active V-ATPase and cholesterol sorting are key requirements for exosomes endocytosis. Taken together, these data further reinforce that the pH perturbations triggered by bLf affect overall intracellular trafficking by preventing cholesterol deliver to the plasma membrane.

The observed differential downregulation of PI3K and AKT levels at the mRNA and protein levels in the highly metastatic cancer cells in comparison with the non-tumorigenic cells is seemingly associated with the bLf lipid raft-disrupting effect. This interpretation is supported by data showing that the main signalling molecules of the PI3K/AKT pathway associate with lipid rafts, and that the pathway activation depends on the integrity of these microdomains [25–27]. Indeed, lipid rafts are known to hold important molecules involved in different signalling pathways in addition to PI3K/AKT/mTOR, functioning as authentic platforms to boost cancer-related signalling [26,32]. There is also a number of studies that dissect the mechanism by which lipid raft-disrupting agents affect the PI3K/AKT/mTOR pathway, which can bring clues about the bLf anticancer mechanism. Treatment of cancer cells with 10-Gingerol, a natural phenolic lipid [27]; edelfosine, a synthetic anticancer lysophospholipid that accumulates in lipid rafts [50]; or schweinfurthins, plant-derived compounds known to disrupt lipid rafts [51], were reported to decrease phosphorylation of the key components of this pathway by displacing them from lipid rafts [25,27,51]. Moreover, both MβCD and simvastatin were shown to decrease the raft levels inhibiting AKT

phosphorylation. Cholesterol suplementation restored the levels of phosphorylated AKT and lipid rafts [52]. Overall, the gathered information suggests that the bLf-induced downregulation of PI3K and AKT is a direct consequence of lipid rafts disruption, which most probably leads to mislocalization of these signalling molecules. To gain further insight into how bLf affects the pathway, immunodetection of phosphorylated AKT and PI3K should be performed, and additional upstream and downstream effectors should be tested and compared between cancer and non-cancer cells. Nonetheless, based on previous works [28–30] [45], we hypothesize that bLf inhibits this pathway in Hs 578T and PC-3 cancer cells. As for the mRNA levels of mTOR, we observed a significant downregulation in the two highly metastatic breast cancer cells but not in the non-cancer Bj5ta cells. However, contrarily to what we were expecting, bLf reduced the protein levels of phospho-mTOR in both highly metastatic and non-cancer cell lines. Based on these data, several hypotheses can be raised: (i) although the levels of AKT and PI3K are not affected in BJ-5ta cells, the levels of their phosphorylated forms (the active molecules) can be downregulated by bLf in a way independent of lipid rafts disruption, as it occurs in both highly metastatic and non-cancer cell lines cell lines; (ii) bLf does not affect PI3K and AKT phosphorylation in Bj5ta cells, but affects other upstream effectors of mTOR that lead to a decrease of phospho-mTOR levels in this cell line; (iii) other pathways downstream of AKT (not via mTOR) may be differentially affected by bLf in non-cancer cells compared to highly metastatic cancer cells. In addition, since no bLf-induced cytotoxicity was detected in the Bj5ta cell line [11], the decrease of mTOR phosphorylation must be a consequence of alterations in signalling pathways that do not culminate in cell death.

Though the connection between the PI3K/AKT/mTOR pathway and glycolysis involves a very intricate molecular machinery and signal transduction processes [reviewed by [34,53]], one of the downstream effectors of this pathway, the hypoxia-inducible factor 1 (HIF-1), seems to be a key element. Activation of the PI3K/AKT/mTOR pathway increases the levels of HIF-1α and inhibition of PI3K with LY294002 or wortmannin impairs its expression [54]. Both activated AKT by itself and HIF-1α were shown to stimulate glycolysis by inducing the expression of glucose transporters and of several glycolytic enzymes (reviewed by [55]). According to bLf putative inhibitory effect towards the PI3K/AKT/mTOR pathway in highly metastatic cancer cells, herein we show that treatment of these cells with bLf leads to inhibition of glycolysis and glycolytic capacity. Apart from PI3K/AKT/mTOR, an intimate regulation exists between glucose flux and V-ATPase, as reviewed by [33]. Indeed, glucose deprivation is the classical trigger of the disassembly of the two domains of V-ATPase, which impairs the functioning of the proton pump. On the other hand, V-ATPase interacts with different glycolysis regulators [33]. One example is the glycolytic enzyme aldolase that was shown to bind to subunit E of V-ATPase [56]. Deletion of V-ATPase

subunit *c* in highly metastatic esophageal cancer cells also resulted in glucose metabolism hindering, and reduction of glucose uptake and glycolytic enzymes expression [57]. Accordingly, we found that bLf-induced V-ATPase inhibition causes glycolysis impairment. Finally, an axis connecting glycolysis, PI3K and V-ATPase was identified in a study showing that the glucose-dependent V-ATPase trafficking to the plasma membrane in kidney cells requires PI3K, as its inhibition abolished plasma membrane staining, and a constitutively active PI3K restored the plasmalemmal localization in glucose-repressed cells [58]. If this causal inhibition of V-ATPase trafficking to the plasma membrane also occurs in bLf-treated cells, it may further contribute to amplify the consequences of the inhibition of V-ATPase activity by bLf. Thus, the bLf-mediated effect on both PI3K/AKT and V-ATPase, and the subsequent intracellular acidification, may contribute to the outcome of glycolysis inhibition.

4.5 Conclusion

Altogether, the data accumulated so far support the idea that bLf operates through a bidirectional mode by double targeting V-ATPase proton pumping activity and lipid rafts integrity of highly metastatic cancer cells, which overexpress this proton pump and exhibit high levels of DRMs [52,59]. Bearing in mind the aforementioned information and our own data, we hypothesize that upon plasmmalemmal V-ATPase inhibition by bLf, the overall ΔpH is perturbed leading to decreased extracellular acidification rate, cytosolic acidification [7] and lysosomal alkalinization [11]. This leads to intracellular trafficking perturbations, trapping of cholesterol likely inside the endo/lysosomes, its subsequent depletion from the plasma membrane and ensuing disruption of cholesterol-rich lipid rafts. As a consequence, PI3K/AKT pathway components are downregulated, impairing glycolysis and leading to cell proliferation inhibition [11] and cell death induction through apoptosis [7,11] (Figure 4.8). These new molecular insights can pave the way for the development of Lf-based anticancer therapies targeted to cancer cells harbouring V-ATPase at the plasma membrane cholesterol-rich patches.

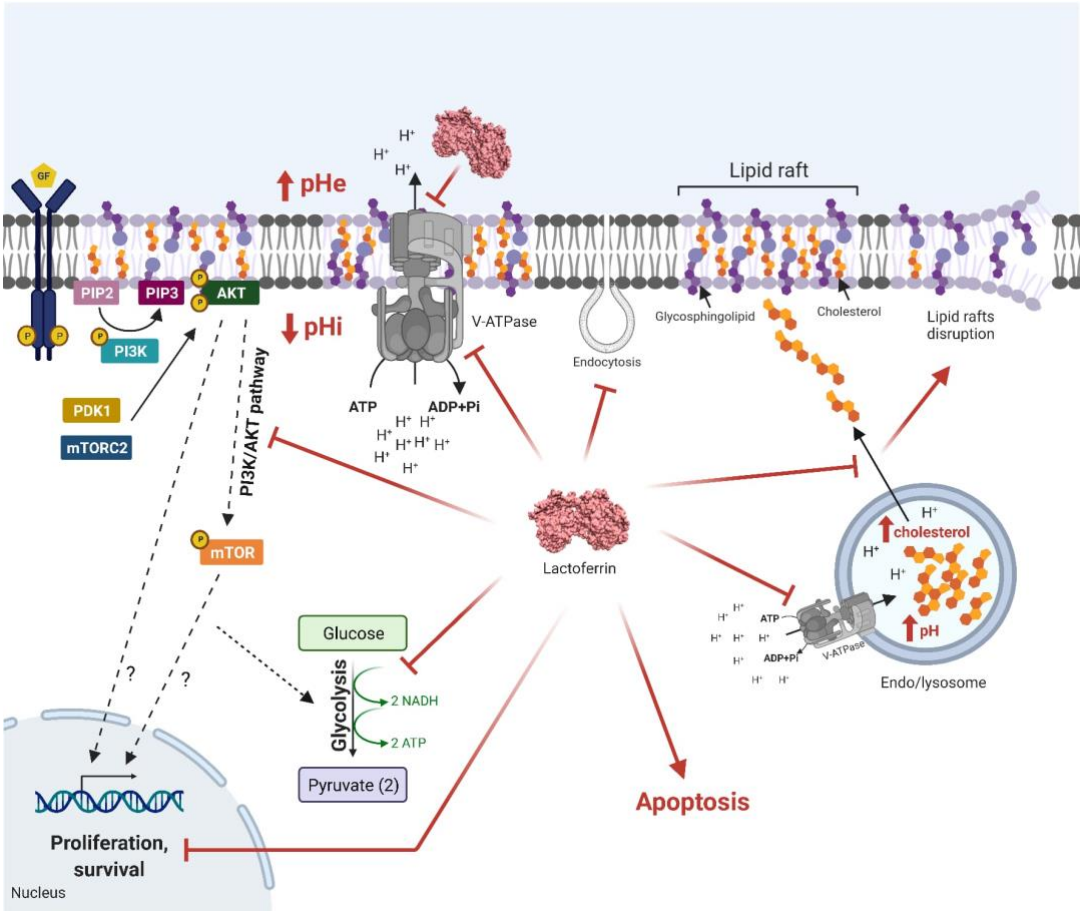

Figure 4.8: Working model on the anticancer activity of bLf against highly metastatic cancer cells. Upon inhibition of plasmmalemmal V-ATPase by bLf, the intracellular pH (pHi) decreases while the extracellular pH (pHe) and lysosomal pH (pHlys) increase. These pH alterations perturb cellular trafficking, leading to intracellular cholesterol accumulation (possibly at the endo/lysosomes), depleting cholesterol from the plasma membrane and inhibiting endocytosis. Consequently, cholesterol-rich lipid rafts are disrupted and the PI3K/AKT pathway is inhibited, which culminates in glycolysis and cell proliferation impairment and apoptotic cell death, either via mTOR or other still unknown downstream effectors. The glycolysis inhibition can either occur directly or as a consequence of PI3K/AKT/mTOR pathway inhibition or through an interaction with other glycolytic regulators. Created with BioRender.com.

References

1. Baruthio F, Quadroni M, Rüegg C, Mariotti A. Proteomic analysis of membrane rafts of melanoma cells identifies protein patterns characteristic of the tumor progression stage. Proteomics. 2008;8: 4733–47. doi:10.1002/pmic.200800169
2. Whitton B, Okamoto H, Packham G, Crabb SJ. Vacuolar ATPase as a potential therapeutic target and mediator of treatment resistance in cancer. Cancer Med. 2018;7: 3800–3811. doi:10.1002/cam4.1594
3. Hryniewicz-Jankowska A, Augoff K, Biernatowska A, Podkalicka J, Sikorski AF. Membrane rafts as a novel target in cancer therapy. Biochim Biophys Acta - Rev Cancer. 2014;1845: 155–165. doi:10.1016/j.bbcan.2014.01.006

4. Badana AK, Chintala M, Gavara MM, Naik S, Kumari S, Kappala VR, et al. Lipid rafts disruption induces apoptosis by attenuating expression of LRP6 and survivin in triple negative breast cancer. Biomed Pharmacother. 2018;97: 359–368. doi:10.1016/j.biopha.2017.10.045

5. Gupta VK, Sharma NS, Kesh K, Dauer P, Nomura A, Giri B, et al. Metastasis and chemoresistance in CD133 expressing pancreatic cancer cells are dependent on their lipid raft integrity. Cancer Lett. 2018;439: 101–112. doi:10.1016/j.canlet.2018.09.028

6. Santos-Pereira C, Andrés MT, Chaves SR, Fierro JF, Gerós H, Manon S, et al. Lactoferrin perturbs lipid rafts and requires integrity of Pma1p-lipid rafts association to exert its antifungal activity against *Saccharomyces cerevisiae*. Int J Biol Macromol. 2021;171: 343–357. doi:10.1016/j.ijbiomac.2020.12.224

7. Pereira CS, Guedes JP, Gonçalves M, Loureiro L, Castro L, Gerós H, et al. Lactoferrin selectively triggers apoptosis in highly metastatic breast cancer cells through inhibition of plasmalemmal V-H^+-ATPase. Oncotarget. 2016;7: 62144–62158. doi:10.18632/oncotarget.11394

8. Sennoune SR, Bakunts K, Martínez GM, Chua-Tuan JL, Kebir Y, Attaya MN, et al. Vacuolar H^+-ATPase in human breast cancer cells with distinct metastatic potential: distribution and functional activity. Am J Physiol Cell Physiol. 2004;286: C1443–C1452. doi:10.1152/ajpcell.00407.2003

9. Perut F, Avnet S, Fotia C, Baglìo SR, Salerno M, Hosogi S, et al. V-ATPase as an effective therapeutic target for sarcomas. Exp Cell Res. 2014;320: 21–32. doi:10.1016/j.yexcr.2013.10.011

10. Smith GA, Howell GJ, Phillips C, Muench SP, Ponnambalam S, Harrison MA. Extracellular and luminal pH regulation by vacuolar H^+-ATPase isoform expression and targeting to the plasma membrane and endosomes. J Biol Chem. 2016;291: 8500–8515. doi:10.1074/jbc.M116.723395

11. Guedes J, Pereira C, Rodrigues L, Côrte-real M. Bovine milk lactoferrin selectively kills highly metastatic prostate cancer PC-3 and osteosarcoma MG-63 cells *in vitro*. Front Oncol. 2018;8: 1–12. doi:10.3389/fonc.2018.00200

12. Maekawa M, Fairn GD. Complementary probes reveal that phosphatidylserine is required for the proper transbilayer distribution of cholesterol. J Cell Sci. 2015;128: 1422–1433. doi:10.1242/jcs.164715

13. Kamerkar S, Lebleu VS, Sugimoto H, Yang S, Ruivo CF, Melo SA, et al. Exosomes facilitate therapeutic targeting of oncogenic KRAS in pancreatic cancer. Nature. 2017;546: 498–503. doi:10.1038/nature22341

14. Koressaar T, Remm M. Enhancements and modifications of primer design program Primer3. Bioinformatics. 2007;23: 1289–1291. doi:10.1093/bioinformatics/btm091

15. Ye J, Coulouris G, Zaretskaya I, Cutcutache I, Rozen S, Madden TL. Primer-BLAST: a tool to design target-specific primers for polymerase chain reaction. BMC Bioinformatics. 2012;13: 134. doi:10.1186/1471-2105-13-134

16. Livak KJ, Schmittgen TD. Analysis of relative gene expression data using real-time quantitative PCR and the $2^{-\Delta\Delta C_T}$ method. Methods. 2001;25: 402–408. doi:10.1006/meth.2001.1262

17. Kruger NJ. The Bradford method for protein quantitation. In: Walker JM (eds) The Protein Protocols Handbook, Springer Protocols Handbooks. Humana Press, Totowa, NJ; 2009. pp 17–24. doi:10.1007/978-1-59745-198-7_4

18. von Haller PD, Donohoe S, Goodlett DR, Aebersold R, Watts JD. Mass spectrometric characterization of proteins extracted from Jurkat T cell detergent-resistant membrane domains. Proteomics. 2001;1: 1010–1021. doi:10.1002/1615-9861(200108)1:8<1010::aid-prot1010>3.0.co;2-l

19. Foster LJ, De Hoog CL, Mann M. Unbiased quantitative proteomics of lipid rafts reveals high specificity for signaling factors. Proc Natl Acad Sci U S A. 2003;100: 5813–5818. doi:10.1073/pnas.0631608100

20. Maxfield FR, Wüstner D. Analysis of Cholesterol Trafficking with Fluorescent Probes. Methods Cell Biol. 2012;108: 367–393. doi:10.1016/B978-0-12-386487-1.00017-1

21. Mahammad S, Parmryd I. Cholesterol depletion using methyl-β-cyclodextrin. In: Owen D (eds) Methods in Membrane Lipids: Second Edition. Humana Press, New York; 2014. pp 91–102. doi:10.1007/978-1-4939-1752-5

22. Lu H, Sun TX, Bouley R, Blackburn K, McLaughlin M, Brown D. Inhibition of endocytosis causes phosphorylation (S256)-independent plasma membrane accumulation of AQP2. Am J Physiol - Ren Physiol. 2004;286: 233–243. doi:10.1152/ajprenal.00179.2003

23. Escrevente C, Keller S, Altevogt P, Costa J. Interaction and uptake of exosomes by ovarian cancer cells. BMC Cancer. 2011;11: 108. doi:10.1186/1471-2407-11-108

24. Kozik P, Hodson NA, Sahlender DA, Simecek N, Soromani C, Wu J, et al. A human genome-wide screen for regulators of clathrin-coated vesicle formation reveals an unexpected role for the V-ATPase. Nat Cell Biol. 2013;15: 50–60. doi:10.1038/ncb2652

25. Reis-Sobreiro M, Roue G, Moros A, Gajate C, De La Iglesia-Vicente J, Colomer D, et al. Lipid raft-mediated Akt signaling as a therapeutic target in mantle cell lymphoma. Blood Cancer J. 2013;3. doi:10.1038/bcj.2013.15

26. Arcaro A, Aubert M, Espinosa del Hierro ME, Khanzada UK, Angelidou S, Tetley TD, et al. Critical role for lipid raft-associated Src kinases in activation of PI3K-Akt signalling. Cell Signal. 2007;19: 1081–1092. doi:10.1016/j.cellsig.2006.12.003

27. Ediriweera MK, Moon JY, Nguyen YT-K, Cho SK. 10-Gingerol targets lipid rafts associated PI3K/Akt signaling in radio-resistant triple negative breast cancer cells. Molecules. 2020;25: 3164. doi:10.3390/molecules25143164

28. Chea C, Miyauchi M, Inubushi T, Ayuningtyas NF, Subarnbhesaj A, Nguyen PT, et al. Molecular mechanism of inhibitory effects of bovine lactoferrin on the growth of oral squamous cell carcinoma. PLoS One. 2018;13: 1–19. doi:10.1371/journal.pone.0191683

29. Xiao Y, Monitto CL, Minhas KM, Sidransky D. Lactoferrin down-regulates G1 cyclin-dependent kinases during growth arrest of head and neck cancer cells. Clin Cancer Res. 2004;10: 8683–8686. doi:10.1158/1078-0432.CCR-04-0988

30. Xu XX, Jiang HR, Li HB, Zhang TN, Zhou Q, Liu N. Apoptosis of stomach cancer cell SGC-7901 and regulation of Akt signaling way induced by bovine lactoferrin. J Dairy Sci. 2010;93: 2344–2350. doi:10.3168/jds.2009-2926

31. Alzahrani AS. PI3K/Akt/mTOR inhibitors in cancer: At the bench and bedside. Semin Cancer Biol. 2019;59: 125–132. doi:10.1016/j.semcancer.2019.07.009

32. Mollinedo F, Gajate C. Lipid rafts as signaling hubs in cancer cell survival/death and invasion: Implications in tumor progression and therapy. J Lipid Res. 2020;61: 611–635.

doi:10.1194/jlr.TR119000439

33. Hayek SR, Rane HS, Parra KJ. Reciprocal regulation of V-ATPase and glycolytic pathway elements in health and disease. Front Physiol. 2019;10: 1–9. doi:10.3389/fphys.2019.00127

34. Xie Y, Shi X, Sheng K, Han G, Li W, Zhao Q, et al. PI3K/Akt signaling transduction pathway, erythropoiesis and glycolysis in hypoxia. Mol Med Rep. 2019;19: 783–791. doi:10.3892/mmr.2018.9713

35. Bezault JA, Bhimani R, Wiprovnick J, Furmanski P. Human lactoferrin inhibits growth of solid tumors and development of experimental metastases in mice. Cancer Res. 1994;54: 2310–2312.

36. Parikh PM, Vaid A, Advani SH, Digumarti R, Madhavan J, Nag S, et al. Randomized, double-blind, placebo-controlled phase II study of single-agent oral talactoferrin in patients with locally advanced or metastatic non-small-cell lung cancer that progressed after chemotherapy. J Clin Oncol. 2011;29: 4129–4136. doi:10.1200/jco.2010.34.4127

37. Hayes TG, Falchook GS, Varadhachary A. Phase IB trial of oral talactoferrin in the treatment of patients with metastatic solid tumors. Invest New Drugs. 2010;28: 156–162. doi:10.1007/s10637-009-9233-9

38. Ramalingam S, Crawford J, Chang A, Manegold C, Perez-Soler R, Douillard JY, et al. Talactoferrin alfa versus placebo in patients with refractory advanced non-small-cell lung cancer (FORTIS-M trial). Ann Oncol. 2013;24: 2875–2880. doi:10.1093/annonc/mdt371

39. Costa GA, de Souza SB, da Silva Teixeira LR, Okorokov LA, Arnholdt ACV, Okorokova-Façanha AL, et al. Tumor cell cholesterol depletion and V-ATPase inhibition as an inhibitory mechanism to prevent cell migration and invasiveness in melanoma. Biochim Biophys Acta - Gen Subj. 2018;1862: 684–691. doi:10.1016/j.bbagen.2017.12.006

40. Lafourcade C, Sobo K, Kieffer-Jaquinod S, Garin J, van der Goot FG. Regulation of the V-ATPase along the endocytic pathway occurs through reversible subunit association and membrane localization. PLoS One. 2008;3. doi:10.1371/journal.pone.0002758

41. Xu M, Xia M, Li XX, Han WQ, Boini KM, Zhang F, et al. Requirement of translocated lysosomal V1 H^+-ATPase for activation of membrane acid sphingomyelinase and raft clustering in coronary endothelial cells. Mol Biol Cell. 2012;23: 1546–1557. doi:10.1091/mbc.E11-09-0821

42. Bartel K, Winzi M, Ulrich M, Koeberle A, Menche D, Werz O, et al. V-ATPase inhibition increases cancer cell stiffness and blocks membrane related Ras signaling - A new option for HCC therapy. Oncotarget. 2017;8: 9476–9487. doi:10.18632/oncotarget.14339

43. Enrich C, Rentero C, Hierro A, Grewal T. Role of cholesterol in SNARE-mediated trafficking on intracellular membranes. J Cell Sci. 2015;128: 1071–1081. doi:10.1242/jcs.164459

44. Jiang R, Lopez V, Kelleher SL, Lönnerdal B. Apo- and holo-lactoferrin are both internalized by lactoferrin receptor via clathrin-mediated endocytosis but differentially affect ERK-signaling and cell proliferation in caco-2 cells. J Cell Physiol. 2011;226: 3022–3031. doi:10.1002/jcp.22650

45. Zhang Y, Nicolau A, Lima CF, Rodrigues LR. Bovine lactoferrin induces cell cycle arrest and inhibits mTOR signaling in breast cancer cells. Nutr Cancer. 2014;66: 1371–85. doi:10.1080/01635581.2014.956260

46. Rawat P, Kumar S, Sheokand N, Raje CI, Raje M. The multifunctional glycolytic protein glyceraldehyde-3-phosphate dehydrogenase (GAPDH) is a novel macrophage lactoferrin receptor. Biochem Cell Biol. 2012;90: 329–338. doi:10.1139/o11-058

47. Gonda A, Kabagwira J, Senthil GN, Wall NR. Internalization of exosomes through receptor-mediated endocytosis. Mol Cancer Res. 2019;17: 337–347. doi:10.1158/1541-7786.MCR-18-0891

48. Ronquist KG, Sanchez C, Dubois L, Chioureas D, Fonseca P, Larsson A, et al. Energy-requiring uptake of prostasomes and PC3 cell-derived exosomes into non-malignant and malignant cells. J Extracell Vesicles. 2016;5. doi:10.3402/jev.v5.29877

49. Koumangoye RB, Sakwe AM, Goodwin JS, Patel T, Ochieng J. Detachment of breast tumor cells induces rapid secretion of exosomes which subsequently mediate cellular adhesion and spreading. PLoS One. 2011;6. doi:10.1371/journal.pone.0024234

50. Ausili A, Torrecillas A, Aranda FJ, Mollinedo F, Gajate C, Corbalán-García S, et al. Edelfosine is incorporated into rafts and alters their organization. J Phys Chem B. 2008;112: 11643–11654. doi:10.1021/jp802165n

51. Koubek EJ, Weissenrieder JS, Neighbors JD, Hohl RJ. Schweinfurthins: Lipid Modulators with Promising Anticancer Activity. Lipids. 2018;53: 767–784. doi:10.1002/lipd.12088

52. Li YC, Park MJ, Ye SK, Kim CW, Kim YN. Elevated levels of cholesterol-rich lipid rafts in cancer cells are correlated with apoptosis sensitivity induced by cholesterol-depleting agents. Am J Pathol. 2006;168: 1107–1118. doi:10.2353/ajpath.2006.050959

53. Agani F, Jiang B-H. Oxygen-independent regulation of HIF-1: novel involvement of PI3K/AKT/mTOR pathway in cancer. Curr Cancer Drug Targets. 2013;13: 245–251. doi:10.2174/1568009611313030003

54. Jiang BH, Jiang G, Zheng JZ, Lu Z, Hunter T, Vogt PK. Phosphatidylinositol 3-kinase signaling controls levels of hypoxia-inducible factor 1. Cell Growth Differ. 2001;12: 363–369.

55. Hoxhaj G, Manning BD. The PI3K–AKT network at the interface of oncogenic signalling and cancer metabolism. Nat Rev Cancer. 2020;20: 74–88. doi:10.1038/s41568-019-0216-7

56. Lu M, Holliday LS, Zhang L, Dunn WA, Gluck SL. Interaction between aldolase and vacuolar H^+-ATPase. Evidence for direct coupling of glycolysis to the ATP-hydrolyzing proton pump. J Biol Chem. 2001;276: 30407–30413. doi:10.1074/jbc.M008768200

57. Son SW, Chau GC, Kim S, Um SH. Vacuolar H^+-ATPase subunit V_0C regulates aerobic glycolysis of esophageal cancer cells via PKM2 signaling. Cells. 2019;8: 1137. doi:10.3390/cells8101137

58. Sautin YY, Lu M, Gaugler A, Zhang L, Gluck SL. Phosphatidylinositol 3-Kinase-mediated effects of glucose on vacuolar H^+-ATPase assembly, translocation, and acidification of intracellular compartments in renal epithelial cells. Mol Cell Biol. 2005;25: 575–589. doi:10.1128/mcb.25.2.575-589.2005

59. Couto-Vieira J, Nicolau-Neto P, Costa EP, Figueira FF, Simão T de A, Okorokova-Façanha AL, et al. Multi-cancer V-ATPase molecular signatures: A distinctive balance of subunit C isoforms in esophageal carcinoma. EBioMedicine. 2020;51: 102581. doi:10.1016/j.ebiom.2019.11.042

CHAPTER 5

Computational approach to unveil the interaction between lactoferrin and V-ATPase

This chapter is adapted from the following publication:

Cátia Santos-Pereira, Juliana F. Rocha, Henrique S. Fernandes, Lígia R. Rodrigues, Manuela Côrte-Real, Sérgio F. Sousa. **The milk-derived lactoferrin inhibits V-ATPase activity by targeting its V1 domain**. Under minor revision in the *International Journal of Biological Macromolecules*

5.1. Background

In the search for the molecular mechanisms underlying both the Lf anticancer and the antifungal activities, in our previous work, we identified for the first time the proton pump V-ATPase as a Lf target [1–3]. However, the molecular basis of this interaction is still unknown. Therefore, in this chapter, we sought to develop a computational approach to understand how Lf and V-ATPase interact and to shed light on the putative residues of both proteins that are critical for their interaction. For this purpose, an *in silico* approach that takes into account different conformational states of both proteins was used to predict the protein-protein complexes by molecular docking, followed by further refinement through molecular dynamics simulations and free energy calculations.

5.2. Methods

5.2.1 Methodology overview

The computational pipeline used in this work is depicted in Figure 5.1. Before performing molecular docking, which is a computational method used to predict the preferred binding pose(s) between two molecules [4], molecular dynamics (MD) simulations of V-ATPase and Lf were carried out. MD is a technique that integrates the Newton's equation of motion for predicting the movements of atoms given the position of the surrounding atoms, as a function of time [5]. This generated a series of conformations of both proteins in solution that were then clustered to identify 10 representative structures of each protein, which were later used in the molecular docking study. This approach allows the sampling of several protein conformations and, consequently, of their interaction. Afterwards, the molecular docking software HADDOCK (High Ambiguity Driven protein–protein Docking) [6] was used to predict the complexes between V-ATPase and Lf. The best scored 20 complexes generated by HADDOCK were then embedded into a membrane bilayer model and subjected to MD simulations. The Molecular Mechanics-Generalized Born Surface Area (MM-GBSA) method [7] was next applied to the equilibrated part of these MD simulations to rescore the complexes based on the free binding energy. Moreover, it was used to calculate the individual contribution of each amino acid and predict the residues from both proteins that are more important for the protein-protein association. Visual Molecular Dynamics (VMD) [8] was used for all visualizations.

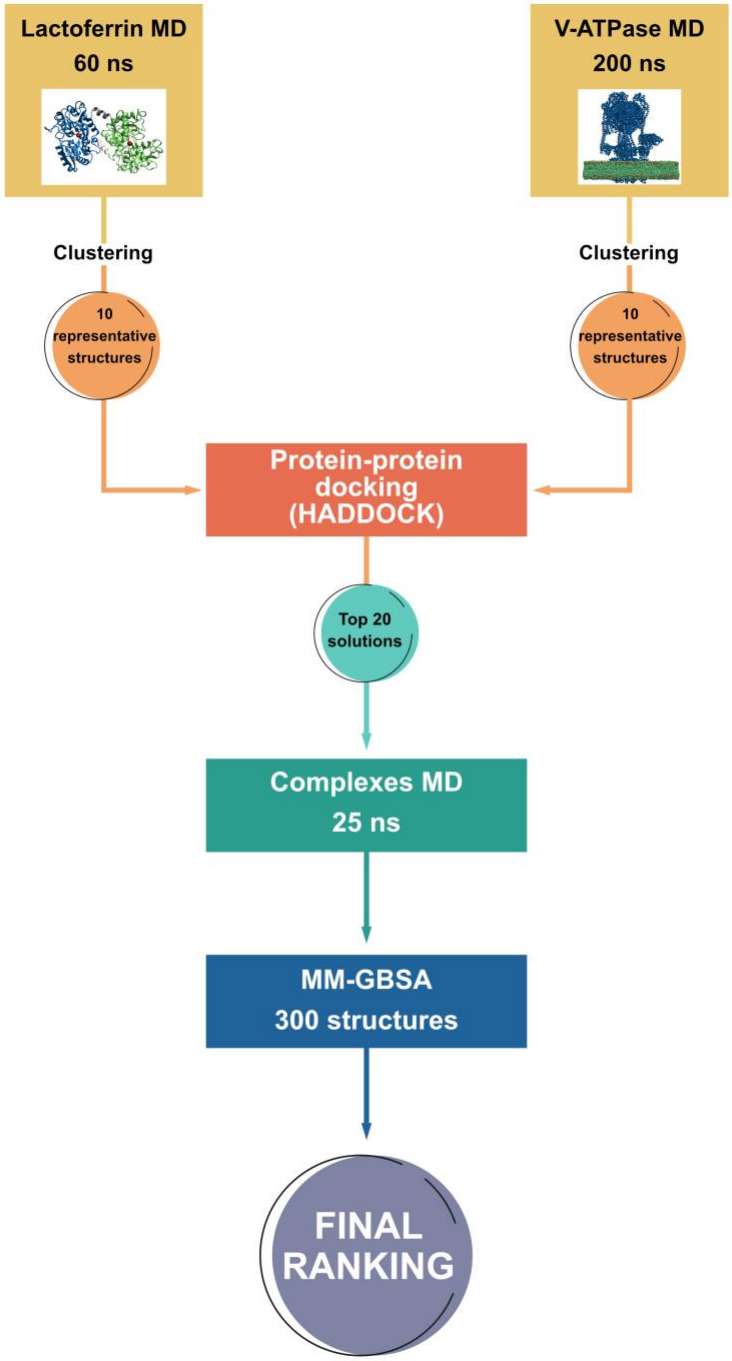

Figure 5.1: Flowchart of the computational pipeline used in this work. ns, nanoseconds; MD, molecular dynamics; HADDOCK, High Ambiguity Driven protein–protein Docking; MM-GBSA, Molecular Mechanics-Generalized Born Surface Area.

5.2.2 Lactoferrin model setup and molecular dynamics simulations

After a literature review and search on the Protein Databank (https://www.rcsb.org) of all available Lf structures (Table A2, Appendix), the 1LFG structure of diferric human lactoferrin [9], obtained by X-ray crystallography at a resolution of 2.2 Å without any mutation, was chosen. The PropKA server version 3.0 [10] was employed to predict the protonation states of the different amino acid residues considering the

physiological pH (pH 7). Lysine and arginine residues were modelled as positively charged, while aspartate and glutamate residues as negatively charged. Histidine residues were modelled as neutral, with a hydrogen at the epsilon-N or delta-N according to the surrounding.

The 1LFG structure contains two iron-binding sites, where one Fe^{3+} and one CO_3^{2-} ions are present along with two tyrosine, one aspartate and one histidine residues (see Chapter 2.1). The iron-coordinated tyrosine and histidine residues (Tyr92, Tyr192, His253, Tyr435, Tyr528 and His597) were modelled as deprotonated according to the literature [11]. The iron coordination spheres were parameterized using the python-based metal center parameter builder MCPB.py [12]. This tool allows the building of force field parameters for the simulation of metal complexes using the bonded model approach, which treats the interaction between metal ions and its ligating residues via bond, angle, dihedral, electrostatic and van der Waals (VDW) terms. These calculations were performed by quantum mechanics using the Gaussian 09 software with Density Functional Theory (DFT) and the B3LYP functional and 6-31G(d) basis set [13]. MCPB and the bonded model approach have been well validated in the past for the simulation of several different metalloproteins and enzymes [14,15]. The system was prepared using AMBER 19 software package [16]. The LEAP program was used to add the hydrogen atoms and to build the topology and parameters of the protein with the biomolecular force fields *ff14SB* [17] for proteins, and the general amber force field *gaff2* [18] for organic molecules. The main empirical biomolecular force field used in this work describes the atomic interactions in molecules by decomposing the atoms motion in intramolecular/bonded energetic terms (E_{bonded}) that consider the bond stretching (E_{bonds}), angle bending (E_{angles}) and dihedral torsion ($E_{dihedrals}$); and intermolecular/electrostatic energetic terms ($E_{non\text{-}bonded}$) that take into account the electrostatic ($E_{electrostatic}$) and van der Waals interactions ($E_{van\ der\ Waals}$) (Equations 1 and 2). This results in a simple equation to describe the potential energy (V) as a function of the atomic positions of the atoms in the system (**r**) [19]:

$$V(\mathbf{r}) = E_{bonded} + E_{non\text{-}bonded} \quad \text{(Eq. 1)}$$

$$V(\mathbf{r}) = E_{bonds} + E_{angles} + E_{dihedrals} + E_{electrostatic} + E_{van\ der\ Waals} \quad \text{(Eq. 2)}$$

$$V(\mathbf{r}) = \sum_{bonds} K_r \left(b - b_{\mathrm{eq}}\right)^2 + \sum_{angles} K_\theta \left(\theta - \theta_{\mathrm{eq}}\right)^2 + \sum_{dihedrals} \left(\frac{V_n}{2}\right)[1 + \cos(n\emptyset - \gamma)] + \sum_{i<j} \left[\frac{A_{ij}}{R_{ij}^{12}} - \frac{B_{ij}}{R_{ij}^{6}} + \frac{q_i q_j}{\varepsilon R_{ij}}\right] \quad \text{(Eq. 3)}$$

In Equation 3, K_r is the bond force constant, b is the bond length and b_{eq} the correspondent bond equilibrium value; K_θ is the angle force constant, θ is the angle amplitude and θ_{eq} the correspondent equilibrium value; $V_n/2$ is the torsional force constant, n is the torsional angle multiplicity, φ is the angle amplitude, and γ is the phase dihedral; ij are the atomic pairs, A_{ij} reflects the degree of "stickiness" of the van der Waals attraction while B_{ij} the degree of "hardness" of the atoms, R_{ij} is the interatomic distance between atoms i and j, ε is the dielectric constant, q_i is the charge of atom i, and q_j the charge of atom j [19].

Periodic boundary conditions were applied in all directions using a cubic box with a minimum distance between the protein and the box wall set to 12 Å. Water molecules were added to the system using the TIP3P function and the *tip3p* force field for water and associated ions. K^+ and Cl^- ions were randomly added to the system to neutralize charges, as well as to achieve a 0.15 M concentration, which approaches the physiological regime. The dimension of the system was 92 889 atoms. The system was then submitted to a 4-step energy minimization process using the SANDER module from AMBER 19 to remove clashes before the MD simulation. Firstly, harmonic forces were used to restrain all atoms positions except those from water molecules (5,000 steps), then constrains were applied only to the heavy atoms allowing the energy minimization of the hydrogen atoms (5,000 steps), next only to the backbone alpha carbons (Cα) and nitrogens were constrained (5,000 steps), and finally all constraints were removed to allow a full energy minimization (25,000 steps). A 20 ps equilibration was subsequently performed in the canonical thermodynamic (NVT) ensemble with constant volume, where the temperature of the system was gradually increased to 303.15K (30˚C) using Langevin thermostat [20,21]. A 60 ns simulation was then conducted with Gromacs software [22] in an isothermal-isobaric thermodynamic ensemble (NPT) at 303.15K using the Berendsen temperature coupling scheme [23]. Pressure was maintained constant (1 bar) using the Parrinello-Rahman barostat with isotropic molecule-based scaling. Particle-Mesh Ewald (PME) method was used for long-range electrostatics, and the non-bond interaction cut-off radius was set to 10 Å. The bond lengths involving hydrogen atoms were constrained using the linear constraint solver (LINCS) algorithm [24], allowing the integration of the equation of motion with a 2 fs time step. The MD trajectory was sampled every 2 ps. The MD simulation was analyzed in terms of backbone root-mean-square deviation (Cα-RMSD) and solvent accessible surface area (SASA) with the CPPTRAJ module of AMBER 19. Clustering was performed with values retrieved from the last 55 ns of the simulation using the hierarchical agglomerative approach, which is based on the distance between frames calculated via the Cα-RMSD, to obtain 10 representative structures of the MD trajectory for further docking analysis.

5.2.3 Modelling of V-ATPase and molecular dynamics simulations

At the time this work started, no human V-ATPase structure was available, thus a list of all V-ATPase structures from *Saccharomyces cerevisiae* was compiled (Table A3, Appendix). From all those structures, only three contained the biological assembly of the entire complex (3J9T-V, 607V-X and 5VOX-Z) obtained by cryo-electron microscopy (cryo-EM) with poor resolution values (6.6 – 6.9 Å). Structure 6OTV [25], which has the better resolution, has only backbone information and no sidechains. Thus, we chose the 3J9T [26], which has backbone and sidechains of all residues. However, this structure misses some subunits of the V_o domain, namely subunits *e* and the assembly factor Voa1, and does not distinguish between *c*, *c'* and *c''* subunits. In this sense, through molecular modelling, we constructed a structure that contains the V_1 subunits of 3J9T and the V_o subunits of 6O7T [25]. The latter has a much better resolution (3.2 Å) and all the subunits. Very recently, the first cryo-EM structure of human V-ATPase at up to 2.9 Å resolution was reported, revealing an overall similar structure with our model [27]. After building the system, the PACKMOL-memgen tool [28] from Ambertools was used to build a membrane lipid bilayer system, where V-ATPase was embedded and positioned parallel to the vertical axis of the membrane. The choice of the lipid types and ratios was based on a work performed by Jo and co-workers [29], who built lipid bilayers that resemble yeast membranes. Thus, the membrane is composed of dipalmitoyl phosphatidylcholine (DPPC), dioleoyl phosphatidylcholine (DOPC), 1-palmitoyl-2-oleoyl phosphatidylethanolamine (POPE), 1-palmitoyl-2-oleoyl phosphatidylamine (POPA), 1-palmitoyl-2-oleoyl phosphatidylserine (POPS) and cholesterol (CHL) in a ratio of 2:10:6:2:1, respectively. The system was placed in a rectangular TIP3P water box with a minimum distance between the protein and the box boundaries of 15 Å, and periodic boundary conditions. Protonation states for all amino acids at pH 7 were considered. The width of the leaflet was set to 23 Å. K^+ and Cl^- ions were included to neutralize the charges and to achieve a final concentration of 0.15 M, as above described for Lf. The size of the system was 1 802 167 atoms. In addition to the force fields used for Lf MD, the *lipid17* force field [30] was also used for the V-ATPase MD simulation. The system was then subjected to a five-stage refinement protocol using the SANDER module from AMBER 19, in which constrains in the protein/lipids were progressively removed. In the first stage, constraints were applied to all atoms expect water (5,000 steps); in a second stage, the constraints were limited to all heavy atoms allowing the hydrogens added by the LEAP program from AMBER 19 to adjust (5,000 steps); in a third stage, constrains were removed from the lipid atoms to allow their fine-tuning (5,000 steps); in a fourth stage, only the backbone atoms were constrained (5,000 steps); and finally, in the fifth stage, all constrains were removed and a full energy minimization of the system (50,000 steps) was performed. Next, the system was heated to 303.15 K by two sequential

equilibration runs keeping the lipids fixed by applying a harmonic restraint of 10 kcal/(mol Å^2). The MD simulations were carried out using the PMEMD module of AMBER 20 [31]. First the system was heated to 100 K using a Langevin thermostat in a NVT ensemble (50 ps); and, in the second step, heated to the production temperature of 303.15 K using a semi-isotropic Berendsen barostat to equilibrate the pressure in a NPT ensemble (50 ps). Aiming to equilibrate the system's periodic boundary dimensions and density, a hold step of 125 ps was performed before MD production, where the lipid restraints were removed and the width of the non-bonded "skin" was increased to 5 Å to cope with the changes in box dimensions during simulation. All production MD simulations were done in the NPT ensemble using the Langevin thermostat to maintain temperature at 303.15 K. Surface tension was kept constant in the xy plane using the semi-isotropic Berendsen pressure coupling algorithm with the pressure set to 1 bar. The time step was 2 fs and the non-bonded interaction cut-off radius was set to 10 Å. Bond lengths using hydrogens were constrained using the SHAKE algorithm [32]. A total simulation time of 200 ns was reached. The trajectory was sampled every 10 ps. Analysis of the MD simulation in terms of SASA, Cα-RMSD and backbone root-mean-square fluctuation (RMSF) was carried out with the CPPTRAJ module of AMBER 19. Clustering was performed with values retrieved from the last 125 ns of the simulation using the hierarchical agglomerative approach to obtain 10 representative structures of the MD trajectory to be used in the docking step.

5.2.4 Protein-protein docking using HADDOCK

The HADDOCK 2.4 webserver [33] was used to predict the complexes between V-ATPase and Lf. This software uses a data-driven approach to perform the molecular docking process that takes into account a combination of energetics, shape and also experimental data, and was previously shown to have high performance rates in predicting protein-protein interactions [34]. Each of the 10 representative structures of the Lf MD trajectory were docked with the 10 representative structures derived from the V-ATPase MD. Due to the large number of V-ATPase atoms, the protein was separated into the two domains (V_o and V_1) and submitted for docking with Lf, which resulted in a total of 200 independent docking runs. Also, due to the large V-ATPase size, when defining HADDOCK settings, the coarse grain option with Martini [35] was activated. The docking protocol comprises three stages, a rigid-body energy minimization (it0), a semi-flexible refinement (it1) and a final refinement in water (itw) [6]. Since there is no data on the possible binding site, no active or passive residues were defined. Instead, random patches, where ambiguous interaction restraints (AIRs) are randomly defined from accessible residues (>20 % relative accessibility), were used. Since we did not define semi-flexible segments, all accessible residues were

considered. For each docking trial, a different residue from both proteins, as well as their neighbors within 5 Å were selected. For this reason, the sampling was increased to 10,000/400/400 structures for it0, it1 and itw stages, respectively. Clustering was performed using the fraction of common contacts (FCC) with a cut-off of 0.6 and a minimum cluster size of 4. The FCC clustering metric calculates the fraction of inter-protein residue pairs, which are common between complexes [36]. The HADDOCK score (HS) was used to narrow down the large number of possibilities of protein-protein interactions to a small subset. The HS function is a linear weighted sum of energetic terms and buried surface area ($HS = 1E_{vdw} + 0.2E_{elec} + 1E_{desol} + 0.1E_{AIR}$), where each term corresponds to van der Waals, Coulomb electrostatics, desolvation and restraint energies, respectively [37]. The OPLS force field [38] is used to calculate the non-bonded terms (E_{vdw} and E_{elec}), while the E_{desol} is calculated via a SASA-dependent empirical term that estimates the energetic gain/penalty of burying specific parts of the protein when the complex is formed [37]. The top 10 structures from each run were first selected and, afterwards, only the solutions with HS below -150 and whose Lf binding site was not located in the V-ATPase regions that are embedded in the cellular membranes were considered. From those, the top 20 were selected to proceed to MD simulations.

5.2.5 Molecular dynamics simulations of V-ATPase-Lf complexes

After being embedded into a lipid bilayer using PACKMOL-memgen as aforementioned, the 20 top docked complexes were further refined from their docking poses by 25 ns MD simulations using the same MD protocol above described for V-ATPase. RMSD and SASA analysis were performed as above stated with CPPTRAJ.

5.2.6 Binding free energy calculations by the MM-GBSA method

The MM-GBSA method was employed to calculate the binding Gibbs free energy (ΔG_{bind}) of each docking solution and to rank them according to their binding affinities. Free energy refers to the amount of internal energy of the system that can be used to accomplish the thermodynamic processes and determines the likelihood of a given system to remain in a given state. MM-GBSA is a free energy calculation method that exhibits a good balance between computational cost and accuracy [39]. It is widely used to predict protein-protein binding affinities and to evaluate docking solutions [40]. Moreover, it allows the identification of the dominant interactions in a given complex by performing free energy decomposition analysis, which calculates the detailed energetic contributions of the individual residues to the system binding [39]. The MM-PBSA.py script [41] from AMBER 20 [31] was herein used to calculate

the binding free energies of each complex and the energy decomposition method was applied to all residues. A total of 300 structures retrieved from the last 10 ns of each complex MD simulation were used for the analysis. The ΔG_{bind} for each complex, as well as for the residues displaying a higher contribution for the top 4 complexes, are presented.

The free energy of binding is calculated from the difference between the total free energy variation when molecules are in bounded or non-bounded state (Equation 4).

$$\Delta G_{bind} = \Delta G_{complex} - (\Delta G_{protein1} + \Delta G_{protein2}) \quad \text{(Eq. 4)}$$

If $\Delta G_{complex}$ is lower (i.e., more negative) than the sum of the ΔG of the separated proteins, then the the ΔG_{bind} is negative and the association of the proteins is thermodynamically favorable. In the MM-GBSA method, the ΔG_{bind} can be described by the sum of different energy terms (Equation 5):

$$\Delta G = \Delta E_{gas} + \Delta G_{sol} - T\Delta S \quad \text{(Eq. 5)}$$

$$\Delta E_{gas} = \Delta E_{int} + \Delta E_{ELE} + \Delta E_{VDW} \quad \text{(Eq. 6)}$$

$$\Delta G_{sol} = \Delta G_{GB} + \Delta G_{Surf} \quad \text{(Eq. 7)}$$

These energy contributions were computed from the atomic coordinates of the V-ATPase, Lf and the complex. The gas-phase interaction energy (ΔE_{gas}) between V-ATPase and Lf is the sum of electrostatic (ΔE_{ELE}) and van der Waals (ΔE_{VDW}) interaction energies. Since V-ATPase, Lf and the complex V-ATPase-Lf were extracted from the same trajectory, the internal energy change (ΔE_{int}) cancels out (Equation 6). Both polar and non-polar solvation free energy terms contribute to the solvation free energy (ΔG_{sol}) (Equation 7). The polar solvation free energy (ΔG_{GB}) is calculated through a modified Generalized Born (GB) method [7]. The non-polar contribution to the solvation free energy (ΔG_{Surf}) is based on the calculation of the SASA by the Linear Combinations of Pairwise Overlaps (LCPO) method [42]. The entropy term ($T\Delta S$) was neglected in the calculation as it is computationally expensive for large systems and tends to introduce low accurate approximations [41].

5.3. Results

5.3.1 General analysis of the Lf MD simulation

Prior to the docking study, an overall analysis of the MD trajectories that generated different protein conformations to be used in the docking study was performed. Lf structural behaviour along the trajectory

was evaluated using the root-mean-square deviation (RMSD) of the protein Cα. It raises in the first 2.5 ns and then reaches a plateau that exhibits maximal values of deviation of 3-4 Å (Figure 5.2A), indicating that the simulation is stabilized and that the overall structure of the protein was well maintained. For this reason, the last 55 ns of the simulation were considered for all the subsequent analysis. We also assessed the total solvent accessible surface area (SASA) as a measure of the area of the protein prompt to interact with other molecules. It is well stabilized since the beginning of the simulation with an average of 27,202 ± 376 $Å^2$ (Figure 5.2B).

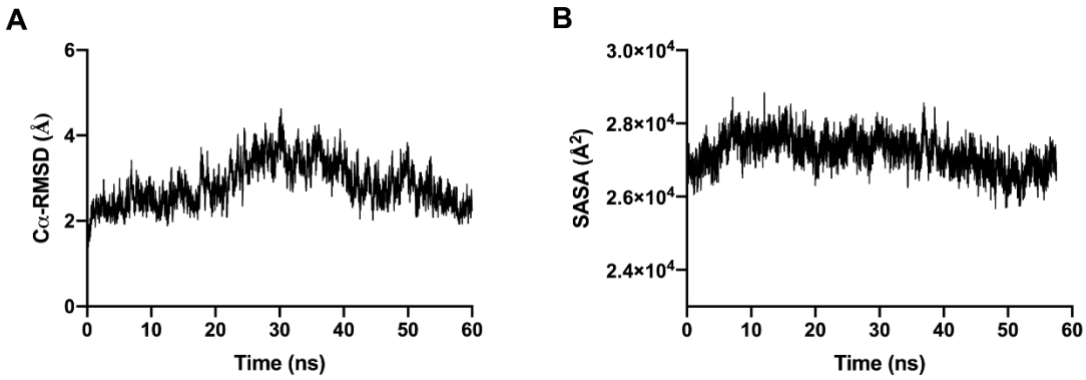

Figure 5.2: Lactoferrin molecular dynamics simulation analysis. (A) RMSD values of the protein backbone Cα atoms as a function of time for the 60 ns of the Lf molecular dynamics simulation, with the final minimized and equilibrated structure as a reference point. **(B)** Variation of the Lf solvent accessible surface area (SASA) along the 60 ns of the simulation.

Afterwards, a clustering method based on the best-fit coordinate RMSD was used taking into account the likeness and conformational variability among the structures generated during the MD simulation, important aspects for the subsequent stages. 10 clusters were created and the total number of frames in each cluster as well as the distribution of the cluster populations along the simulation is depicted in Figure A6 (Appendix). A representative/average structure from each cluster was selected and used in the docking stage.

5.3.2 General analysis of the V-ATPase MD simulation

The V-ATPase model assembled in this study can be observed in Figure 5.3A, where all its 16 subunits are identified. The system was then embedded into a lipid bilayer and subjected to a long MD simulation of 200 ns. The Cα-RMSD undergoes a sudden augment in the first ns of the simulation, then increasing slightly until 125 ns, moment from which the trajectory stabilizes, and the model is well equilibrated exhibiting an average deviation from the initial structure of 7 Å for the entire complex and of 6.5 Å for the V_1 domain. In contrast, the Cα-RMSD of the V_o domain atoms stabilizes right in the beginning

of the MD simulation, showing a much lower average deviation value – 4.0 Å (Figure 5.3B; Table 5.1, 2nd column). Taking into account these observations, the last 125 ns were considered for the clustering analysis. Regarding the SASA of the entire complex, it increases in the first nanoseconds of the simulation and then stabilizes to an average of 318,731 ± 1394 Å^2, with no significant changes being observed along the simulation (Figure 5.3C). From these, an average of about 92,000 Å^2 is devoted to the V_o domain, while about 226,000 Å^2 are accessible to the solvent in the V_1 domain (Table 5.1, 4th column). From these data, it is clear that the majority of the V-ATPase area available to interact with other molecules is located at the cytosolic domain.

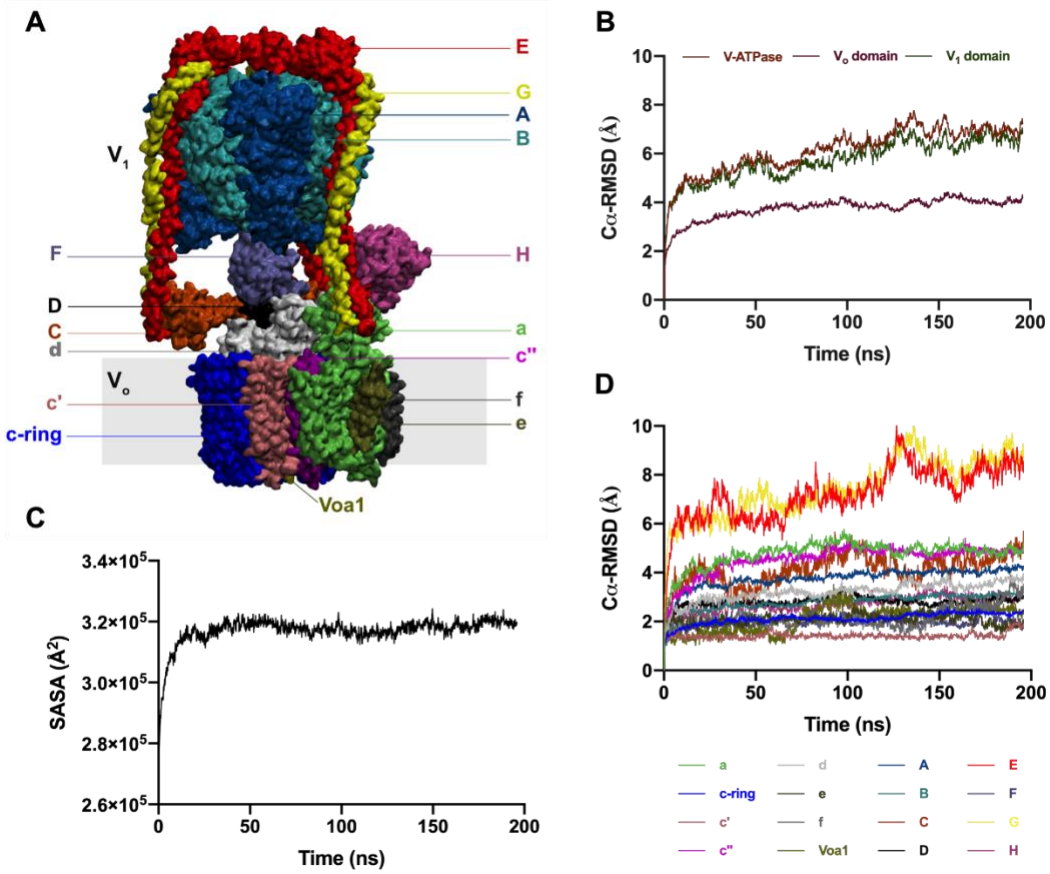

Figure 5.3: V-ATPase molecular dynamics simulation analysis. (A) Structure of the V-ATPase model assembled in this work with each subunit identified in a different colour. **(B)** RMSD representation of the protein Cα atoms as a function of time for the 200 ns of the simulation. The RMSD of atoms belonging to the membrane (V_o) or cytosolic (V_1) domains is also depicted. **(C)** Variation of the V-ATPase solvent accessible surface area (SASA) along the 200 ns of simulation. **(D)** Cα-RMSD of the atoms belonging to the individual V-ATPase subunits. RMSD valued for subunits A, B, E and G correspond to atoms belonging to 3 different chains each whereas the c-ring contains atoms of 8 different chains.

Table 5.1: Analysis of the last 75 ns of the V-ATPase molecular dynamics simulation. Average values of the backbone RMSD, RMSF and SASA calculated from the last 75 ns of the V-ATPase simulation for the whole system, the two domains and the individual subunits. Values are Å or Å^2 ± standard deviation.

V-ATPase/domain/ subunit	Cα-RMSD (Å)	RMSF (Å)	SASA (Å^2)
V-ATPase	7.0±0.2	2.6±0.6	318,731±1394
V_o domain	4.0±0.1	2.4±0.4	92,727±884
V_1 domain	6.5±0.2	2.7±0.7	226,005±1105
A	4.1±0.1	2.4±0.5	67,603±570
B	3.1±0.1	2.2±0.4	45,713±529
C	4.4±0.3	3.2±0.6	20,027±331
D	2.8±0.1	4.1±1.7	9,617±226
E	8.2±0.4	3.9±1.0	36,157±387
F	2.0±0.2	2.0±0.3	5,037±235
G	8.7±0.4	3.6±0.8	19,630±233
H	3.0±0.1	3.0±0.6	21,993±328
a	4.9±0.1	2.3±0.3	29,098±515
c-ring	2.3±0.1	2.5±0.4	32,892±601
c'	1.4±0.1	2.7±0.3	4,351±172
c''	4.8±0.1	2.5±0.4	5,971±177
d	3.5±0.1	2.1±0.3	14,068±256
e	2.1±0.2	2.5±0.3	1,773±129
f	2.4±0.4	2.7±0.5	1,860±180
Voa1	2.4±0.1	2.7±0.5	2,503±87

The analysis of the behaviour of the individual subunits along the MD simulation revealed that E and G subunits are those that undergo a higher deviation from the initial structure reaching an average Cα-RMSD of 8.2 Å and 8.7 Å, respectively, in the last 75 ns of the simulation. Subunits A, C, a and c'' display an average Cα-RMSD of about 4 Å, while the values for the other subunits are below 3.5 Å (Figure 5.3D; Table 5.1, 2nd column). Although these values are slightly high, they are acceptable for regions that are very exposed to the solvent as it is the case of subunits A, a, C, E and G, as it can be observed in Figure 5.3A. Moreover, these values are within the expected range for a protein that was modulated and whose resolution is not the ideal. Contrary to this, no important variations were observed when the average root mean square fluctuations (RMSF) for all the residues of each subunit, which ranged from 2.0 to 4.1 Å, was analysed (Table 5.1, 3rd column). The SASA values were in accordance with the size of each subunit and remained almost constant along the last 75 ns of the simulation as indicated by the low standard deviation values (Table 5.1, 4th column).

From the last ns of the V-ATPase simulation, 10 clusters were generated and a representative structure from each cluster was used in the docking protocol. Figure A7 (Appendix) shows the total number of frames in each cluster and the distribution of the cluster populations during the simulation time.

5.3.3 V-ATPase-Lf molecular docking

After clustering, the sampled structures from the Lf and V-ATPase MD simulations were subjected to protein-protein molecular docking with the HADDOCK 2.4 software using the *ab-initio* mode, which defines random restrains considering all the solvent accessible residues with relative accessibility higher than 20 %. From these calculations, numerous complexes that predict the preferable binding pose between Lf and V-ATPase were generated. Only the solutions obtained after the final refinement in water were considered. The Haddock scoring function considers several aspects of biomolecular recognition by combining van der Waals, Coulomb electrostatics, desolvation and restraint energies, and was used in this work to rank the complexes since it was previously shown to have high success rates [37]. Considering the Haddock score and the visual analysis to discard those complexes in which Lf was docked in the V-ATPase membrane region, the top 20 complexes were selected (Figure 5.4, Table 5.2).

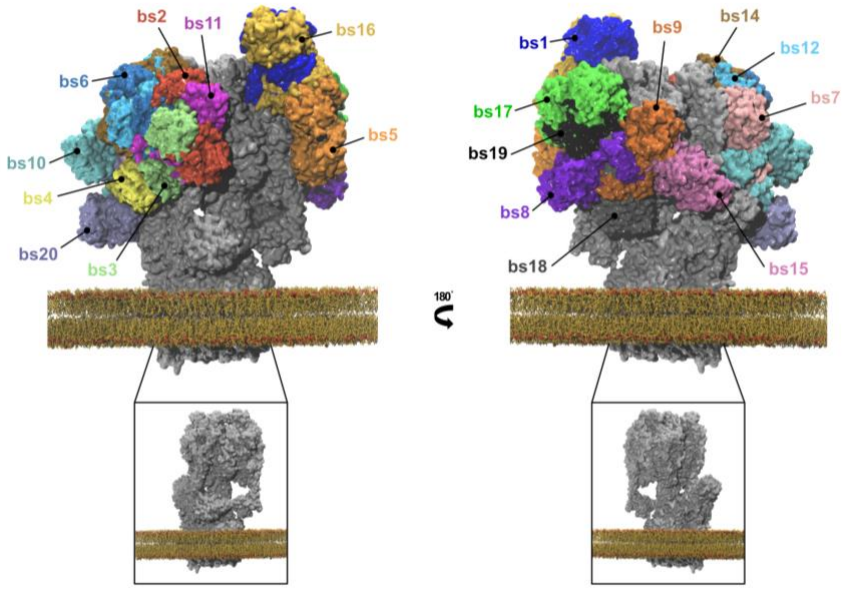

Figure 5.4: Docking solutions provided by the HADDOCK software. The top 20 solutions were selected based on the Haddock score and visual analysis, and the 19 solutions, with exception of bs13, that were further analysed are represented. V-ATPase is coloured in white while Lf, which adopts a different binding pose in each solution, is coloured differently according to the solution as labelled. The membrane bilayer used in the MD simulations is also depicted and the following colour scheme was applied: dark yellow for carbon, nitrogen and oxygen and red for phosphate.

Consistently, all the best scored complexes exhibited Lf docked in the cytosolic V_1 domain with a good exploration of the conformational space (Figure 5.4). All the selected complexes showed a good (negative) Haddock score ranging from -202.8 to -151.4 and a buried surface area that ranged from 3,535 to 1,733 $Å^2$ (Table 5.2, 2nd and 5th columns). Van der Waals and electrostatic interactions seem to favour the binding in all cases (Table 5.2, 3rd and 4th columns). Taking a closer look to the Lf-binding subunit in each complex (Table 5.2, 6th column), in 85% of the top 20 complexes Lf binds to the A subunits, in 60% to E subunits, in 40% to B subunits, in 35% to G subunits and in 15% to the H subunit. Clearly, there is a Lf preference to bind to the V-ATPase region responsible for ATP hydrolysis.

Table 5.2: Protein-protein docking results. HADDOCK data highlighting the Haddock score, the van der Waals and electrostatic energies, the buried surface area and the V-ATPase subunit to which Lf binds in each docking solution, identified in the first column. bs, best solution; au, arbitrary units.

Complex	Haddock score (au)	van der Waals Energy (kcal/mol)	Electrostatic energy (kcal/mol)	Buried surface area ($Å^2$)	Binding subunit
bs 1	-202.8	-129.5	-711.0	3,176	A1, E1
bs 2	-188.9	-92.5	-704.6	3,020	A2, E2, G2
bs 3	-183.5	-114.7	-486.6	3,535	A2, G3
bs 4	-178.2	-121.8	-354.6	3,353	A2, B2, E3, H
bs 5	-176.1	-96.9	-424.7	2,723	A1
bs 6	-170.9	-84.9	-478.7	2,364	A1, E1
bs 7	-169.3	-83.2	-543.4	2,865	A2, B2, E1, G1
bs 8	-164.8	-92.3	-514.8	2,496	A3, B3
bs 9	-161.9	-103.7	-450.9	2,8812	A3, B3
bs 10	-161.3	-111.2	-319.2	3,065	B2, E3, G3, H
bs 11	-158.1	-82.8	-520.7	2,756	A2, G2
bs 12	-157.0	-113.2	-296.1	2,968	A2, E3
bs 13	-156.4	-88.0	-435.3	2,567	A2, E3
bs 14	-156.1	-99.9	-412.6	2,617	A2, E3
bs 15	-156.1	-73.9	-456.0	2,326	A3
bs 16	-154.6	-98.4	-374.9	2,441	A1
bs 17	-153.0	-65.2	-606.7	1,733	A3, E1, G1
bs 18	-152.9	-73.9	-370.0	2,238	A3, B3
bs 19	-152.8	-93.9	-509.6	2,981	B3, E1, G1
bs 20	-151.4	-94.4	-355.6	2,369	B2, E3, H

5.3.4 Post-docking dynamic refinement of V-ATPase-Lf complexes

Given the well-known limitations of docking scoring functions to predict the protein-protein binding affinity [reviewed by [43]], the docked complexes were further refined and rescored through 25 ns long MD simulations, which provides a dynamic perspective to the protein-protein interactions, and binding free energies calculations (ΔG_{bind}) by the MM-GBSA method. Due to lack of convergence, complex bs13 was discarded at this stage. Before simulations, all the complexes were embedded into a membrane bilayer. MD simulations were performed to evaluate the structural stability and showed that, overall, all the models were equilibrated after the first 15 ns (Figure A8, Appendix). In the following 10 ns, the Lf structural behaviour remained stabilized, exhibiting average Cα-RMSD values that ranged between 1.7 and 3.4 Å among the different docking solutions (Table 5.3, 2nd column). Based on the decrease in the Lf solvent accessible area in the complexes MD compared to the MD of Lf alone, the mean area and percentage of Lf buried in each solution was estimated. The buried area varied between 357 and 2,281 $Å^2$, which corresponds to a percentage of 1.3 to 8.4% of Lf buried (Table 5.3, 3-5th columns).

5.3.5 Binding free energy calculations and detailed analysis of the top four docking solutions

Binding free energy calculations by the MM-GBSA method have been previously shown to approach the experimentally determined binding affinities [44–46]. Rescoring of docking solutions based on these calculations is thus regarded as an excellent strategy to increase the reliability of the final ranking [45,47]. For this reason, the ΔG_{bind} was calculated from the last 10 ns of the complexes MD trajectories. Looking at the overall picture, the analysis of the individual energy terms suggests that electrostatic and, to a lesser extent, van der Waals interactions are the major driving forces for protein-protein binding, which are able to compensate for the observed high penalty in polar solvation energy. In total, with the exception of solution bs19, polar energies favor the binding of Lf to V-ATPase over non-polar ones (Table 5.4).

Table 5.3: Analysis of the last 10 ns of docked complexes molecular dynamics simulations. The average RMSD, SASA as well as average area and percentage of lactoferrin buried is given in comparison to the molecular dynamics simulation of lactoferrin alone. Values are Å or Å^2 ± standard deviation or percentage.

Lf/Complex	Average Lf RMSD (Å)	Average Lf SASA (Å^2)	Average Lf buried (Å^2)	Average Lf buried (%)
Lf	2.9±0.4	27,203±376	0	0.0
bs 1	1.6±0.1	24,922±350	2,281±513	8.4
bs 2	1.7±0.1	25,671±397	1,531±546	5.6
bs 3	3.4±0.2	24,974±281	2,229±469	8.2
bs 4	1.7±0.2	25,236±306	1,967±484	7.2
bs 5	1.6±0.1	25,886±240	1,317±446	4.8
bs 6	1.9±0.2	25,546±310	1,657±487	6.1
bs 7	2.1±0.1	25,087±300	2,115±480	7.8
bs 8	2.0±0.3	26,223±263	980±458	3.6
bs 9	2.0±0.2	25,132±277	2,071±467	7.6
bs 10	1.7±0.1	25,722±304	1,481±483	5.4
bs 11	2.5±0.2	26,140±253	1,062±453	3.9
bs 12	2.0±0.1	26,813±337	390±505	1.4
bs 14	1.7±0.1	25,837±260	1,366±457	5.0
bs 15	1.9±0.3	25,783±265	1,420±460	5.2
bs 16	2.1±0.4	26,325±462	877±595	3.2
bs 17	2.2±0.2	26,334±317	869±491	3.2
bs 18	2.0±0.2	25,953±289	1,250±474	4.6
bs 19	2.2±0.3	26,846±369	357±526	1.3
bs 20	2.2±0.1	26,100±309	1,103±484	4.1

Table 5.4: Binding free energies (ΔG_{bind}) and related energy terms calculated by the MM-GBSA method. Calculations were conducted in 300 structures of the last 10 ns of the docked complexes MD simulations. The polar ΔG is the sum of polar contribution to the solvation free energy (ΔG_{GB}) and electrostatic energies (ΔE_{ELE}), while the non-polar ΔG is the sum of non-polar contribution to the solvation free energy (ΔG_{Surf}) and van der Waals energies (ΔE_{VDW}). The four best solutions based on MM-GBSA calculations that were analyzed in more detail in this work are in bold. Values are kcal/mol ± standard deviation.

Complex	ΔE_{VDW} (kcal/mol)	ΔE_{ELE} (kcal/mol)	ΔG_{GB} (kcal/mol)	ΔG_{Surf} (kcal/mol)	ΔG Non-polar (kcal/mol)	ΔG Polar (kcal/mol)	ΔG_{bind} Total (kcal/mol)
bs 1	-134.3±1.6	-5878.6±15.0	5987.2±15.3	-22.0±0.2	-156.2±1.8	108.6±30.3	-47.7±1.4
bs 2	-126.7±2.6	-5310.5±25.2	5448.1±23.9	-18.7±0.4	-145.4±3.0	137.6±49.0	-7.8±1.8
bs 3	**-197.9±1.8**	**-2687.7±19.4**	**2827.3±18.5**	**-30.4±0.2**	**-228.3±2.0**	**139.6±37.9**	**-88.8±2.8**
bs 4	-161.0±1.7	-2983.1±38.8	3144.1±38.3	-22.6±0.4	-183.6±2.1	161.0±77.0	-22.5±3.2
bs 5	-155.6±4.2	-6685.2±60.4	6804.3±62.2	-21.1±0.6	-176.7±4.8	119.1±122.6	-57.6±4.9
bs 6	-85.1±1.8	-3165.0±28.7	3214.3±26.5	-13.0±0.3	-98.1±2.1	49.3±55.2	-48.8±1.6
bs 7	**-180.7±3.4**	**-5670.1±22.2**	**5800.0±21.4**	**-30.6±0.5**	**-211.3±3.9**	**129.9±43.6**	**-81.4±3.0**
bs 8	**-111.9±1.7**	**-6392.3±24.3**	**6422.2±22.7**	**-19.4±0.1**	**-131.3±1.9**	**29.9±47.0**	**- 101.5±2.5**
bs 9	**-129.1±1.5**	**-5851.7±26.6**	**5903.6±25.6**	**-20.9±0.2**	**-150.0±1.7**	**51.9±52.5**	**-98.1±1.5**
bs 10	-153.9±2.2	-2945.6±41.1	3086.4±39.5	-21.0±0.4	-174.9±2.6	140.8±80.7	-34.0±2.3
bs 11	-177.8±2.4	-2817.4±26.9	2981.9±27.7	-23.7±0.4	-201.4±2.8	164.4±54.7	-36.9±1.9
bs 12	-97.5±1.4	-3745.0±20.1	3832.7±20.1	-14.2±0.2	-111.6±1.6	87.7±40.2	-23.9±1.1
bs 14	-143.5±2.4	-2698.2±39.7	2833.1±39.9	-19.2±0.4	-162.7±2.8	134.9±79.6	-27.8±2.3
bs 15	-129.3±1.9	-4784.6±29.3	4877.8±27.3	-21.2±0.3	-150.6±2.2	93.2±56.7	-57.4±3.0
bs 16	-114.4±2.6	-5830.9±62.5	5904.4±60.8	-17.7±0.6	-132.1±3.2	73.5±123.3	-58.6±4.8
bs 17	-80.1±1.3	-5481.4±27.4	5533.3±26.7	-12.7±0.1	-92.7±1.4	51.9±54.1	-40.2±1.7
bs 18	-135.1±2.6	-2863.2±23.8	2968.1±23.5	-19.4±0.4	-154.5±3.0	104.9±47.3	-49.5±2.9
bs 19	-106.7±2.5	-4013.3±27.8	4144.3±26.9	-15.6±0.4	-122.2±2.9	131.0±54.7	8.7±2.9
bs 20	-99.6±3.5	-2577.1±26.3	2668.5±27.5	-13.0±0.4	-112.6±3.9	91.4±53.8	-21.2±2.8

Taking into account the total ΔG_{bind}, there are clearly four docking complexes that stand out, owing to their lowest binding free energies: complexes bs3, bs7, bs8 and bs9 (Figure 5.5; Table 5.4, 8th column). Complex bs8 has the lowest ΔG_{bind} (-101.5±2.5 kcal/mol) and a HS of -164.8, followed by complex bs9 (ΔG: -98.1±1.5 kcal/mol, HS: -161.9), complex bs3 (ΔG: -88.8±2.8 kcal/mol, HS: -183.5) and finally, complex bs7 (ΔG: -81.4±3.0 kcal/mol, HS: -169.3). The next solution with more favorable ΔG_{bind} has more 22.8 kcal/mol, therefore the molecular interactions of these four complexes were subject to a more detailed analysis (Figure 5.5B, Table 5.4).

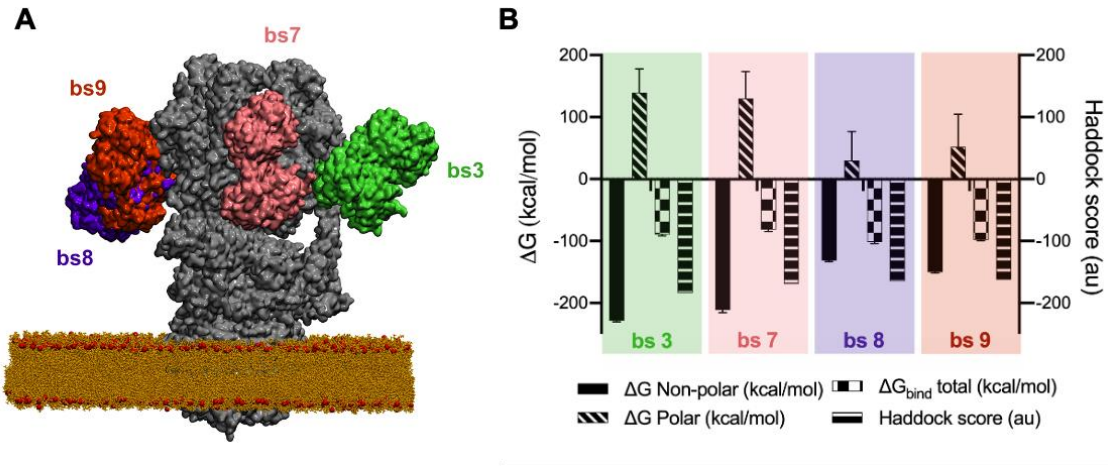

Figure 5.5: Global analysis of the top four solutions. (A) Visual representation of the docking poses of the top four solutions (bs3, bs7, bs8 and bs9). V-ATPase is coloured in gray whereas Lf is coloured differently according to the docking pose. A snapshot of the lipid bilayer is also represented applying the following colour scheme: dark yellow for carbon, nitrogen and oxygen and red for phosphate. Water molecules are omitted for clarity. **(B)** Comparison between total, polar and non-polar binding free energies calculated by the MM-GBSA method, as well as Haddock score for the best four solutions. au, arbitrary units.

To identify the residues of both proteins, as well as the interactions critical for the protein-protein binding, energy per-residue decomposition analysis was performed also using the MM-GBSA approach. This analysis allows the calculation of the energetic contribution of the individual amino acids to the total free energy. Figure A9 (Appendix) shows the free binding energy of the three V-ATPase residues with higher contribution to the binding in each complex. Naturally, the residues belong to the subunits already identified (Table 5.2) as the Lf-binding subunits in each complex (subunits A, B, E, G and H). However, with this analysis, a finer level is achieved as the most contributing residues of each particular subunit are identified. Importantly, about 49% of the residues belong to subunits A and 28% to subunits B, which are the V-ATPase nucleotide binding subunits.

Focusing on the top four docking solutions (Figure 5.6), in complexes bs8 and bs9, which have the lowest ΔG_{bind}, Lf binds to the interface between subunits A3 and B3 through its highly cationic N-terminal

lobe (N-lobe). In complex bs3, Lf binds, once again through its N-lobe, in the interface between subunit A2 and G3, and finally, in complex bs7, both Lf lobes bind to the interface between subunits A2 and B2, as well as to the interface between subunit B2 with subunits E1 and G1 (Figure 5.6).

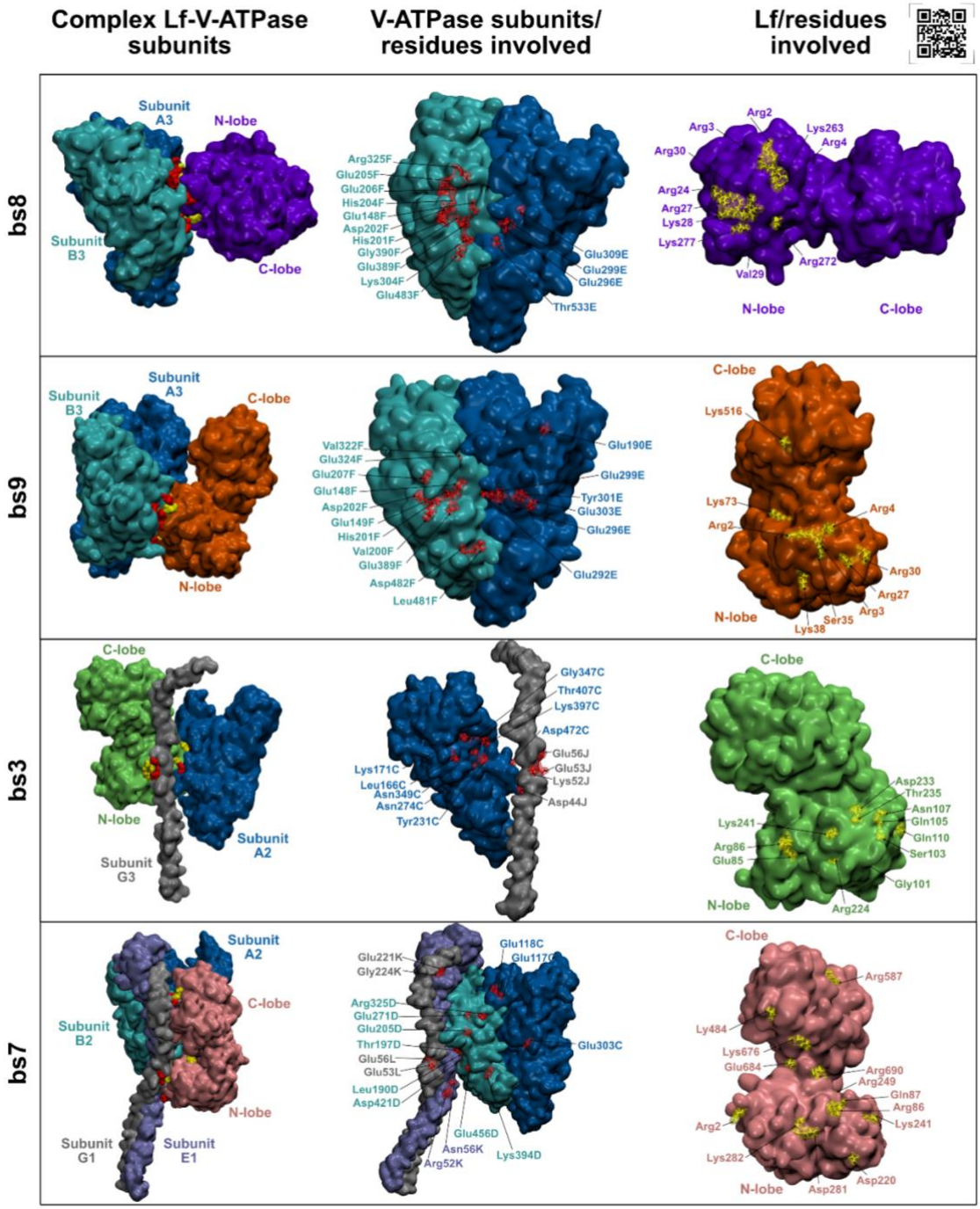

Figure 5.6: Identification of the critical interacting subunits and most important residues in the top four docking solutions. Lactoferrin is coloured in purple, orange, green or pink depending on the docked complex. Subunits A are coloured in blue, subunits B in cyan, subunits G in grey and subunit E1 in lilac. On the left, the Lf binding poses in each docking complex, as well as the binding V-ATPase subunits are depicted. The interacting residues of Lf and V-ATPase are coloured in yellow and red, respectively. The Lf N- or C-terminal lobes (N- or C-lobe) are also identified. On the right, the interacting

residues identified by both the decomposition analysis by the MM-GBSA method and visual inspection of the interaction maps, are labeled according to the colour of the respective location. Interactive view QR code: https://biosim.pt/lactoferrin/

Based on the decomposition data and visual inspection, the atomistic interaction spectra for the top four docking complexes were scrutinized (Table 5.5). Several salt bridges/ionic networks between the sidechains of oppositely charged amino acids (Asp, Glu vs Arg, Lys) connected with several hydrogen bonds can be observed in all complexes. Salt bridges are among the strongest non-covalent interactions, contributing to a strong binding between molecules. This, together with the observed high number of amino acidic interactions (Table 5.5), is perfectly aligned with the very favourable free binding energies calculated by the MM-GBSA method (ranging from -101.5±2.5 to -81.4±3.0) for these complexes. The network includes single, as well as complex salt bridges that join more than two charged residues. In complex bs3, Lf and V-ATPase interact through a salt bridge triad Glu56J-Arg86-Glu53J, as well as 3 single salt bridges (Glu85-Lys52J, Arg224-Asp44J and Lys241-Asp472C). A network of 11 hydrogen bonds mainly involving polar amino acids further strengthens the proteins interaction. In complexes bs7, bs8 and bs9 a strong salt bridge network generally between the positively charged residues from Lf (Arg, Lys) and the negatively charged amino acids from V-ATPase subunits A, B, E and G (Glu, Asp) characterizes the interaction between the two proteins. In bs7, 7 single and 5 complex salt bridges were identified; in bs8, 6 single and 2 complex; and in bs9, 5 single and 2 complex. Several backbone and sidechain hydrogen bonds involving both charged and polar residues are also present and reinforce the protein-protein interaction (5 in bs7, 9 in bs8 and 10 in bs9) (Table 5.5).

5.3.6 Identification of critical V-ATPase and lactoferrin binding residues and insights for future experimental studies

The free energy decomposition study allowed us to gather a detailed atomistic analysis of the V-ATPase-Lf interactions in the different docked complexes affording the identification of some important protein-protein interaction patterns. Indeed, by performing an overall analysis of the residues with more favorable free binding energies that appear in more than one docking solution (Figure 5.7), several residues belonging to particular regions of both proteins were identified as those that mainly contribute to the binding in several complexes.

Table 5.5: Interactions formed between lactoferrin and V-ATPase in the top four docking solutions. The type of bond formed between the different amino acid pairs is indicated as HB for hydrogen bonds and SB for salt bridges. Moreover, for each residue, it is indicated whether the bond is through its sidechain functional group (s) or its backbone (b) group. The letter after the number in V-ATPase residues corresponds to the chain to which the residue belongs. The information regarding the V-ATPase subunit is also depicted.

Lf residue	V-ATPase residue	V-ATPase subunit	Bond type
bs 3			
Glu85 (s)	Lys52J (s)	G3	SB
Arg86 (s)	Glu56J (s)	G3	SB
	Glu53J (s)	G3	SB
Gly101 (b)	Tyr231C (s)	A2	HB
Ser103 (s)	Asn274C (b)	A2	HB
Ser103(b)	Asn274C (b)	A2	HB
	Asn349C (s)	A2	HB
Gln105 (s)	Thr407C (b)	A2	HB
Asn107 (s)	Gly347C (b)	A2	HB
Asn107 (b)	Lys171C (s)	A2	HB
Gln110 (s)	Leu166C (b)	A2	HB
Arg224 (s)	Asp44J (s)	G3	SB
Asp233 (b)	Thr407C (b)	A2	HB
	Thr407C (s)	A2	HB
Thr235 (s)	Lys397C (s)	A2	HB
Lys241 (s)	Asp472C (s)	A2	SB

Lf residue	V-ATPase residue	V-ATPase subunit	Bond type
bs 7			
Arg2 (s)	Glu303C (s)	A2	SB
Arg86 (s)	Leu190D (b)	B2	HB
	Asp421D (s)	B2	SB
	Glu456D (s)	B2	SB
Gln87 (s)	Thr197D (s)	B2	HB
Asp220 (s)	Arg52K (s)	E1	SB
	Asn56K (s)	E1	HB
Lys241 (s)	Glu53L (s)	G1	SB
	Glu56L (s)	G1	SB
Arg249 (s)	Asp202D (s)	B2	SB
Asp281 (b)	Lys394D (b)	B2	HB
Ser482 (s)	Glu117C (b)	A2	HB
Lys484 (s)	Glu118C (s)	A2	SB
Arg587 (s)	Glu221K (s)	E1	SB
	Gly224K (s)	E1	SB
Lys676 (s)	Glu271D (s)	B2	SB
Arg690 (s)	Glu205D (s)	B2	SB
Glu684 (s)	Arg325D (s)	B2	SB

Lf residue	V-ATPase residue	V-ATPase subunit	Bond type
bs 8			
Arg2 (s)	Glu205F (s)	B3	SB
Arg3 (s)	Glu206F (s)	B3	SB
	Arg325F (b)	B3	HB
	Asp199F (s)	B3	SB
Arg4 (s)	Asp199F (b)	B3	HB
	His201F (b)	B3	HB
	Gly390F (b)	B3	HB
Arg4 (b)	His204F (s)	B3	HB
Arg24 (s)	Glu309E (s)	A3	SB
Arg27 (s)	Glu296E (s)	A3	SB
	Glu299E (s)	A3	SB
Lys28 (s)	Glu296E (s)	A3	SB
	Glu299E (s)	A3	SB
Val29 (b)	Lys394F (s)	B3	HB
	Glu148F (b)	B3	HB
Arg30 (s)	Gly388F (b)	B3	HB
	Glu389F (b)	B3	HB
Lys263 (s)	Asp202F (s)	B3	SB
Arg272 (s)	Glu483F (s)	B3	SB
Lys277 (s)	Thr533E (s)	A3	HB

Lf residue	V-ATPase residue	V-ATPase subunit	Bond type
bs 9			
Arg2 (s)	Glu292E (s)	A3	SB
	Glu296E (s)	A3	SB
	Glu299E (s)	A3	SB
Arg3 (s)	Glu389F (s)	B3	SB
	Glu148F (b)	B3	HB
Arg4 (s)	Glu148F (s)	B3	SB
	Glu148F (b)	B3	HB
	Val322F (b)	B3	HB
	Gly324F (b)	B3	HB
Arg27 (s)	Glu149F (s)	B3	SB
	Val200F (b)	B3	HB
	His201F (b)	B3	HB
	Asp202F (b)	B3	HB
Arg30 (s)	Glu205F (s)	B3	SB
	Asp202F (s)	B3	SB
Ser35 (s)	Glu389F (s)	B3	HB
Lys38 (s)	Leu481F (b)	B3	HB
	Asp482F (s)	B3	SB
Lys73 (s)	Glu303F (s)	A3	SB
	Tyr301F (s)	A3	HB
Lys516 (s)	Glu190F (s)	A3	SB

Almost all the Lf residues with a maximum contribution to the total free binding energy below -8 kcal/mol that appear in more than one solution are arginine residues with the exception of Gln666 (Figure 5.7A, B). Noticeably, three consecutive N-terminal arginine residues at positions 2-4 together with Arg27, which locates nearby, form a highly cationic N-terminal stretch that seems to be involved in the binding of different complexes as it can be observed in Figure 5.6 for the top two solutions (bs8 and bs9). These residues exhibit a maximum contribution to the total ΔG_{bind} below -10 kcal/mol and appear in more than 3 solutions (Figure 5.7A), being thus excellent candidates for mutagenesis studies. In accordance, they are involved in different single and complex salt bridges with the negatively charged amino acids from V-ATPase (Table 5.5). Three additional arginine residues also located at the Lf N-lobe (Arg86, Arg89 and Arg249) also display highly favorable ΔG (below -8 kcal/mol). A special remark to Arg86 that appears as an important binding residue in 8 of 19 solutions with a maximum contribution bellow -10 kcal/mol and that forms salt bridge triads with aspartates and glutamates from V-ATPase in solutions bs3 and bs7 (Table 5.5). At the Lf C-lobe, three arginine residues (Arg587, Arg608 and Arg652) as well as Gln666 appear as important interactors in two or three docking solutions and exhibit maximum contribution bellow 8 kcal/mol. It is clear though from these data that the N-terminal Lf lobe is enriched in residues that appear in more than one solution and exhibit maximum contribution to the total ΔG below -4 kcal/mol (Figure 5.7A, B).

The V-ATPase portrait of residues that display a maximum contribution to the total ΔG below -2 kcal/mol and appear in more than one docking complex is enriched in charged residues. As for their location, the great majority belong to subunits A and B (38% and 41%, respectively), 15% to subunit E and only 1 residue to subunits G and H (Figure 5.7C). Looking at the overall picture and focusing on those with ΔG below -5 kcal/mol, a group of four negatively charged amino acids (Glu149F, Asp199F, Glu206F and Glu389F) together with Arg466F and Phe484F located at subunit B3 immediately grabs our attention (Figure 5.7D). Some of those are involved in strong salt bridges with the positively charged residues from Lf in the top four solutions (Table 5.5). Subunit B3 comprises the only three residues with maximum contribution below -8 kcal/mol that appear in more than one solution (Glu206F, Glu389F and Arg466F) (Figure 5.7C, D) and is involved in the binding to Lf in the top two solutions (Figure 5.6). Site-directed mutagenesis studies targeting these residues, as well as deletion of subunit B are thus promising approaches that can be further explored experimentally.

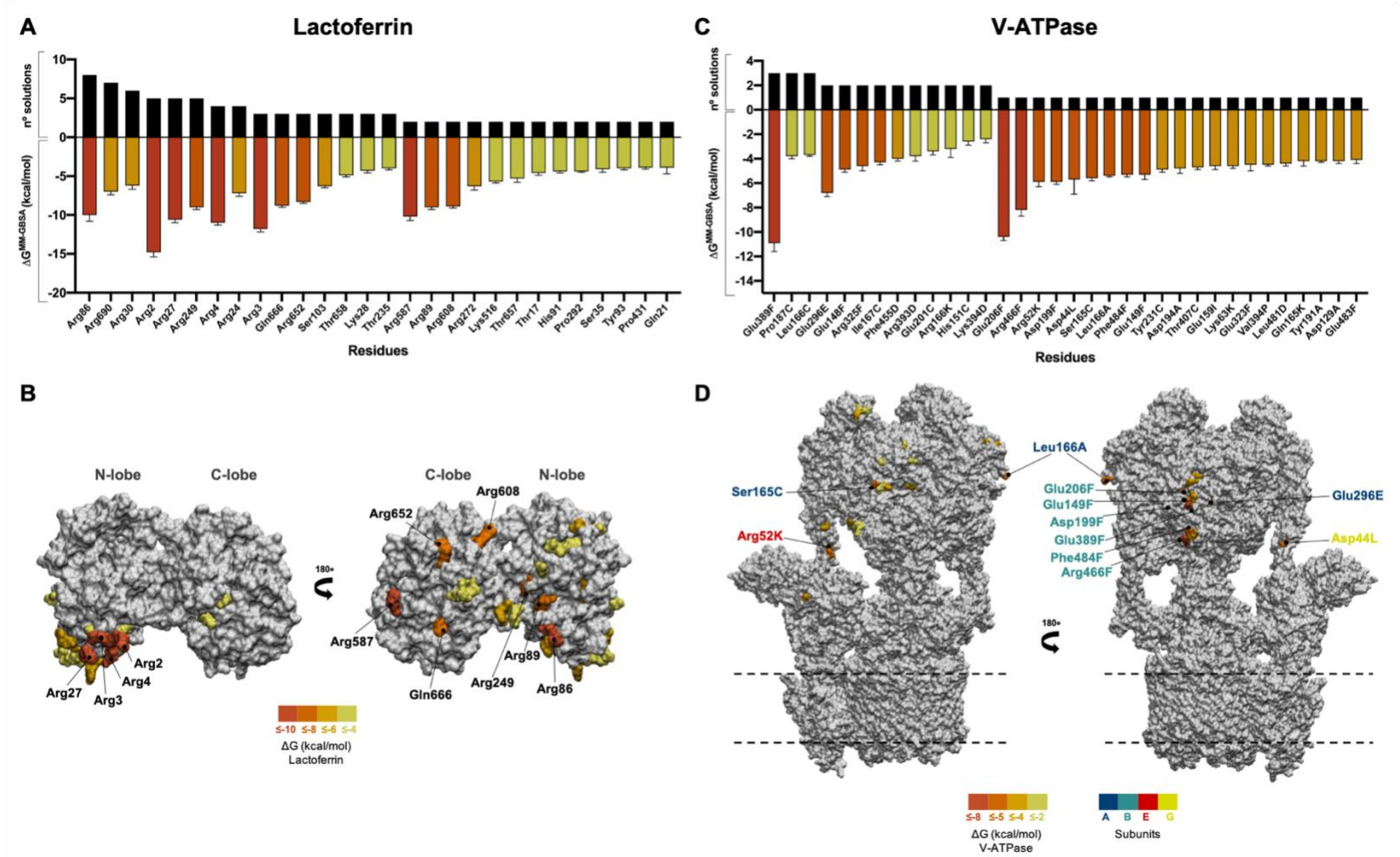

Figure 5.7: General analysis of the critical lactoferrin and V-ATPase binding residues based on the decomposition of the binding free energy calculated using the MM-GBSA method. (A) Per-residue ΔG in kcal/mol of the lactoferrin amino acids with maximum contribution to the total free binding energy bellow -4 kcal/mol that appear in more than one docking solution as important binding residues. The number of solutions is indicated in the positive part of the y-axis while the ΔG is depicted in the negative portion. **(B)** Surface model of lactoferrin (in white) showing the location of the residues with maximum contribution below -4 kcal/mol. Four different categories were defined based on residues ΔG (below -10, -8, -6 and -4 kcal/mol) that are coloured differently as indicated in the colour legend. The names of the residues with ΔG bellow -8 kcal/mol are depicted. **(C)** Same as in A but representing the V-ATPase residues with maximum contribution to the total binding free energy bellow -2 kcal/mol. **(D)** Surface model of V-ATPase (in white) showing the location of the residues with maximum contribution below -2 kcal/mol. Four different categories were defined based on residues ΔG (below -8, -5, -4 and -2 kcal/mol) that are coloured differently as indicated in the colour legend. The residues with ΔG bellow -5 kcal/mol are labelled with the letting colour according to the V-ATPase subunit they belong as indicated. The dashed lines indicate the approximate location of the membrane.

Residues Ser165C, Leu166A and Glu296E from subunits A, as well as Asp44L from subunit G and Arg52K from subunit E also display a particularly favorable maximum contribution to the total ΔG (Figure 5.7C, D) and participate in salt bridges in the top four solutions (Table 5.5). In summary, our energy decomposition study by the MM-GBSA method allowed the identification of critical Lf and V-ATPase residues that can greatly aid in the rational design of experimental studies.

5.4. Discussion

Lf was shown to inhibit V-ATPase activity in three different models: yeast vacuoles [3], highly metastatic cancer cells and liver lysosomes [1]. However, the molecular basis of this interaction has not been disclosed. In this study, a computational approach to predict, at the atomistic level, how Lf and V-ATPase interact was developed and employed also aiming to provide insights for future experimental studies of protein-protein interaction.

Proteins are dynamic and flexible entities that inter-convert into different conformational states to accomplish their functions [48]. X-ray crystallography or cryo-EM provide static pictures of the macromolecules that do not always represent the main conformation of the proteins in solution [49]. Moreover, before complexation with a binding partner, proteins undergo changes to conformational states that are more predisposed to form a stable complex [50]. In this context, one of the main bottlenecks of the docking programs is to not take into account the full extent of conformational changes exhibited by the unbounded proteins. To mitigate these pitfalls, first, MD simulations of Lf and V-ATPase in water and clustering analysis were conducted to obtain a robust sampling of the conformational landscape of both proteins. Approaches with the same goal have been previously shown to improve the reliability of the generated docking poses [50]. Through this methodology, a set of ten different states for each protein, likely with different degrees of stability and occupancy, were obtained from the equilibrated part of the MD trajectories and subjected to several docking runs. The top 20 docking complexes based on the Haddock score, which was previously shown to be successful [37], were selected for post-docking dynamic refinement. This stage consisted in performing MD simulations of the docked complexes for structural refinement and quality/reliability assessment of the docking poses. The non-favorable binding poses/interactions would produce unstable trajectories that would reflect significant changes in the RMSD and likely in the SASA values; whereas stable complexes would lead to a constant behavior after an initial period of system equilibration [51]. All the docked complexes' MD were equilibrated after 15 ns indicating that all the selected solutions form stable complexes and attesting the reliability of our docking approach. To refine, validate and rescore the final ranking of the docking solutions, free binding energy calculations

by the MM-GBSA method were performed to predict the binding affinities of each docked complex. Although the MM-GBSA method is not accurate enough to quantitatively predict the absolute free binding energies, it is computationally efficient [51] and has been shown to improve the docking solutions scoring [44,46].

Right after the first docking results, it was clear that the preferable Lf binding sites were on the V-ATPase cytosolic V_1 domain and, specifically, on subunits A, B, E and G, in all the different solutions considered. Each V-ATPase has three subunits A and B that together form the so-called catalytic hexamer A_3B_3. They are located in an alternating fashion comprising three ATP-hydrolyzing catalytic sites in the AB interfaces. During rotational catalysis, the AB pairs undergo conformational changes to accomplish the ATP hydrolysis [25–27], adopting an "open", "loose" or "tight" conformation depending on whether they are nucleotide-free, bound to ADP or to ATP, respectively [26]. Work performed with the *Enterococcus hirae* V-ATPase shed some light on the hydrolysis mechanism. Subunits A and B have an overall similar structure that consists of a N-terminal β-barrel domain, a central α/β domain and a C-terminal helical domain. The C-terminal half of A subunits was found to be the responsible for the different conformations of the AB pairs. The nucleotide-binding site is composed by a phosphate-binding loop know as P-loop with the consensus sequence GXXXXGKT(S) (256-263) and Glu 285 and Arg286 both located at the central domain of A subunits. Additionally, an arginine located at the B subunit (the so-called Arg finger) is also involved [52]. Each V-ATPase pump has also three subunits E and G that form three heterodimers. Their major function is to connect the catalytic hexamer to subunits H and C and to the N-terminal domain of *a* subunit of V_o domain, connecting in this way ATP hydrolysis to proton transport. They are known as "peripheral stalks" and together with their associated subunits form a stator complex, which ensures that only the central rotor rotates during catalysis, preventing the catalytic subunits and the membrane embedded C-terminal domain of *a* subunit to turn with the rotor [53].

Considering the overall docking results, Lf binds to subunits A, which hold the nucleotide binding sites, in 85% of the solutions, suggesting that the most probable mechanism through which Lf inhibits V-ATPase activity is by interfering with the hydrolysis mechanism (Figure 5.8). Accordingly, in three of the four top solutions, Lf establishes a strong interaction map that counts with several single and complex salt bridges, as well as a hydrogen bond network with the central α/β domain of the ATP-hydrolyzing interfaces of the AB pairs (where the key residues for nucleotide binding are located), reinforcing our hypothesis. By binding to the AB interfaces, Lf may (i) inhibit ATP binding by a competitive mechanism or (ii) limit the accessibility of ATP to the catalytic sites. Moreover, its binding may (iii) impair the conformational changes of the AB pairs required to continue the rotational reaction after the ATP

hydrolysis and ADP release [54]. Depending on the docking solution, Lf binds to either AB pair 1, 2 or 3. Therefore, similarly to the bacterial effector SidK from *Legionella pneumophila* [55], different Lf proteins may bind to the same V-ATPase complex further boosting the inhibitory activity. Indeed, the V-ATPase-SidK complexes were determined by cryo-EM and showed that three SidK molecules bound to the three A subunits reducing their flexibility. Complementary *in vitro* experiments revealed that SidK reduces V-ATPase activity and decreases its affinity for ATP [55]. In another study, the insecticidal compound celangulin V was shown to inhibit ATP hydrolysis and, by a docking approach, suggested to bind to the ATP binding site of the AB subunits [56]

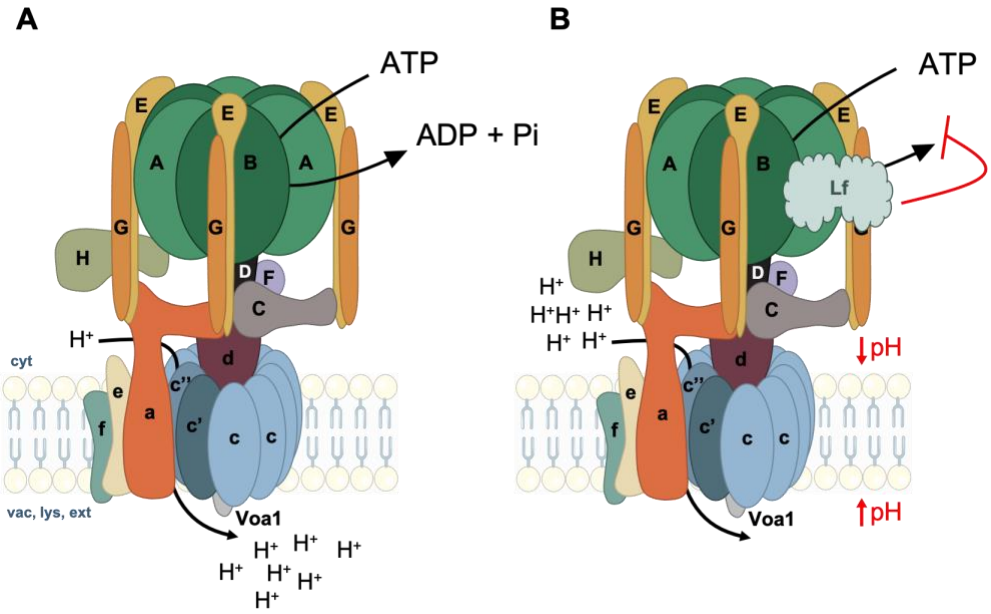

Figure 5.8: Working model of the mode of V-ATPase inhibition by lactoferrin. (A) In physiological conditions, V-ATPase located either at the vacuolar, lysosomal or plasma membrane couples the energy of ATP hydrolysis to pump protons from the cytosol (cyt) to the vacuolar (vac) or lysosomal lumen (lys) or to the extracellular milieu (ext). **(B)** In the presence of Lf, it binds to the interface between the V-ATPase AB pairs, hindering ATP hydrolysis which, in turn, inhibits proton translocation, leading to intracellular acidification and organelle/extracellular space alkalinization.

Based on all the aforementioned evidences, we hypothesize that Lf targets the AB pairs, hindering ATP hydrolysis by binding to their interfaces which, in turn, impairs proton transport and the overall V-ATPase activity (Figure 5.8). In agreement with this model, in our previous work, we demonstrated that Lf inhibits both the hydrolytic and proton pumping activities of V-ATPase in lysosomes isolated from rat liver [1], and its proton pumping activity in vacuoles isolated from yeast [3]. In the future, it would be interesting to study the Lf effect on the V-ATPase hydrolytic activity in vacuoles isolated from yeast. This

Lf inhibitory activity towards V-ATPase culminates in lethal pH perturbations in both yeast [3] and highly metastatic cancer cells [1,2], as discussed in the introduction section.

Our free binding energy calculations allowed the identification of key residues for V-ATPase-Lf interaction that are prime candidates for future experimental work. Concerning Lf, the majority of the most contributing residues for the total free binding energy were located at the N-terminal lobe. Particularly, a cluster of 3 consecutive arginine residues (2-4) at the N-terminal region as well as Arg27 were identified. In fact, due to its highly cationic nature, the N-terminal part of Lf has been suggested to be responsible for the binding of Lf to a wide collection of molecules and to be the source of strong antimicrobial peptides [57]. In accordance with our results, two clusters composed by the first 6 Lf amino acids (GRRRRS) and RKVR residues located at positions 28-31 were previously identified to be the Lf binding site for some glycosaminoglycans (GAGs) including chondroitin sulfate [58] and heparin [59]. The positively charged sidechains of the residues belonging to these two clusters, which are juxtaposed in the folded protein, were suggested to form a "cationic cradle" for the GAGs binding [59]. Residues belonging to these clusters were also found to be important for the binding of hLf to the pneumococcal surface protein A from *Streptococcus pneumoniae*, which acts as a microbial defense mechanism [60]. These two clusters are also involved in the V-ATPase-Lf binding in our top two docking solutions (Figure 5.6). Other residues from the Lf N-lobe also seem to be important for the V-ATPase-Lf interactions including Arg86, Arg89 and Arg249. The Lf C-lobe residues Arg587, Arg608, Arg652 and Gln666 were also predicted to be important for binding in our calculations. The Lf C-lobe has previously been implicated in the binding to different molecules including the Lf-binding proteins A and B from Gram-negative bacteria [61,62] and some anti-inflammatory drugs [63]. It is worth mentioning that three different drugs were found to bind to the same ligand-binding site at the Lf C-lobe [63] that are near the Arg652 and Gln666 identified in our study. Our results are thus in line with published work, which attests the reliability of our computational pipeline. Different charged amino acid residues from V-ATPase subunits A, B, E and G, the main binding subunits according to the docking results, were also identified as main contributors. As the identified residues from both proteins appear to be determinant for their binding, the development of experimental methods to ascertain their true relevance for the interaction are critical to validate the atomistic interactions unveiled in this study and, in this way, take computational biochemistry to the bench.

5.5. Conclusion

Concluding, the computational strategy used in this work identified the V_1 domain of V-ATPase as a Lf target, and allowed us to infer upon the molecular basis of Lf-driven V-ATPase inhibition and to propose key binding residues from both proteins that can be explored experimentally. Taking into account our results and the fact that Lf was also shown to inhibit the bacterial F-ATPase [64], which is functionally and structurally similar to V-ATPase [65], a comparable mechanism may be involved in the F-ATPase inhibition by Lf and may underly the antibacterial activity of this protein. Indeed, ATP hydrolysis in F-ATPases occurs in the catalytic hexamer $\alpha_3\beta_3$ (A_3B_3 in V-ATPase) [65], which can be a putative Lf target in bacteria.

References

1. Pereira CS, Guedes JP, Gonçalves M, Loureiro L, Castro L, Gerós H, et al. Lactoferrin selectively triggers apoptosis in highly metastatic breast cancer cells through inhibition of plasmalemmal V-H+-ATPase. Oncotarget. 2016;7: 62144–62158. doi:10.18632/oncotarget.11394
2. Guedes J, Pereira C, Rodrigues L, Côrte-real M. Bovine milk lactoferrin selectively kills highly metastatic prostate cancer PC-3 and osteosarcoma MG-63 cells *in vitro*. Front Oncol. 2018;8: 1–12. doi:10.3389/fonc.2018.00200
3. Santos-Pereira C, Andrés MT, Chaves SR, Fierro JF, Gerós H, Manon S, et al. Lactoferrin perturbs lipid rafts and requires integrity of Pma1p-lipid rafts association to exert its antifungal activity against *Saccharomyces cerevisiae*. Int J Biol Macromol. 2021;171: 343–357. doi:10.1016/j.ijbiomac.2020.12.22
4. Sousa SF, Ribeiro AJM, Coimbra JTS, Neves RPP, Martins SA, Moorthy NSHN, et al. Protein-ligand docking in the new millennium – a retrospective of 10 years in the field. Curr Med Chem. 2013;20: 2296–2314. doi:10.2174/0929867311320180002
5. Preto AJ, Matos-Filipe P, Koukos PI, Renault P, Sousa SF, Moreira IS. Structural characterization of membrane protein dimers. In: Kister A. (eds) Protein supersecondary structures. Methods in Molecular Biology, vol 1958. 2019. Humana Press, New York,. doi:10.1007/978-1-4939-9161-7_21
6. De Vries SJ, Van Dijk M, Bonvin AMJJ. The HADDOCK web server for data-driven biomolecular docking. Nat Protoc. 2010;5: 883–897. doi:10.1038/nprot.2010.32
7. Onufriev A, Bashford D, Case DA. Exploring protein native states and large-scale conformational changes with a modified generalized born model. Proteins Struct Funct Genet. 2004;55: 383–394. doi:10.1002/prot.20033
8. Humphrey W, Dalke A, Schulten K. VMD: Visual Molecular Dynamics. J Molec Graph. 1996;14: 33–38. doi:10.1016/0263-7855(96)00018-5
9. Haridas M, Anderson BF, Baker EN. Structure of human diferrric lactoferrin refined at 2.2 Angstrom resolution. Acta Crystallogr - Sect D Biol Crystallogr. 1995;51: 629–646. doi:10.1107/S0907444994013521

10. Olsson MHM, SØndergaard CR, Rostkowski M, Jensen JH. PROPKA3: Consistent treatment of internal and surface residues in empirical p K a predictions. J Chem Theory Comput. 2011;7: 525–537. doi:10.1021/ct100578z

11. Anghel L, Radulescu A, Erhan RV. Structural aspects of human lactoferrin in the iron-binding process studied by molecular dynamics and small-angle neutron scattering. Eur Phys J E. 2018;41. doi:10.1140/epje/i2018-11720-x

12. Li P, Merz KM. MCPB.py: a python based metal center parameter builder. J Chem Inf Model. 2016;56: 599–604. doi:10.1021/acs.jcim.5b00674

13. Sousa SF, Fernandes PA, Ramos MJ. General performance of density functionals. J Phys Chem A. 2007;111: 10439–10452.

14. Sousa SF, Fernandes PA, Ramos MJ. Effective tailor-made force field parameterization of the several Zn coordination environments in the puzzling FTase enzyme: Opening the door to the full understanding of its elusive catalytic mechanism. Theor Chem Acc. 2007;117: 171–181. doi:10.1007/s00214-006-0170-9

15. Neves RPP, Sousa SF, Fernandes PA, Ramos MJ. Parameters for molecular dynamics simulations of manganese-containing metalloproteins. J Chem Theory Comput. 2013;9: 2718–2732. doi:10.1021/ct400055v

16. Case D, Belfon K, Ben-Shalom I, Brozell S, Cerutti D, Cheatham T, et al. AMBER 19. University of California, San Francisco; 2019. doi:10.1007/s10637-020-01020-2

17. Maier JA, Martinez C, Kasavajhala K, Wickstrom L, Hauser KE, Simmerling C. ff14SB: improving the accuracy of protein side chain and backbone parameters from ff99SB. J Chem Theory Comput. 2015;11: 3696–3713. doi:10.1021/acs.jctc.5b00255

18. Wang J, Wolf R, Caldwell J, Kollman P, Case D. Development and testing of a general amber force field. J Comput Chem. 2004;25: 1157–1174. doi: 10.1002/jcc.20035

19. Cornell W, Cieplak P, Bayly C, Gould I, Merz K, Ferguson D, et al. A second generation force field for the simulation of proteins, nucleic acids, and organic molecules. J Am Chem Soc. 1995;117: 5179–5197. doi:10.1021/ja955032e

20. Lemons DS, Gythiel A. Paul Langevin's 1908 paper "On the theory of brownian motion" ["Sur la théorie du mouvement brownien," C. R. Acad. Sci. (Paris) 146 , 530–533 (1908)] . Am J Phys. 1997;65: 1079–1081. doi:10.1119/1.18725

21. Izaguirre JA, Catarello DP, Wozniak JM, Skeel RD. Langevin stabilization of molecular dynamics. J Chem Phys. 2001;114: 2090–2098. doi:10.1063/1.1332996

22. Abraham MJ, Murtola T, Schulz R, Páll S, Smith JC, Hess B, et al. Gromacs: High performance molecular simulations through multi-level parallelism from laptops to supercomputers. SoftwareX. 2015;1–2: 19–25. doi:10.1016/j.softx.2015.06.001

23. Berendsen HJC, Postma JPM, Van Gunsteren WF, Dinola A, Haak JR. Molecular dynamics with coupling to an external bath. J Chem Phys. 1984;81: 3684–3690. doi:10.1063/1.448118

24. Hess B, Bekker H, Berendsen HJC, Fraaije JGEM. LINCS: a linear constraint solver for molecular simulations. J Comput Chem. 1997;18: 1463–1472. doi:10.1002/(SICI)1096-987X(199709)18:12<1463::AID-JCC4>3.0.CO;2-H

25. Vasanthakumar T, Bueler SA, Wu D, Beilsten-Edmands V, Robinson C V., Rubinstein JL. Structural comparison of the vacuolar and Golgi V-ATPases from *Saccharomyces cerevisiae*. Proc Natl Acad

Sci U S A. 2019;116: 7272–7277. doi:10.1073/pnas.1814818116

26. Zhao J, Benlekbir S, Rubinstein JL. Electron cryomicroscopy observation of rotational states in a eukaryotic V-ATPase. Nature. 2015;521: 241–245. doi:10.1038/nature14365

27. Wang L, Wu D, Robinson C V., Wu H, Fu T-M. Structures of a complete human V-ATPase reveal mechanisms of its assembly. Mol Cell. 2020;80: 501-511.e3. doi:10.1016/j.molcel.2020.09.029

28. Schott-Verdugo S, Gohlke H. PACKMOL-Memgen: a simple-to-use, generalized workflow for membrane-protein-lipid-bilayer system building. J Chem Inf Model. 2019;59: 2522–2528. doi:10.1021/acs.jcim.9b00269

29. Jo S, Lim JB, Klauda JB, Im W. CHARMM-GUI membrane builder for mixed bilayers and its application to yeast membranes. Biophys J. 2009;97: 50–58. doi:10.1016/j.bpj.2009.04.013

30. Dickson CJ, Madej BD, Skjevik ÅA, Betz RM, Teigen K, Gould IR, et al. Lipid14: The amber lipid force field. J Chem Theory Comput. 2014;10: 865–879. doi:10.1021/ct4010307

31. Case D, Belfon K, Ben-Shalom I, Brozell S, Cerutti D, Cheatham T, et al. AMBER 2020. University of California, San Francisco; 2020.

32. Ryckaert JP, Ciccotti G, Berendsen HJC. Numerical integration of the cartesian equations of motion of a system with constraints: molecular dynamics of n-alkanes. J Comput Phys. 1977;23: 327–341. doi:10.1016/0021-9991(77)90098-5

33. Van Zundert GCP, Rodrigues JPGLM, Trellet M, Schmitz C, Kastritis PL, Karaca E, et al. The HADDOCK2.2 web server: user-friendly integrative modeling of biomolecular complexes. J Mol Biol. 2016;428: 720–725. doi:10.1016/j.jmb.2015.09.014

34. Koukos PI, Faro I, van Noort CW, Bonvin AMJJ. A membrane protein complex docking benchmark. J Mol Biol. 2018;430: 5246–5256. doi:10.1016/j.jmb.2018.11.005

35. Roel-Touris J, Don CG, Honorato RR, Rodrigues JPGLM, Bonvin AMJJ. Less is more: coarse-grained integrative modeling of large biomolecular assemblies with HADDOCK. J Chem Theory Comput. 2019;15: 6358–6367. doi:10.1021/acs.jctc.9b00310

36. Rodrigues JPGLM, Trellet M, Schmitz C, Kastritis P, Karaca E, Melquiond ASJ, et al. Clustering biomolecular complexes by residue contacts similarity. Proteins Struct Funct Bioinforma. 2012;80: 1810–1817. doi:10.1002/prot.24078

37. Vangone A, Rodrigues JPGLM, Xue LC, van Zundert GCP, Geng C, Kurkcuoglu Z, et al. Sense and simplicity in HADDOCK scoring: lessons from CASP-CAPRI round 1. Proteins Struct Funct Bioinforma. 2017;85: 417–423. doi:10.1002/prot.25198

38. Jorgensen W, Tirado-Rives J. The OPLS [optimized potentials for liquid simulations] potential functions for proteins, energy minimizations for crystals of cyclic peptides and crambin. J Am Chem Soc. 1988;110: 1657–1666. doi:10.1021/ja00214a001

39. Wang E, Sun H, Wang J, Wang Z, Liu H, Zhang JZH, et al. End-point binding free energy calculation with MM/PBSA and MM/GBSA: strategies and applications in drug design. Chem Rev. 2019;119: 9478–9508. doi:10.1021/acs.chemrev.9b00055

40. Sgobba M, Caporuscio F, Anighoro A, Portioli C, Rastelli G. Application of a post-docking procedure based on MM-PBSA and MM-GBSA on single and multiple protein conformations. Eur J Med Chem. 2012;58: 431–440. doi:10.1016/j.ejmech.2012.10.024

41. Miller BR, McGee TD, Swails JM, Homeyer N, Gohlke H, Roitberg AE. MMPBSA.py: an efficient program for end-state free energy calculations. J Chem Theory Comput. 2012;8: 3314–3321. doi:10.1021/ct300418h

42. Weiser J, Shenkin PS, Still WC. Approximate atomic surfaces from linear combinations of pairwise overlaps (LCPO). J Comput Chem. 1999;20: 217–230. doi:10.1002/(SICI)1096-987X(19990130)20:2<217::AID-JCC4>3.0.CO;2-A

43. Pantsar T, Poso A. Binding affinity via docking: fact and fiction. Molecules. 2018;23: 1899. doi:10.3390/molecules23081899

44. Shen M, Zhou S, Li Y, Pan P, Zhang L, Hou T. Discovery and optimization of triazine derivatives as ROCK1 inhibitors: molecular docking, molecular dynamics simulations and free energy calculations. Mol Biosyst. 2013;9: 361–374. doi:10.1039/c2mb25408e

45. Zhang X, Perez-Sanchez H, Lighstone F. A Comprehensive Docking and MM/GBSA rescoring study of ligand recognition upon binding antithrombin. Curr Top Med Chem. 2017;17: 1631–1639. doi:10.2174/1568026616666161171

46. Suenaga A, Okimoto N, Hirano Y, Fukui K. An efficient computational method for calculating ligand binding affinities. PLoS One. 2012;7. doi:10.1371/journal.pone.0042846

47. Aamir M, Singh VK, Dubey MK, Meena M, Kashyap SP, Katari SK, et al. *In silico* prediction, characterization, molecular docking, and dynamic studies on fungal SDRs as novel targets for searching potential fungicides against fusarium wilt in tomato. Front Pharmacol. 2018;9: 1–28. doi:10.3389/fphar.2018.01038

48. Nevin Gerek Z, Kumar S, Banu Ozkan S. Structural dynamics flexibility informs function and evolution at a proteome scale. Evol Appl. 2013;6: 423–433. doi:10.1111/eva.12052

49. Shoemaker SC, Ando N. X-rays in the Cryo-electron microscopy era: structural biology's dynamic future. Biochemistry. 2018;57: 277–285. doi:10.1021/acs.biochem.7b01031

50. Torchala M, Gerguri T, Chaleil RAG, Gordon P, Russell F, Keshani M, et al. Enhanced sampling of protein conformational states for dynamic cross-docking within the protein-protein docking server SwarmDock. Proteins Struct Funct Bioinforma. 2020;88: 962–972. doi:10.1002/prot.25851

51. Yunta MJR. Docking and ligand binding affinity: uses and pitfalls. Am J Model Optim. 2016;4: 74–114. doi:10.12691/ajmo-4-3-2

52. Arai S, Saijo S, Suzuki K, Mizutani K, Kakinuma Y, Ishizuka-Katsura Y, et al. Rotation mechanism of *Enterococcus hirae* V1-ATPase based on asymmetric crystal structures. Nature. 2013;493: 703–707. doi:10.1038/nature11778

53. Vasanthakumar T, Rubinstein JL. Structure and roles of V-type ATPases. Trends Biochem Sci. 2020;45: 295–307. doi:10.1016/j.tibs.2019.12.007

54. Suzuki K, Mizutani K, Maruyama S, Shimono K, Imai FL, Muneyuki E, et al. Crystal structures of the ATP-binding and ADP-release dwells of the V1 rotary motor. Nat Commun. 2016;7: 13235. doi:10.1038/ncomms13235

55. Zhao J, Beyrakhova K, Liu Y, Alvarez CP, Bueler SA, Xu L, et al. Molecular basis for the binding and modulation of V-ATPase by a bacterial effector protein. PLoS Pathog. 2017;13: 1–21. doi:10.1371/journal.ppat.1006394

56. Ding L, Guo Z, Xu H, Li T, Wang Y, Tao H. The inhibitory effect of celangulin V on the ATP hydrolytic activity of the complex of V-ATPase subunits A and B in the midgut of mythimna separata. Toxins

(Basel). 2019;11. doi:10.3390/toxins11020130

57. Zarzosa-Moreno D, Avalos-Gómez C, Ramírez-Texcalco L, Torres-López E, Ramírez-Mondragón R, Hernández-Ramírez J, et al. Lactoferrin and its derived peptides: an alternative for combating virulence mechanisms developed by pathogens. Molecules. 2020;25: 5763. doi:10.3390/molecules25245763

58. Wu HM, Church FC. Arginine 25 and Arginine 28 of lactoferrin are critical for effective heparin neutralization in blood. Arch Biochem Biophys. 2003;412: 121–125. doi:10.1016/S0003-9861(03)00035-3

59. Mann DM, Romm E, Migliorini M. Delineation of the glycosaminoglycan-binding site in the human inflammatory response protein lactoferrin. J Biol Chem. 1994;269: 23661–23667. doi:10.1016/s0021-9258(17)31566-1

60. Senkovich O, Cook WJ, Mirza S, Hollingshead SK, Protasevich II, Briles DE, et al. Structure of a complex of human lactoferrin N-lobe with Pneumococcal Surface Protein A provides insight into microbial defense mechanism. J Mol Biol. 2007;370: 701–713. doi:10.1016/j.jmb.2007.04.075

61. Ostan NKH, Yu RH, Ng D, Lai CCL, Pogoutse AK, Sarpe V, et al. Lactoferrin binding protein B - a bi-functional bacterial receptor protein. PLoS Pathog. 2017;13. doi:10.1371/journal.ppat.1006244

62. Wong H, Schryvers AB. Bacterial lactoferrin-binding protein A binds to both domains of the human lactoferrin C-lobe. Microbiology. 2003;149: 1729–1737. doi:10.1099/mic.0.26281-0

63. Mir R, Singh N, Vikram G, Sinha M, Bhushan A, Kaur P, et al. Structural and binding studies of C-terminal half (C-lobe) of lactoferrin protein with COX-2-specific non-steroidal anti-inflammatory drugs (NSAIDs). Arch Biochem Biophys. 2010;500: 196–202. doi:10.1016/j.abb.2010.05.026

64. Andrés MT, Fierro JF. Antimicrobial mechanism of action of transferrins: Selective inhibition of H+-ATPase. Antimicrob Agents Chemother. 2010;54: 4335–4342. doi:10.1128/AAC.01620-09

65. Nakanishi-Matsui M, Sekiya M, Nakamoto RK, Futai M. The mechanism of rotating proton pumping ATPases. Biochim Biophys Acta - Bioenerg. 2010;1797: 1343–1352. doi:10.1016/j.bbabio.2010.02.014

CHAPTER 6

Concluding remarks and future directions

6.1 Conclusions and final remarks

The main goal of the present thesis was to improve the knowledge on the mechanisms through which Lf exerts its cytotoxic activity against fungal and cancer cells, aiming to contribute to its rational, targeted and more efficient application. Since previous works from our group and our collaborators have identified proton pumping ATPases as targets of this protein in bacteria [1], yeast [2] and cancer cells [3], we focused our work on exploring the cellular consequences and downstream effects of targeting these proton pumps. A diverse collection of cell-based cellular, genetic and biochemical approaches in combination with computational tools were employed to achieve our goals. Our data are presented in three different chapters. Chapter 3 and Chapter 4 are dedicated to highlight the mechanisms underlying the antifungal and anticancer activities of Lf against *S. cerevisiae* and highly metastatic cancer cell lines, respectively, while Chapter 5 is focused on the development of a computational approach to predict how Lf and V-ATPase interact.

Regarding Lf antifungal activity, it has been previously demonstrated that hLf binds and inhibits Pma1p in *Candida albicans*, leading to intracellular acidification and ATP accumulation [2,4]. Given that lipid rafts were previously reported to be essential for Pma1p surface targeting, stability and oligomerization [5–8], we decided to study the role of these membrane microdomains in the context of Lf-driven fungal cytotoxicity. Our data demonstrated for the first time that bLf displays a lipid rafts-disrupting activity that greatly contributes to its cytotoxicity against fungi. Indeed, we showed that bLf induces intracellular accumulation of ergosterol, leading to lipid rafts disruption. Moreover, using yeast mutant strains lacking lipid rafts-associated proteins or enzymes involved in the synthesis of ergosterol and sphingolipids (the major lipid rafts components), we found that modifications of the composition of these membrane domains leads to an increased resistance of yeast cells to bLf-induced yeast cell death. In fact, the alterations in lipid rafts composition prevented bLf from perturbing lipid rafts and from affecting both Pma1p proton pumping and hydrolytic activities. Furthermore, when Pma1p-lipid rafts association was compromised by point mutations in Pma1p, or in the absence of the Pma1p-binding protein Ast1p, the bLf killing activity was impaired. Besides Pma1p, we also identified V-ATPase as a target of bLf in yeast cells. bLf inhibited V-ATPase proton pumping activity in isolated yeast vacuoles and promoted vacuolar alkalinization. Altogether, our results showed that the perturbation of lipid rafts and the inhibition of both Pma1p and V-ATPase activities mediate the antifungal activity of bLf. Since it is suggested that the combination of conventional antifungals with lipid rafts-disrupting compounds is a powerful antifungal approach, our data will help to pave the way for the use of bLf alone or in combination for the treatment/eradication of clinically and agronomically relevant yeast pathogens/fungi.

As for Lf anticancer activity, we have previously found that it is selectively cytotoxic to highly metastatic cancer cells in comparison with lowly metastatic and non-cancer cells [3,9]. This selectivity comes from its targeting to the proton pump V-ATPase, which is differentially located at the plasma membrane of highly metastatic cancer cells, but not in the other two cell types. Interestingly, and in line with the results obtained with the yeast model, our data revealed that bLf induces intracellular accumulation of cholesterol, the equivalent to ergosterol in mammalian cells, likely due to inhibition of its delivery to the plasma membrane caused by intracellular acidification following V-ATPase inhibition by bLf. This subsequently leads to cholesterol depletion from the plasma membrane and ensuing disruption of cholesterol-rich lipid rafts, in a way dependent on the presence of V-ATPase at the plasma membrane lipid rafts. As such, bLf did not affect the lipid rafts of human cells that do not display plasmalemmal V-ATPase. Accordingly, as with Pma1p, a close interplay between lipid rafts and V-ATPase has been reported, in which V-ATPase activity is critical for lipid rafts clustering and, in turn, lipid rafts integrity is essential for V-ATPase assembly and activity [10–12]. bLf-triggered lipid rafts disruption was also associated with cellular trafficking perturbations, as observed by delayed endocytosis of exosomes and their abnormal intracellular processing. Moreover, the perturbation of lipid rafts led to downregulation of PI3K and AKT, which are involved in the PI3K/AKT/mTOR pathway, one of the most important cell survival signalling pathways, whose effectors have been shown to co-localize with lipid rafts; and also to inhibition of glycolysis. Our results lay the foundation for future Lf-based targeted anticancer strategies, as they unravel a novel cascade of molecular events triggered by bLf that explains its selectivity for cancer cells displaying V-ATPase at the plasma membrane lipid rafts. Indeed, our data further reinforces the need for a personalized cancer treatment when choosing Lf as a therapeutic agent. Immunohistochemistry to find V-ATPase cellular localization should be performed in the cancer biopsies of a given patient before Lf therapy is prescribed. If V-ATPase is at the plasma membrane, Lf would be efficient; otherwise, the proton pump, the lipid rafts and, consequently, the cancer cells will not be affected.

Since a common feature among Lf-treated cancer [3] and fungal cells [13] is the inhibition of V-ATPase and given that a detailed elucidation of how Lf and V-ATPase interact is still missing, we aimed to fill this gap by employing a multi-level computational approach to find how these two proteins interact. Molecular dynamics (MD) simulations of both proteins were performed to obtain a robust sampling of their conformational landscape, followed by clustering, which allowed retrieving representative structures, to then perform protein-protein docking. Subsequently, MD simulations of the docked complexes and free binding energy calculations were carried out to evaluate the dynamic binding process and build a final

ranking based on the binding affinities. Detailed atomist analysis of the top ranked complexes clearly indicated that Lf binds to the V_1 cytosolic domain of V-ATPase. Particularly, our data suggest that Lf binds to the interfaces between A/B subunits, where the ATP hydrolysis occurs, inhibiting this process. The free energy decomposition analysis further identified key binding residues that will certainly aid in the rational design of follow-up experimental studies, thus bridging computational and experimental biochemistry.

Although the experimental part of this thesis was performed with bLf, in the computational work we used hLf. This choice was based on the resolution that was higher for the diferric hLf structure available (2.2 Å) than for the diferric bLf (2.8 Å). Nonetheless, both proteins share a great percentage of similarity (69% at the sequence level [14], and 77% at the mRNA level [15]) and have been shown to exhibit similar biological effects in different scenarios [16,17]. Particularly, in what regards Lf effect against yeast, hLf was previously shown to induce cell death [18], and to bind and inhibit Pma1p [2], as we also showed in our work with bLf. Importantly, a cluster of positively charged amino acid residues located at the Lf N-terminal domain constitutes an example of a surface patch identified in our work as very important for the interaction with V-ATPase that exists in both human and bovine Lfs [19]. As for V-ATPase, our computational work was performed with the yeast V-ATPase, since no structure of the human V-ATPase was available at the beginning of this work. In the meanwhile, the structure of human V-ATPase was published [20], nevertheless, it is important to refer that it holds an identical overall structure to the yeast counterpart.

One of the conclusions we retrieved by performing an overall analysis of the work presented in this thesis is the success of double targeting proton pumps and lipid rafts as a strategy to eradicate cancer cells and undesirable fungi. In contrast with the controversy that prevailed for years regarding the nature and relevance of lipid rafts for cellular functions, nowadays both their important physiological rules and their great potential as therapeutic targets are well recognized. Indeed, very recently, a set of interesting review articles were published that focus on the potential of lipid rafts as targets for cancer therapy [21], bacterial infections [22], and even as a strategy against SARS-CoV-2 [23,24], the virus that is causing the viral pandemic that started in 2020. As for proton pumps, they have long been recognized as appealing targets for various types of infections [25,26] and cancer [27,28]. The work herein presented suggests that by double targeting these two biological entities, Lf affects the overall pH and trafficking regulation, being thus effective against cancer and fungal cells (Figure 6.1). These effects may also occur in Lf-treated bacteria and multicellular fungi.

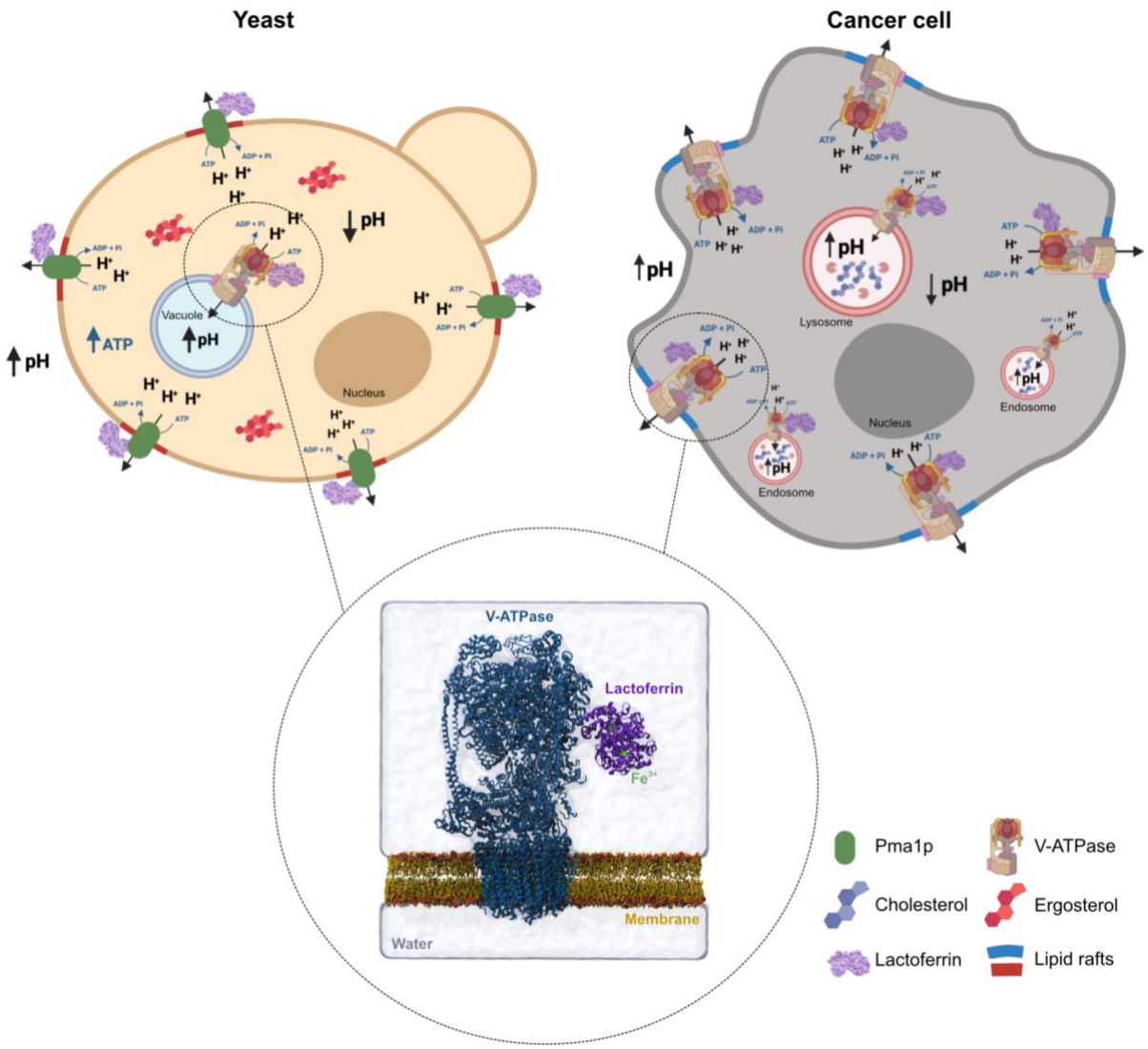

Figure 6.1: Comparison between Lf-driven perturbations of cellular pH and ergosterol/cholesterol localization in yeast and cancer cells. The main similarities between Lf-driven cellular effects in yeast and cancer cells are depicted as well as the predicted complex between the two proteins. These effects are a direct consequence of Pma1p and V-ATPase inhibition in yeast and yeast/cancer cells, respectively. The main cellular events include intracellular accumulation of ergosterol/cholesterol, lipid rafts disruption, intracellular acidification, extracellular acidification rate impairment and vacuolar/lysosomal alkalinization. The image within the circle represents the system containing the best scored complex that was submitted to the molecular dynamics simulations and free energy calculations in this work.

Additionally, our work highlights the power of yeast a model system to tackle the processes occurring in higher eukaryotes. Indeed, we have previously shown that Lf induces cell death through apoptosis in yeast [18] and then confirmed in highly metastatic cancer cells [3,9]. In this thesis, we further demonstrated that bLf impairs the extracellular acidification rate, disrupts lipid rafts and leads to intracellular accumulation of cholesterol/ergosterol, in both yeast and highly metastatic cancer cells (Figure 6.1). Wild type yeast cells thus appear as an excellent model to mimic Lf effect on highly

metastatic cancer cells and not non-cancer cells, because the former cell models display the Lf molecular target at their plasma membranes (Pma1p and V-ATPase, respectively), while non-cancer cells do not. Moreover, yeast has emerged as a versatile and robust model system in biology since it has several advantages over other experimental systems. For instance, many yeast genes and proteins are evolutionarily and functionally related with those of higher eukaryotes, and most of the fundamental cellular processes such as cell cycle control and apoptosis are well conserved [29,30]. Moreover, it has a short life-cycle, an easy handling and technical tractability, and a high rate of homologous recombination that allows its easy genetic manipulation and analysis of the resulting phenotypes [30,31]. In addition, this model has a huge set of available resources including a broad collection of mutants deleted in non-essential genes (the EUROSCARF collection) and dedicated integrated databases, which are easily accessible online [32]. Taking all of this into account, we can consider yeast as an authentic "launch pad" for novel discoveries regarding the mechanisms of action of Lf or of other compounds/drugs of interest, which can then be transposed to cell lines and/or animal models and be used to design more effective applications of these compounds.

6.2 Future directions

As every scientific work, our data answered several biological questions but also raised many new ones. Bellow, we suggest experimental follow-up studies and future directions that would be interesting to follow in order to address some of the new open questions and to further deepen our understanding of the mechanisms underlying Lf bioactivities.

6.2.1 Do Pma1p oligomerization, lipid rafts lipidic/proteic content and membrane biophysical properties matter for Lf cytotoxicity?

Regarding the effect of bLf treatment in yeast cells, the main open question is whether Pma1p oligomerization is crucial for the interaction between this proton pump and bLf, and if it determines the susceptibility of yeast cells to this protein. When trying to understand the bLf-resistance phenotype exhibited by the yeast mutant strains deleted in proteins or enzymes important for lipid rafts composition, we found that, despite bLf binding to Pma1p, the activity levels of the proton pump remained unchanged between bLf-treated and untreated cells. Given that neither the basal Pma1p activity, localization or expression levels of the mutant strains were different from the wild type strain, and that bLf was still able to bind Pma1p but not to inhibit it, the most reasonable explanation is that Pma1p acquires a different

conformation or oligomeric state within the already abnormally constituted lipid rafts, which impairs bLf inhibitory action. Thus, the future directions of this work should be to perform a deeper characterization of the consequences of eliminating Erg6p, Lac1p, Isc1p and Rvs161p proteins in terms of Pma1p oligomerization and conformation. Moreover, our data indicates that the reasons underlying the bLf-resistance phenotype of the mutant strains must be the unbalanced ceramide/complex sphingolipids ratio, accumulation of ergosterol precursors, or the lipid rafts abnormal protein content. However, the specific nature of these alterations is still unknown. Therefore, it would be interesting to isolate DRMs from these mutant strains and perform both lipidomic and proteomic studies to identify the specific alterations caused by the deletion of each gene. At the same time, those methodologies could be applied to the DRMs isolated from bLf-treated cells to ascertain its putative effects. Finally, biophysical approaches could be implemented to evaluate the properties of the mutants' plasma membranes including rigidity, fluidity, membrane order, among other parameters. It should also be worth assessing the effect of bLf on these features and also on Pma1p localization in the wild type cells. These experiments should help elucidate how Pma1p oligomerization and conformation and lipid rafts characteristics determine bLf cytotoxicity.

6.2.2 Which is the temporal order of the cellular alterations triggered by bLf, its specific localization and additional effectors?

Regarding bLf cytotoxicity against highly metastatic cancer cells, a novel set of intracellular events triggered by bLf was unravelled by our data. However, there are still some aspects and temporal relations that would be interesting to explore. One of the most intriguing questions regards the time course of the bLf-induced pH alterations: is the cytosolic acidification caused by plasmalemmal V-ATPase inhibition that causes the lysosomal and extracellular alkalinization? Or is the simultaneous inhibition of both plasmalemmal and lyso/endosomal V-ATPase that causes the overall pH deregulation? Measurement of the pH alterations caused by bLf along time in the different compartments (extracellular medium, cytosol and lysosomes/endosomes) should be performed to answer these questions. Our data show that bLf-induced perturbation of lipid rafts is associated with intracellular accumulation of cholesterol due to a hindrance of cholesterol delivery to the plasma membrane, rather than to its depletion from the plasma membrane as revealed by our time-lapse assay. Though the results suggest that cholesterol is sequestered within the lysosomes, experimental data to sustain this hypothesis is still missing. Co-localization with lysosomal markers and cholesterol quantification in lysosomal fractions could be performed to confirm this hypothesis. Additionally, since Lf is internalized as vesicle-like structures in the

cytosol, it would also be worth finding if those structures are endo/lysosomes and whether bLf co-localizes with V-ATPase in endo/lysosomal membranes of cancer cells. This kind of experiments should elucidate the chronological order of the cellular alterations triggered by bLf in highly metastatic cancer cells.

Regarding the inhibitory effect of bLf on the PI3K/AKT pathway, besides testing the levels of phosphorylated PI3K and AKT, it would be interesting to find if it is associated with perturbation of the localization of these signalling molecules out of the lipid rafts. For that, immunofluorescence of bLf-treated cells with lipid rafts markers and antibodies against for example PI3K and AKT could be performed. Alterations in the PI3K/AKT pathway are known to be associated with alterations in HIF-1α expression levels, which in turn regulate glycolysis. Given that we showed that bLf inhibits glycolysis, the next logical step would be to analyze the bLf effect on HIF-1α to better understand its effect on glycolysis and establish a straighter relation between the observed effects. Additionally, other upstream and downstream effectors of PI3K/AKT/mTOR pathway should be tested to unravel other signalling pathways affected by bLf.

The response of lowly metastatic cancer cells/non-cancer cells to bLf is still puzzling. Indeed, these cells are insensitive to bLf in terms of cytotoxicity, pH deregulation and lipid rafts disruption. Nonetheless, we showed that bLf is internalized in these cells, acquiring a similar cytosolic vesicle-like pattern as in the highly metastatic cancer cells. Though absence of plasmalemmal V-ATPase in lowly metastatic and non-cancer cells can partially explain their higher resistance to bLf, the bLf internalization would allow it to inhibit vesicular V-ATPase. However, no effect was detected. The most likely explanation for this phenotype is that these cells rely on pH control mechanisms that differ from the highly metastatic cancer cells, and that are activated when V-ATPase is inhibited by bLf, therefore compensating this bLf-inhibitory effect. Different experiments can be performed to clarify this issue, for example, measure the activity and expression of other membrane transporters, like the Na^+/H^+-ATPases, in bLf-treated non-cancer cells; or assess the sensitivity of non-cancer cells treated with bLf and inhibitors of such pH control transporters to find if they became sensitive to bLf. Moreover, bLf can suffer some conformational alteration when internalized in these cells that does not occur in the highly metastatic cancer cells. To assess this hypothesis, highly metastatic cancer cells could be incubated with whole cell extracts from bLf-treated cells to find if bLf loses its cytotoxic effect in extracts from non-cancer and lowly metastatic cancer cells.

6.2.3 How do Lf and V-ATPase interact *in vivo*?

Our computational approach identified ATP hydrolysis as the direct V-ATPase process inhibited by Lf. It also provided a set of Lf and V-ATPase residues that are predicted to be important for the proteins binding based on free energy calculations. Based on this, a considerable number of experimental

approaches can be designed to validate these computational results. First, since Lf seems to bind near the V-ATPase ATP binding site, it would be interesting to perform biochemical approaches to identify the type of interaction in comparison with ATP (competitive binding, non-competitive binding, etc) and characterize the inhibition kinetics. Our previous data with lysosomes isolated from rat liver suggest that an uncompetitive binding is more likely to occur since the percentage of ATP hydrolysis inhibition does not change with increasing ATP concentrations and both kinetic parameters (Vmax and Km) are altered [3]. However, a similar approach should be used in vacuoles isolated from yeast and with different Lf concentrations. Furthermore, a Lf expression system should be developed to produce Lf forms harbouring single or multiple mutations in the identified residues. These mutated forms could then be tested in terms of binding and inhibitory activity towards V-ATPase, to identify those whose mutation impairs the interaction. These results could next be validated by treating yeast and cancer cells with the mutated forms, to find whether mutated Lfs lose the ability to induce cytotoxicity. At the same time, the phenotypes of yeast mutants deleted in single V-ATPase subunits in response to Lf could be assessed. Alternatively, cryo-EM or X-ray crystallography of the V-ATPase-Lf complexes could be performed to clearly find how they interact. Altogether, these experiments would unravel the interaction between V-ATPase and Lf.

6.2.4 What more can be done?

Besides the experiments that could directly follow those performed in this thesis, our work can also be the basis for additional applied work. For example, to test if the newly identified antifungal mechanisms also occur in agronomically relevant multicellular fungi and clinical isolates and explore different combinations of bLf and antifungals for their eradication. Another challenge is to validate whether the bLf efficiency *in vivo* against cancer cells requires V-ATPase located at the plasma membrane lipid rafts. To this end, *in vivo* experiments using mice harbouring highly metastatic cancer cells with plasmalemmal V-ATPase and appropriate controls should be carried out. Also, computational and related experimental approaches similar to those used in this thesis could be performed to uncover the interaction between Lf and bacterial F-ATPase and/or fungal Pma1p, as we did for the yeast V-ATPase. This could allow identifying a putative conserved residues' signature required for the interaction between Lf and different types of proton pumps, which ultimately will unveil the molecular basis underlying the multifunctional activities against bacteria, yeast/fungi, as well as highly metastatic cancer cells.

References

1. Andrés MT, Fierro JF. Antimicrobial mechanism of action of transferrins: Selective inhibition of H+-ATPase. Antimicrob Agents Chemother. 2010;54: 4335–4342. doi:10.1128/AAC.01620-09

2. Andrés MT, Acosta-Zaldívar M, Fierro JF. Antifungal mechanism of action of lactoferrin: Identification of H+-ATPase (P3A-type) as a new apoptotic-cell membrane receptor. Antimicrob Agents Chemother. 2016;60: 4206–4216. doi:10.1128/AAC.03130-15

3. Pereira CS, Guedes JP, Gonçalves M, Loureiro L, Castro L, Gerós H, et al. Lactoferrin selectively triggers apoptosis in highly metastatic breast cancer cells through inhibition of plasmalemmal V-H+-ATPase. Oncotarget. 2016;7: 62144–62158. doi:10.18632/oncotarget.11394

4. Andrés MT, Acosta-Zaldívar M, González-Seisdedos J, Fierro JF. Cytosolic acidification is the first transduction signal of lactoferrin-induced regulated cell death pathway. Int J Mol Sci. 2019;20: 5838. doi:10.3390/ijms20235838

5. Gong X, Chang A. A mutant plasma membrane ATPase, Pma1-10, is defective in stability at the yeast cell surface. Proc Natl Acad Sci. 2001;98: 9104–9109. doi:10.1073/pnas.161282998

6. Bagnat M, Chang A, Simons K. Plasma membrane proton ATPase Pma1p requires raft association for surface delivery in yeast. Mol Biol Cell. 2001;12: 4129–4138. doi:10.1091/mbc.12.12.4129

7. Lee MCS, Hamamoto S, Schekman R. Ceramide biosynthesis is required for the formation of the oligomeric H+-ATPase Pma1p in the yeast endoplasmic reticulum. J Biol Chem. 2002;277: 22395–22401. doi:10.1074/jbc.M200450200

8. Wang Q, Chang A. Sphingoid base synthesis is required for oligomerization and cell surface stability of the yeast plasma membrane ATPase, Pma1. Proc Natl Acad Sci U S A. 2002;99: 12853–12858. doi:10.1073/pnas.202115499

9. Guedes J, Pereira C, Rodrigues L, Côrte-real M. Bovine milk lactoferrin selectively kills highly metastatic prostate cancer PC-3 and osteosarcoma MG-63 cells *in vitro*. Front Oncol. 2018;8: 1–12. doi:10.3389/fonc.2018.00200

10. Costa GA, de Souza SB, da Silva Teixeira LR, Okorokov LA, Arnholdt ACV, Okorokova-Façanha AL, et al. Tumor cell cholesterol depletion and V-ATPase inhibition as an inhibitory mechanism to prevent cell migration and invasiveness in melanoma. Biochim Biophys Acta - Gen Subj. 2018;1862: 684–691. doi:10.1016/j.bbagen.2017.12.006

11. Xu M, Xia M, Li XX, Han WQ, Boini KM, Zhang F, et al. Requirement of translocated lysosomal V1 H +-ATPase for activation of membrane acid sphingomyelinase and raft clustering in coronary endothelial cells. Mol Biol Cell. 2012;23: 1546–1557. doi:10.1091/mbc.E11-09-0821

12. Lafourcade C, Sobo K, Kieffer-Jaquinod S, Garin J, van der Goot FG. Regulation of the V-ATPase along the endocytic pathway occurs through reversible subunit association and membrane localization. PLoS One. 2008;3. doi:10.1371/journal.pone.0002758

13. Santos-Pereira C, Andrés MT, Chaves SR, Fierro JF, Gerós H, Manon S, et al. Lactoferrin perturbs lipid rafts and requires integrity of Pma1p-lipid rafts association to exert its antifungal activity against *Saccharomyces cerevisiae*. Int J Biol Macromol. 2021;171: 343–357. doi:10.1016/j.ijbiomac.2020.12.224

14. Pierce A, Colavizza D, Benaissa M, Maes P, Tartar A, Montreuil J, et al. Molecular cloning and sequence analysis of bovine lactotransferrin. Eur J Biochem. 1991;196: 177–84. doi:10.1111/j.1432-1033.1991.tb15801.x

15. Liao YL, Jiang RL, Lonnerdal B. Biochemical and molecular impacts of lactoferrin on small intestinal growth and development during early life. Biochem Cell Biol Biol Cell. 2012;90: 476–484. doi:10.1139/o11-075

16. El-Fakharany EM, Sánchez L, Al-Mehdar H a, Redwan EM. Effectiveness of human, camel, bovine and sheep lactoferrin on the hepatitis C virus cellular infectivity: comparison study. Virol J. 2013;10: 199. doi:10.1186/1743-422X-10-199

17. Zhang JL, Han X, Shan YJ, Zhang LW, Du M, Liu M, et al. Effect of bovine lactoferrin and human lactoferrin on the proliferative activity of the osteoblast cell line MC3T3-E1 in vitro. J Dairy Sci. 2018;101: 1827–1833. doi:10.3168/jds.2017-13161

18. Acosta-Zaldívar M, Andrés MT, Rego A, Pereira CS, Fierro JF, Côrte-Real M. Human lactoferrin triggers a mitochondrial- and caspase-dependent regulated cell death in *Saccharomyces cerevisiae*. Apoptosis. 2016;21: 163–173. doi:10.1007/s10495-015-1199-9

19. Baker HM, Baker EN. A structural perspective on lactoferrin function. Biochem Cell Biol. 2012;90: 320–328. doi:10.1139/o11-071

20. Wang L, Wu D, Robinson C V., Wu H, Fu T-M. Structures of a Complete Human V-ATPase Reveal Mechanisms of Its Assembly. Mol Cell. 2020;80: 501-511.e3. doi:10.1016/j.molcel.2020.09.029

21. Preta G. New insights into targeting membrane lipids for cancer therapy. Front Cell Dev Biol. 2020;8: 1–10. doi:10.3389/fcell.2020.571237

22. Yeh J, Lin H, Kuo C, Feng C. *Campylobacter jejuni* cytolethal distending toxin C exploits lipid rafts to mitigate *Helicobacter pylori*-induced pathogenesis. Front Cell Dev Biol. 2021;8: 1–10. doi:10.3389/fcell.2020.617419

23. Sviridov D, Miller YI, Ballout RA, Remaley AT, Bukrinsky M. Targeting lipid rafts - a potential therapy for COVID-19. Front Immunol. 2020;11: 1–5. doi:10.3389/fimmu.2020.574508

24. Sorice M, Misasi R, Riitano G, Manganelli V, Martellucci S, Longo A, et al. Targeting lipid rafts as a strategy against Coronavirus. Front Cell Dev Biol. 2021;8: 1–11. doi:10.3389/fcell.2020.618296

25. Ahmad Z, Okafor F, Azim S, F. Laughlin T. ATP Synthase: a molecular therapeutic drug target for antimicrobial and antitumor peptides. Curr Med Chem. 2013;20: 1956–1973. doi:10.2174/0929867311320150003

26. Yatime L, Buch-Pedersen MJ, Musgaard M, Morth JP, Winther AML, Pedersen BP, et al. P-type ATPases as drug targets: Tools for medicine and science. Biochim Biophys Acta - Bioenerg. 2009;1787: 207–220. doi:10.1016/j.bbabio.2008.12.019

27. Whitton B, Okamoto H, Packham G, Crabb SJ. Vacuolar ATPase as a potential therapeutic target and mediator of treatment resistance in cancer. Cancer Med. 2018;7: 3800–3811. doi:10.1002/cam4.1594

28. Kulshrestha A, Katara GK, Ibrahim SA, Riehl V, Sahoo M, Dolan J, et al. Targeting V-ATPase isoform restores cisplatin activity in resistant ovarian cancer: inhibition of autophagy, endosome function, and ERK/MEK pathway. J Oncol. 2019;2019: 2343876. doi:10.1155/2019/2343876

29. Carmona-Gutierrez D, Eisenberg T, Büttner S, Meisinger C, Kroemer G, Madeo F. Apoptosis in yeast: triggers, pathways, subroutines. Cell Death Differ. 2010;17: 763–773. doi:10.1038/cdd.2009.219

30. Duina AA, Miller ME, Keeney JB. Budding yeast for budding geneticists: A primer on the *Saccharomyces cerevisiae* model system. Genetics. 2014;197: 33–48. doi:10.1534/genetics.114.163188

31. Farrugia G, Balzan R. Oxidative stress and programmed cell death in yeast. Front Oncol. 2012;2: 1–21. doi:10.3389/fonc.2012.00064

32. Mell JC, Burgess SM. Yeast as a model genetic organism. Encycl Life Sci. 2002. doi:10.1038/npg.els.0000821

APPENDIX

Appendix Figures

Figure A1 - Exogenous addition of C2-ceramide sensitizes cells to bLf and rescues the resistance phenotype of the *lac1*Δ strain

Since *LAC1* encodes a component of ceramide synthase, the enzyme involved in the *de novo* synthesis of ceramide, we investigated the effect of exposing wild type and *lac1*Δ cells to exogenous addition of N-Acetyl-D-sphingosine (C2-ceramide), a membrane-permeable form of ceramide. For that purpose, and since C2-ceramide was found to induce cell death in yeast [1], we chose a non-toxic dose of this agent for both strains. The combined exposure of cells to bLf and C2-ceramide yielded a significantly higher sensitivity than the individual exposure to each compound in both strains. Notably, the resistance of the *lac1*Δ mutant is rescued by addition of C2-ceramide, as it becomes more sensitive than wild type cells treated only with bLf.

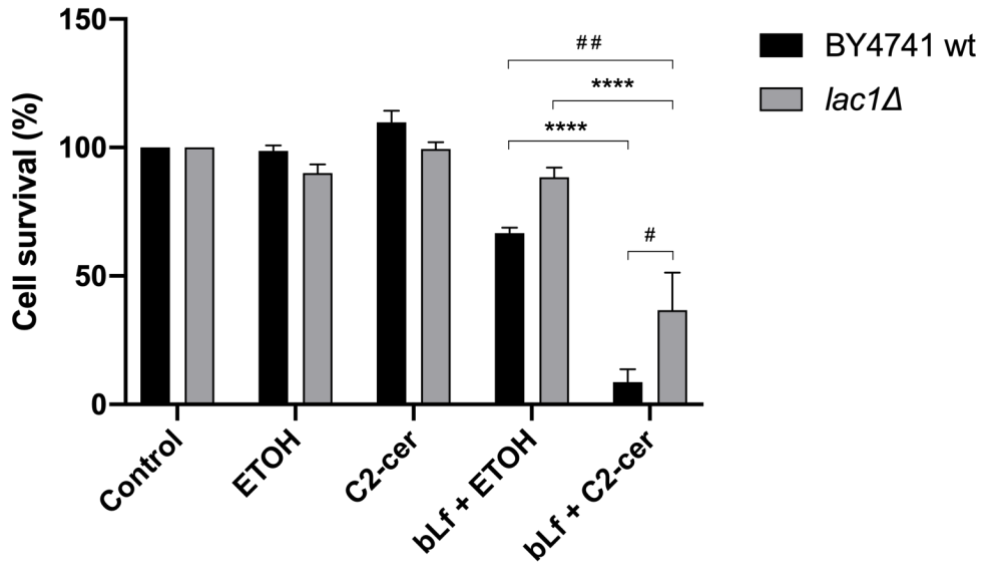

Figure A1: Exogenous addition of C2-ceramide sensitizes cells to bLf and rescues the higher resistance of the *lac1*Δ strain. Cell survival assays of *S. cerevisiae* BY4741 wild type and *lac1*Δ mutant strains after 90 min of incubation at 30 ˚C with 250 µg/ml bLf and/or 20 µM C2-ceramide (C2-cer) in 10 mM Tris-HCl, pH 7.4, evaluated by colony forming units counting. Absolute ethanol (ETOH) is the C2-cer solvent. Values are mean ± standard deviation normalized to time zero of incubation and considering the control without bLf as 100% cell survival. **** P<0.0001 between the indicated conditions in the same strain; * P<0.05, ## P<0.01 between the indicated conditions of different strains.

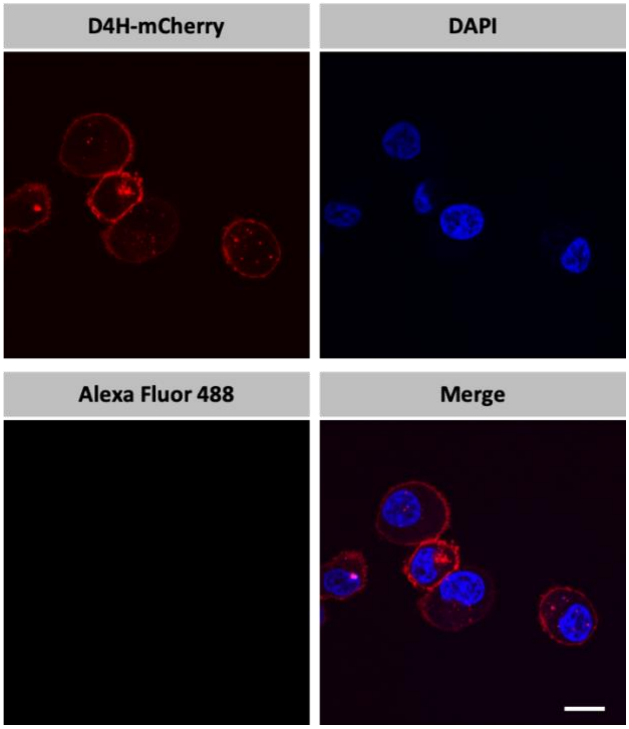

Figure A2: Specificity control of immunofluorescence experiments. PC-3 cells were transfected with the D4H-mCherry cholesterol biosensor, following which the immunofluorescence control was performed by incubating cells only with the secondary antibody Alexa Fluor 488 (no primary antibody was added). No fluorescence was detected using the same intensity settings attesting the specific labelling of V-ATPase *c* subunit observed in Figure 4.1A (green fluorescence). Nuclei were stained with DAPI. Bar: 10 μm.

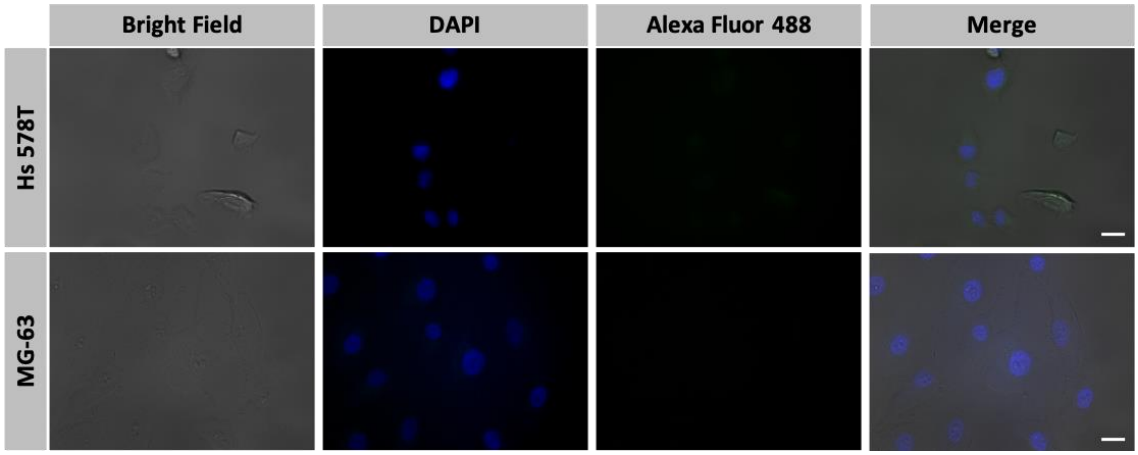

Figure A3: Specificity control of bLf uptake experiments. Hs 578T and MG-63 cells were incubated for 24 h with free Alexa Fluor 488 submitted to the exact same procedure used to produce Alexa Fluor 488-labelled bLf. No fluorescence was detected on the green channel demonstrating that the green staining shown in Figure 4.4 is indeed specific for bLf. Nuclei were stained with DAPI. Bar: 20 μm.

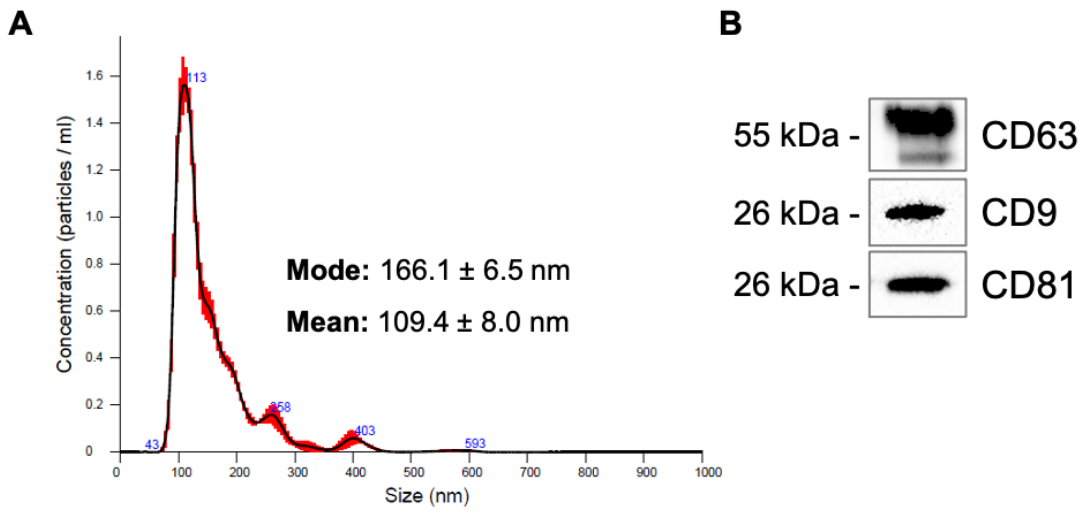

Figure A4: Characterization of exosomes derived from Bj-5ta cell line. (A) Size distribution/concentration determined by nanoparticle tracking analysis. **(B)** Western blot analysis for the putative exosomal markers CD63, CD9 and CD81.

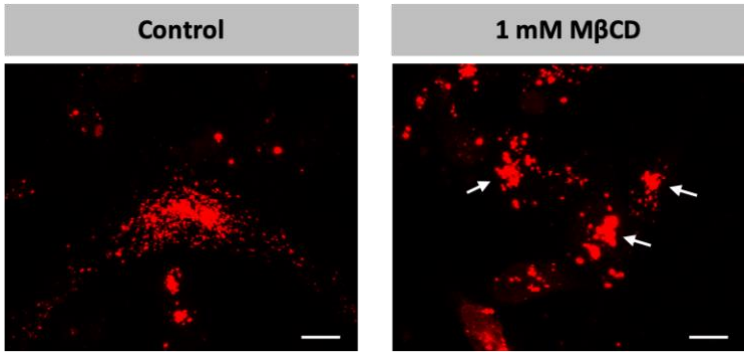

Figure A5: Methyl-β-cyclodextrin perturbs the intracellular trafficking of exosomes. Representative fluorescence microscopy images of MDA-MDA-231 cells incubated with 1 mM MβCD for 24 h and then incubated for 24 h with DiI-labelled exosomes derived from Bj-5ta cell line. Arrows point to aggregated exosomes. Bar: 10 μm.

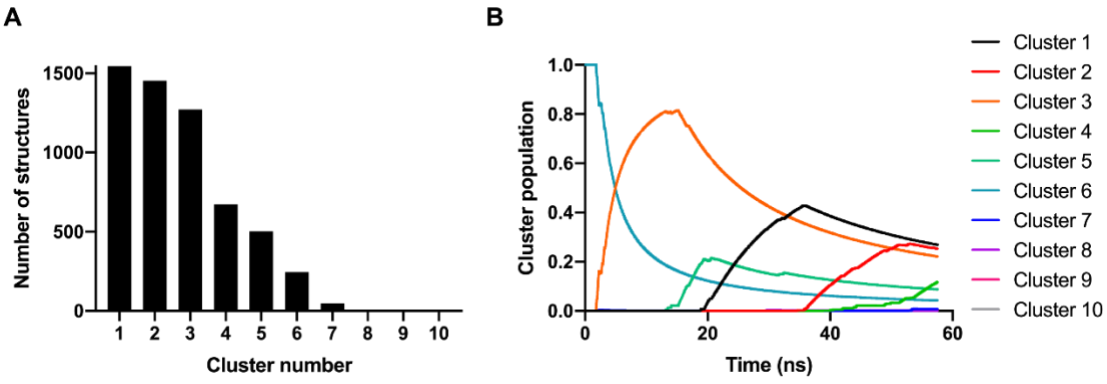

Figure A6: Lactoferrin molecular dynamics clustering results. (A) Total number of frames in each cluster. **(B)** Cluster population distribution along the last 55 ns of the MD simulation.

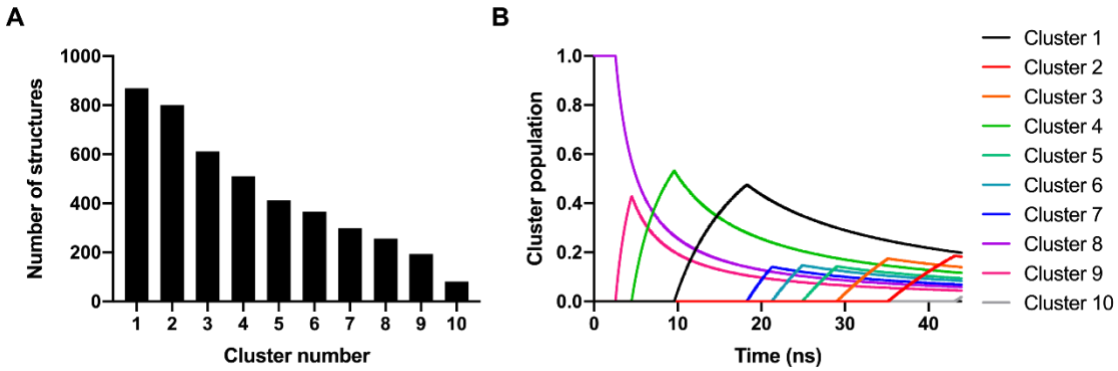

Figure A7: V-ATPase molecular dynamics clustering results. (A) Total number of frames in each cluster. **(B)** Cluster population distribution along the last 45 ns of the MD simulation.

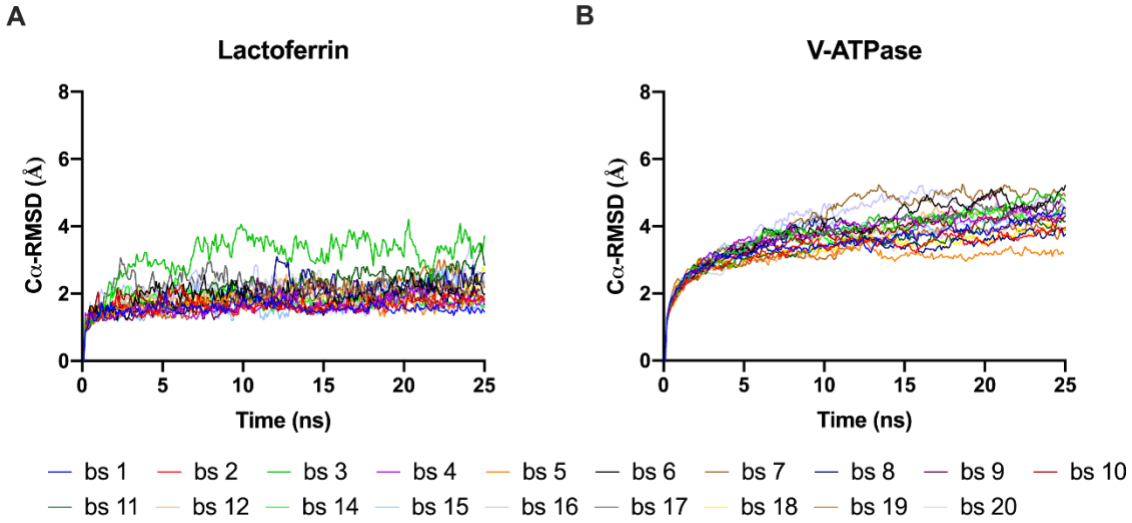

Figure A8: Analysis of the molecular dynamics simulations of docked complexes. RMSD values of the backbone Cα atoms as a function of time along the 25 ns of simulation for the lactoferrin **(A)** and V-ATPase **(B)** atoms. Each docking solutions is represented by a different colour. The final minimized and equilibrated structure was taken as a reference point.

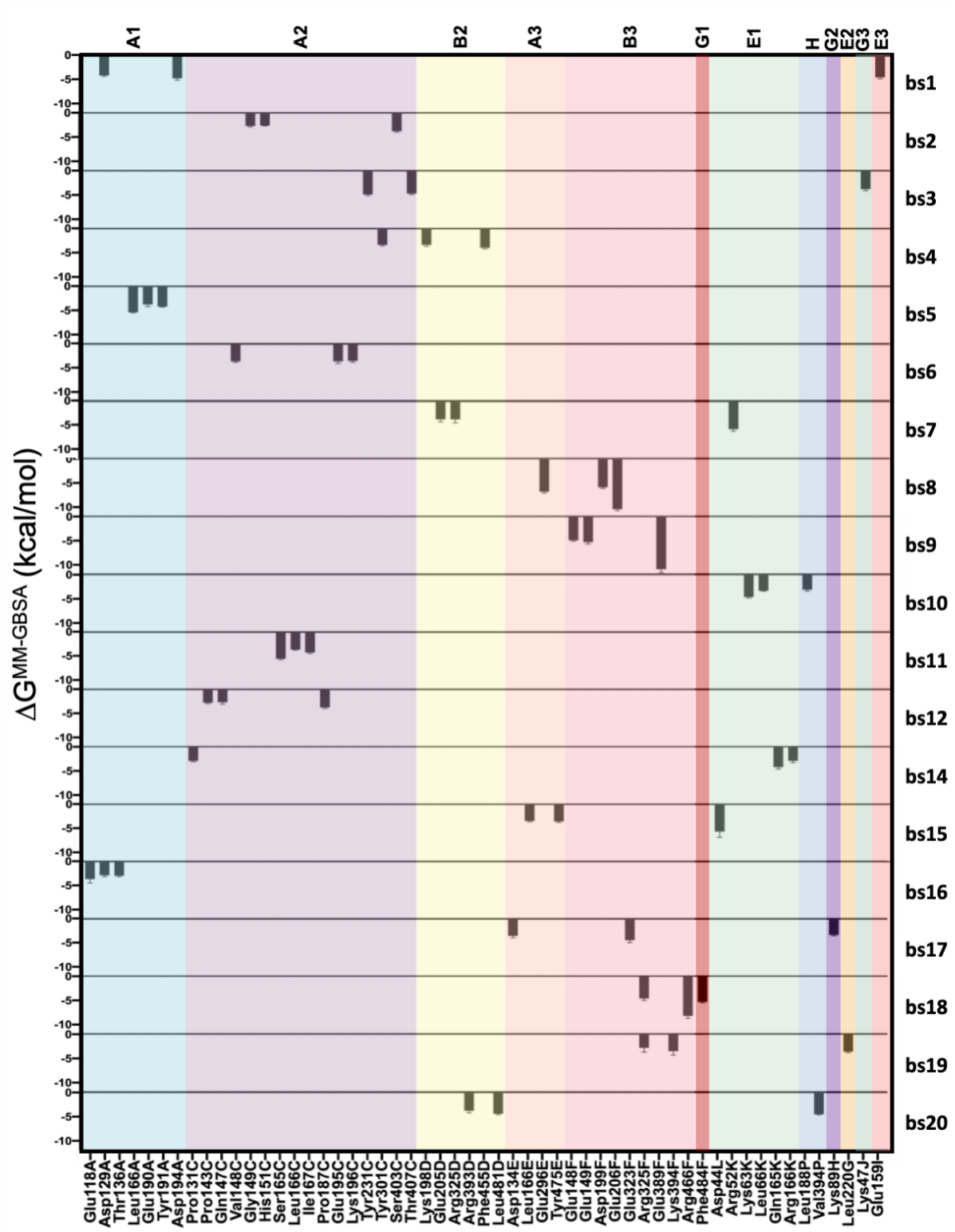

Figure A9: Analysis of the V-ATPase decomposition of the free binding energy calculated using the MM-GBSA method. Per-residue ΔG in kcal/mol ± standard deviation of the three V-ATPase amino acids with higher contribution to the total free binding energy in each docking solution (bs1-bs20) and respective V-ATPase subunit (A1, A2, A3, B2, B3, E1, E3, G1, G2, G3 and H).

Appendix Tables

Table A1: Effect of V-ATPase inhibition by several inhibitors or siRNA against different types of cancer cells.

Cancer type	Model	V-ATPase inhibition approach	Evidences	Reference
Esophageal	TE-1 and ECA-109 cell lines	Diphyllin	Cell proliferation, migration, mTORC1/HIF-1α/VEGF pathway inhibition and cell cycle arrest	[2]
Liver	HepG2 cell line	ZT-25 (diphyllin derivative)	Apoptosis induction, cell cycle arrest, mitochondrial membrane potential perturbation, ATP depletion, pro-apoptotic proteins increase, anti-apoptotic proteins decrease, autophagy induction, reactive oxygen species production	[3]
Melanoma	B16F0 and B16F10 cell lines, and mice harbouring B16F10 cells	Myrtenal	*In vitro*: cell death induction, migration inhibition/ *In vivo*: metastasis inhibition	[4]
Breast	MDA-MB-231 and Hs578T cell lines	Lactoferrin	Proliferation inhibition, apoptosis induction, extracellular acidification rate decrease and intracellular acidification	[5]
Osteosarcoma, breast, prostate	MDA-MB-231, PC-3, MG-63 cell lines		Cell death induction, cell proliferation inhibition, lysosomal pH perturbation and intracellular acidification	[6]
Breast	MDA-MB-231 cell line	Cleistanthin A	Migration/invasion inhibition, MMP-2/9 and β-catenin expression decrease	[7]
Melanoma	A375 cell line		Migration/invasion inhibition, MMP-2/9 expression decrease, lysosomal pH alteration	[8]
Colorectal, liver, cervical	HT-29, HepG2, and HeLa cell lines	ECDD-S27 (cleistanthin A derivative)	Cell survival reduction, autophagic flux inhibition	[9]
Breast and ovarian	MDA-MB-468, MDA-MB-231, MCF-7, A2780, Cis-A2780 and PA-1 cell lines	Bisbenzimidazole derivative (2e)	Cell viability diminishing	[10]
Breast	MCF-7 and MDA-MB-231 cell lines	Vitamin D	Acidification of intracellular organelles decrease, extracellular pH alkalinization, migration inhibition, cell stiffness diminution	[11]

Table A1: Effect of V-ATPase inhibition by several inhibitors or siRNA against different types of cancer cells (cont).

Cancer type	Model	V-ATPase inhibition approach	Evidences	Reference
Gastric, melanoma	Vincristine-induced multidrug resistance SGC7901/VCR cell line, mice harbouring A375 cells	Verucopeptin	*In vitro*: V-ATPase and mTORC1 inhibition, cell proliferation impairment/ *In vivo*: tumor growth decrease	[12]
Hepatocellular carcinoma	HUH-7 and HepG2 cell lines, mice harbouring HUH-7 cells	Archazolid A	*In vitro*: Depletion of free cholesterol, migration/invasion and cell proliferation inhibition/ *In vivo*: reduction of tumor size and growth rate	[13]
Breast	Immortalized human mammary epithelial cells transduced with Twist1-ER		Epithelial-mesenchymal transition impairment, inhibition of tumor initiation cells generation, E-cadherin recycling perturbation	[14]
Leukemia	Jurkat T cell line		Growth/proliferation inhibition, cell death induction, cell cycle arrest, iron metabolism inhibition	[15]
Breast	MDA-MB-231, MCF-7 and 4T1 cell lines, and mice harbouring 4T1 cells	Archazolid A, $V_o c$ siRNA	*In vitro*: iron deprivation, cell cycle arrest, double stranded DNA breaks, apoptosis induction/ *In vivo*: tumor growth reduction, caspase-3 activation	[16]
Breast	MDA-MB-231, T-47D and MCF-7 cell lines	Lansoprazole, omeprazole, pantoprazole and raloxifene	Cell proliferation inhibition, cell death triggering	[17]
Oral epidermoid carcinoma	KB and KB/V cell lines	Pantoprazol	Cell proliferation inhibition, lysosomal pH alteration, inhibition of lysosomal enzyme activity	[18]
Ovarian	Paclitaxel-resistant A2780/Taxol cell line	Esomeprazole	Viability decrease, paclitaxel-mediated cell death increase, V_1D_1 subunit protein levels reduction, cytosolic acidification	[19]
Lung	Paclitaxel-resistant A549/Taxol cell line		pH decrease via V-ATPase inhibition, paclitaxel-mediated cell death and cell cycle arrest increase	[20]
Bladder, colorectal, renal	T-24, HCT116 and RCC4 cell lines	Bafilomycin A1, Concanamycin A, Diphyllin	Cell growth inhibition, acidification of intracellular compartments impairment, amino acid levels decrease, endoplasmic reticulum stress, micropinocytosis inhibition	[21]
Mantle cell lymphoma	Z138, GRANTA-519 and JEKO-1 cell lines	Bafilomycin A1, Concanamycin A	Proliferation inhibition preferentially in cells expressing low levels of the neural transcription factor SOX11	[22]

Table A1: Effect of V-ATPase inhibition by several inhibitors or siRNA against different types of cancer cells (cont).

Cancer type	Model	V-ATPase inhibition approach	Evidences	Reference
Prostate	PC-3 cell line		F-actin cytoskeleton reorganization, endo-lysosomal pH increase, vesicle trafficking impairment, migration/invasion inhibition	[23]
Prostate	LNCaP and PC-3 cell lines	Bafilomycin A1	Lipid droplets velocity decrease and alteration of intracellular distribution of lipid droplets	[24]
Melanoma	B16F0 and B16F10 cell lines	Concanamycin A	Migration/invasion and H^+ efflux inhibition	[25]
Prostate	LAPC4 and LNCaP cell lines		Repression of androgen receptor expression, decreased levels of prostate-specific antigen	[26]
Breast	MDA-MB231 cell line		Cathepsin B activity and expression decrease	[27]
Pancreatic	BxPC-3 and Panc-1 cell lines		Proliferation inhibition, cell death induction, autophagic flux decrease	[28]
Prostate	PC-3M-1E8, PC-3M, PC-3 and PC-3M-2B4 cell lines	V_oc siRNA	Migration/invasion inhibition, MMP-9 activation decrease and extracellular [H^+] diminishing	[29]
Prostate	PC-3M-1E8 cell line		Migration/invasion and MMP-9 activity inhibition	[29]
Ovarian	Cisplatin resistant cis-A2780 cell line	V_oa2 shRNA	Sphere-forming ability decrease, cisplatin-mediated cell death increase, early endosome trafficking disruption	[30]
Breast	Mice harbouring 4T1 wild type or V_oa2 shRNA cells		Tumour growth delay, increased number of M1 antitumor macrophages	[31]
Esophageal	TE8 cell line	V_1E1 siRNA	Cell motility, glucose uptake, lactate levels and ATP production decrease, glycolytic enzyme expression inhibition	[32]
Ovarian	A2780 and SKOV-3 cell lines, mice harbouring A2780 cells	V_oa2 antibody	*In vitro*: V-ATPase inhibition/ *In vivo*: tumor growth delay, high immune cell infiltration, caspase-3 expression increase, apoptosis-related genes upregulation	[33]

Table A2: List of lactoferrin 3D structures. The structure used in this work is identified in bold.

PDB code	Name	Year of publication	Resolution	Method	Species	Mutations
1B0L	Recombinant diferric hLf	1999	2.2 Å	X-ray diffraction	*Homo sapiens*	1
1LFG	**Diferric hLf**	**1994**	**2.2 Å**	**X-ray diffraction**	***Homo sapiens***	**0**
1BLF	Diferric bLf	1997	2.8 Å	X-ray diffraction	*Bos taurus*	0
1CB6	Human apo-Lf	1999	2.0 Å	X-ray diffraction	*Homo sapiens*	0
1DTZ	Camel apo-Lf	2001	2.65 Å	X-ray diffraction	*Camelus dromedarius*	0
1B1X	Diferrin mare Lf	1999	2.62 Å	X-ray diffraction	*Equus caballus*	0
1BIY	Diferrin buffalo Lf	1999	3.37 Å	X-ray diffraction	*Bubalus bubalis*	0
1CE2	Diferrin buffalo Lf	1999	2.5 Å	X-ray diffraction	*Bubalus bubalis*	0
1FCK	Diceric hLf	2001	2.2 Å	X-ray diffraction	*Homo sapiens*	0
1LCF	Copper- and oxalate-substituted hLf	1994	2.0 Å	X-ray diffraction	*Homo sapiens*	0

Table A3: List of V-ATPase 3D structures. The structures used in this work are identified in bold. Vph1 and Stv1 are the vacuolar and Golgi *a* subunits of V_o complex, respectively. The states correspond to the different rotational states of V-ATPase and the percentual values refer to the relative abundance of each state.

PDB code	Name	Year of publication	Resolution	Method	Species	Mutations
BIOLOGICAL ASSEMBLY OF THE V-ATPASE MULTI-SUBUNIT COMPLEX						
3J9T (state 1) - 47% 3J9U (state 2) - 36% 3J9V (state 3) - 17%	**V-ATPase Vph1- V_1V_o**	**2015**	**6.9 Å (state 1)**	**Electron microscopy**	***Saccharomyces cerevisiae***	**0**
6O7V (state 1) - 49% 6O7W (state 2) - 37% 6O7X (state 3) - 14%	V-ATPase Stv1-V_1V_o	2019	6.6 Å (state 1)	Electron microscopy	*Saccharomyces cerevisiae*	0
5VOX (state 1) - 49% 5VOY (state 2) - 23% 5VOZ (state 3) - 28%	Yeast V-ATPase in complex with *Legionella pneumophila* effector SidK	2017	6.8 Å (state 1)	Electron microscopy	*Saccharomyces cerevisiae*	0
BIOLOGICAL ASSEMBLY OF V_o OR V_1 DOMAINS						
6C6L	V-ATPase V_o in lipid nanodisc	2018	3.5 Å	Electron microscopy	*Saccharomyces cerevisiae*	0
5TJ5	Membrane-embedded V-ATPase (V_o)	2016	3.9 Å	Electron microscopy	*Saccharomyces cerevisiae*	0
5BW9	V-ATPase V_1 in the autoinhibited form	2016	7 Å	X-ray diffraction	*Saccharomyces cerevisiae*	0
6O7T	**V-ATPase Vph1-V_o**	**2019**	**3.2 Å**	**Electron microscopy**	***Saccharomyces cerevisiae***	**0**
5D80	V-ATPase V_1 in the autoinhibited form	2016	6.2 Å	X-ray diffraction	*Saccharomyces cerevisiae*	0

Appendix References

1. Carmona-Gutierrez D, Reisenbichler A, Heimbucher P, Bauer MA, Braun RJ, Ruckenstuhl C, et al. Ceramide triggers metacaspase-independent mitochondrial cell death in yeast. Cell Cycle. 2011;10: 3973–3978. doi:10.4161/cc.10.22.18212

2. Chen H, Liu P, Zhang T, Gao Y, Zhang Y, Shen X, et al. Effects of diphyllin as a novel V-ATPase inhibitor on TE-1 and EC A-109 cells. Oncol Rep. 2018;39: 921–928. doi:10.3892/or.2018.6191

3. Lu Y, Zhang R, Liu S, Zhao Y, Gao J, Zhu L. ZT-25, a new vacuolar H+-ATPase inhibitor, induces apoptosis and protective autophagy through ROS generation in HepG2 cells. Eur J Pharmacol. 2016;771: 130–138. doi:10.1016/j.ejphar.2015.12.026

4. Martins BX, Arruda RF, Costa GA, Jerdy H, de Souza SB, Santos JM, et al. Myrtenal-induced V-ATPase inhibition - A toxicity mechanism behind tumor cell death and suppressed migration and invasion in melanoma. Biochim Biophys Acta - Gen Subj. 2019;1863: 1–12. doi:10.1016/j.bbagen.2018.09.006

5. Pereira CS, Guedes JP, Gonçalves M, Loureiro L, Castro L, Gerós H, et al. Lactoferrin selectively triggers apoptosis in highly metastatic breast cancer cells through inhibition of plasmalemmal V-H+-ATPase. Oncotarget. 2016;7: 62144–62158. doi:10.18632/oncotarget.11394

6. Guedes J, Pereira C, Rodrigues L, Côrte-real M. Bovine milk lactoferrin selectively kills highly metastatic prostate cancer PC-3 and osteosarcoma MG-63 cells *in vitro*. Front Oncol. 2018;8: 1–12. doi:10.3389/fonc.2018.00200

7. Liu S, Wang L, Ding W, Wang D, Wang X, Luo Q, et al. Cleistanthin A inhibits the invasion of MDA-MB-231 human breast cancer cells: involvement of the β-catenin pathway. Pharmacol Reports. 2020;72: 188–198. doi:10.1007/s43440-019-00012-1

8. Pan S, Cai H, Gu L, Cao S. Cleistanthin A inhibits the invasion and metastasis of human melanoma cells by inhibiting the expression of matrix metallopeptidase-2 and-9. Oncol Lett. 2017;14: 6217–6223. doi:10.3892/ol.2017.6917

9. Paha J, Kanjanasirirat P, Munyoo B, Tuchinda P, Suvannang N, Nantasenamat C, et al. A novel potent autophagy inhibitor ECDD-S27 targets vacuolar ATPase and inhibits cancer cell survival. Sci Rep. 2019;9: 1–16. doi:10.1038/s41598-019-45641-x

10. Patil R, Kulshrestha A, Tikoo A, Fleetwood S, Katara G, Kolli B, et al. Identification of novel bisbenzimidazole derivatives as anticancer vacuolar (H+)-ATPase inhibitors. Molecules. 2017;22: 1–14. doi:10.3390/molecules22091559

11. Santos JM, Hussain F. VD3 mitigates breast cancer aggressiveness by targeting V-H+-ATPase. J Nutr Biochem. 2019;70: 185–193. doi:10.1016/j.jnutbio.2019.05.005

12. Wang Y, Zhang L, Wei Y, Huang W, Li L, Wu A an, et al. Pharmacological targeting of Vacuolar H+-ATPase via subunit V_1G combats multidrug-resistant cancer. Cell Chem Biol. 2020;27: 1359–1370. doi:10.1016/j.chembiol.2020.06.011

13. Bartel K, Winzi M, Ulrich M, Koeberle A, Menche D, Werz O, et al. V-ATPase inhibition increases

cancer cell stiffness and blocks membrane related Ras signaling - A new option for HCC therapy. Oncotarget. 2017;8: 9476–9487. doi:10.18632/oncotarget.14339

14. Merk H, Messer P, Ardelt M, Lamb D, Zahler S, Muller R, et al. Inhibition of the V-ATPase by Archazolid A: a new strategy to inhibit EMT. Mol Cancer Ther. 2017;16: 2329–2339.

15. Zhang S, Schneider LS, Vick B, Grunert M, Menche D, Müller R, et al. Anti-leukemic effects of the V-ATPase inhibitor Archazolid A. Oncotarget. 2015;6: 43508–43528.

16. Schneider LS, Schwarzenberg K Von, Lehr T, Ulrich M, Liebl J, Trauner D, et al. Vacuolar-ATPase inhibition blocks iron metabolism to mediate therapeutic effects in breast cancer. Cancer Res. 2015;75: 2863–2874. doi:10.1158/0008-5472.CAN-14-2097

17. Ihraiz WG, Ahram M, Bardaweel SK. Proton pump inhibitors enhance chemosensitivity, promote apoptosis, and suppress migration of breast cancer cells. Acta Pharm. 2020;70: 179–190. doi:10.2478/acph-2020-0020

18. Lu ZN, Shi ZY, Dang YF, Cheng YN, Guan YH, Hao ZJ, et al. Pantoprazole pretreatment elevates sensitivity to vincristine in drug-resistant oral epidermoid carcinoma *in vitro* and *in vivo*. Biomed Pharmacother. 2019;120: 109478. doi:10.1016/j.biopha.2019.109478

19. He J, Shi XY, Li ZM, Pan XH, Li ZL, Chen Y, et al. Proton pump inhibitors can reverse the YAP mediated paclitaxel resistance in epithelial ovarian cancer. BMC Mol Cell Biol. 2019;20: 1–14. doi:10.1186/s12860-019-0227-y

20. Bai Z, Ding N, Ge J, Wang Y, Wang L, Wu N, et al. Esomeprazole overcomes paclitaxel-resistance and enhances anticancer effects of paclitaxel by inducing autophagy in A549/Taxol cells. Cell Biol Int. 2020. doi:10.1002/cbin.11481

21. Kitazawa S, Nishizawa S, Nakagawa H, Funata M, Nishimura K, Soga T, et al. Cancer with low cathepsin D levels is susceptible to vacuolar (H+)-ATPase inhibition. Cancer Sci. 2017;108: 1185–1193. doi:10.1111/cas.13240

22. Emruli VK, Olsson R, Ek F, Ek S. Identification of V-ATPase as a molecular sensor of SOX11-levels and potential therapeutic target for mantle cell lymphoma. BMC Cancer. 2016;16: 1–9. doi:10.1186/s12885-016-2550-4

23. Licon-Munoz Y, Michel V, Fordyce CA, Parra KJ. F-actin reorganization by V-ATPase inhibition in prostate cancer. Biol Open. 2017;6: 1734–1744. doi:10.1242/bio.028837

24. Nardi F, Fitchev P, Brooks KM, Franco OE, Cheng K, Hayward SW, et al. Lipid droplet velocity is a microenvironmental sensor of aggressive tumors regulated by V-ATPase and PEDF. Lab Investig. 2019;99: 1822–1834. doi:10.1038/s41374-019-0296-8

25. Costa GA, de Souza SB, da Silva Teixeira LR, Okorokov LA, Arnholdt ACV, Okorokova-Façanha AL, et al. Tumor cell cholesterol depletion and V-ATPase inhibition as an inhibitory mechanism to prevent cell migration and invasiveness in melanoma. Biochim Biophys Acta - Gen Subj. 2018;1862: 684–691. doi:10.1016/j.bbagen.2017.12.006

26. Licon-Munoz Y, Fordyce CA, Hayek SR, Parra KJ. V-ATPase-dependent repression of androgen

receptor in prostate cancer cells. Oncotarget. 2018;9: 28921–28934. doi: 10.18632/oncotarget.25641

27. Uhlman A, Folkers K, Liston J, Pancholi H, Hinton A. Effects of Vacuolar H+-ATPase inhibition on activation of cathepsin B and cathepsin L secreted from MDA-MB231 breast cancer cells. Cancer Microenviron. 2017;10: 49–56. doi:10.1007/s12307-017-0196-7

28. Flinck M, Hagelund S, Gorbatenko A, Severin M, Pedraz-Cuesta E, Novak I, et al. The Vacuolar H+ ATPase α3 subunit negatively regulates migration and invasion of human pancreatic ductal adenocarcinoma cells. Cells. 2020;9: 1–22. doi:10.3390/cells9020465

29. Zou P, Yang Y, Xu X, Liu B, Mei F, You J, et al. Silencing of vacuolar ATPase c subunit ATP6V0C inhibits the invasion of prostate cancer cells through a LASS2/TMSG1-independent manner. Oncol Rep. 2018;39: 298–306. doi:10.3892/or.2017.6092

30. Kulshrestha A, Katara GK, Ibrahim SA, Riehl V, Sahoo M, Dolan J, et al. Targeting V-ATPase isoform restores cisplatin activity in resistant ovarian cancer: inhibition of autophagy, endosome function, and ERK/MEK pathway. J Oncol. 2019;2019: 2343876. doi:10.1155/2019/2343876

31. Katara GK, Kulshrestha A, Jaiswal MK, Pamarthy S, Gilman-Sachs A, Beaman KD. Inhibition of vacuolar ATPase subunit in tumor cells delays tumor growth by decreasing the essential macrophage population in the tumor microenvironment. Oncogene. 2016;35: 1058–1065. doi:10.1038/onc.2015.159

32. Son SW, Kim SH, Moon EY, Kim DH, Pyo S, Um SH. Prognostic significance and function of the vacuolar H+-ATPase subunit V1E1 in esophageal squamous cell carcinoma. Oncotarget. 2016;7: 49334–49348. doi:10.18632/oncotarget.10340

33. Kulshrestha A, Katara GK, Ibrahim SA, Riehl VE, Schneiderman S, Bilal M, et al. *In vivo* anti-V-ATPase antibody treatment delays ovarian tumor growth by increasing antitumor immune responses. Mol Oncol. 2020;14: 2436–2454. doi:10.1002/1878-0261.12782